

**The Growth of Brightest Cluster
Galaxies and Intracluster Light in X-ray
Selected Clusters**

Kate Emily Furnell

A thesis submitted in partial fulfilment of the requirements of
Liverpool John Moores University for the degree of Doctor of Philosophy

June 2019

Declaration

The work presented in this thesis was carried out at the Astrophysics Research Institute, Liverpool John Moores University. Unless otherwise stated, it is the original work of the author.

While registered as a candidate for the degree of Doctor of Philosophy, for which submission is now made, the author has not been registered as a candidate for any other award. This thesis has not been submitted in whole, or in part, for any other degree.

Kate Emily Furnell
Astrophysics Research Institute
Liverpool John Moores University,
IC2,
Liverpool Science Park,
146 Brownlow Hill,
Liverpool,
L3 5RF

SEPTEMBER 2019

Abstract

In this work, we examine the properties with respect to environment of brightest cluster galaxies (BCGs), the most massive population of galaxies in the known Universe, and also, the link between these galaxies and the intracluster light component (ICL) within galaxy clusters. The ICL is a flat, diffuse, low surface brightness (LSB) feature thought to contain a significant fraction of stellar mass contained within galaxy clusters; it is believed primarily to be formed from stripped stars during galaxy-galaxy interactions in the cluster core. Through our work, we attempt to discern the well-known observational and theoretical tensions which exist regarding the accretion history of stellar mass in the cores of galaxy clusters, as well as attempting to address some of the commonly-known systematics that accompany such studies.

In Part I (Chapters 2-3), we analyse the structural parameters of a sample of 329 optically-confirmed, X-ray selected clusters in the SPectroscopic IDentification of eROSITA Sources Survey (SPIDERS) out to $z \sim 0.3$ with respect to three environmental properties (velocity dispersion-based halo mass, X-ray luminosity and optical richness). We quantify the morphologies of our BCGs by modelling their light profiles using GALFIT 3 (via the SIGMA pipeline), which we also use to obtain integrated magnitude-based stellar masses. We test the software thoroughly using $\sim 20,000$ mock galaxies implanted across 8 arbitrary cluster fields within our sample, which include field PSF convolutions and an idealised Poisson noise component. We find that we are able to recover our SDSS r -band profiles (with similar results in i and g) accurately out to ~ 16.5 magnitudes; fainter than this, we begin to observe biases in our results, especially in recovered Sérsic index; such surface brightness-dependent structural biases have important consequences for evolutionary claims regarding BCG structure. Regarding environment, we find no evidence for any correlations between the structural properties of our science sample of 198 BCGs and any of the environmental properties used here, beyond BCG stellar mass. This observed

homogeneity leads us to conclude that the majority of structural evolution of BCGs is likely to have occurred at earlier cosmic epochs than $z \sim 0.3$, with little evidence for much evolutionary activity at more recent epochs.

In Part II, (Chapters 4-5), we attempt to quantify the ICL within a sample of 19 clusters detected in XMM Cluster Survey (XCS) data, with optical counterparts in the SDSS footprint. To do so, we use deep (~ 26.8) Hyper Suprime Cam Subaru Strategic Program DR1 (HSC-SSP DR1) i -band data. We apply a rest-frame $\mu_B = 25\text{mag/arcsec}^2$ isophotal threshold to our clusters, below which we define light as the ICL within an aperture of $R_{X,500}$ centered on the BCG. We apply extensive masking and careful post-processing correction techniques to address the persistent challenges which face observers attempting to analyse ICL; through application of our post-processing method, we recover a significant fraction ($\sim 1/5$) of ICL flux previously lost during processing, significantly higher than our estimate of the image background at the same isophotal level. We find, on average, that the ICL makes up about $\sim 25\%$ of the total cluster stellar mass on average ($\sim 41\%$ including the flux contained in the BCG within 50kpc); this value is well-matched with other observational studies and SAM/numerical simulations, but is significantly smaller than results from recent hydrodynamical simulations (even when measured in an observationally consistent way). We find no evidence for any links between the amount of ICL flux with cluster mass, but find a growth rate of 2 – 4 for the ICL between $0 < z < 0.5$; however, we find no evidence for any growth in our BCGs, finding the fractional contribution of BCG light to be strongly anti-correlated with halo mass at fixed redshift. We conclude that the ICL is the dominant evolutionary component of stellar mass in clusters from $z \sim 1$.

Publications

In the course of completing the work presented in this thesis, the contents of Chapters 2-3 have been submitted and accepted for the following publication in a refereed journal:

1. Furnell, K.E., Collins, C.A., Kelvin, L.S., Clerc, N., Baldry, I.K., Finoguenov, A., Erfanianfar, G., Comparat, J. and Schneider, D.P., (2018), '**Exploring Relations Between BCG & Cluster Properties in the SPectroscopic IDentification of eROSITA Sources Survey from $0.05 \leq z \leq 0.3$** ', *Monthly Notices of the Royal Astronomical Society*, Volume 478, Issue 4, p.4952-4973.

Actions by the author during their PhD also led to the following piece in a refereed journal:

2. Furnell, K.E., (2018), '**Breaking the Silence**', *Science*, Volume 361, Issue 6409, p. 1410-1410.

Acknowledgements

Nobody completes a PhD on their own, and I am certainly no exception. There are many people who I owe a deep debt of gratitude to, and if there are any I have missed in these pages, I extend to them my sincere apologies.

Firstly, I would like to thank my supervisor/‘Astro-Dad’, Chris Collins. It was not an easy job looking after the scientific and personal interests of a person like me, and you did it splendidly. Thank you Chris, for every cup of tea, every outlandish idea, every confused look, every receptive ear, every ounce of patience and every time you sent me off around the world on a wild adventure. I will never, ever forget it.

Secondly, I would like to thank my friends and colleagues at the ARI, who have been like family to me on this journey. In no particular order, love and hugs to Maisie Rashman, Danielle Coogan, Helen Jermak and Rhana Nicholson. All of you have been my heroes, my rocks and my sisters throughout my PhD. I would also like to extend my thanks to my comrades in arms: Alex Lisboa-Wright, Sam Walton, Adrien Thob, Emma Beasor, Lawrence Short, Ted Mackereth, Kevin Tsang, Ben Mummery, Tricia Sullivan, Rob Williams, Katie Hollyhead, Hannah Dagleish, Joe Fernandez and Jessica Reis-Kitamura, for many excellent cups of tea and many more barrels of laughs. I give my thanks to the NSO staff, for the incredible work they do (and for all the times they let me loose at a school/community centre/festival), in particular Martin Coulby, Stacey Habergham-Mawson, Alison Keen and Andrew Newsam. Deepest thanks also to Lee Kelvin, Ivan Baldry, Ian McCarthy, Phil James and Claire Burke, for all of your advice and help with the work in this thesis (which absolutely could not exist without you). Thanks to Toby Moore, Dan Harman, Matt Darnley and Ian Steele, for my adventure in Tenerife and for my teaching experience as a whole. Thank you as well to the wonderful admin staff, Anna, Maureen and Caroline, who have been nothing short of helpful and

kind. A special shout out too to Marie Martig, for being a champion and an inspiration to me and to the ARI as a whole. I am immensely proud to have worked alongside you all.

Thirdly, I would like to thank my wider friends and family. My mother, Pam, who I look up to and am inspired by every day. My brother, Nathan, for being tough and straight spoken. Julie, my unofficial second mum, for being sweet, kind, caring and endlessly supportive. My partner, Thomas, for putting up with my stress and cheering me up when I was struggling. Kate, Rachel and Natalie, my best friends in the world, who have been there with me through thick and thin. Lastly, special thanks to Chris, who has been wonderfully supportive throughout the whole process, and remains a firm and wonderful friend. You have all carried me through in more ways than you'll ever know, and you mean the world to me.

Penultimately, I would like to extend my gratitude to my collaborators and colleagues far and wide for their ideas, patience, encouragement and cooperation. Many thanks to the SPIDERS team - especially Nicolas Clerc, Alexis Finoguenov and Ghazaleh Erfanianfar. Also thanks to the XCS team, in particular Kathy Romer, Maria Manolopoulou, Matt Hilton and Reese Wilkinson (the latter for keeping me company for two long weeks in Chile). I would also like to thank John Stott for his assistance as an examiner (and for all his cheery jokes, advice and amazing leadership of the EWASS Special Session 13: 'Galaxy Clusters and Groups Across Cosmic Time') and Nina Hatch. A special final thanks to Simon Dye for getting me through my undergraduate degree in one piece, and showing me I could do this with just a little more faith in myself. I couldn't have asked for a better tutor, or friend, during my time as an undergrad.

Finally, I would like to particularly thank Penny Bradshaw, of the LJMU Counselling service. You saved my life and brought me back from the brink, so that I could become a doctor. I will never forget everything you did for me.

This work primarily makes use of the PYTHON programming language, in particular the ASTROPY, MATPLOTLIB, NUMPY, SCIPY and COSMOLOGY packages. This work also, to a lesser extent, makes use of the AAO IRAF software suite, the DS9 visualisation software, the TOPCAT table manipulation JAVA applet and the MATLAB programming language.

KATE EMILY FURNELL

SEPTEMBER 2019

Declaration of Authorship

I, Kate Furnell, declare that this thesis titled, ‘The Growth of Brightest Cluster Galaxies and Intracluster Light in X-ray Selected Clusters’ and the work presented in it are my own. I confirm that:

- This work was done wholly or mainly while in candidature for a research degree at this University.
- Where any part of this thesis has previously been submitted for a degree or any other qualification at this University or any other institution, this has been clearly stated.
- Where I have consulted the published work of others, this is always clearly attributed.
- Where I have quoted from the work of others, the source is always given. With the exception of such quotations, this thesis is entirely my own work.
- I have acknowledged all main sources of help.
- Where the thesis is based on work done by myself jointly with others, I have made clear exactly what was done by others and what I have contributed myself.

Signed:

Date:

*‘ Alice laughed: “There’s no use trying,” she said; “one can’t believe impossible things.”
“I daresay you haven’t had much practice,” said the Queen. “When I was younger, I
always did it for half an hour a day. Why, sometimes I’ve believed as many as six
impossible things before breakfast.” ’*

From *Through the Looking-Glass, and What Alice Found There* by Lewis Carroll

‘ The only difference between genius and insanity is that genius has its limits. ’

Albert Einstein

Contents

Declaration	ii
Abstract	iii
Publications	v
Acknowledgements	vi
Declaration of Authorship	ix
List of Figures	xiv
List of Tables	xx
Physical Constants	xxii
Chapter 1	1
1 Introduction	1
1.1 Cosmology and Large-Scale Structure	1
1.1.1 Cosmological Simulations	7
1.2 Galaxy Clusters	11
1.3 Cluster Surveys	14
1.3.1 Optical	14
1.3.2 X-ray	18
1.3.3 On the CMB and the Sunyaev-Zeldovich (SZ) Effect	23
1.4 Stellar Mass in Galaxy Clusters	27
1.4.1 Brightest Cluster Galaxies	27
1.4.2 Intracluster Light	30
1.5 Motivation	36
Chapter 2	38
2 Part I - Investigation into Systematic Biases within BCG Parameter Estimation using SPIDERS	38
2.1 Overview of Contents	38
2.2 The SPIDERS Survey	39
2.3 Sample Selection	43
2.4 BCG Identification	44

2.5	Analysis	50
2.5.1	Cluster Properties	50
2.5.2	Profile Modelling using SIGMA	55
2.6	SIGMA Pipeline and Implementation	60
2.6.1	Probing Surface Brightness Limits with Simulated Profiles	63
2.6.2	Consequences of Systematics within Fitting	72
2.7	Summary of Chapter	74
Chapter 3		76
3	Part I - BCG Properties with Respect to Environment	76
3.1	Overview of Contents	76
3.1.1	BCG Stellar Masses and Discussion of Systematics	77
3.1.2	Correlations Between BCG Parameters	80
3.1.3	How do BCG Parameters Scale with the Cluster Environment?	84
3.2	Discussion	91
3.3	The SPIDERS BCG Value Added-Catalogue	93
3.4	Summary of Chapter	96
Chapter 4		98
4	Part II - The ICL in XCS-HSC: Data and Systematics	98
4.1	Overview of Contents	98
4.2	Hyper Suprime-Cam Subaru Strategic Program	99
4.2.1	Survey Description	99
4.2.2	Data Reduction	99
4.3	The XMM Cluster Survey	101
4.4	Sample Selection	103
4.5	Analysis	108
4.5.1	Quantifying ICL	108
4.5.2	BCG Photometry	110
4.5.3	Masking	113
4.5.4	Background Over-subtraction - The ‘Divot Correction’ Method	118
4.5.5	Quantifying Systematic Background	121
4.6	Results	125
4.7	Summary of Chapter	127
Chapter 5		132
5	Part II - The ICL in XCS-HSC: Results and Discussion	132
5.1	Overview of Contents	132
5.2	Results	133
5.2.1	What Drives ICL Growth?	133
5.2.2	Comparison with Other Studies	137
5.3	Summary of Chapter	146
Chapter 6		149

6	Conclusions and Future Work	149
6.1	Conclusions	149
6.1.1	<i>Motivation 1</i> : How does cosmological dimming affect the recovered structure of BCGs, measured using conventional observational methods in the context of surveys?	149
6.1.2	<i>Motivation 2</i> : How do BCGs evolve with respect to their host cluster?	151
6.1.3	<i>Motivation 3</i> : How do conventional image-processing methods affect the recovery of ICL?	152
6.1.4	<i>Motivation 4</i> : How does the ICL grow over time? Is its evolution linked to its corresponding BCG, or to the properties of the host cluster?	154
6.2	Future Work	156
A	Part I - Supplementary Material	159
A.1	Part I - Partial Spearman Analysis	159
B	Part II - Supplementary Material	162
B.1	Part II - Alternative $k_{i,B}$ -correction parameters	162
B.2	Part II - Partial Spearman Analysis	163
	Bibliography	164

List of Figures

1.1	The effect of different temperatures of dark matter on large-scale structure. Rightmost is cold dark matter, which produces a large number of satellites and fragmentation (‘bottom up’ evolution). Furthest left is hot dark matter, which produces smooth structure with little fragmentation (‘top down’ evolution). In the centre is predominantly cold dark matter with a warm neutrino component (figure courtesy of Ben Moore at the University of Zurich), most similar to the LSS observed in our Universe.	6
1.2	An example of a dark matter halo merger tree from Lacey & Cole 1993. Time increases from the top of the diagram to the bottom. Such diagrams demonstrate the ‘bottom-up’ hierarchical merging process in Λ CDM which leads to observed structures in the local Universe.	8
1.3	A chronological plot of the progress of cosmological hydrodynamical simulations with respect to resolution elements (up to 2014) from Vogelsberger et al. 2014.	9
1.4	Examples of morphologies of galaxies in the EAGLE simulation (adapted from figure 2 of Correa et al. 2017). The top axis describes viewing orientation. The x -axis represents the stellar mass of the objects, whereas the y -axis is a metric used to describe the ‘ordered’ co-rotation. As is shown, disk and spheroid structures arise in EAGLE similar to the bimodality of galaxies seen in our Universe.	11
1.5	Abell 2744, one of the optically selected clusters catalogued by George O. Abell. The image is a false-colour composite from Hubble Frontier Fields data (e.g. Lotz et al. 2017) Two brightest cluster galaxy candidates (see Section 1.4.1 are present at its centre, along with distinctive strong lensing arcs from background objects.	15
1.6	Figure 7 of Mehrrens et al. (2012) which highlights sources of contaminant extended X-ray emission. The top panel represents individual optical images from SDSS with overlaid X-ray contours; the bottom panel the equivalent X-ray image. The cores of local galaxies, background AGN and concentrated emission from stars along the line of sight have motivated candidate eyeballing in such cluster surveys as the XMM Cluster Survey (e.g. Romer et al. 2001).	20
1.7	Map of the CMB, as observed by Planck. ‘Colder’, underdense regions are depicted in blue, ‘warmer’ overdense regions in red (fluctuations on the order of $\sim 10^{-5}$ K).	24

1.8	The Planck cosmology results from cluster counts, as of 2015, from Planck Collaboration et al. (2016b). The range of possible σ_8 (a measure of perturbation scale) and matter density parameter values, Ω_m are shown as contours, with ‘SZ’ in the legend denoting results derived from the SZ-selected cluster sample and differing colours representing a different mass bias value. As is shown, there is a significant deviation from the peak cosmological parameter probability derived from cluster counts with respect to the constraints from measurements of CMB fluctuations.	25
1.9	An adapted version of figure 3 from Hasselfield et al. (2013), which shows an 148 GHz band ACT observation. Three cluster candidates are highlighted (black rings).	26
1.10	An example of nine BCG 1-D surface brightness profiles from Bai et al. (2014); surface brightness, μ , is plotted on the y -axis versus $r^{1/4}$ on the x -axis, where r is measured along the major axis of the elliptical isophotes fit to the galaxy (see Chapter 4 for a similar method used in this work). The structure of the BCGs ranges dramatically in terms of concentration and extent.	28
1.11	Figure 3 from Collins et al. 2009, comparing the observed and predicted masses of BCGs. The BCGs (measured using deep Subaru data, PI: John Stott) are marked as red points in the diagram, with the results of simulations carried out in De Lucia & Blaizot (2007) as black points. Whereas the BCGs are predicated to have a steep gradient in growth from $1 < z < 0$, the results from Collins et al. 2009 suggest their growth curve to be predominantly flat.	31
1.12	Figure 1 from Mihos et al. (2005), showing the core of the Virgo Cluster imaged by the 0.6m Burrell-Schmidt telescope. Bright sources have been masked, and the contrast has been adjusted to highlight structure. The ICL is clear in this image, with streams of stars existing between M87 (the BCG, bottom left) and its neighbouring galaxies.	34
2.1	A equatorial map of the SPIDERS target selection (figure 1 from Clerc et al. 2016). Each circular pointing is 3° in diameter. The dashed, bold black line indicates the boundary between the German and Russian skies, with eROSITA data being shared between the two international project leads. The key in the legend refers to various regions of the eBOSS field regarding target priority and observation scheduling (not relevant here).	40
2.2	An example of plots produced by the diagnostic interface used when visually inspecting SPIDERS cluster candidates. There are velocity, probability and spatial distribution diagnostic plots, with cluster members identified through REDMAPPER highlighted.	42
2.3	An example of an SDSS frame zoom where a BCG has been incorrectly assigned (r band, log-scaled). The ‘true’ BCG can clearly be seen (marked with a black dot), but has not been marked as the optical centroid for the cluster (blue square), or included in the object list (likely due to it being too bright to meet the magnitude cut). The red square denotes the X-ray centroid for the cluster.	46

2.4	Spectroscopic redshift of the visually-inspected BCGs (z_{BCG}) versus photometric cluster redshift (z_{RM}) comparison for the sample of 329 objects (typical errors are $\Delta z_{\text{BCG}} \sim 10^{-5}$ and $\Delta z_{\lambda} \sim 0.01$ respectively). The black dashed line is the 1:1 relation. In general, the BCG redshifts agree well with the cluster photometric values, albeit with some scatter at higher z (see section 2.5.1).	47
2.5	Example false-colour SDSS <i>gri</i> composites - namely, colourised JPEG stacks of SDSS <i>g</i> -, <i>r</i> - and <i>i</i> -band data - of 15 BCGs used in this study (100×100 kpc for each tile). Each of the three vertical panels represents a sample of five randomly drawn BCGs about the 16 th , 50 th and 84 th redshift percentiles from top to bottom (0.1, 0.18 and 0.25, respectively).	49
2.6	The $L_X - z_{\text{RM}}$ relation for the BCGs in our sample. The black circles show the initial 329 clusters which passed our visual inspection, whereas the red points represent the 198 clusters used in our final analysis (see Section 3.1.1). We discuss the consequences to the underlying BCG distribution in Section 2.6.1 within this chapter.	51
2.7	Comparison plot between 81 velocity dispersion values computed here (<i>y</i> -axis) and those computed by von der Linden et al. (2007) and by Clerc et al. (2016) for 27 and 54 common clusters respectively (the latter did not cite errors in their paper), accounting for duplicates (<i>x</i> -axis). The average 1σ errors for each of the two samples are plotted in the bottom right hand corner.	54
2.8	A comparison between the model magnitude values for the 416 VAC BCGs in Erfanianfar et al., (in review). The subscripts ($s, s + x, v$) indicate the choice of model (Sérsic, Sérsic+Exponential, de Vaucouleurs), while the colour (green, red, black) indicates the band (<i>g, r, i</i> respectively). The zero deviation line is included (blue dashed horizontal line) along with an annotation on each plot providing the median deviation and rms.	57
2.9	An example data product from SIGMA for the BCG in SPIDERS cluster 1.1365 (100×100 kpc, $z \sim 0.05$). Clockwise from top left: SDSS <i>r</i> -band image, Sérsic model from GALFIT, image mask, residual (enhanced to bring out faint artifacts). Except for the binary mask, all other quadrants are scaled logarithmically; hence, the high feature contrast in the bottom-left panel for the PSF-sensitive central region of the galaxy.	61
2.10	Example <i>r</i> -band simulated profiles at 15 th magnitude (tiles scaled to 100×100 kpc with an assumed redshift of 0.2). Top: for a fixed n of 4, $R_e = 20, 80$ kpc. Bottom: for a fixed R_e of 40 kpc, $n = 2, 8$. Note the change in surface brightness distribution in either case.	64
2.11	The results of fitting simulated profiles with SIGMA in the <i>r</i> -band. Each of the four horizontal panels represents the output for one of the eight fixed input magnitudes (12 – 19, descending). The coloured lines represent the biweighted average across the runs (assuming at least 3/8 models at each point were successfully fit; corresponding legend key $[n R_e]$ for a given colour, interchange for the relevant panel). The black dashed line represents the median $[n R_e]$ of the coloured lines. There is a clear decline in output-to-input Sérsic index with effective radius at 17 th – 19 th magnitude (second column).	66
2.12	As in figure 2.11, but for the <i>g</i> -band.	67
2.13	As in figure 2.11, but for the <i>i</i> -band.	68

2.14	The fitting ‘success’ rates (i.e. models which completed fitting) from SIGMA fitting of mock profiles. SIGMA’s performance clearly degrades with both wavelength and input magnitude.	69
2.15	The raw fit magnitudes for the SPIDERS sample from SIGMA (N=326), prior to any k-correction or dust correction. The histograms have been normalised by area.	71
2.16	Outputs from modelling ~ 4000 artificially-redshifted galaxies from Vika et al. (2013) (their figure 13), showing a comparison in output parameters with respect to the lowest artificial redshift ($z = 0.01$). Note the rapid decline in output Sérsic index with increasing redshift in every band.	73
3.1	Comparison between the output structural parameters for the BCG sample (N=198) in 3 different passbands (<i>gri</i>). The dashed line represents the 1:1 relation and the crosshairs in the bottom two plots represent the 1σ scatter in x and y . In general, there is a good agreement across bands, albeit with increased scatter at large n and R_e . This has also been demonstrated in our simulations (Section 2.6.1).	78
3.2	Comparison between the stellar mass estimates for our BCGs using a scaling relation from Taylor et al. (2011) and those in the MPA-JHU value-added catalogue, for a common sample of 192/198 BCGs (x -axis and y -axis, respectively). The crosshairs give the typical error value in each respective axis (for the MPA-JHU catalogue, drawn from the 16 th and 84 th percentile estimates).	79
3.3	Correlations between the BCG structural parameters. For clarity, the data have been binned using a Scott’s-rule optimised bin width to illustrate structure (omitting bins with fewer than 15 objects). The errorbars mark the 16 th and 84 th percentiles of each bin. The solid line is the relation for SDSS ‘early-type’ galaxies ($n > 2.5$) from Shen et al. (2003), with the dashed lines marking the 1σ scatter.	83
3.4	Correlations between the environmental parameters outlined in this study with BCG structural parameters and stellar mass. Binned medians are shown with $N \geq 15$ objects. The correlation between BCG mass and the properties of the host cluster appear more compelling than with the structural parameters, where we observe few significant correlations (see Table 3.1 and partial Spearman analysis).	85
3.5	Correlations between characteristics of the host cluster (binned medians shown with $N \geq 15$ objects). The physical properties of clusters are highly correlated; hence the importance of accounting for selection.	86
3.6	Correlations between luminosity-weighted environmental density, $\log_{10}[\rho]$, with BCG properties (binned medians shown with $N \geq 5$ objects) for 102 BCGs in common with the catalogues of Tempel et al. (2012). As before, there is a correlation with mass, but no correlation with the structural parameters.	89
3.7	The $M_\star - M_{200}$ relation for BCGs in Erfanianfar et al., (in press). The solid points represent the medians of the data when binned; the transparent points represent the sample BCGs. The blue dashed and red dot-dashed lines represent the best-fitting power law relations for the low and high redshift bins respectively. There is a typo present in the key of this figure, in that x refers to redshift (z).	93

3.8	The stellar mass to halo mass ratio relation from Erfanianfar et al., (in press); as shown, there is good agreement with prior observations of this relation (Behroozi & Silk 2018) and current simulations (Yang et al. 2012, Moster et al. 2013).	95
4.1	The $M_{X,500} - z$ relation for the clusters used in this work (see text for details). The redshifts are spectroscopic, with errors $\Delta z \sim 10^{-5}$.	104
4.2	The 7 clusters (1.5×1.5 Mpc on each frame) omitted from the sample due to poor photometry or bright source contamination. BCGs, if present on the frame, are marked with cyan diamonds. The images have been log-scaled and Gaussian-smoothed to show structure.	107
4.3	Differential comparison between the input and output parameters for the cluster BCGs in this sample, with and without an added divot correction. The value at the top of each frame represents the median deviation and rms respectively; the top and bottom panels represent the outputs for a free Sérsic profile and a de Vaucouleurs profile respectively.	112
4.4	Cumulative distributions of the BCG flux contributions (plus divot correction) to the overall stellar flux of the clusters (see Table 4.4), where green represents the aperture values, red the de Vaucouleurs values and blue the Sérsic values.	114
4.5	An example of the 'divot correction' method used in this work (shown here for cluster XMMXCS J232923.6-004854.7); all images have the exact same scaling (from Kelvin et al., in prep). The first image depicts the data prior to correction; as is visible, there is a dearth of flux in the regions around the BCG and its satellites. The second shows the estimated divot correction; the third shows the resultant image after implementation. As is visible, there is a vast improvement, with the sky level varying far more smoothly.	120
4.6	The results from performing photometry on ~ 2000 mock ICL profiles injected into HSC data (without divot corrections). Each frame in the subplot represents a given control field; each plot shows the relative percentage deviation in flux ($(f_{\text{out}} - f_{\text{in}})/f_{\text{in}}$, where f_{in} is the raw mock profile flux measurement and f_{out} is the flux measurement of the profile after implantation in a HSC control frame) for a given 'ICL-like' profile (see text) with respect to mean surface brightness (the average surface brightness across a mock profile).	123
4.7	Stack of median deviations of recovered profiles across all frames with respect to mean surface brightness, with all definitions and conditions the same as in figure 4.6. The grey shaded region indicates the 1σ scatter.	124
4.8	The stacked ICL fraction to total light fraction at a selection of equivalent surface brightnesses, comparing the divot corrected and uncorrected cases. The errorbars depict the $1-\sigma$ scatter across all clusters in the sample.	126
4.9	Comparison between the divot corrected and uncorrected stacks as measured by IRAF ellipse. The shaded region represents the 16 th and 84 th percentiles of the stacks. The dot-dashed lines are the median Sérsic model from SIGMA in each respective case. It is clear that the Sérsic models miss a great deal of the flux on the outskirts of the BCGs, which previous authors have argued is a plateau of either ICL, or an extended stellar halo. There is little difference in the median n values, with values of 4.65 and 4.57 for the non-corrected and corrected models respectively.	127

4.10	The final equivalent 25 mag/arcsec ² masked and divot-corrected images, zoomed to 40% of the R_{500} value of each respective cluster centred on the BCG (with the exception of panel 7). The cyan line at the top left of each panel is equivalent to 30". To show structure, the images have been log-scaled and smoothed.	128
5.1	The rest-frame BCG absolute magnitude (M_i , i -band aperture) versus cluster mass measured in X-rays ($M_{X,500}$, left) and redshift (z , left). For ease of comprehension, we have inverted the y -axis.	135
5.2	Comparison of the relative fluxes of ICL+BCG versus halo mass. The legend key is as follows: Puchwein et al. (2010) with/without an AGN prescription (P10, AGN/-AGN) and Gonzalez et al. (2013) (G13).	139
5.3	As in figure 5.2, but for ICL flux only (see text). The legend key is as follows: Tang et al. (2018) at redshift z (T18), Burke et al. (2015) (B15) and Contini et al. (2014) (C14).	140
5.4	Comparison of the relative fluxes of ICL+BCG versus redshift, with the points from Gonzalez et al. (2013) (G13).	143
5.5	As in figure 5.4, but for ICL flux only. The legend key is as follows: Burke et al. (2015) (B15), Rudick et al. (2011) (R11) and Tang et al. (2018) (T18). The best least-squares fit has been included for comparison (slope = -54.50, intercept = +40.01).	144

List of Tables

2.1	Summary of the BCG selection.	45
2.2	Cluster fields used when inserting mock galaxies. The ID column refers to the corresponding ID string in the SPIDERS catalogues.	64
3.1	Full Spearman rank analysis for all the variables examined in this study for the r -band morphological parameters. The top half of the table lists the Spearman rank correlation coefficient (r_s), whereas the bottom half of the table provides the log of its corresponding p-value ($\log_{10}[p_s]$).	81
4.1	A summary table of the average limiting depths for the HSC-SSP survey. In this work, we use the ‘Deep’ layer in the i band.	100
4.2	The main parameters of the 19 XCS-HSC clusters used in this work. The BCG rest-frame i -band absolute magnitudes (M_i) are derived from aperture values as described in Section 4.5.2. The relative errors are derived using the HSC variance maps and are typically quite small ($\Delta M_i < 0.01$ mag).	106
4.3	The k -correction ($k_{i,B}$), cosmological dimming and equivalent B -band surface brightness limits for our clusters below which we consider light as ICL ($\mu_{B,rest} = 25$), used to generate isophotal masks.	117
4.4	A summary of the results from this work, where f_{ICL}/f_{tot} is the percentage of cluster light that is ICL at $\mu_{B,rest} = 25\text{mag/arcsec}^2$ within $R_{X,500}$ and Δf is the percentage difference in the ICL contribution between the divot corrected and uncorrected cases. The equivalent BCG flux (f_{BCG}) is also included (Sérsic model, de Vaucouleurs model and 50 kpc aperture respectively).	131
5.1	Full Spearman analysis of all the parameters used in this study: the fractional contribution of the ICL and of the BCG (f_{ICL}/f_{tot} and f_{BCG}/f_{tot} respectively), the cluster redshift (z) and the cluster mass $M_{X,500}$. The top half of the table lists the Spearman rank correlation coefficient (r_s), whereas the bottom half of the table provides the log of its corresponding p-value ($\log_{10}[p_s]$).	134
A.1	As in table 3.1, but for fixed R_e	159
A.2	As in table 3.1, but for fixed L_X	159
A.3	As in table 3.1, but for fixed M_{200}	160
A.4	As in table 3.1, but for fixed n	160
A.5	As in table 3.1, but for fixed M_\star	160
A.6	As in table 3.1, but for fixed λ	160
A.7	As in table 3.1, but for fixed z	161

B.1	The mean $k_{i,B}$ correction values for 3 formation redshifts z_f at 3 metallicity values (where Z_{\odot} = solar) across all BC03 models for all sample clusters within $0 < z < 0.28$. The ones selected for the clusters used in this work sit in the central cell of the table.	162
B.2	As in table B.1, but for clusters within $0.28 < z < 0.5$	162
B.3	Partial Spearman analysis for the parameters discussed in Chapter 5, with f_{ICL}/f_{tot} held constant.	163
B.4	Partial Spearman analysis for the parameters discussed in Chapter 5, with f_{BCG}/f_{tot} held constant.	163
B.5	Partial Spearman analysis for the parameters discussed in Chapter 5, with z held constant.	163
B.6	Partial Spearman analysis for the parameters discussed in Chapter 5, with $\log_{10}M_{X,500}$ held constant.	163

Physical Constants

Speed of Light	$c = 3.00 \times 10^8 \text{ ms}^{-1}$
Gravitational Constant	$G = 6.67 \times 10^{-11} \text{ Nkg}^{-2}\text{m}^2$
Hubble Constant (Local)	$H_0 \sim 70 \text{ kms}^{-1}\text{Mpc}^{-1}$
Matter Density Parameter (Local)	$\Omega_{M,0} \sim 0.3$
Dark Energy Density Parameter (Local)	$\Omega_{\Lambda,0} \sim 0.7$
Planck's Constant	$h = 6.63 \times 10^{-34} \text{ Js}$
Boltzmann Constant	$k = 1.38 \times 10^{-23} \text{ JK}^{-1}$
Atomic Mass Unit	1 amu = $1.67 \times 10^{-27} \text{ kg}$
Electron Rest Mass	$m_e = 9.11 \times 10^{-31} \text{ kg}$

Chapter 1

Introduction

1.1 Cosmology and Large-Scale Structure

Everything we perceive exists within the Universe, of which the science of cosmology seeks to address five fundamental questions: its origin, its composition, its physics, its evolution and its eventual fate. Cosmology has its early roots in the philosophers and astronomers of ancient Greece, with many thinkers of old looking to the skies and asking questions which, to this day, remain unsatisfactorily answered. To name but a few examples: some of the earliest recorded theories on the nature of stars were produced by Plato and Aristotle, the concept of a heliocentric solar system by Aristarchus of Samos (the latter to be famously used to refute the Ptolemaic epicyclic theory of planetary motion almost two thousand years later by Nicolas Copernicus) and the first measurement of the circumference of the Earth by Eratosthenes (within a remarkable error of $\sim 10\%$). Such astronomical feats possible before the invention of modern optical telescopes highlight humanity's lifelong fascination with the cosmos, and our creative ways of studying the Universe from our place within it.

In modern times, however, much progress has been made towards a more quantitative understanding of the Universe, using a joint theoretical and observational approach. The bulk of this advancement in knowledge took place during the great scientific revolution of the 19th and 20th centuries, where the scientific method of quantifiable, evidence-backed conjectures was fast becoming mainstream practice (see, for example, discussions within [Popper 1959](#)).

The 20th century was revolutionary in the context of cosmology and wider astrophysics as a whole. Most notably during this time was the discovery by Edwin Hubble on the ‘flow’ of ‘nebulae’ (Hubble 1929, Hubble & Humason 1931), namely, the result that almost all galaxies were moving away contrary to our frame of reference. This led cosmologists (as predicted by Georges Lemaître shortly before Hubble’s measurements, see Lemaître 1927) to conclude that the Universe was not as unchanging and everlasting as one thought - that, in fact, it had a beginning: the so called ‘Big Bang Theory’ (famously coined by one of its major opponents, Professor Fred Hoyle of the University of Cambridge in 1949). Evidence for the notion of a cosmic ‘beginning’ mounted in the wake of Penzias & Wilson (1965) with the discovery of the cosmic microwave background (CMB, first predicted by Gamow 1948); ‘afterglow’ from the primordial Universe ($\sim 10^5$ yr), consisting of free-flowing photons post decoupling, when the Universe transitioned from an opaque plasma to transparent upon recombination (see discussion in Section 1.3.3).

Moreover, this time period in history was also a renaissance for the field of theoretical cosmology. Most notably was the feat of Albert Einstein whom, in 1905, composed his theory of special relativity. His feat was followed by his general theory of relativity in 1915, a new theorem of gravity which proposed that massive bodies ‘warp’ space. His work was subsequently tested against (and proven superior to) Newtonian predictions during the 1919 solar eclipse (Einstein 1919).

Soon after, Cosmologists began applying the consequences of Einstein’s theories to the evolution of the Universe. Alexander Friedmann (Friedmann 1922) solved the Einstein field equations (e.g. Einstein 1915) for the Friedmann-Lemaître-Robertson-Walker metric; namely, the general case of an isotropic, homogeneous Universe undergoing hydrostatic expansion. For brevity here, one can put forward a quasi-Newtonian argument for the Friedmann equation if one makes the base assumption that the gravitational field inside a uniform shell is zero (this is not quite the case for Newtonian dynamics in the case of massive spheres at large radii, but the assumption does hold in general relativity, see Birkhoff & Langer 1923). In its most well-known form, the Friedmann equation can be written as:

$$\dot{R}^2 - \frac{8\pi G}{3}\rho R^2 = -kc^2, \quad (1.1)$$

where R is the product of the dimensionless scale factor, a , which characterises Universal

expansion, ($a \equiv \frac{R}{R_0}$, where R_0 is the scale length at our current epoch) and the co-moving distance, ρ is the density of the Universe, c is the speed of light, G is Newton's gravitational constant and k is a constant which we will define here as 'curvature' for simplicity.

In cosmology, the value range of k is what governs the eventual fate of the Universe. In general, the value of k results in three eventualities: $k < 0$, an open Universe (which expands indefinitely), a closed Universe which eventually collapses under gravity ($k > 0$) or a 'flat' Universe ($k = 0$, which expands indefinitely but at a declining pace). Our most accurate cosmological observations of the cosmic microwave background to date (see Section 1.3.3, [Planck Collaboration et al. 2014](#)) infer a Universe which is very close to flat ($k \sim 10^{-3}$ - see [Planck Collaboration et al. 2016a](#)). The remarkable result of the Friedmann equation is its inference that Universal geometry affects its eventual fate; something that was explored further in the studies of Robertson and Walker (e.g. [Robertson 1932](#), [Walker 1933](#)).

In defining the criterion of a 'flat' Universe, one can define a so-called 'critical' density as follows:

$$\rho_c = \frac{3H^2}{8\pi G}, \quad (1.2)$$

where ρ_c is the critical density and H is the Hubble parameter (otherwise defined as $\frac{\dot{a}}{a}$). Here, it is valuable to consider the constituents of the Universe as a whole, namely to determine which components dominate the majority of its density. One can therefore define the 'density parameter', Ω , as follows:

$$\Omega \equiv \frac{\rho}{\rho_c} = \frac{8\pi G\rho}{3H^2}. \quad (1.3)$$

As the Universe expands and evolves, ρ and H change over time; therefore, equation 1.3 is dependent on epoch. As an aside, it is therefore useful to define a dimensionless Hubble parameter with respect to our present epoch:

$$h \equiv \frac{H_0}{100 \text{ kms}^{-1}\text{Mpc}^{-1}}, \quad (1.4)$$

where H_0 is the local measure of the Hubble parameter.

A simplified means of characterising the energy content of the Universe is to consider it to be composed of three principal components, and to model how the density of these components evolve. These are: pressureless matter ($\rho_m \propto a^{-3}$), radiation ($\rho_r \propto a^{-4}$) and ‘vacuum energy’ ($\rho_v = \text{constant}$). One can therefore expand the Friedmann equation in terms of the density parameters for these three components as follows:

$$\frac{kc^2}{H^2 R^2} = \Omega_m a^{-3} + \Omega_r a^{-4} + \Omega_v. \quad (1.5)$$

It is possible to write the above equation in terms of redshift, z (defined such that $R = \frac{R_0}{(1+z)}$). By doing so, we arrive at one of the most important equations in cosmology:

$$R_0 dr = \frac{c}{H(z)} dz = \frac{c}{H_0} [1 - \Omega(1+z)^2 + \Omega_v + \Omega_m(1+z)^3 + \Omega_r(1+z)^4]^{-1/2} dz, \quad (1.6)$$

where Ω is the total density parameter, Ω_m is the matter density parameter, Ω_r is the radiation density parameter and Ω_v is the vacuum energy density parameter. This version of the Friedmann equation describes how the rate of expansion changes over cosmic time; enabling one to monitor the rate of expansion of the Universe with respect to the distribution of its constituents.

The growth of large-scale structure is largely dependent on the values of the density parameters. Initially, during the majority of the 20th century, it was assumed that the Universe was composed only of visible pressureless matter and radiation, namely the ‘Einstein-de Sitter’ cosmological model ([Einstein & de Sitter 1932](#)). With observational evidence mounting in the 1930s for an excess of unseen mass affecting the velocity dispersion of galaxies in the Coma Cluster (e.g. [Zwicky 1933](#), see also studies of galaxy rotation curves for a galaxy-scale detection of this phenomenon, such as in [Rubin & Ford 1970](#)), cosmology underwent a massive paradigm shift. There appeared to be, due to its gravitational influence, an exotic variety of matter which did not appear to undergo any electromagnetic interactions whatsoever, estimated to make up about 85% of the overall matter content of the Universe (e.g. [Trimble 1987](#)). Thus began an extensive, currently ongoing search for the nature of ‘dark matter’.

Cosmologists and particle physicists have used numerous methods to attempt to detect dark matter candidates, from experiments using cryogenics designed to directly measure low energy particle recoils (e.g. the Large Underground Xenon experiment, [Akerib et al.](#)

2013), to attempting to observe radiation indirectly from dark matter relic annihilations (e.g. [Ellis et al. 1988](#)), to placing limits upon the ‘cross section’ (linked to the probability of interaction) of a dark matter particle by observing the collision of galaxy clusters (e.g. [Markevitch et al. 2002](#)).

Arguably the most popular dark matter candidates are Weakly Interacting Massive Particles (see [de Swart et al. 2017](#) for a recent review), which gained popularity over candidates such as MACHOS (MAssive Compact Halo Objects, e.g. black holes, see [Hawkins 2011](#) for a comprehensive discussion) due to tight constraints on the number density of such objects from nucleosynthesis (e.g. [Carr et al. 2010](#)), or neutrinos, where LSS simulations produce far different structures than those observed when using ‘hot’ dark matter candidates such as neutrinos (see figure 1.1). WIMPS have grown in popularity as a ‘cold’ dark matter candidate, as they appear to do a reasonable job of reproducing the observed ‘web-like’ structure of the cosmos (see discussion below).

Although the ‘cold’ dark matter model presents a reasonable description of the cosmos, it is not perfect; for example, it has been found to produce an excess of satellites and overly-cuspy haloes in simulations (see discussions in [Navarro et al. 1996](#) and Section 1.1.1). The model has therefore been adapted by numerous groups in recent years to include an amount of ‘warm’ dark matter (assumed to be massive neutrinos, where $m_\nu \sim 10\text{eV}$) as doing so produces more realistic results by ‘ironing out’ some unrealistic consequences of a solely cold dark matter model. This includes overly cuspy haloes (e.g. [McCarthy et al. 2016](#)) due to their associated ‘smoothing’ lengths (~ 50 Mpc). Such massive neutrinos however have yet to be found observationally (should they exist at all), with observations from Planck ruling out neutrino masses of ≥ 0.05 eV/ c^2 ([Planck Collaboration et al. 2016a](#)).

Although studies have been somewhat successful in placing constraints on the nature (e.g. cross section, mass) of any potential dark matter candidates such as WIMPS (see [van Waerbeke & Zhitnitsky 2018](#) for a recent example), thus far none have been successful at detecting them. Some groups have therefore turned to MODified Newtonian Dynamics (MOND) as an alternative theory to dark matter due to the latter’s observationally elusive nature, despite the difficulty of most MOND models in reproducing the observed angular power spectrum (see Section 1.3.3 for additional discussion, and arguments in

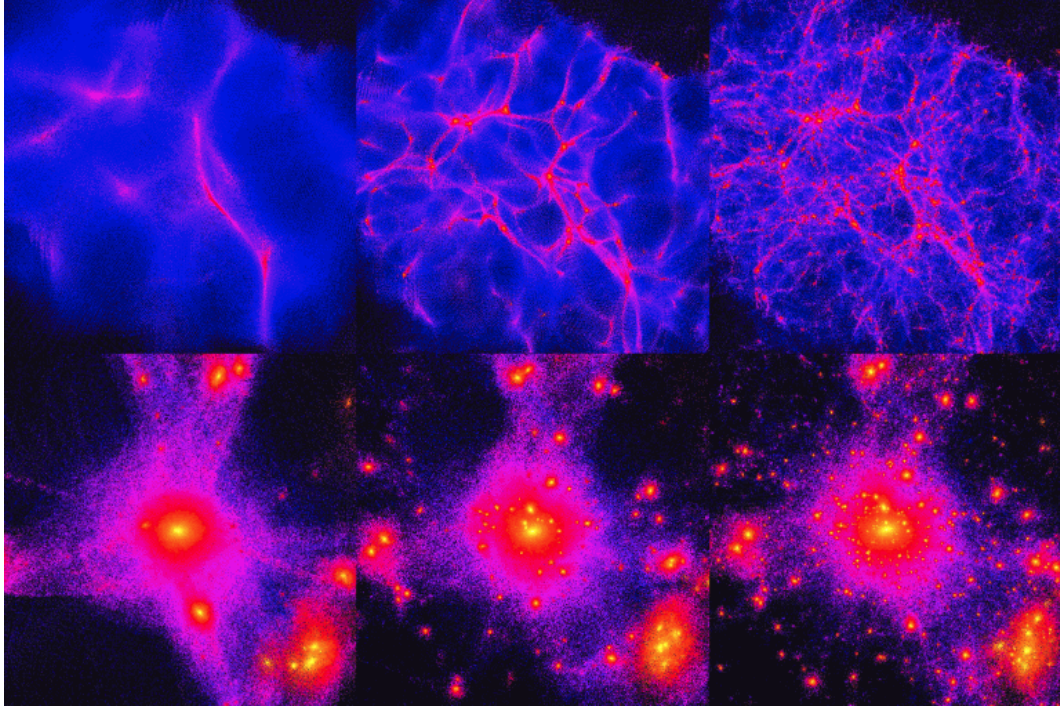


FIGURE 1.1: The effect of different temperatures of dark matter on large-scale structure. Rightmost is cold dark matter, which produces a large number of satellites and fragmentation (‘bottom up’ evolution). Furthest left is hot dark matter, which produces smooth structure with little fragmentation (‘top down’ evolution). In the centre is predominantly cold dark matter with a warm neutrino component (figure courtesy of Ben Moore at the University of Zurich), most similar to the LSS observed in our Universe.

[Planck Collaboration et al. 2016a](#)). Ergo, our means of characterising dark matter in greater detail, for the moment at least, remain largely restricted.

In the late 20th century came the ‘re-proposal’ to include a cosmological constant, Λ , from remarkable studies of extragalactic type Ia supernovae by groups lead by Adam Riess ([Riess et al. 1997](#)), Saul Perlmutter ([Perlmutter et al. 1997](#)) and Brian Schmidt ([Schmidt et al. 1998](#)). Type Ia supernovae, namely thermonuclear detonations of sub-Chandrasekhar mass white dwarfs primarily through external envelope accretion from a binary companion (see [Minkowski 1941](#)), can be used effectively as standard candles due to the small scatter in their absolute magnitudes, (± 0.3 mag, see [Kowal 1968](#) for an early observation of this phenomenon). It was found, beyond observational errors, that the brightnesses of the distant supernovae in these studies were significantly dimmer than expected given the distances implied by their spectroscopic redshifts. It was concluded that there therefore must indeed be a component of vacuum energy within the Friedmann equation (termed ‘dark energy’); the Einstein de Sitter model was therefore replaced by our current cosmological model, cold dark matter with a cosmological constant (Λ CDM).

The most unexpected result from the discovery of dark energy is arguably exactly how much it dominates the energy content of the Universe at present epochs. The most recent estimates from Planck (as of 2016) place the overall dark energy contribution at $\sim 68.5\%$ of the overall content of the Universe, with dark/baryonic matter at $\sim 31.5\%$ (as an aside, radiation density contributes little at current epochs, at $< 0.001\%$). The discovery of dark energy also shattered expectations regarding the eventual fate of the Universe; unless another unknown source of energy were to dominate at a future stage, the Universe would continue to not only indefinitely expand, but accelerate exponentially. The domination of Λ stems from the Friedmann equation (specifically, the form in equation 1.6); as there is no expansion dependence on the ‘vacuum energy’ term, Ω_ν (henceforth Ω_Λ), unlike the density of matter (dark+baryonic) and radiation (which scale with the expansion of the universe as $\rho_m \propto a^{-3}$ and $\rho_r \propto a^{-4}$ respectively). The current consensus, given our understanding of cosmology, therefore describes a Universe under exponentially-accelerated expansion through present Λ domination.

1.1.1 Cosmological Simulations

The earliest precursors to modern cosmological simulations were carried out as N-body realisations of up to several hundred particles in the 1960s and 1970s (e.g. [Peebles & Yu 1970](#), [White 1976](#), [Press & Schechter 1974](#)); which, given the limitations of computers during that period, were state of the art. Over the coming four decades, their particle number grew, resulting in the modern hydrodynamical simulations we have today. Of these, perhaps the well known and certainly the most sophisticated for its time was the 2005 ‘Millennium’ simulation (see [Springel et al. 2005](#)), of 10^{10} particles. Millennium adopted an approach using ‘smoothed particle hydrodynamics’ (SPH, see more detailed description of the method in the accompanying paper [Springel 2005](#)), and also, a scale far larger than any previously attempted (ten times more than, for example, [White et al. 1987](#); see also figure 1.3). Millennium was revolutionary, in that it was able to recreate the evolution of the structure in the Universe that we observe to a far greater resolution than any previous simulation had before (to the $\sim 10\text{kpc}$ level). Being a dark-matter only simulation, subsequent studies used the dark matter halo merger trees originating from Millennium (see below discussion, and figure 1.2) alongside semi-analytic models (SAMs) to emulate galaxy evolution (see [De Lucia & Blaizot 2007](#) for a relevant famous example in the context of this thesis). Briefly, SAMs couple empirical relations from

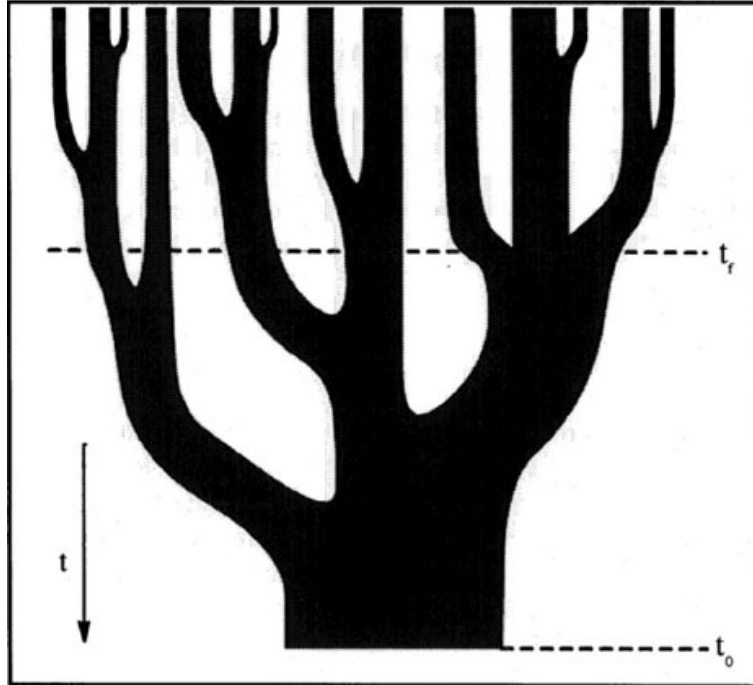


FIGURE 1.2: An example of a dark matter halo merger tree from [Lacey & Cole 1993](#). Time increases from the top of the diagram to the bottom. Such diagrams demonstrate the ‘bottom-up’ hierarchical merging process in Λ CDM which leads to observed structures in the local Universe.

observations (e.g. the galaxy stellar mass function, scaling relations, predicted modes of evolution, etc.) with simplified physical treatments for more complex baryonic physics (e.g. AGN feedback, gas cooling, star formation, etc.). They have the benefit that they are often far faster to run on large volumes than hydrodynamical simulations, with the downside being that they struggle to provide a high-resolution picture (e.g. [Somerville & Primack 1999](#)).

Later simulations implemented more complex physics models alongside particle hydrodynamics in order to emulate greater physical realism. The Illustris simulation ([Vogelsberger et al. 2014](#)) was among the first modern cosmological-scale hydrodynamic simulations to include complex gas physics, as well as feedback effects on the ICM from active galactic nuclei (AGN, e.g. [McNamara et al. 2014](#) for a recent observed example of AGN feedback in the context of clusters) and supernovae (see [Springel & Hernquist 2003](#) for a demonstration of supernova feedback in simulations, also [Dekel & Silk 1986](#) for a discussion of the theory of how such processes disrupt structure growth). Most cosmological simulations are purposefully ‘tuned’ to produce the expected galaxy stellar mass function from observations (GSMF, for some commonly-used ones from observations, see [Muzzin et al. 2013](#); [Baldry et al. 2012](#)), but even so, the resulting morphologies

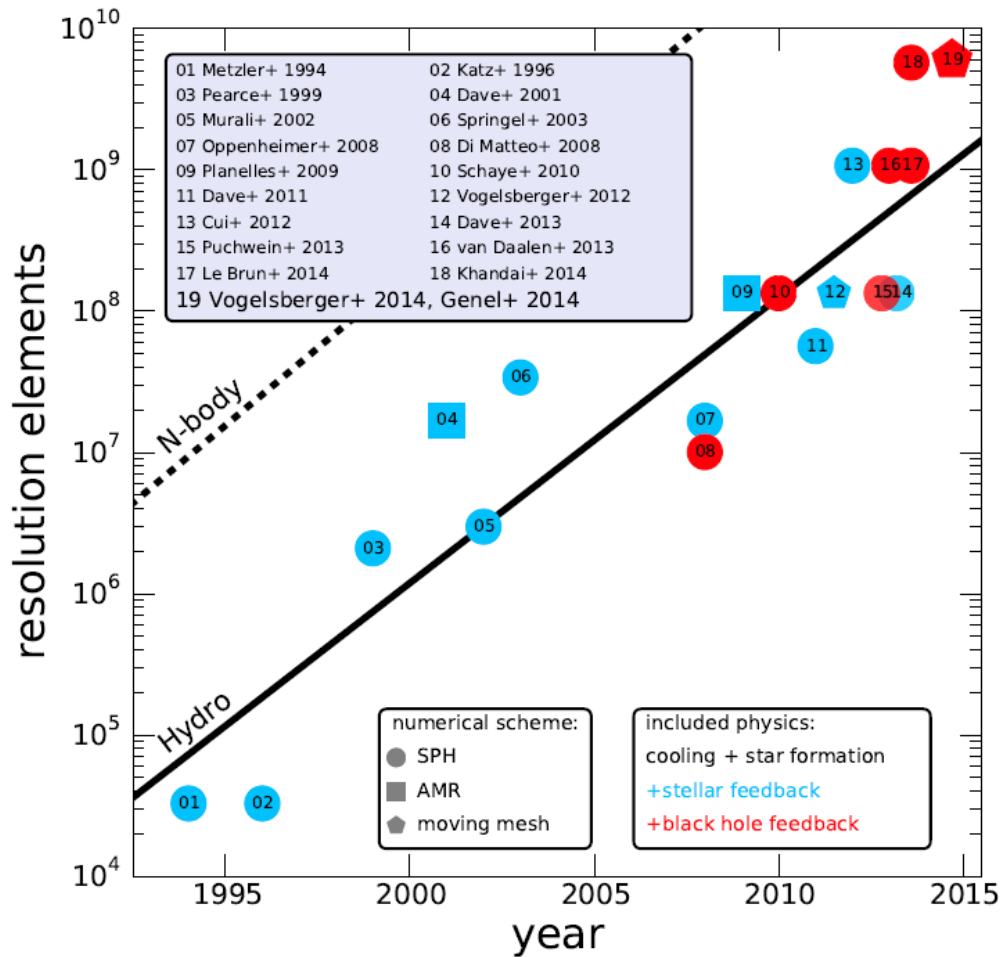


FIGURE 1.3: A chronological plot of the progress of cosmological hydrodynamical simulations with respect to resolution elements (up to 2014) from [Vogelsberger et al. 2014](#).

which originate from the model galaxies produced by these simulations are remarkable; for example, the EAGLE simulation ([Schaye et al. 2015](#)) produces morphologies which match observations very well, due to the more sophisticated physics treatment involved in their galaxy evolution models; within EAGLE, we observe massive elliptical galaxies and grand-design spirals, much like those observed in nature (see figure 1.4).

Because of the nature of large-scale hydrodynamical simulations and the limits of computation, ‘compromises’ must be made in terms of the sophistication and/or scale of the physics models used. Such scale-level compromises have inevitable effects on the final simulation outputs. For example, as mentioned previously, a notorious prediction of cosmological hydrodynamical simulations following a Λ CDM cosmology is an overpopulation of satellite galaxies, which have not been detected in comparable numbers observationally (e.g. [Klypin et al. 1999](#)). Although some observational groups have made efforts to detect

these objects (e.g. [McConnachie et al. 2009](#); [van der Burg et al. 2017a](#); [Williams et al. 2016](#)), doing so is difficult given current technological limits; the largest modern optical telescopes struggle to observe objects of surface brightnesses fainter than 28 mag/arcsec², even with multiple stacked epochs (for a recent exploration into the current frontiers of low surface brightness astronomy, see [Trujillo & Fliri 2016](#)). Instruments in the coming decade are expected to break this limit (e.g. the ‘Thirty Meter Telescope’, technical case in [Skidmore et al. 2015](#); the ‘European Extremely Large Telescope’, e.g. [Ramsay et al. 2010](#); the Large Synoptic Survey Telescope, or LSST, [Ivezic et al. 2008](#)), however, these projects are several years prior to completion (at the time of writing). Among other tensions which arise in simulations are the presence of dark matter haloes with steeper density profiles than expected, which do not mimic the ‘cored’ haloes seen in observations (e.g. [de Blok 2010](#)) and the unrealistically rapid growth rates of massive central galaxies (e.g. [De Lucia & Blaizot 2007](#)).

Present observational frictions have thus motivated simulators to produce high-resolution ‘zoom’ simulations of structures of interest, in order to model complex baryonic physics more realistically via improved resolution. Some groups, for example, have used inventive ways of distributing the resolution of their simulations to push computational limits, for example, through using Voronoi-tessellated meshes (e.g. [Curtis & Sijacki 2016](#)). These simulations have the benefit of focusing on small-scale effects which require an otherwise globally-increased resolution to produce realistic outputs. They have the pitfall of still being computationally expensive to run, but have comparably promising results (especially given the context of realistic AGN activity in [Curtis & Sijacki 2016](#)).

In the context of galaxy clusters, the C-EAGLE simulations (e.g. [Barnes et al. 2017b](#)) fall amongst the most state-of-the-art ‘zooms’ currently available. The C-EAGLE sample consists of 30 massive haloes ($10^{14} - 10^{15.4} M_{\odot}$) selected from the MACSIS simulation suite of [Barnes et al. \(2017a\)](#), with galaxy evolution and feedback models adopted from the EAGLE simulations (see [Schaye et al. 2015](#) and references therein). The sample will be used to test the growth rates of central galaxies, the nature of their satellites, the physics of the intracluster medium and, crucially, the build-up of the ICL using a full hydrodynamical approach, in comparison to (predominantly SAM-based) previous work (e.g. [Rudick et al. 2011](#), see discussions in [Section 1.2](#)).

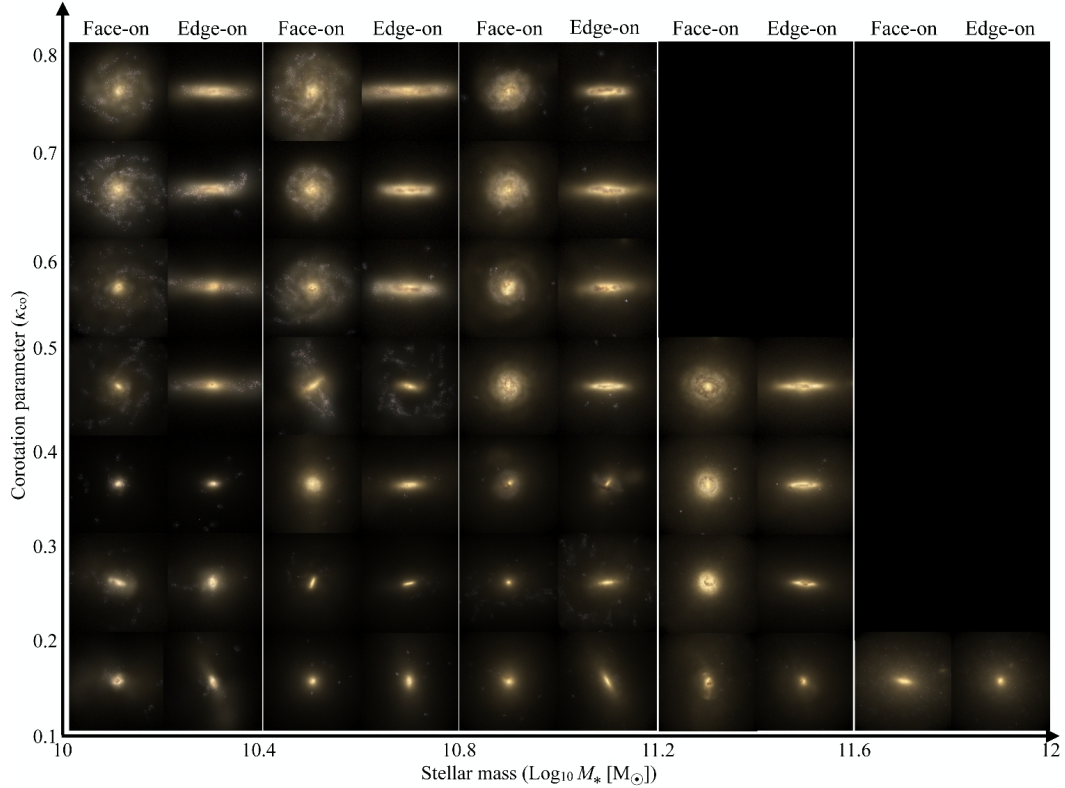


FIGURE 1.4: Examples of morphologies of galaxies in the EAGLE simulation (adapted from figure 2 of [Correa et al. 2017](#)). The top axis describes viewing orientation. The x -axis represents the stellar mass of the objects, whereas the y -axis is a metric used to describe the ‘ordered’ co-rotation. As is shown, disk and spheroid structures arise in EAGLE similar to the bimodality of galaxies seen in our Universe.

1.2 Galaxy Clusters

Large-Scale Structure within the Universe is formed of three main components ‘voids’ (underdensities of matter), ‘filaments’ (‘flows’ of matter) and ‘nodes’ (overdensities of matter). ‘Nodes’ represent galaxy groups and clusters, and are the largest gravitationally bound structures in the Universe. Galaxy clusters range in size, consisting of small groups of a few dozen members ($\sim 10^{13}M_{\odot}$) to rich clusters ($\sim 10^{15}M_{\odot}$) containing thousands of bound galaxy members (e.g. Coma).

Galaxy clusters are coveted observationally by astronomers, as they represent excellent laboratories to test theories of galaxy formation and the growth of structure (e.g. STAGES, [Gray et al. 2009](#); the ACS Fornax Cluster Survey, [Jordán et al. 2007](#); EDisCS, [White et al. 2005](#)). Clusters represent ‘extreme’ environments within the Universe, where there are often observational relics from various interaction processes; there are often, for example, galaxy-galaxy mergers observed in clusters, especially those which are dynamically

disturbed such as in the Abell 520 system (e.g. [Deshev et al. 2017](#)). Interactions between the intergalactic medium of infalling galaxies and the intracluster medium also have a profound effect on galaxy evolution, notably through gas stripping due to ram pressure (see case of NGC 4911, e.g. [Gregg et al. 2003](#)). The rate at which clusters grow in mass is highly influenced by the cosmology of the Universe, which has led to halo mass functions from simulations being measured against observations of cluster counts (e.g. [Tinker et al. 2008](#)). Changing the values of the cosmological parameters affects which constituents of the Universe dominate at a given timescale; as an example, for $\Omega_{M,0} < 0.3$, comparably slower evolution would be observed for LSS, and vice versa.

Clusters of galaxies have been observed unwittingly for centuries; William Herschel, for example, described his observations of the Coma cluster in the late 18th century, well before the knowledge that galaxies beyond the Milky Way existed (previously termed ‘nebulae’). Numerous studies of the Coma cluster by the astronomer Fritz Zwicky in the first half of the 20th added enormous insights into our understanding of cluster structure, finding that they contained significant fractions of dark matter (see [Zwicky 1933](#)) and stars bound to the cluster potential not associated with a specific galaxy (see discussion on ICL in [1.4.2](#), see also [Zwicky 1952](#)). Later observations of clusters in soft X-rays found them to also contain significant fractions of their mass within a bound halo of hydrogen plasma, termed the ‘intracluster medium’ (ICM, see [Forman & Jones 1982](#) for a historical review prior to ROSAT).

Characterising the fundamental properties of galaxy clusters, such as mass, X-ray luminosity/temperature (see [Section 1.3.2](#)) and scale size remains an ongoing challenge, and there are many approaches in the literature (for a recent comparison of multiple approaches to a simulated sample of clusters, see [Old et al. 2015](#)). With respect to scale size, from simulations, it is often useful to define a cluster ‘scale radius’ via a density ‘yardstick’ in relation to the wider Universe as a whole. This is often defined in terms of multiples of the ‘critical’ density of the Universe at the epoch of the cluster (usually $200\times$ or $500\times$, depending on convention), where R_{200} is the radius at which the mean enclosed density is $200 \times \rho_c$. This stems predominantly from the aforementioned assumption that clusters are reasonably approximated by an NFW profile ([Navarro et al. 1996](#)), which

takes the following form:

$$M_{200} = \int_0^{R_{200}} 4\pi \frac{\rho_{200}}{\frac{r}{R_{200}} \left(1 + \frac{r}{R_{200}}\right)^2} dr = 4\pi \rho_{200}^2 R_{200}^3 \left[\ln(1+c) - \frac{c}{1+c} \right], \quad (1.7)$$

where M_{200} is the characteristic halo mass, R_{200} is the characteristic cluster ‘virial’ radius, ρ_{200} is the characteristic density (defined here as $200\times$ the critical density) and c is the ‘concentration’ of the halo, i.e. the ratio between the isothermal scale radius (r_s) and virial radius (r_{vir}), such that

$$c \equiv \frac{r_{\text{vir}}}{r_s}. \quad (1.8)$$

The NFW profile implies that clusters follow roughly isothermal profiles ($\rho \propto r^2$, except at very large ($r \gg R_{200}$) or very small ($r \ll R_{200}$) scales, with a dependence on halo concentration. However, it tends to predict dark matter haloes which are overly ‘cuspy’ (i.e. more centrally concentrated) than the ‘cored’ (i.e. less centrally concentrated) systems seen in nature (e.g. [de Blok 2010](#)), such as those observed for brightest cluster galaxies (see [1.4.1](#), e.g. [Harvey et al. 2017](#)).

Dynamically however, this profile is an approximation of the idealised case; clusters are complex systems, often harbouring infalling satellite groups ([Haines et al. 2018](#)) or undergoing mergers with similarly massive systems (e.g. [Deshev et al. 2017](#)). Thus, one must often look for other approaches when estimating mass which do not require the system to be virialised (e.g. velocity dispersion, see [Section 2.5.1](#)). These methods generally fall into three main categories: masses obtained from observations of cluster gas (see [Sections 1.3.2](#) and [1.3.3](#), e.g. [Maughan et al. 2016](#)), from richness-based abundance matching (e.g. [Old et al. 2015](#)) and via weak gravitational lensing (e.g. [Tyson et al. 1990](#), [Jauzac et al. 2014](#)). The latter, arguably, is among the more accurate measures of mass due to the fact that it makes fewer assumptions about the dynamical state of the cluster, or the mass content of its constituent galaxies. However, it presents an observational challenge; in the case of weak lensing with insufficient observations, stacking is often required in order to produce an accurate shape profile (e.g. [Cibirka et al. 2017](#)).

1.3 Cluster Surveys

1.3.1 Optical

One of the largest early cluster surveys was conducted by George O. Abell (e.g. [Abell 1958](#) and later extended in the southern sky by [Abell et al. 1989](#)) in the mid 20th century, leading to the famous ‘Abell’ catalogues consisting of several thousand local clusters and groups (see figure 1.5 for an example). One obvious caveat of the Abell cluster sample however is that the clusters were detected solely through manually ‘eyeballing’ photographic plates (e.g. the Palomar Photographic Survey, [Lund & Dixon 1973](#)), so the exact methodology as to which structures are selected for inclusion within the catalogues is nearly impossible to define quantitatively. Fully digitised surveys in the 1980s and 1990s using plate scanners such as COSMOS ([MacGillivray & Stobie 1984](#)) vastly improved upon such systematics, allowing for accurate sample selection functions to be defined (e.g. the COSMOS/UKST survey, [Collins et al. 1995](#)).

Optical detection of groups and clusters, however, becomes challenging as one looks toward increasingly early epochs, given the changing evolutionary state of large-scale structure. Often, ‘protoclusters’, namely cluster candidates undergoing gravitational collapse can be separated by enormous distances (tens of megaparsecs, e.g. [Hatch et al. 2011](#)). Therefore, it becomes challenging to determine exactly what structures are at the verge of becoming gravitationally bound. Some surveys look to observational ‘beacons’ such as radio-loud AGN (e.g. the CARLA survey, [Wylezalek et al. 2013](#)), but what effect such selection has on the nature of the detections remains characteristically nebulous. There is also high risk of contamination in distant, optically-selected cluster samples due to projection effects, which affect richness values and the interpretation of member characteristics (e.g. [Rykoff et al. 2014](#)).

At later epochs ($z < 0.5$), the primary means of detecting clusters optically via quantitative methods follow either a photometric or spectroscopic approach, depending on the nature of the survey. For example, photometric algorithms have been highly successful in producing increasingly large catalogues of cluster candidates over the past two decades, as photometric surveys have increased in scope. Such finders principally work on the basis of searching iteratively for projected overdensities of galaxies lying within the nominally passive region of the colour-magnitude diagram (e.g. [Gladders et al. 1998](#);



FIGURE 1.5: Abell 2744, one of the optically selected clusters catalogued by George O. Abell. The image is a false-colour composite from Hubble Frontier Fields data (e.g. [Lotz et al. 2017](#)) Two brightest cluster galaxy candidates (see Section 1.4.1) are present at its centre, along with distinctive strong lensing arcs from background objects.

[Gladders & Yee 2000](#)). For example, [Miller et al. \(2005\)](#) produced a catalogue of 748 clusters via a red-sequence finder at low redshift ($z < 0.1$) using SDSS data; the flow chart describing their algorithm is shown in their figure 2. More recently, the redMaPPer algorithm (e.g. [Rykoff et al. 2014](#)) has become a highly effective tool in the context of observational cosmology and cluster science. Developed to maximise efficiency and produce a well-defined selection function (aka, how the number counts of clusters vary with redshift), the algorithm has provided detections of 10^5 cluster candidates in SDSS DR8 data, as well as 10^4 candidate detections from 100 deg^2 made public from Dark Energy Survey (see [The Dark Energy Survey Collaboration 2005](#)) science verification data (e.g. [Rykoff et al. 2016](#)).

Briefly, the redMaPPer algorithm works through the use of a preliminary ‘seed’ catalogue of red galaxies with spectroscopic data (in the case of SDSS DR8, a colour cut was used to select a ‘clean’ sample of red seed galaxies, see Section 6.2 of [Rykoff et al. 2014](#)). These ‘seeds’ are used to ‘train’ the algorithm, providing a baseline for photometric redshift estimates. Cluster galaxies are assigned a probability of being a member of a detected overdensity of photometrically-grouped red galaxies about a ‘seed’ galaxy, with the sample undergoing simultaneous filtration in luminosity ($L \geq 0.2L_*$) and projected distance corresponding to the size of a ‘typical’ cluster at the redshift of the ‘seed’ galaxy (~ 1 Mpc).

The obvious benefit of redMaPPer is its significant potential to create large and rather complete samples of clusters; as well as this, it is possible to run the algorithm on realistic mock catalogues in order to obtain an understanding of its selection function for a given survey. However, as we discuss later in this thesis (and at length in [Furnell et al. 2018](#)), there are still caveats in using catalogues created using algorithms such as redMaPPer if one is interested in galaxy science within a cluster context, primarily due to biases which arise at the membership selection stage. A promising approach, for example, using photometric data (images only) was introduced recently by [Chan & Stott \(2019\)](#); the team adopted the use of neural networking to classify cluster images, finding it to be an effective non-parametric method requiring minimal priors.

Alternatively, cluster finders can take a spectroscopic approach. The GALaxies and Mass Assembly (GAMA, [Driver et al. 2011](#)) survey, for example, is a highly spectroscopically complete optical survey ($\sim 95\%$ to $r = 19.8$) covering ~ 286 deg² of the southern sky on the 3.9m Anglo Australian Telescope (AAT). One can therefore use a ‘friends-of-friends’ algorithm (e.g. [Press & Davis 1982](#)) to define bound groups and clusters (see the GAMA group catalogue paper, [Robotham et al. 2011](#), for more details). The benefit of spectroscopic surveys is that one can define a bound halo in terms of membership arguably more robustly, as well as producing more accurate halo parameters. Spectroscopic redshift estimates of individual galaxies, when non-catastrophic, have a mean error in z of $\sim 10^{-5}$, at least three orders of magnitude less than for photometric redshifts (for a recent comparison, see [Clerc et al. 2016](#)). However, spectroscopy is observationally more expensive to carry out than photometry (the SDSS, for example, has at least $100\times$ more photometric observations than spectroscopic, e.g. [Abolfathi et al. 2018](#) for DR14 release statistics); two additional caveats of redshift space cluster finder algorithms is that

they often have multiple solutions describing a bound object which can be dependent on the initial priors such as the pre-designated mean ‘linking length’ between pairs, or additionally be influenced by neighbouring substructure (as noted, for example, by [More et al. 2011](#)).

Optical cluster surveys suffer from numerous caveats which affect their completeness, depth, consistency of sampling and detection reliability. From a cosmological standpoint, all (not just optical) observations are crucially limited through surface brightness dimming (see related discussion in Section 1.1). Due to changing volume alongside the effect of cosmological expansion on photon wavelength, surface brightness, μ , scales as

$$\mu(z) = \frac{\mu(z=0)}{(1+z)^4}. \quad (1.9)$$

The effect of surface brightness dimming therefore causes a steep decline in apparent brightness with increasing redshift, presenting a challenge to observers wishing to observe low surface brightness features such as ICL (see Section 1.4.2). Increasing the size of a telescope’s field of view and light collecting area (neglecting, of course, the obvious infrastructural, technical and financial challenges) is a possible approach to remedy such issues, as well as the creation of more space-based observatories such as the Hubble Space Telescope (e.g. to reduce background noise, see discussion in Chapter 4). Alternatively, other means include the use of sophisticated data stacking methods (e.g. [Zibetti et al. 2005](#)) to increase signal, but have the additional caveat of ‘washing out’ detailed structure in data, providing only a general picture of the subject of study. To minimise observational errors from an image processing standpoint, accurate ‘flat-fields’ (to gauge detector-by-detector sensitivity and remove instrument defects) and sky background estimation are critical in low surface brightness science (refer to Section 1.4.2 for further discussion).

In addition, because astronomers cannot directly achieve bolometric photometric measurements, observations often require an accompanying ‘ k -correction’. Because astronomers use band/filter systems (e.g. Johnson-Cousins UBVRI, e.g. [Johnson & Morgan 1953](#); Sloan *ugriz*, [Fukugita et al. 1996](#)), distant objects which suffer from cosmological ‘reddening’ (where their rest-frame colours are often ‘bluer’ than their observed colours), are ‘shifted’ between bands (incidentally, this same effect is very useful for picking out high redshift objects, e.g. [Cooke et al. 2014](#)). Thus, to correct for this ‘band-shifting’ effect, a k -correction term, $k(z)$, is included when computing a (distant) object’s effective

rest-frame magnitude (e.g. [Hogg et al. 2002](#)):

$$M = M' + k(z), \quad (1.10)$$

where M is an object's absolute rest frame magnitude, M' is its observed-frame absolute magnitude and the $k(z)$ term is defined as

$$k(z) = -2.5 \log_{10} \left[\frac{L_{\lambda}}{L_{\lambda'}(1+z)} \right], \quad (1.11)$$

where λ denotes the restframe wavelength, L_{λ} is the restframe luminosity at λ , λ' is the redshifted wavelength and $L_{\lambda'}$ is the luminosity at λ' .

Necessitating the inclusion of a k -correction term in the case of distant objects, however, introduces an additional layer of uncertainty in one's results, as it involves making assumptions about the evolutionary history and stellar population(s) of the object to be k -corrected, assumptions which are often greatly oversimplified (e.g. most globular clusters, once assumed to contain simple, single-stellar populations, are now widely thought to host multiple populations of stars, e.g. [Martocchia et al. 2018](#)). Indeed, there are fields of study within astronomy dedicated to understanding this complex problem, and many codes exist to compute k -corrections, evolution corrections ('e-corrections') and spectral energy distributions (SEDs) of galaxies based on multi-band photometry. We discuss these in more detail in our analysis in Chapters 3 and 5.

1.3.2 X-ray

Galaxy clusters, in general, appear as bright, extended sources in the 'soft' X-ray part of the electromagnetic spectrum (< 10 keV, e.g. [Gursky & Schwartz 1977](#)). Their emission is attributed to a large, gravitationally bound halo of superheated, diffuse plasma known as the intracluster medium (or ICM), which emits X-ray emission due to thermal bremsstrahlung (see [Gunn & Gott 1972](#)). Bremsstrahlung, or so-called 'braking radiation', occurs due to electron deceleration in the electric field generated by the ions within a plasma. For a hydrogen plasma, the emissivity from bremsstrahlung is

$$\epsilon_{\nu}/\text{Wm}^{-3}\text{Hz}^{-1} = 6.8 \times 10^{-32} T^{-1/2} n_e^2 e^{-h\nu/kT} (1 + \log_{10} kT/h\nu), \quad (1.12)$$

where ϵ_ν is the emissivity, T is the plasma temperature, n_e is the electron number density, h is Planck's constant, k is the Boltzmann constant and ν is the frequency of the emission (Hz). The emissivity of the plasma varies with frequency, such that it declines rapidly at increasingly large ν as the $1 + \log_{10}(kT/h\nu)$ term in equation 1.12 dominates. Modern X-ray telescopes used in part for cluster observations (such as XMM-Newton) are therefore designed to operate at soft X-ray frequencies, where clusters produce the majority of their emission. Cluster X-ray luminosities, L_X , generally range from 10^{43} ergs $^{-1}$ (groups) to 10^{46} ergs $^{-1}$ (very massive clusters) in X-rays, and 1 keV to 15 keV respectively with temperature, T_X (e.g. [Peterson & Fabian 2006](#)).

There are numerous benefits to X-ray cluster surveys over optical surveys in detecting galaxy clusters. Firstly, clusters give off a strong and distinctive signal in X-rays (e.g. [Lloyd-Davies et al. 2011](#)) which contrasts starkly against the X-ray background count rate (~ 0.100 counts s $^{-1}$ for $T_X = 10$ keV and $z = 0.1$ versus $\sim 2.6 \times 10^{-3}$ counts s $^{-1}$ acsec $^{-2}$ for the sky background, [Romer et al. 2001](#)). This is not the case with optical surveys, where there are often issues with projection effects which are difficult to resolve cleanly (Section 1.3.1). Secondly, X-ray detection allows for insights into the dynamical state of the intracluster medium which is not offered by any other method of cluster selection (e.g. [Walker et al. 2017](#) and upcoming discussion). Thirdly, X-ray detection readily yields physically bound systems due to the X-ray emission being linked to the presence of a deep potential well. Finally, X-ray cluster samples tend to be flux limited and relatively unbiased (with the exception of unbound systems, see upcoming discussion), making their selection functions comparably easier to model than cluster samples in legacy optical surveys (Section 1.3.1, e.g. [Böhringer et al. 2015](#)).

There are, however, important caveats to consider. Other sources of X-ray emission, for instance, can cause false detections in X-ray observations and lead to biased mass estimates. Photospheric hard X-ray emission from AGN accretion disks can produce artifacts which resemble extended sources (e.g. [Mehrtens et al. 2012](#), see figure 1.6), and lead to false detections. Unbound (or disturbed) cluster systems also present a challenge, as they often appear as having multiple ‘cores’ on X-ray images (e.g. [Mehrtens et al. 2012](#)). Modern X-ray source detection algorithms struggle to derive accurate measurements for the properties of such objects (e.g. XAPA, see [Lloyd-Davies et al. 2011](#)). In addition, in the densest parts of rich clusters which have reached a state of dynamical relaxation, so called ‘cool cores’ can also occur, which can lead to various

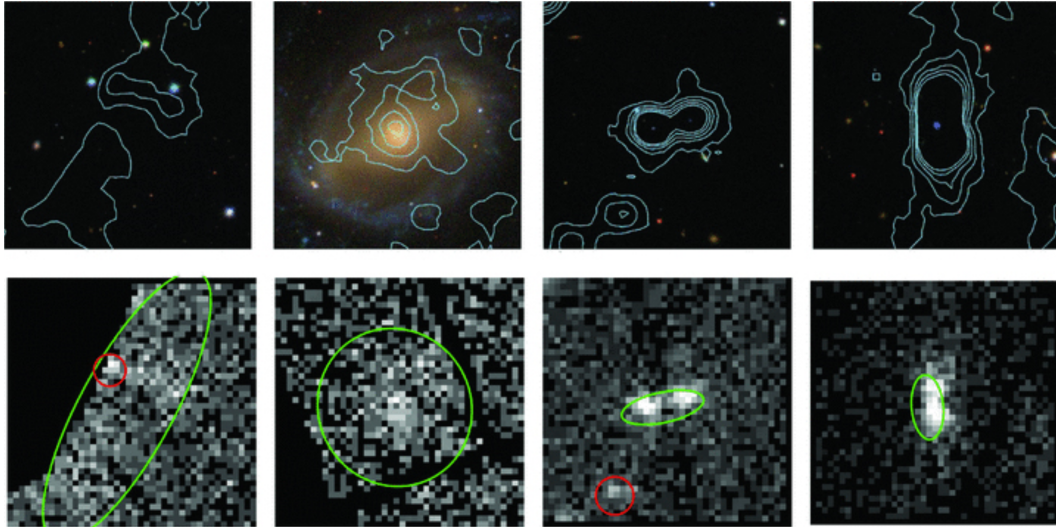


FIGURE 1.6: Figure 7 of [Mehrtens et al. \(2012\)](#) which highlights sources of contaminant extended X-ray emission. The top panel represents individual optical images from SDSS with overlaid X-ray contours; the bottom panel the equivalent X-ray image. The cores of local galaxies, background AGN and concentrated emission from stars along the line of sight have motivated candidate eyeballing in such cluster surveys as the XMM Cluster Survey (e.g. [Romer et al. 2001](#)).

biases in the ICM properties of a cluster (see upcoming discussion). These result due to runaway radiative cooling as infalling gas is compressed, the thermal energy of which must balance the energy radiated from the dense gas at the cluster core. One can relate the mass deposition rate and luminosity via the following equation

$$L(< r) = \frac{5kT}{2\mu m} \dot{M}, \quad (1.13)$$

where L is the X-ray luminosity contained within an arbitrary radius r , \dot{M} is the rate of mass deposition and μm is the mean mass of a plasma particle (0.5 amu for hydrogen plasma). Cooling timescales for the ICM due to this effect are predicted to be short (< 1 Gyr), so naively one might expect an abundance of cool core clusters; however, observations have not met such predictions, finding fewer extreme cool cores than naively expected in clusters which appeared to be dynamically relaxed systems ([Eckert et al. 2011](#)). This may be the case primarily because of AGN feedback into the ICM halting the process (e.g. [McNamara et al. 2014](#) and references therein). These effects (AGN heating plus radiative cooling) lead to a so-called ‘multiphase’ ICM, where the gas density and temperature differ radially across a cluster (e.g. [Fabian et al. 1994](#)).

Much of X-ray astronomy in the context of clusters aims to produce accurate scaling relations of cluster properties from the observed properties of the ICM (see, for example,

e.g. [Lloyd-Davies et al. 2011](#), [Leauthaud et al. 2010](#)), as there is a well-established empirical relationship between the luminosity and temperature of the X-ray plasma and the halo mass of the cluster (e.g. [Reiprich & Böhringer 2002](#)). Aforementioned cool cores, a common presence in massive, dynamically-relaxed systems (e.g. [Fabian et al. 1994](#)), have the effect of steepening the slope of the luminosity-halo mass relation due to their elevated X-ray brightness, leading to masses which are biased high (e.g. [Eckert et al. 2011](#)). To avoid this phenomenon affecting cluster mass estimates through X-ray measurements, groups often take the approach of providing ‘core excised’ masses (e.g. [Mehrtens et al. 2012](#)), or use X-ray temperature over luminosity as a mass proxy, due to it arguably being a more representative global (or, at least less radially-dependent) descriptor of the thermodynamical state of the gas (e.g. [Lloyd-Davies et al. 2011](#)).

Observations of X-ray emission within groups and clusters of galaxies allow for the evolutionary history of the ICM to be probed. Most studies assume that the evolution of X-ray emission is self-similar in terms of collapse; that is to say, the rate of collapse occurs independently of initial conditions and follows a power law:

$$\bar{\rho}(r|t) = 5.55\rho_b(t)f\left(\frac{r}{r_{\text{turn}}(t)}\right) \quad (1.14)$$

where t is the timescale and r_{turn} is the radius of a shell at the critical point of breaking away from Hubble expansion into collapse (density perturbations generally grow as $\rho \propto t^{-2/3}$). The coefficient of 5.55 arises from the fact that this so-called ‘shell reversal’ occurs at a fixed multiple of the background density (for a classic derivation of the spherical collapse model, see [Gunn & Gott 1972](#)). In general, X-ray studies of clusters appear to show evidence that the assumption of self-similar collapse is a reasonable descriptor of cluster evolution (e.g. [Teyssier et al. 1997](#)), though this has been debated by some ([Finoguenov et al. 2001](#)); a greater consensus on the best physical treatment for cluster evolution will likely emerge as the size and data quality of X-ray cluster samples continues to increase (see upcoming discussion).

X-ray surveys of clusters came at a later stage than optical surveys, predominantly because of the need for space-based telescopes to be able to observe them effectively due to the transmission window of the atmosphere not allowing for space-based sources of X-ray emission to be detected by ground based telescopes. For example, EXOSAT ([White & Peacock 1988](#)) was a 3-year mission from 1983-1986, providing one of the first detailed

glimpses of cosmic X-ray emitting phenomena; it accumulated nearly 2,000 observations in total over the course of its mission, including galaxy clusters and X-ray binaries. Among the earliest successful all-sky X-ray surveys was the ROEntgenSATellit (ROSAT) All Sky Survey (RASS, e.g. [Voges 1992](#)), data from which remains in widespread use to this day (e.g. COntstrain Dark Energy with X-ray clusters, CODEX, Finoguenov et al., in prep.). RASS was the first all-sky survey in soft X-rays (0.1-2.4 keV), with the ROSAT mission lasting nearly a decade (1990-1999). Amongst the largest and most successful studies involving RASS data was the REFLEX sample of clusters (outlined in [Böhringer et al. 2001](#)). REFLEX-II produced ~ 1000 new cluster candidates over the subsequent 10 years; a recent study, for example, used REFLEX data to probe the presence of a ‘local void’ in the southern sky, which would bias the local value of the Hubble parameter ([Böhringer et al. 2015](#)).

Because of the low all-sky survey resolution ($\sim 2'$) of ROSAT, however, detections often have large margins of error attributed to the positional peak of cluster X-ray emission, often used as a useful proxy for the position of the bottom of the cluster potential well (see upcoming discussion on BCGs in Section 1.4.1), as well as little detail in terms of ICM structure. Subsequent missions from telescopes with higher (sub-arcminute) angular resolution (e.g. Chandra, [Weisskopf et al. 2000](#); XMM-Newton, [Jansen et al. 2001](#)) therefore enabled significantly more highly-resolved observations of the ICM. Such studies have supplied an unprecedented window into ICM physics, revealing complex structures, shock fronts, Kelvin-Helmholtz instabilities (e.g. [Walker et al. 2017](#)) and even cavities thought to be produced by radio AGN (e.g. [Russell et al. 2017](#)).

Another of the most successful surveys of clusters in X-rays to date is the XMM Cluster Survey (XCS). XCS uses legacy XMM archival data to serendipitously search for potential clusters, which are then matched to optical candidates. Candidates are then internally screened by collaboration members using a ‘Galaxy Zoo-like’ approach (e.g. [Lintott et al. 2011](#); for the latest published results from XCS, refer to [Mehrtens et al. 2012](#)). At the time of writing, XCS has detected over 1200 clusters, many of them serendipitous ([Manolopoulou et al.](#), in prep). Further details on XCS will follow in Chapter 4 of this Thesis.

A future X-ray mission significant to cluster science is eROSITA (e.g. [Merloni et al. 2012](#)), due for launch (at the latest notice of this thesis, Alexis Finoguenov, priv. comm),

in 2019. eROSITA has been designed with full sky survey capabilities, with high angular resolution ($15''$) compared to ROSAT ($1.8'$). It is predicted to detect all galaxy clusters in the Universe above $10^{14} M_{\odot}$ ($\sim 137,000$ total group/cluster detections, [Pillepich et al. 2012](#)), creating the largest and most complete X-ray selected sample of galaxy clusters to date. We discuss eROSITA in the context of the SPIDERS survey in Section 2.1.

1.3.3 On the CMB and the Sunyaev-Zeldovich (SZ) Effect

A great deal of our modern understanding of cosmological structure stems from measurements of the CMB, for which there have been numerous missions. The earliest, all-sky space based COsmic Background Explorer (COBE, see [Smoot et al. 1990](#) for instrument design) mission took place between 1989 and 1993, and was able to measure anisotropies in the CMB at an amplitude of 10^{-5} K. This feat earned two of the principal investigators, George Smoot and John Mather, the 2006 Nobel Prize in Physics for demonstrating that CMB anisotropy measurements represent a rich, precision science. Two further space-based missions have followed since: the Wilkinson Microwave Anisotropy Probe (WMAP, 2001-2010, e.g. [Bennett et al. 2003](#)) mission and the Planck mission (2009-2013, e.g. [Planck Collaboration et al. 2014](#), see figure 1.7), the latter representing the current standard in CMB observations. There are also numerous ground-based missions observing the CMB (for example, the South Pole Telescope/SPT, [Carlstrom et al. 2011](#) and the Atacama Cosmology Telescope/ACT, e.g. [Swetz et al. 2011](#)), which are often used to carry out redshift-independent searches for galaxy clusters via the Sunyaev-Zeldovich effect (e.g. [Sunyaev & Zeldovich 1972](#), see discussion below).

Precise measurements of CMB anisotropies provide crucial tests of our theoretical understanding of cosmology (e.g. Figure 1.8), which have supplied numerous constraints for modern cosmological simulations. The scale and amplitude of CMB anisotropies encode information on the scale of the physics affecting said anisotropy; for example, in theory, (see discussions in [Guth 1981](#)) ‘inflation’ should affect all scales equally, whereas radiation diffusion damping (first outlined in [Silk 1968](#)) is a small-scale effect. Observations of the CMB, alongside other means of generating cosmological constraints (in the context of this work, co-moving volume density of galaxy clusters) can therefore affirm the validity of our current best theories of cosmological evolution. Our current mainstream cosmological model, cold dark matter with a cosmological constant (Λ CDM)

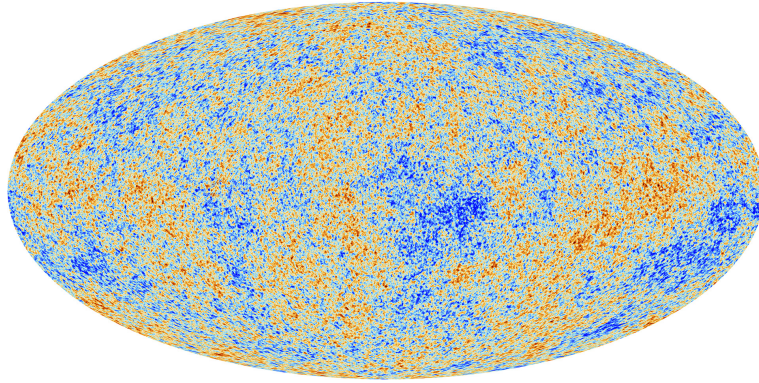


FIGURE 1.7: Map of the CMB, as observed by Planck. ‘Colder’, underdense regions are depicted in blue, ‘warmer’ overdense regions in red (fluctuations on the order of $\sim 10^{-5}$ K).

is the basis of the majority of most modern cosmological simulations (see earlier discussions in Section 1.1.1), which we use against observations to scrutinise our understanding.

Galaxy cluster surveys have exploited the Sunyaev-Zeldovich (SZ) effect in recent years successfully to detect cluster candidates, detections of which are not affected by surface brightness dimming as is the case in optical and X-ray surveys, due to the dependence of the SZ effect solely on the properties of the scattering medium (for a detailed discussion, see Birkinshaw 1999). This allows one to successfully create large catalogues of redshift-independent sources, where one is limited only by angular scale (numerous clusters at local scales, for example, have much larger angular sizes than the beam size of observatories capable of detecting the SZ effect such as Planck).

The frequency-dependent Sunyaev-Zeldovich effect is caused by inverse Compton scattering (briefly, electron-photon collisional scattering) of CMB photons by the ICM, and is described via the following formula:

$$\frac{\delta I_\nu}{I_\nu} = \frac{\delta n}{n} = -y \frac{h\nu e^{h\nu/KT}}{kT (e^{h\nu/kT} - 1)} \left[4 - \coth \left(\frac{h\nu}{2kT} \right) \right], \quad (1.15)$$

where $\frac{\delta I_\nu}{I_\nu}$ is the fractional change with respect to the background intensity (also proportional to the change in temperature $\frac{\delta T}{T}$), $\frac{\delta n}{n}$ is the change in photon phase space occupation number, and y is the dimensionless Compton ‘ y ’ parameter:

$$y \equiv \int \sigma_T n_e \frac{kT}{m_e c^2} dl, \quad (1.16)$$

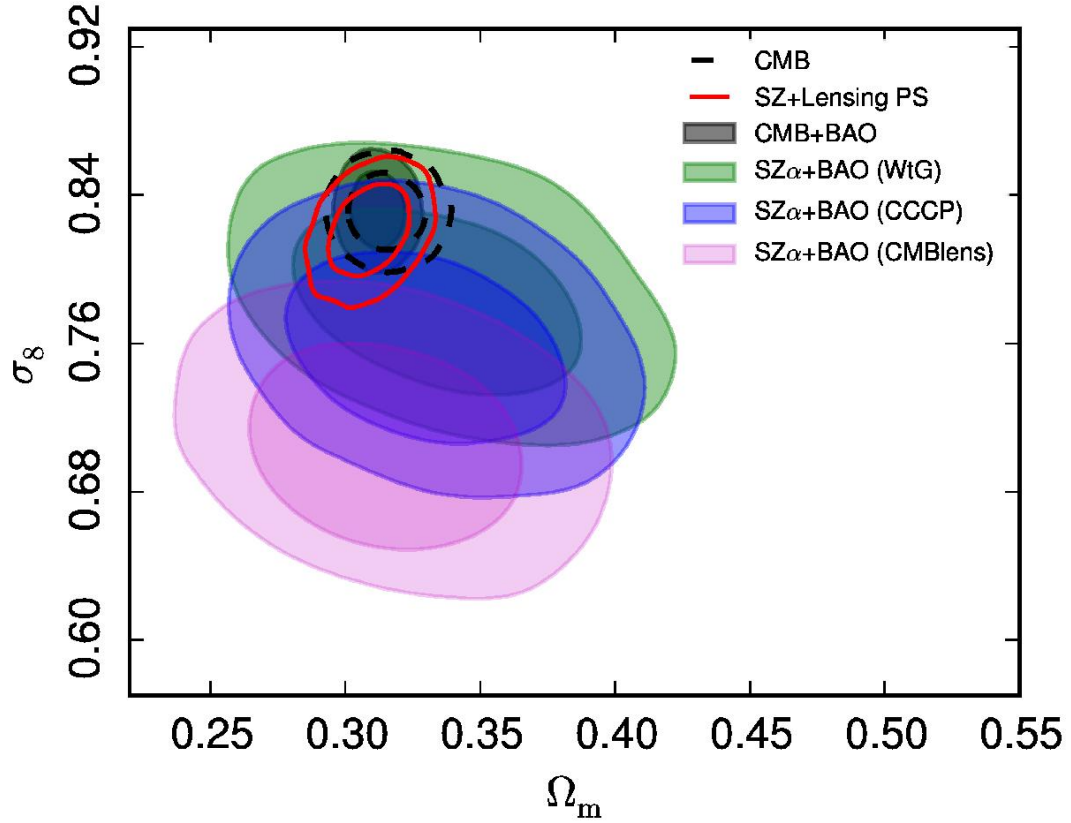


FIGURE 1.8: The Planck cosmology results from cluster counts, as of 2015, from [Planck Collaboration et al. \(2016b\)](#). The range of possible σ_8 (a measure of perturbation scale) and matter density parameter values, Ω_m are shown as contours, with ‘SZ’ in the legend denoting results derived from the SZ-selected cluster sample and differing colours representing a different mass bias value. As is shown, there is a significant deviation from the peak cosmological parameter probability derived from cluster counts with respect to the constraints from measurements of CMB fluctuations.

where σ_T is the Thomson cross section for an electron (b), n_e is the electron number density, m_e is the electron mass and l is the scattering length (m).

How the SZ effect appears on a CMB map is regime-dependent; at low frequencies, the result is a fractional cooling of the background; at high frequencies, beyond the peak of the CMB spectrum, the equation results in a change in sign, resulting in a strong observational signature. The low frequency effect is the one most commonly observed for galaxy clusters, which appear as ‘holes’ in CMB flux maps (e.g. [Hasselfield et al. 2013](#), see figure 1.9). Observations of the SZ effect, as an aside, therefore provide valuable measurements for the amount of gas ‘clumping’ in clusters (due to the dependence of the equation on electron density).

In recent years, SZ measurements of galaxy clusters have posed a challenge to current cosmological constraints, specifically the results from the Planck catalogues (e.g. [Planck](#)

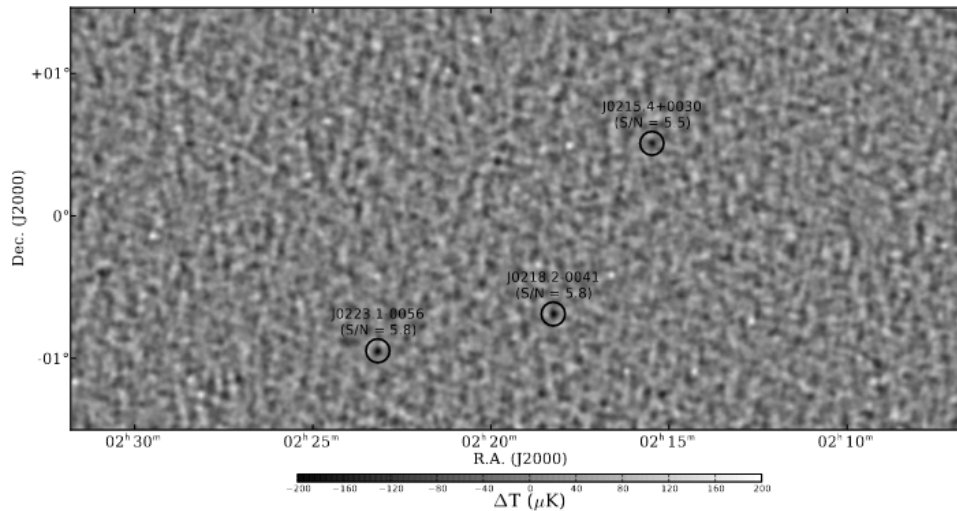


FIGURE 1.9: An adapted version of figure 3 from [Hasselfield et al. \(2013\)](#), which shows an 148 GHz band ACT observation. Three cluster candidates are highlighted (black rings).

[Collaboration et al. 2016b](#)). There exists a significant tension ($1 - 4\sigma$) between the estimated cosmology from cluster counts versus from analysis of fluctuations within the CMB; figure 1.8. This phenomenon itself is not unique to Planck (e.g. there is agreement with results from the South Pole Telescope, see [Bocquet et al. 2015](#)), and is primarily thought to be dominated by uncertainties in the cluster mass ‘bias’.

Most X-ray surveys make the broad assumption that the gas within clusters is in approximately hydrostatic equilibrium; simulations, however, have shown that is is not always the case, due to non-thermal pressure (for example, magnetic fields) and bulk gas motion (e.g. [Nagai et al. 2007](#)). An assumed mass bias factor therefore became canonical when using clusters for cosmology ($\sim 20\%$) to compensate for this offset. There are also significant systematic uncertainties in the X-ray analysis, such as differing detector calibrations and various reduction pipeline algorithms. The associated error around the time of writing in the estimated mass bias stands at approximately 10%, even using the current ‘gold standard’ of weak lensing for cluster mass measurements (e.g. ‘Weighing the Giants’, or WtG, [von der Linden et al. 2014](#)); [Planck Collaboration et al. \(2016b\)](#) suggest that, to obtain more representative results, the margin of error needs to be brought down by at least a factor of 10 in order to tighten priors and disentangle the effect of cluster mass measurement error on cosmological results.

1.4 Stellar Mass in Galaxy Clusters

1.4.1 Brightest Cluster Galaxies

One of the most distinctive features of galaxy clusters is that they commonly host one or more ‘brightest cluster galaxies’, or BCGs, at their cores. The distinction between cluster and field galaxies gained significant traction in the middle of the 20th century, when interest in what drove their distinctive morphologies grew. For example, [Morgan & Lesh \(1965\)](#) created a catalogue of central supergiant ‘D’ (where ‘D’ stands for ‘diffuse’ in the Yerkes classification scheme of [Morgan 1958, 1959](#); the preamble ‘c’, i.e. ‘cD’, indicating a very large galaxy) type galaxies from Abell clusters (e.g. see their figure 1). It was subsequently observed that these BCGs were distinctive features in clusters, and often much more luminous than their neighbours (e.g. [Sandage 1976](#); [Tremaine & Richstone 1977](#)).

It was realised shortly after the first catalogues of these supergiant galaxies were compiled that BCGs, at least in the local Universe, were relatively homogeneous in terms of luminosity and structure. Generally classified as elliptical galaxies, BCG light profiles approximately follow a $I(r) \propto r^{1/4}$ de Vaucouleurs profile (where $I(r)$ is the intensity at a given radius r from the ‘centre’ of the galaxy, e.g. [de Vaucouleurs 1948](#)). This homogeneous nature motivated researchers to investigate their use as astronomical ‘standard candles’ (e.g. [Sandage 1972](#)), however, this has long fallen out of favour due to the large amount of associated scatter compared with other methods such as type Ia supernovae. This relative homogeneity, however, such as their small scatter in absolute magnitude values (~ 0.3 mag, e.g. [Aragon-Salamanca et al. 1998](#)) has been observed in samples of BCGs as distant as $z \sim 1$ (e.g. [Whiley et al. 2008](#), see discussion below).

Since their discovery, researchers have attempted to understand BCGs features in the context of the environment in which they reside (e.g. [Bautz & Morgan 1970](#)). Canonically, BCGs are generally thought to represent a distinct population of galaxies (e.g. [Djorgovski & Davis 1987](#)) separate from the general elliptical non-BCG population (e.g. [von der Linden et al. 2007](#)). This is because BCGs often have distinct characteristics (particularly at local scales, such as in the Virgo Cluster in figure 1.12), with many hosting obvious, extended envelopes of stars (e.g. figure 1.5, for some early detailed photometric work on BCGs, see [Oemler 1976](#)). For example, work by [Schombert \(1986\)](#) highlighted the

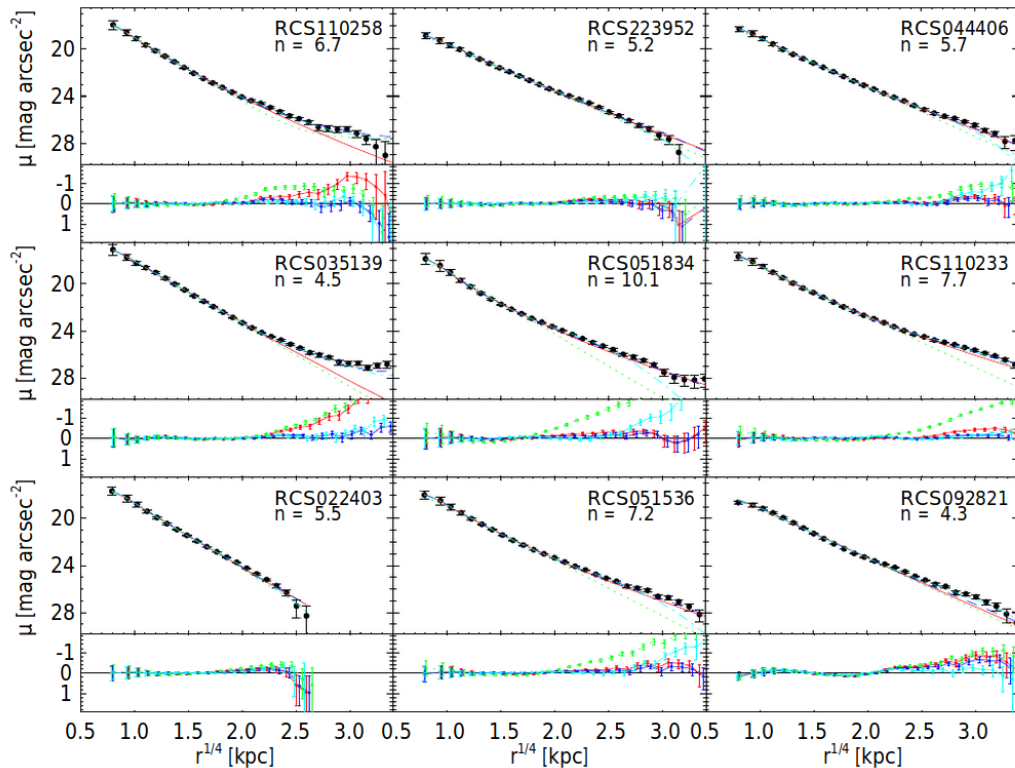


FIGURE 1.10: An example of nine BCG 1-D surface brightness profiles from Bai et al. (2014); surface brightness, μ , is plotted on the y -axis versus $r^{1/4}$ on the x -axis, where r is measured along the major axis of the elliptical isophotes fit to the galaxy (see Chapter 4 for a similar method used in this work). The structure of the BCGs ranges dramatically in terms of concentration and extent.

widely-varying profile shapes of BCGs across a range of cluster masses; they found generally that more massive clusters tended to host BCGs with shallower light profiles. This was also found to be the case as well using X-ray luminosity as a mass proxy by Brough et al. (2005), who found their result was robust independently of selection (see figure 1.10 for examples of profiles from Bai et al. 2014).

For the majority of galaxy clusters which are dynamically ‘relaxed’, BCGs reside close to the peak of cluster X-ray emission (e.g. Lin & Mohr 2004, Hudson et al. 2010), often used as a proxy for the location of the potential well of the cluster (see discussion in Section 1.3.2, e.g. Lea et al. 1973; Fabian & Nulsen 1977). The picture however is somewhat more complicated for clusters out of dynamic equilibrium (i.e. ones which have undergone recent mergers with neighbouring groups). As a deep potential well is often not present in such cases, this proxy is ineffective, with such systems tending to host multiple, similarly-luminous candidate BCGs and numerous X-ray peaks (e.g. Markevitch et al. 2002). Identifying BCGs is therefore often non-trivial in more distant clusters (e.g.

Zhao et al. 2017), in comparison to the classical, distinct BCGs observed at low redshift. Moreover, merger activity (galaxy-galaxy within clusters as well as cluster-cluster) is more common in high-redshift systems, as it is a dominant mechanism behind the growth of galaxy clusters in cosmic large-scale structure (e.g. White & Frenk 1991).

Due to the location of BCGs at the peak of X-ray emission in relaxed clusters, there has been speculation in the literature that BCGs gain stellar mass through ongoing star formation as a result of condensing cluster gas regulated by some feedback mechanism (Fabian et al. 1994, McNamara et al. 2014, Voit et al. 2016). For many hydrodynamical simulations, AGN activity remains the favoured dominant candidate for feedback (e.g. McCarthy et al. 2016, Schaye et al. 2015, Vogelsberger et al. 2014), although some studies are moving towards closer examination of external baryonic processes such as ram-pressure stripping and shock heating (e.g. Steinhauser et al. 2016). Indeed, high rates of star formation ($10^1 - 10^2 M_{\odot}\text{yr}^{-1}$), have been detected in some BCGs within clusters hosting cool-cores (e.g. O’Dea et al. 2008, Edge 2001) as well as enhanced AGN activity (e.g. Burns 1990) and giant molecular gas outflows (e.g. Russell et al. 2014). However, mass deposition rates may still be too slow to reproduce the mass range of BCGs through in-situ star formation alone (e.g. Peterson & Fabian 2006), alongside strong cool-core systems being relatively rare at higher redshifts where observations suggest BCGs gain the bulk of their mass (e.g. Collins et al. 2009).

BCG formation scenarios based on classical hierarchical merging have risen as a popular alternative to growth through star formation since $z \sim 1$ (e.g. Ostriker & Tremaine 1975, Merritt 1985). Broadly, these models fall into two categories: ‘galactic merging’, where many similarly-sized galaxies violently merge together in a short amount of time to form the BCG, or ‘galactic cannibalism’, a slower process where mass is accumulated over time from smaller galaxies sinking to the bottom of the cluster potential well.

Currently, a two-step scenario behind BCG formation is favoured (e.g. Johansson et al. 2012), with the bulge forming first at early times ($z > 2$) followed by the envelope feature at late times ($z < 1$). This approach has gained popularity as an explanation behind the ‘cD-type’ morphologies (i.e. bulge + halo) seen in many BCGs at low redshift, as well as the apparent ‘puffing up’ of elliptical-types (e.g. van Dokkum et al. 2008, van der Wel et al. 2008). Indeed, there is convincing indirect evidence that merger events happen at some point in the formation history of BCGs (e.g. Burke & Collins 2013, Burke et al.

2015), with many examples of BCGs hosting multiple nuclei at their centres (e.g. Lauer 1988, Schneider et al. 1983).

One of the great mysteries surrounding BCG evolution, however, is the nature of their mass growth. There remains a significant discrepancy between the mass deposition rates of BCGs in simulations and BCGs which have been observed. As aforementioned, BCGs exhibit surprising homogeneity, with many studies finding uniformly-luminous BCGs in similarly massive clusters up to redshifts of $z \sim 1$ (Aragon-Salamanca et al. 1998, Whiley et al. 2008, Collins et al. 2009, see also figure 1.11). This remains contrary to many recent simulations, which struggle to reproduce the observed homogeneity seen in BCGs up to redshifts of $z \sim 1$. Although they are often successful in reproducing the colours of observed BCGs, they fail to accurately model BCG growth, over-predicting the observed amount by between a factor of 2–4 (e.g. De Lucia & Blaizot 2007, Ragone-Figueroa et al. 2013). Improvements have been made in recent years, but most simulations still cannot reproduce the observed morphologies of BCGs in general, especially within their central regions (e.g. Laporte & White 2015, Tonini et al. 2012). It has been therefore recognised that understanding the growth of BCGs and the global accumulation of baryons in cluster cores may be critical for solving some of the aforementioned discrepancies suffered by clusters in hydrodynamical simulations.

1.4.2 Intracluster Light

Studies of intracluster light have gained popularity throughout the era of modern hydrodynamical simulations as an attempt to understand the difference in apparent mass growth rate between observed and simulated BCGs. Intracluster Light, or ICL, is a low surface brightness stellar component that exists (predominantly) in the cores of evolved, massive galaxy clusters. One of the first detections of an ICL component is again attributed to the astronomer Fritz Zwicky (e.g. Zwicky 1952), who noted ‘a diffuse light’ present on photographic plate observations of the Coma Cluster. Studies following Zwicky’s work in the 1960s and 1970s (predominantly on the Coma Cluster) on ICL varied in terms of success, due to the challenging nature of measuring low surface brightness features, which are significantly and rapidly affected by cosmological surface brightness dimming with increasing redshift (as discussed previously in Section 1.3.1), using the limited tools available for image processing and data reduction (e.g. de Vaucouleurs

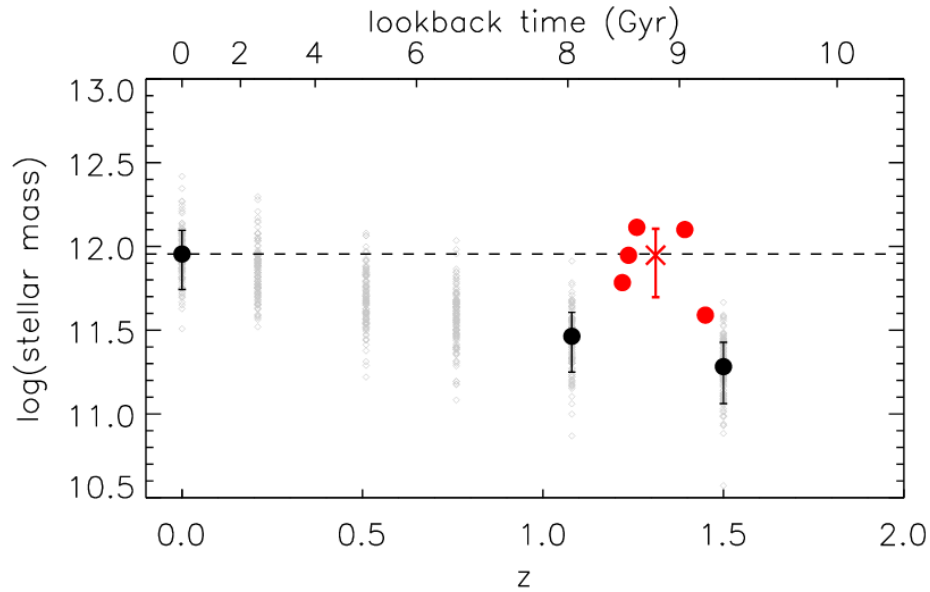


FIGURE 1.11: Figure 3 from [Collins et al. 2009](#), comparing the observed and predicted masses of BCGs. The BCGs (measured using deep Subaru data, PI: John Stott) are marked as red points in the diagram, with the results of simulations carried out in [De Lucia & Blaizot \(2007\)](#) as black points. Whereas the BCGs are predicted to have a steep gradient in growth from $1 < z < 0$, the results from [Collins et al. 2009](#) suggest their growth curve to be predominantly flat.

1960, [Oemler 1973](#), see also [Vílchez-Gómez 1999](#) for a brief review on early ICL science and references therein).

As computer technology and data processing methodologies have become more advanced over the last 20 years, an increasing number of authors have reported ‘successful’ detections of the ICL in more distant clusters than Coma or Virgo. Research groups have taken many different approaches over the years when measuring the ICL, which are often dependent on both data quality and sample size. For example, [Zibetti et al. \(2005\)](#) attempted to measure the ICL in SDSS DR1 data by stacking g , r and i band data for 683 cluster candidates in the range $0.2 < z < 0.3$. They found that BCGs contributed almost twice the amount of light to the overall cluster than the ICL ($\sim 22\%$ compared to $\sim 11\%$ for ICL), with both having similar colours. Other groups have attempted this measurement through parametric fitting and subtraction; [Gonzalez et al. \(2005\)](#), for example, modelled the surface brightness distributions of BCGs in 24 clusters, interpreting the 2-component fit ($2 r^{1/4}$ components) to comprise of BCG+ICL. In contrast to [Zibetti et al. \(2005\)](#), they found the outer component to consist of ~ 10 times the inner component. Others have measured the ICL at various surface brightness thresholds instead (e.g. [Burke et al. 2012, 2015](#)), or ‘guessed’ at where the light domination by ICL over the BCG halo may

begin, for example, using a set radius where the BCG light profile appears to deviate from a Sérsic model (e.g. [Krick & Bernstein 2007](#), [Krick et al. 2010](#); [Montes & Trujillo 2018](#) and discussion in Chapter 5). Perhaps best put by [Uson et al. \(1991\)](#), disentangling the cD envelope from a BCG is often still a ‘matter of semantics’ in modern observational studies, with little solid observational evidence for a clear dividing line between the two.

Results from studies attempting ICL measurements are therefore highly methodologically dependent, and there is no consensus on a generalised ‘best practice. This predominantly stems from the fact that there is currently no physically-motivated method of observationally disentangling the BCG and the ICL (except possibly dynamically via IFU measurements, which are observationally expensive); as a result, its formal observational ‘definition’ is often somewhat arbitrary. To date, the range of estimated ICL contribution to the overall cluster light falls between 5 – 50%, with sample selection/size, sample redshift, image processing/quality and measurement methodology all being contributing factors to the large scatter.

The scatter in observational results leads to numerous difficulties making like-for-like comparisons with ICL in simulated clusters of galaxies. There have been relatively few theoretical studies using a full hydrodynamical treatment, however, with the majority being N-body based with a semi-analytical prescription. For example, a relatively early study, [Murante et al. \(2007\)](#), simulated ICL buildup by selecting 117 $M > 10^{14} M_{\odot}$ haloes (identified via a friends-of-friends, or FOF, method) from a cosmological hydrodynamical simulation (see [Borgani et al. 2004, 2006](#) for further details), from $0 < z < 3.5$ in 17 redshift bins. Resolution effects were tested on 3 clusters, with a mass resolution $45 \times$ higher than for the original simulation. They define ICL dynamically, using a threshold based on the number of bound star particles (with a minimum of 32 corresponding to a ‘bound’ object). They found a steady increase in the fraction of star particles defined as being ICL (with more ICL being present in more massive haloes), with no ‘preferred’ redshift value where the build-up of material begins. Most star particles were found to originate primarily from merging processes onto the central galaxy of the halo (i.e. the BCG). [Rudick et al. \(2006, 2011\)](#) simulated 7 clusters via an N-body approach, neglecting computationally-expensive hydrodynamical methods with a focus on the influence of gravitational effects rather than gas dynamics. They applied several common observational approaches to mock images of their simulated clusters, finding that the total ICL varied up to a factor of 2 depending on the method used. They found

a large amount of scatter in their simulated values, with no halo mass-dependent trends. A similar result was found in [Contini et al. \(2014\)](#) following a semi-analytic approach with N-body dark matter halo merger trees.

Although the observational and simulated results show consistent halo-to-halo scatter in terms of the exact amount of ICL, they disagree completely on the rate of formation of the ICL; observations reveal a much more rapid build-up of ICL between $0 < z < 1$ than the smooth, power law-like increase seen in simulations (e.g. [Murante et al. 2007](#), [Rudick et al. 2011](#)). More sophisticated simulation suites with high resolution and full hydrodynamics may prove crucial at resolving this tension (e.g. [Barnes et al. 2017b](#)).

The exact nature of the ICL is notoriously difficult to characterise, due to its relative faintness with respect to the sky background (approximately $100\times$ fainter, e.g. [Bernardi et al. 2017](#)) and susceptibility to sources of flux contamination (e.g. [Duc et al. 2015](#) and discussion further on in this section). The background issue in the context of ICL is especially problematic (see discussion in [Chapter 4](#)) as historically, most surveys have not been designed with observing strategies which optimise detection of low-surface brightness features. Often, they instead take an approach where observations are not contiguous, rather than taking a ‘drift-scan’ approach such as the SDSS (e.g. DES, [The Dark Energy Survey Collaboration 2005](#)). The benefit of this means one can optimise their strategy to obtain observations of transient objects, or allow for condition-dependent observations to take place; the caveats, however, involve the statistical uncertainties concurrent with background estimation and weighting images.

In most cases, such observing strategies do not cause a great deal of ‘headache’ for astronomers who are solely interested in stars, bright galaxy structure or light profiles (features of relatively high surface brightness); however, approaching the low surface brightness regime ($> 25 \text{ mag/arcsec}^2$), artifacts resulting from coaddition often represent a large contribution to the overall noise due to increasing uncertainty of the epoch-dependent value of the sky background (see for example, imaging from KIDS, Kelvin et al., in prep). One can attempt to correct these features using a ‘weight map’ to account for the frame-by-frame sky variance, but it is often instead more straightforward to deal with observational data carried out in such a way as to minimise these effects a priori (see, for example, [Burke et al. 2012](#)), such as through random dithering, or via periodic measurements of the background off-target (e.g. [Trujillo & Fliri 2016](#)).

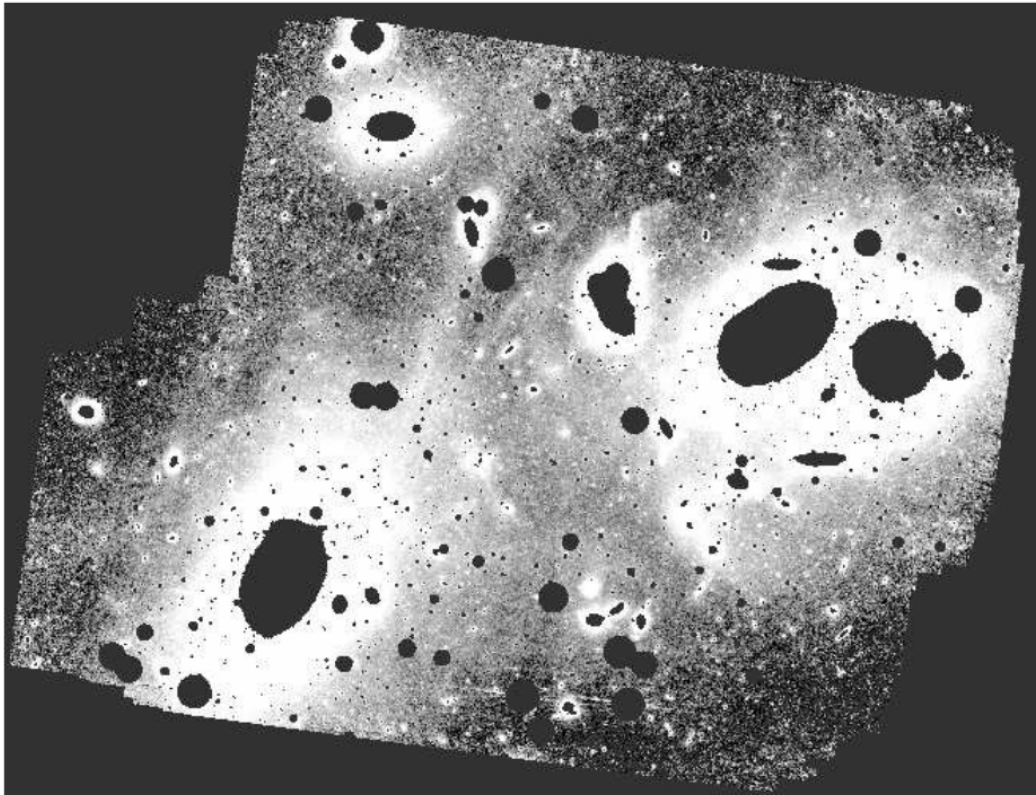


FIGURE 1.12: Figure 1 from [Mihos et al. \(2005\)](#), showing the core of the Virgo Cluster imaged by the 0.6m Burrell-Schmidt telescope. Bright sources have been masked, and the contrast has been adjusted to highlight structure. The ICL is clear in this image, with streams of stars existing between M87 (the BCG, bottom left) and its neighbouring galaxies.

An additional problem arises with algorithms implemented in commonly-used software packages used to estimate and subtract sky background. By far the most commonly used of these is Source Extractor, or SExtractor ([Bertin & Arnouts 1996](#)), which estimates sky background by ‘splitting’ the sky into a grid of regions, the size of which is specified by the user. SExtractor then fits a spline to these regions, and subtracts the ‘background’. Issues arise however due to the dependence on the grid size with respect to field objects; if, for example, one selects a grid size which is too small, SExtractor will often over-subtract flux around extended objects such as galaxies (see discussion in Chapters 2 and 4). This leads to ‘divots’ if one should choose to apply this background estimate to their image ([Kelvin et al., in prep](#)), ‘dearth’s’ of flux around objects. However, if one chooses a mesh size which is too large, SExtractor cannot interpolate correctly, leading to an inaccurate value of the global field sky (see [Bertin & Arnouts 1996](#)).

Researchers have therefore started to consider alternative approaches to sky subtraction beyond SExtractor. One promising, unique approach in the literature is the ‘Noise Chisel’

software ([Akhlaghi & Ichikawa 2015](#); see also Kelly et al., in prep). Designed to detect irregular galaxies/features, Noise Chisel attempts to create a ‘bottom up’ approach to sky subtraction, making no parameter-based assumptions (see figure 2, [Akhlaghi & Ichikawa 2015](#)). Alternatively, observers have begun to create pipelines with sophisticated data processing sequences with which to approach the issue (see for example, later discussions on the HSC pipeline), often re-estimating the sky multiple times with the inclusion of improved priors upon each pass.

Beyond sky estimation and methods of measurement, observational effects also arise which can lead to flux contamination of the ICL. These include, but are in no means limited to: cirrus, flat field errors, psf wings from bright objects such as stars, CCD bleed trails from oversaturated objects, ghosts, satellite trails and so on (see extensive discussion in [Duc et al. 2015](#)). Such effects can be difficult to fully remove via an automated basis (ghosts, for example, are notorious - see [Bosch et al. 2018](#), their figure 3), and often remain in a ‘diluted’ form after coaddition. This is also especially true for the wings of stars, which can bias the colour profile of the ICL. A deeper understanding of the field PSF out to arcminute scales may rectify this issue, although this remains difficult to model accurately (e.g. [DeMaio et al. 2018](#), [Montes & Trujillo 2018](#)). It therefore remains to be seen in future ICL measurements if novel, ‘gold-standard’ techniques will be developed to do so observationally; this is being attempted using hydrodynamical simulations in upcoming studies, where one is able to disentangle stars, dark matter and gas in a dynamically robust way (Kelvin et al., in prep).

1.5 Motivation

From the concepts discussed in Sections 1.1 to 1.4.2, the study of galaxy clusters presents a wealth of science. From providing fundamental tests of cosmology (Section 1.3) to a laboratory to explore the effect of extreme processes on the evolution of galaxies (Section 1.4), clusters continue to provide clues to the history and future evolution of the cosmos. For the purposes of this thesis, we focus our interests primarily on the evolution of stellar mass within galaxy clusters, and its relationship to the host halo. As established in this chapter, it is still not yet fully understood why there is a growth discrepancy between the co-evolution of BCGs and their host cluster in observations and simulations. It is thought that this difference may be partially solved by more in-depth, quality analyses of intracluster light, as well as a deeper understanding of the systematics which may lie behind photometric measurements of both BCGs and ICL.

We therefore explore the question of the evolution of stellar mass in the cores of galaxy clusters, via addressing the following:

1. How does cosmological dimming affect the recovered structure of BCGs, measured using conventional observational methods in the context of surveys?
2. How do BCGs evolve with respect to their host cluster?
3. How do conventional image-processing methods affect the recovery of ICL?
4. How does the ICL grow over time? Is its evolution linked to its corresponding BCG, or to the properties of the host cluster?

Part 1 (Chapters 2 - 3) of this thesis is focused on the link between the properties of BCGs with those of their host cluster, along with the effect of surface brightness dimming and systematics on BCG morphological parameter estimations. Numerous studies have reported a positive correlation between BCG stellar masses and environmental properties such as the overall halo mass (e.g. Bhavsar & Barrow 1985; Lin & Mohr 2004 and numerous others), with some finding tentative environmental links between various BCG morphological properties and their host clusters (e.g. Brough et al. 2005; Guo et al. 2009). However, others have found little-to-no dependence at low redshift (Zhao et al. 2015a), or have argued that the effect strengthens for central galaxies with late-type

morphologies but is not strongly observed in early types (e.g. [Weinmann et al. 2009](#)). We attempt to address the question of the BCG-cluster relationship using data from the SPIDERS survey, using a sample of 329 X-ray selected clusters, along with bespoke simulations to trace the recoverability of BCG parameters obtained through model fitting against surface brightness.

Part 2 (Chapters 4 - 5) of this thesis is dedicated to the study of ICL in state-of-the-art, public domain imaging data. We study the ICL component of a sample of 19 X-ray selected galaxy clusters from the XMM-Cluster Survey, using deep (~ 26.8 mag/arcsec²) Hyper Suprime-Cam DR1 imaging. Measuring the ICL through a thresholding approach (see, for example, [Burke et al. 2012](#)), we explore the relationship between the ICL and its host cluster. We also explore the use of a novel post-processing technique, which demonstrates significant potential in regaining ‘lost’ ICL flux. We conclude our findings in Chapter 6, which immediately precedes an appendix of supplementary material.

We adopt, where applicable, a standard Λ CDM concordance cosmology throughout this thesis, with $H_0 = 70$ km s⁻¹Mpc⁻¹, $h_{100} = 0.7$, $\Omega_\Lambda = 0.7$ and $\Omega_M = 0.3$.

Chapter 2

Part I - Investigation into Systematic Biases within BCG Parameter Estimation using SPIDERS

2.1 Overview of Contents

In this chapter, we present our investigation into the relationship between BCGs and their cluster environment, including a comprehensive investigation into the systematics behind galaxy parameter estimation. We present details of the SDSS-IV SPIDERS survey, which provides the parent sample for the clusters used in this work, alongside our selection methodology. We highlight the cluster parameters used as measures of environment, and establish how they are computed. We also outline our means of quantifying BCG morphology using the SIGMA fitting pipeline and provide a detailed discussion of its mode of operation. Finally, we then present, motivate and discuss the results of a bespoke set of simulations designed to test the robustness of the pipeline used to parameterise the galaxies in our sample.

This chapter primarily addresses motivation 1: “How does cosmological dimming affect the recovered structure of BCGs, measured using conventional observational methods in the context of surveys?”, referenced in Section 1.5.

2.2 The SPIDERS Survey

The SPIDERS survey (i.e. SPectroscopic IDentification of eRosita Sources) is a spectroscopic survey which aims to investigate sources of X-ray emission detectable by the eROSITA mission prior to launch. eROSITA, a joint German-Russian mission, is a highly sophisticated, space-based X-ray survey telescope, predicted to detect all observable massive clusters in the Universe ($> 10^{14} M_{\odot}$, [Merloni et al. 2012](#)). The instrument is anticipated to be at least 20 times more sensitive than the ROSAT All Sky Survey (RASS, e.g. [Voges et al. 1999](#), see discussions in Introduction), with comparably exquisite resolution ($\sim 15''$ FWHM versus $\sim 30'$). It will also produce coverage of $\sim 3 \times 10^6$ ‘hard’ X-ray sources such as AGN (hard band photon energy range 2-10 keV).

Running as a part of SDSS-IV ([Blanton et al. 2017](#)), optical spectroscopy for SPIDERS targets are, at the time of this thesis, being performed within the eBOSS (extended Baryon Acoustic Spectroscopic Survey, [Dawson et al. 2016](#)) footprint with the BOSS spectrograph on the Sloan Digital Sky Survey (SDSS, [York et al. 2000](#)) 2.5m Apache Point Observatory telescope (e.g., [Smee et al. 2013](#), [Gunn et al. 2006](#)) and will continue until the end of the current project cycle in 2020. Overall, SPIDERS will produce follow-up spectroscopy for $\sim 10^4$ X-ray targets detectable by eROSITA prior to its currently anticipated launch at the time of writing in March 2020 (see figure 2.1). The benefit of the preemptive approach taken by SPIDERS (especially given that eROSITA’s anticipated launch at the beginning of this PhD was in 2017) ensures that the survey is capable of producing scientific products independently of the anticipated data from the eROSITA mission.

Two primary science programs (with respect to targets) exist within SPIDERS: optical follow up of X-ray selected active galactic nuclei (AGN, see [Dwelly et al. 2017](#) for details of the target selection) and galaxy clusters (see [Clerc et al. 2016](#) for further information). All targets selected for optical follow-up have an associated X-ray component, predominantly from RASS, but also a smaller number from XMM-Newton via the XCLASS survey as well (~ 300 , [Clerc et al. 2012](#), [Sadibekova et al. 2014](#)), the latter of which we do not use here. Spatial object matches are carried out between the X-ray source lists and the SDSS photometric object catalogue at its most recent release (DR15 as of the time of writing).

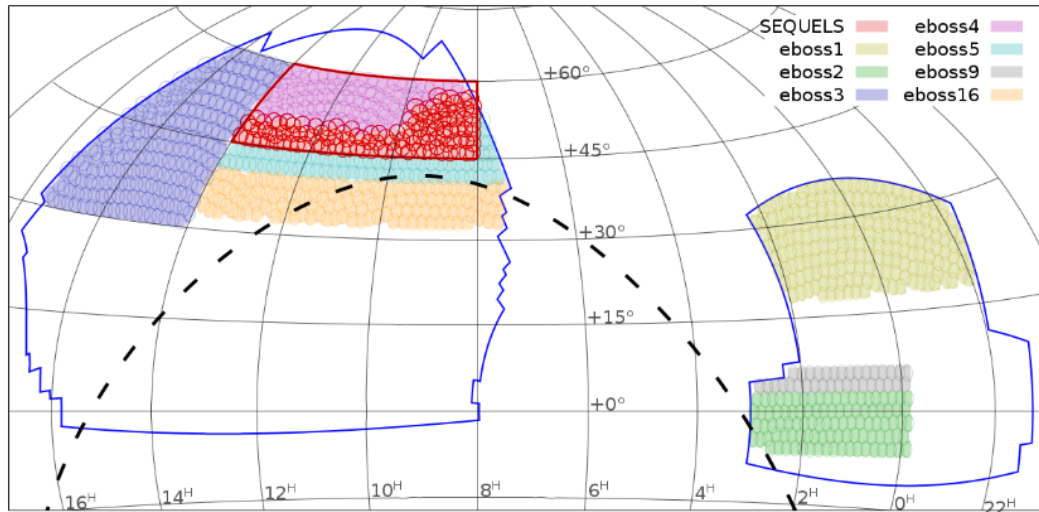


FIGURE 2.1: A equatorial map of the SPIDERS target selection (figure 1 from Clerc et al. 2016). Each circular pointing is 3° in diameter. The dashed, bold black line indicates the boundary between the German and Russian skies, with eROSITA data being shared between the two international project leads. The key in the legend refers to various regions of the eBOSS field regarding target priority and observation scheduling (not relevant here).

Due to the delayed launch of eROSITA, the subsample of cluster candidates in SPIDERS used for this study originates from the COntstrain Dark Energy with X-ray Clusters survey (CODEX; Finoguenov et al. in prep). Essentially, CODEX combines all-sky $[0.5 - 2]$ keV band ROSAT X-ray data with optical data from REDMAPPER (i.e. the red-sequence Matched-filter Probabilistic Percolation algorithm; see Rykoff et al. 2014), an optical cluster finder used on SDSS DR8 data (e.g., Aihara et al. 2011).

In simplified terms, REDMAPPER is effectively a more sophisticated take on the ‘red sequence’ cluster detection method, where clusters are detected by seeking out galaxies which are redder and more massive than the general population (within either a fixed or spatially adaptive threshold) grouped together within a set angular extent on the sky (see, for example, Gladders & Yee 2000). The algorithm works through the use of a preliminary ‘seed’ catalogue of red galaxies with spectroscopic data; in the case of the REDMAPPER SDSS catalogue, these ‘seeds’ were taken from galaxies within the BOSS footprint (Dawson et al. 2013 and figure 2.1 for the extended ‘eBOSS’ footprint). These ‘seeds’ are used to ‘train’ the algorithm, providing a baseline for photometric redshift estimates. Cluster galaxies are assigned a probability, P_{MEM} , of being a member of a detected overdensity of photometrically-grouped red galaxies about a given ‘seed’ galaxy, with the sample undergoing simultaneous filtration in luminosity ($L \geq 0.2L_\star$)

and projected distance corresponding to the size of a typical cluster at the redshift of the ‘seed’ galaxy ($R_{500} \sim 1\text{Mpc}$ at $z \sim 0$). Relevant parameters derived from the algorithm include: a probability-ranked membership estimate (down to a limiting magnitude in the SDSS of $i < 21.0$), photometric redshift estimates of both the overall cluster and its members, a richness estimate and a luminosity-weighted cluster centroid estimate (see later discussion).

The innovative approach taken by REDMAPPER has led to its enormous success in both the SDSS and the Dark Energy Survey (DES; [The Dark Energy Survey Collaboration 2005](#), see also [Rykoff et al. 2016](#)), with the algorithm finding $> 10^5$ optical cluster candidates in total. REDMAPPER represents a ‘bottom-up’ approach regarding its photometric selection method through searching for a red sequence with few priors, rather than applying a ‘friends-of-friends’ method to available spectroscopic data; this latter method is more effectively used by spectroscopic surveys with large volumes and high completeness (e.g., GAMA; [Robotham et al. 2011](#)). It does, however, have numerous drawbacks, which we will later discuss.

As of November 2015, the CODEX catalogue contains 6693 X-ray detections with corresponding REDMAPPER targets within the largest region of the SDSS footprint. The catalogue includes numerous cluster physical properties derived directly from X-rays or indirectly through X-ray scaling relations, including: rest-frame $[0.5 - 2]$ keV band L_X measurements, cluster mass estimates and T_X measurements (refer to [Cibirka et al. 2017](#) for a recent use of the CODEX sample). As of August 2016, 1633 cluster candidates from CODEX with X-ray peaks within $30'$ of the corresponding luminosity-weighted centroids in SPIDERS have thus far undergone observations (with 1337 having been fully completed). This sample of cluster candidates forms the basis of our BCG sample. All of the optical imaging data used here were taken from the SDSS DR12 release ([Dawson et al. 2016](#); data is calibrated as in DR10), which includes all BOSS data from SDSS-III and offers improved sky-subtraction over previous releases (see [Häußler et al. 2013](#), [Blanton et al. 2011](#)). The benefit of the CODEX survey is its high cluster yield potential, with a (theoretically) well-defined selection function ([Finoguenov et al., in prep](#)); a drawback, unfortunately, is the high level of contamination due to the selection criteria for inclusion of cluster candidates (see discussion below and in [2.3](#)).

The SPIDERS team as a result have developed infrastructure to remedy this issue, by

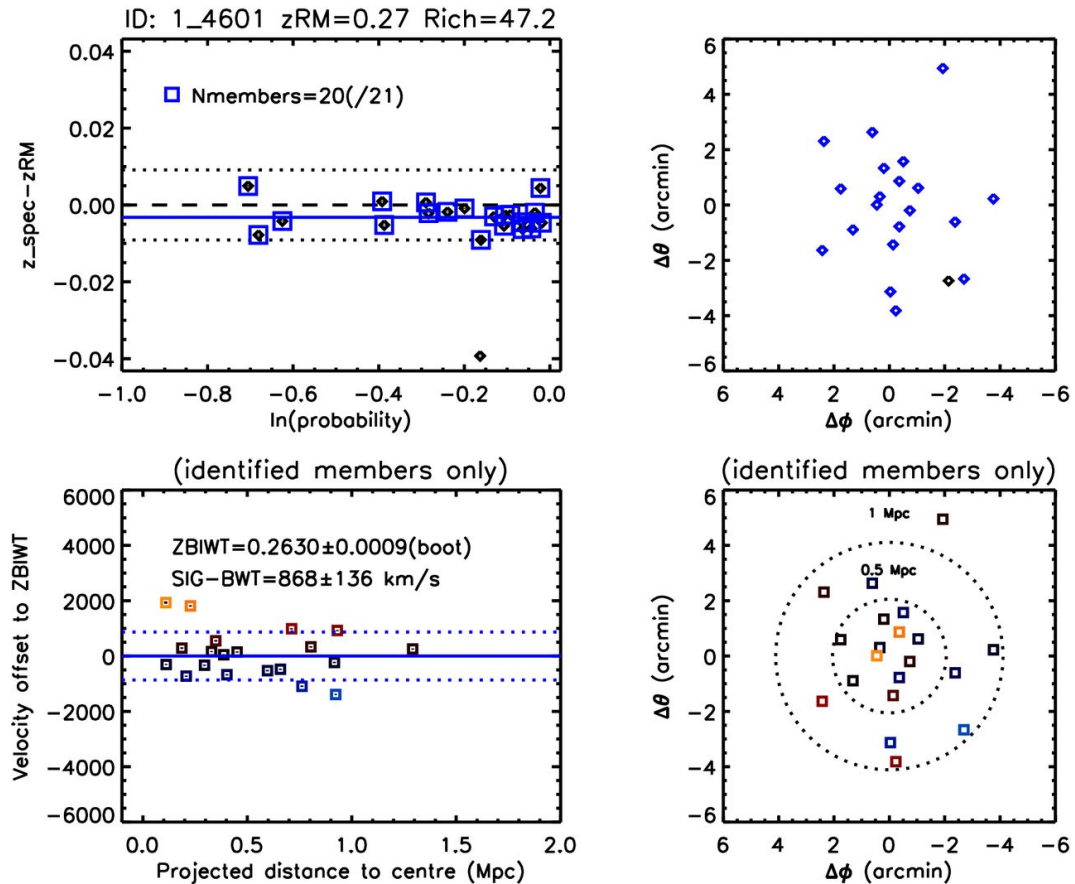


FIGURE 2.2: An example of plots produced by the diagnostic interface used when visually inspecting SPIDERS cluster candidates. There are velocity, probability and spatial distribution diagnostic plots, with cluster members identified through REDMAPPER highlighted.

creating a visual inspection tool for members of the collaboration to use (an early version of plots produced from the diagnostic tool, developed by Clerc et al. 2016, can be seen in figure 2.2). The interface is fully interactive, and enables the user to check the velocity, spatial and spectroscopic redshift distributions of REDMAPPER-defined cluster members. The user can then comment on the robustness of the detection, identify multiple velocity components, manually remove contaminants and produce a quality flag for the object. Inspection runs are carried out by volunteers of the collaboration (including several hundred inspections by the author of this thesis), carried out approximately every six months (when there has been sufficient new spectroscopic data received). There are often disagreements however on how to best classify objects, so many classifications are sent back for another round of inspections, or discarded; a caveat of most ‘zoos’ (A.K. Romer, priv. comm., e.g. Lintott et al. 2011). Nevertheless, the tool provides a useful qualitative baseline as to the levels of contamination present in the survey.

2.3 Sample Selection

Initial cuts to CODEX catalogues to provide the SPIDERS main target list are outlined in Clerc et al. (2016). These are an SDSS i -band magnitude cut (measured in a $2''$ aperture) of $17.0 \leq \text{FIBER2MAG_I} \leq 21.2$ (where FIBER2MAG_I is the apparent object magnitude measured directly from the SDSS fibre) to maximise the efficiency of the redshift detection algorithm and a requirement that any source must have ≥ 4 X-ray counts from ROSAT. These cuts are deliberately lax to retain as many candidates as possible; as mentioned in the previous section, visual inspection efforts on the velocity distributions of cluster candidates are ongoing by the SPIDERS collaboration at the time of this thesis in order to better characterise and identify cluster membership (see upcoming paper, Clerc et al. in prep and section 2.5.1).

To form our cluster sample, we impose several additional cuts, as follows:

1. Firstly, we follow the prescription of Stott et al. (2012) and impose a cut on the REDMAPPER photometric redshift estimates (Z_LAMBDA, henceforth z_{RM}) of our objects such that $\text{Z_LAMBDA} \leq 0.3$, in order to ensure the i -band magnitudes of our BCGs quoted in the REDMAPPER catalogues were at least 2 magnitudes above the survey limit (for i -band, $10\sigma = 21.3$, 765 objects).
2. Secondly, we then adopt a richness cut of $\text{LAMBDA_CHISQ_OPT} \geq 20$ (where LAMBDA_CHISQ_OPT, henceforth referred to as λ , is the optical richness estimated by REDMAPPER) to minimise the number of objects in our sample which are not true clusters (Alexis Finoguenov, priv. comm.; see also Rykoff et al. 2014), such as apparent red sequences with spectroscopic redshifts exhibiting large differences ($\Delta z > 0.05$) from the redMaPPer-estimated photometric value for the ‘cluster’, or X-ray loud AGN affiliated to a red-sequence identified by REDMAPPER (470 objects). The latter detections are accommodated for in richness measurements by applying an AGN halo occupation distribution (HOD) model; roughly 2% of clusters at $z < 0.3$ and with $\lambda > 30$ are thought to be affected.
3. Finally, we required $\text{NHASZ} \geq 10$ (i.e., more than 10 REDMAPPER-determined cluster members with at least one SDSS-DR14 spectroscopic measurement). We do so following Collins et al. (1995), who recommend a minimum of 10 spectroscopic

members in order to obtain a robust estimate of velocity dispersion, our chosen method to estimate cluster dynamical masses (see section 2.5.1).

After these criteria were applied, a total of 433 cluster candidates remained. The cluster images were then inspected visually, in order to check the robustness of the BCG candidates in the cluster membership lists.

2.4 BCG Identification

In this work, an object which we call a ‘BCG’ may not always be the object designated the ‘brightest’ magnitude in a given red sequence detected by REDMAPPER. Here, we adopt the definition of a ‘Brightest Cluster Galaxy’ as being the ‘brightest’ galaxy in closest angular proximity to the measured X-ray centre of our clusters (e.g. [Lin & Mohr 2004](#)); as a practical example of this classification, if there were two similarly bright galaxies in close proximity to the X-ray centre, the brightest of the two would be designated as the BCG. This definition has led several authors to preferentially adopt the term ‘central galaxy’, or CEN/CG (e.g. [Guo et al. 2009](#); [Oliva-Altamirano et al. 2017](#) and others) to clarify their selection, for example, in the case of clusters with two or more comparably bright galaxies. In our case, however, as we do not probe the group regime where designating a central galaxy is often much more ambiguous (e.g. [Yang et al. 2005](#)), we instead use the term as a synonym for the classical, high-mass galaxies which reside in cluster centres.

There are several issues which can result in incomplete cluster membership. From an instrumental standpoint, the fibres on the BOSS spectrograph have a minimum separation limit of $62''$ ($55''$ for the SDSS I/II spectrograph), corresponding to a physical scale of ~ 100 kpc at $z = 0.1$; this may exceed the projected separation between objects in dense source fields (e.g. rich clusters or regions close to the galactic plane), thereby causing incompleteness issues. As an example, [von der Linden et al. \(2007\)](#) and [Miller et al. \(2005\)](#) reported cluster core spectroscopic completeness levels of $\sim 50\%$. In such cases of high source density, the fibre assignment algorithms in the SDSS may break down and measure objects outside of the prior targeting order (as explained in [Blanton et al. 2003](#)). With these caveats in mind, some groups have opted instead to use Integral Field Unit (or IFU) observations on clusters rather than traditional slit spectroscopy, where

TABLE 2.1: Summary of the BCG selection.

Description	Number
CODEX-SPIDERS 30' match	1633
+ Z_LAMBDA \leq 0.3	765
+ LAMBDA_CHISQ_OPT \geq 20	470
+ NHASZ \geq 10	433
Omitted	104
a) Image issues	36
b) Missing	61
c) Major merger	7
BCG candidates (including legacy SDSS)	329

simultaneous observations of objects can be taken readily at increased source density (e.g. [Karman et al. 2015](#)).

Alongside instrumental issues, there are also photometric ones. For instance, the survey design, in particular the magnitude threshold of $m_i > 17.0$, may also lead to BCGs being omitted in some SPIDERS clusters from the targeting process, due to their brightness in comparison to other cluster members (as discussed in section 1.4.1). There are also other factors which can affect how REDMAPPER selects red-sequence objects which it identifies as clusters; for example, the wings of bright sources (i.e., stars) may affect the photometry of fainter objects in close projection on the sky, which can lead to misclassifications or omissions from the colour-magnitude decision tree method used by REDMAPPER. BCGs which have colours statistically atypical with respect to other cluster members may also not be included, such as those that have high central star formation rates and therefore significantly bluer central regions (e.g. NGC 1275, [Fabian et al. 2003](#)).

For these reasons, we deemed it necessary to visually inspect all BCG assignments and clusters by eye. At this stage, we do not make any additional effort to characterise other members than the BCG; details on the automated clipping procedure and velocity dispersion algorithms can be found in section 2.5.1. As aforementioned, we acknowledge that this sample may be slightly biased against objects significantly outside of the red-sequence of their parent cluster because of REDMAPPER selection criteria. However, BCGs with abnormally large central star formation rates ($> 100 M_{\odot} \text{ yr}^{-1}$) are rare with respect to the general population of BCGs at the redshift range in this work (e.g. [Loubser et al. 2009](#), [Green et al. 2016](#)), with recent estimates on the order of 10% or fewer. Moreover, we believe that any omitted objects are predominantly due to fibre

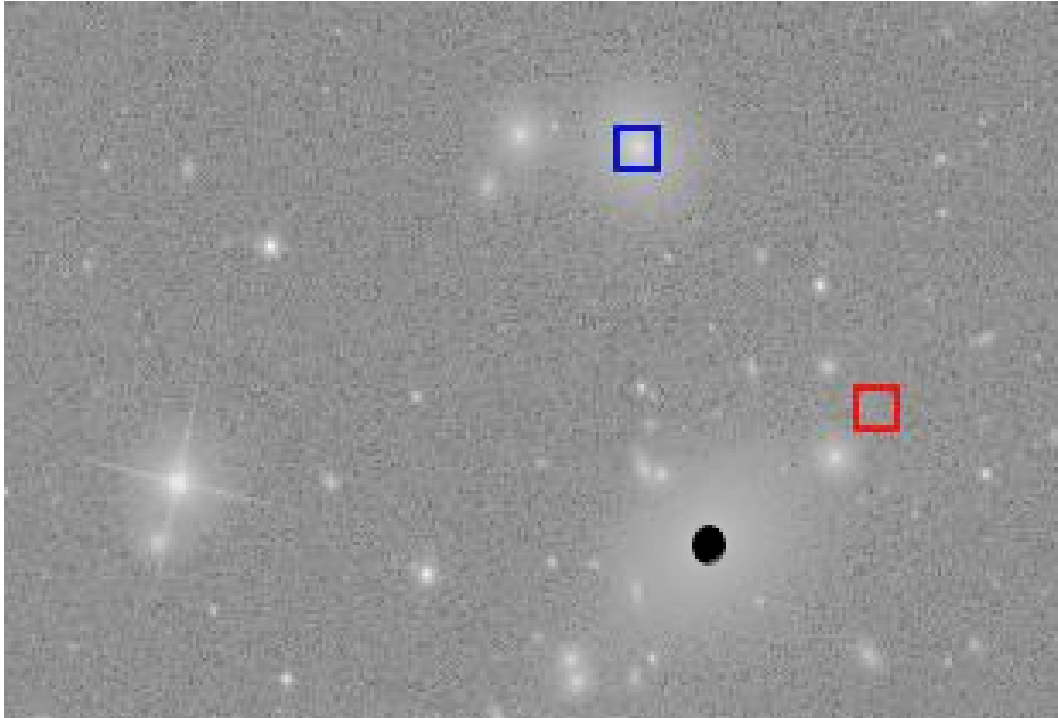


FIGURE 2.3: An example of an SDSS frame zoom where a BCG has been incorrectly assigned (r band, log-scaled). The ‘true’ BCG can clearly be seen (marked with a black dot), but has not been marked as the optical centroid for the cluster (blue square), or included in the object list (likely due to it being too bright to meet the magnitude cut). The red square denotes the X-ray centroid for the cluster.

collision problems rather than a result of the REDMAPPER algorithm, which we discuss further on.

The *gri* composite fields - namely, false-colour JPEG images of combined *gri* SDSS observations - were predominantly used to visually inspect the cluster candidates (inspection carried out primarily by K. Furnell, with assistance by C.A. Collins). During inspection, member coordinates were extracted from the SPIDERS catalogues and displayed on the images, along with the X-ray centroid, in order to check the robustness of the assignments. We followed a similar selection prescription to [Stott et al. \(2012\)](#), where we select the brightest galaxy at the tip of the red sequence within R_{200} of the X-ray centroid (see [Finoguenov et al. in prep.](#)). As well as being the most robust identifier of BCGs (e.g. [Lin & Mohr 2004](#)), this definition was also found by [George et al. \(2012\)](#) to be the best observational proxy for the centre of clusters in general. The R_{200} values used here were taken from the CODEX estimates from X-rays, estimated via a scaling relation (see [Clerc et al. 2016](#)).

In $\sim 20\%$ of clusters, the true BCG was either incorrect or missing from the SPIDERS

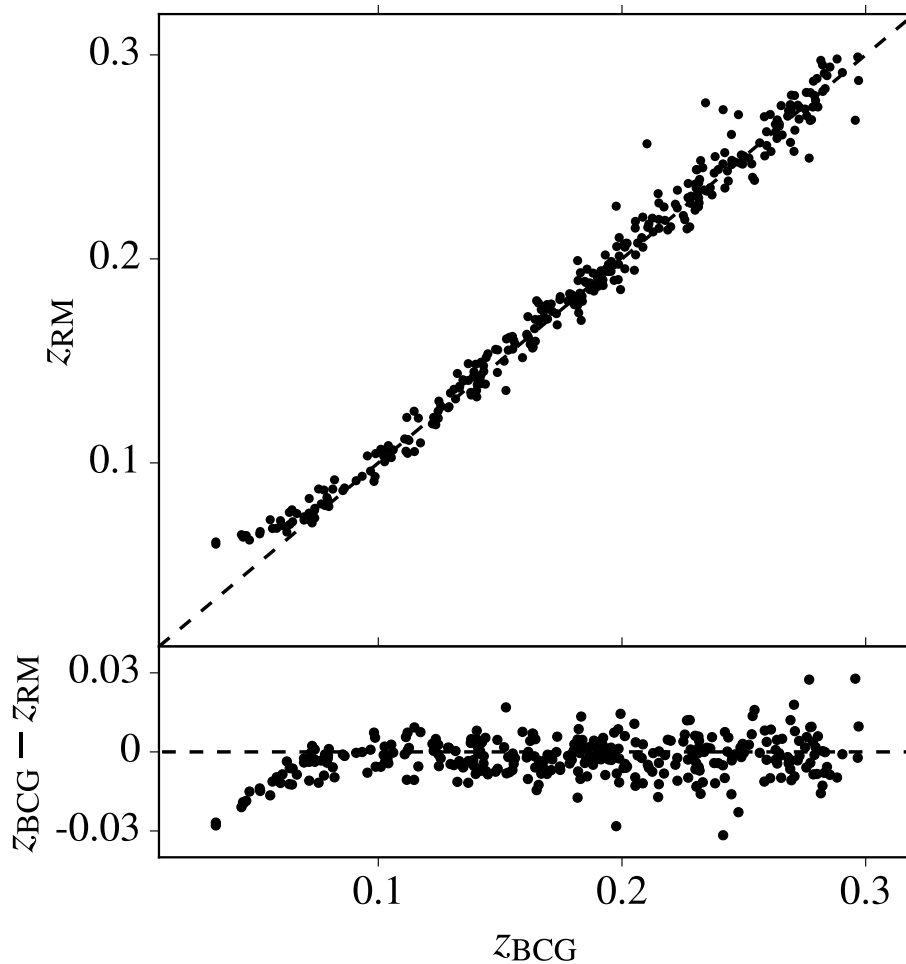


FIGURE 2.4: Spectroscopic redshift of the visually-inspected BCGs (z_{BCG}) versus photometric cluster redshift (z_{RM}) comparison for the sample of 329 objects (typical errors are $\Delta z_{\text{BCG}} \sim 10^{-5}$ and $\Delta z_{\lambda} \sim 0.01$ respectively). The black dashed line is the 1:1 relation. In general, the BCG redshifts agree well with the cluster photometric values, albeit with some scatter at higher z (see section 2.5.1).

catalogues. There were occasional cases where the likelihood ranking of an object being the BCG was incorrectly stated in the catalogue, with the BCG candidate which met our selection criteria ranked lower in the listing (12/433 candidates). More often, however, the BCG listed in the catalogues tended to have been omitted during the SPIDERS selection process (86/433). In these cases, the most likely BCG candidate with respect to our criteria was extracted via `SExtractor` and cross-matched with all publicly available SDSS spectroscopy up to DR14 (over 4 million objects in total) within $5''$. Only 29% (25/86) of BCGs were recovered in this way ($\sim 5\%$ of the selected sample after cuts), leaving 61 objects without spectroscopy (reason b in Table 2.1). We therefore argue that most omissions are due to fibre collision issues, as there is no spectroscopy for these objects across the SDSS available despite a red sequence identified by `REDMAPPER`.

This value is in line with [Rykoff et al. \(2014\)](#), which quotes an estimate of misidentified centrals at the 5% level. Recent efforts have gone into quantifying the ability of the REDMAPPER algorithm to correctly centre clusters, with similar results ([Hikage et al. 2017](#)). A summary of the various cuts applied to form the sample are shown in [Table 2.1](#), as well as an example of a ‘missed’ BCG in [figure 2.3](#).

In total, 329/433 objects passed the visual inspection stage and cuts. A comparison between the photometric and spectroscopic object redshift values is shown in [figure 2.4](#); in general, they agree well ($\sigma \sim 0.01$). The clear discrepancy below $z = 0.05$ is due to the redMaPPer algorithm being unable to function effectively in very low-redshift cases, where cluster counts in general are very small and photometric redshifts have large margins of error (refer to [Rykoff et al. 2014](#) for further details).

In this analysis, we opted to reject BCGs with obvious tidal features from undergoing a major merger (7/104, reason c in [Table 2.1](#)) as well as ones with obvious image issues (reason a in [Table 2.1](#)), such as exceptionally bright stars, extensive field overcrowding (e.g. for a few fields close to the galactic plane - although none lie within $-25^\circ \leq b \leq +25^\circ$, where b is the galactic latitude) and object truncation due to proximity to field edges (22/104). The remainder were either algorithm ‘artifacts’ (such as an aforementioned incorrectly-attributed CODEX X-ray source to a red sequence detected by REDMAPPER, or a projected overdensity of objects with similar photo- z values from REDMAPPER but highly variable spec- z values (14/104)). A number of example BCGs can be seen in [figure 2.5](#); all of them have early type morphologies.

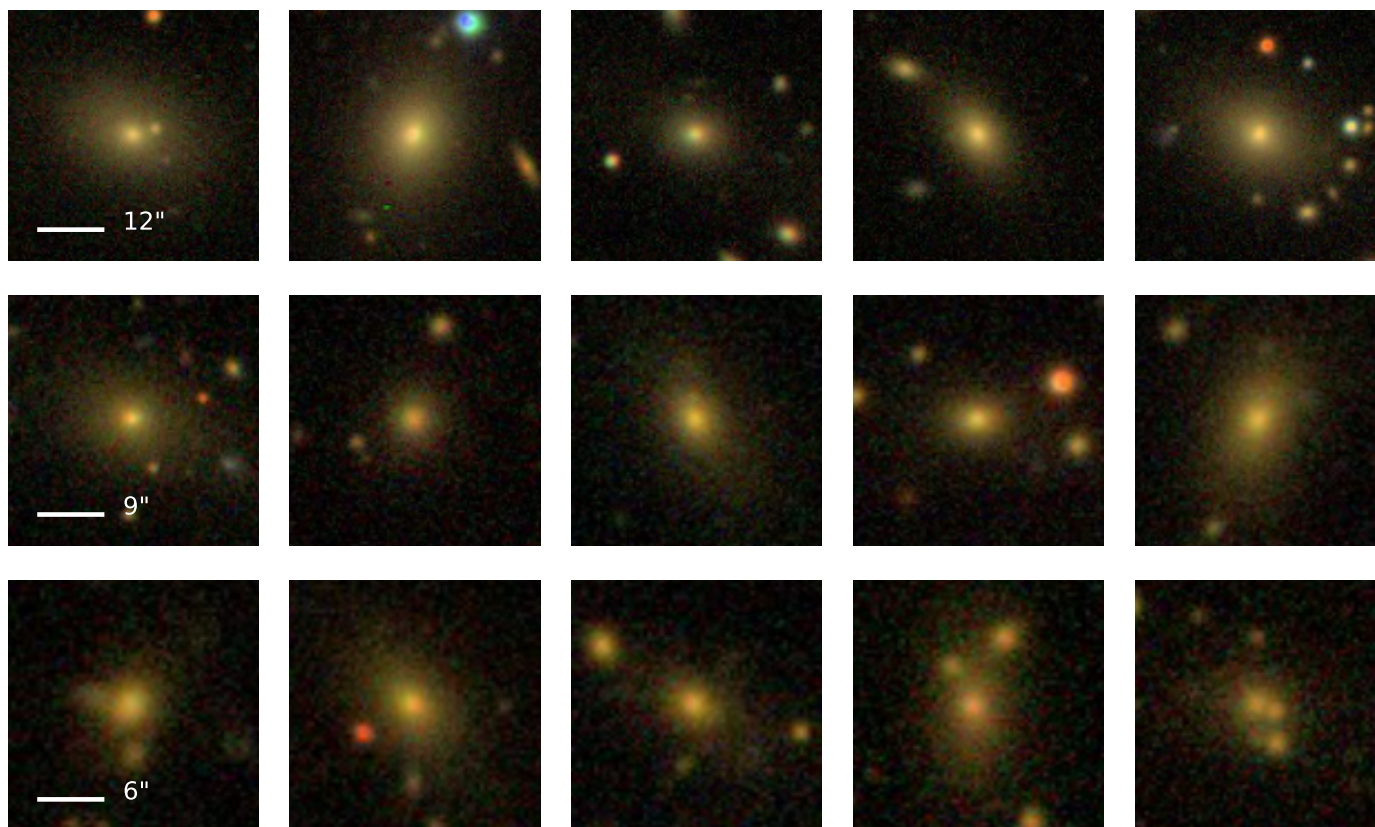


FIGURE 2.5: Example false-colour SDSS *gri* composites - namely, colourised JPEG stacks of SDSS *g*-, *r*- and *i*-band data - of 15 BCGs used in this study (100×100 kpc for each tile). Each of the three vertical panels represents a sample of five randomly drawn BCGs about the 16th, 50th and 84th redshift percentiles from top to bottom (0.1, 0.18 and 0.25, respectively).

2.5 Analysis

2.5.1 Cluster Properties

Three independently measured cluster properties are used to characterise the clusters in our sample: halo mass M_{200} (with respect to the critical density), X-ray luminosity L_X , and cluster richness λ , the latter two of which we take directly from the SPIDERS catalogues. As mentioned in Section 2.1, the richness values we use originate from REDMAPPER and represent the summed *probability* of galaxy membership for a given cluster accounting for redshift, shown by Rykoff et al. (2012) to be a superior measure of total membership than imposing a basic colour cut criterion. In addition, the L_X values represent the total aperture-corrected luminosity across the entire [0.5 – 2] keV band (see Finoguenov et al. 2007 for the correction method). The corresponding $L_X - z_{\text{RM}}$ distribution for our clusters is shown in figure 2.6. We limit our clusters at the analysis stage to those above 10^{43} ergs s^{-1} . This was done primarily because such objects constitute poor clusters and low mass groups, often with less well-constrained X-ray measurements in the context of RASS data (e.g. Böhringer et al. 2001), as well as this, it helps mitigate Malmquist bias (i.e. catalogue incompleteness due to ‘missing’ fainter objects below the survey limit). If included, however, we observe very little change to the values of the correlations discussed in Chapter 3 (less than 5% in most cases).

In this work, we rely on velocity dispersion as a proxy for dynamical cluster mass. The velocity dispersion of a cluster is known to be an effective tracer of the overall mass of the cluster halo (e.g. Caldwell et al. 2016) and ranges from < 200 kms^{-1} for group-level systems to ~ 1000 kms^{-1} for massive clusters. However, the proxy is also subject to various biases (see also Section 1.2). For example, in the case of merging clusters, atypically high galaxy peculiar velocities can also arise due to the cluster being out of dynamical relaxation (as an example, the Bullet cluster has a velocity dispersion of ~ 1500 kms^{-1} , which produces a dynamical mass ($> 10^{16} M_{\odot}$) incongruent with measurements from other mass proxies, see Markevitch et al. 2002). In addition, interlopers along the line of sight can cause significant problems if not accounted for correctly, which is often a non-trivial task (e.g., Miller et al. 2005). In the context of recent studies, Maughan et al. (2016) found that cluster masses derived from velocity-based caustics were biased high by $\sim 20\%$. Although their caustic-based method differs from

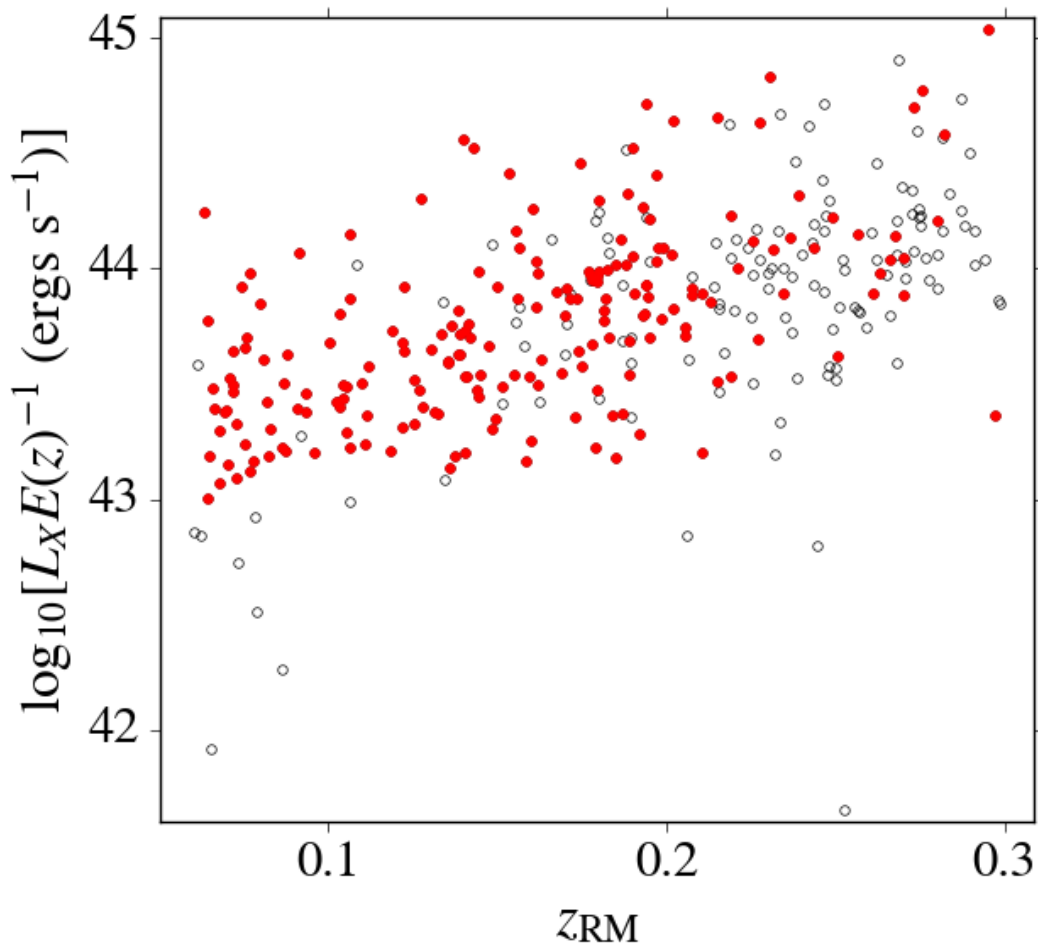


FIGURE 2.6: The $L_X - z_{\text{RM}}$ relation for the BCGs in our sample. The black circles show the initial 329 clusters which passed our visual inspection, whereas the red points represent the 198 clusters used in our final analysis (see Section 3.1.1). We discuss the consequences to the underlying BCG distribution in Section 2.6.1 within this chapter.

that used here, their work represents a useful indication as to how much of a deviation one should expect using velocity-based mass proxies.

We use a similar prescription in this work to that of Clerc et al. (2016) when computing the velocity dispersions of our clusters. We make no prior assumptions about the membership of objects contained in the SPIDERS catalogues, requiring only that they meet our quality cuts (see Section 2.3). We do, however, apply an additional cut before computing our velocity dispersion estimates to remove projected interlopers, in that we require a galaxy to lie within a projected distance of $R \leq 2 \times R_{200}$ from the designated BCG.

For a given cluster member, we follow the standard practice of computing its velocity with respect to the cluster rest-frame (e.g., [Carlberg et al. 1996](#)):

$$\frac{v_i}{c} = \frac{z_i - z_{\text{clus}}}{1 + z_{\text{clus}}}, \quad (2.1)$$

where v_i is the recession velocity of a member galaxy, z_i is its corresponding redshift value and z_{clus} is the redshift of the cluster. We apply an iterative clip to our cluster redshift values in velocity space, imposing a $\pm 3000 \text{ km s}^{-1}$ threshold about the median velocity of the cliplist, which was recalculated at each step. We then estimated the final cluster redshift using a biweight (see upcoming discussion in this section for details).

We apply the same cut in velocity space to our object list, requiring again that a given galaxy be within $\pm 3000 \text{ km s}^{-1}$ with respect to the median cluster velocity; galaxies outside this limit were flagged as interlopers and discarded. The final object list underwent an iterative 3σ clip, which was allowed to run until convergence. Clipped object lists with $N < 10$ members were rejected and a mass was not computed for the cluster, due to there being an insufficient number of objects remaining to meet our minimum requirements (Section 2.3).

Following the methodology outlined in [Beers et al. \(1990\)](#), we use two different measures of velocity dispersion, dependent on the number of remaining cluster members. For $10 < N \leq 15$, we apply the ‘gapper’ method, which is optimised for clusters with a low member count (see [Beers et al. 1990](#)), estimated by [Wainer & Thissen \(1976\)](#) to have an approximately 90% robustness for samples $n \sim 10$. For a list of member galaxy line-of-sight velocities in ranked order, one can use the ‘gaps’ between them to achieve a sense of scale for the underlying distribution:

$$\sigma_{200} = \frac{\sqrt{\pi}}{n(n-1)} \sum_{i=1}^{n-1} w_i g_i, \quad (2.2)$$

where σ_{200} is the velocity dispersion and n is the variable rank. The ‘gaps’, g_i , are defined as:

$$g_i = v_{i+1} - v_i, \quad (2.3)$$

for $1 \leq i < n - 1$, where v_i is the velocity of a galaxy ranked at i . These gaps are then ‘weighted’ with (roughly Gaussian) rank-dependent weights w_i :

$$w_i = i(n - i) . \quad (2.4)$$

For clusters with a larger number of remaining members ($N > 15$), we adopt a biweight technique as it generally represents a more robust statistic. The biweight has the following form:

$$\sigma_{\text{BI}} = (n')^{1/2} \frac{[\sum_{|u_i| < 1} (x_i - M)^2 (1 - u_i^2)^4]^{1/2}}{|\sum_{|u_i| < 1} (1 - u_i^2)(1 - 5u_i^2)|} , \quad (2.5)$$

where n' is the number of data points with $|u_i| > 1$ and M is the biweight location (a measure for the central point of a distribution). The u_i are given by:

$$u_i = \frac{(x_i - M)}{c \times MAD} , \quad (2.6)$$

with MAD equivalent to the median absolute deviation and c being a ‘tuning constant’, set in this work to a value of 9. Unlike the gapper method, the variables need not be ranked.

In both cases, errors on our velocity dispersions are estimated from 68% confidence limits taken from 10,000 bootstrap realisations. The bootstrap technique used here regenerates the data at random with replacement, as established by Efron (1979), with which we re-run our analysis. From doing so, we find an estimated mean error $\Delta\sigma_{200} \sim 20\%$.

For mass estimates, this work follows Finn et al. (2005), who adopt the following equation for cluster mass based on haloes from N-body simulations:

$$M_{200} = 1.2 \times 10^{15} \left(\frac{\sigma_{200}}{1000 \text{ km s}^{-1}} \right)^3 \frac{1}{\sqrt{\Omega_\Lambda + \Omega_M(1 + z)^3}} h_{100}^{-1} M_\odot . \quad (2.7)$$

Of the clusters used in this work, 318 have measured velocity dispersions and thereby corresponding dynamical mass estimates (with 11 either failing to converge, or their respective cliplists falling below 10 members and therefore leading to a rejection). The clusters themselves span a large range of masses, from $10^{13} \leq M_{200} \leq 10^{15} M_\odot$, with a median of $1.4 \times 10^{14} M_\odot$. It was found at this stage that a further two BCGs had large deviations in redshift from their corresponding z_{clus} (SPIDERS ID 1_6003 and 1_21735);

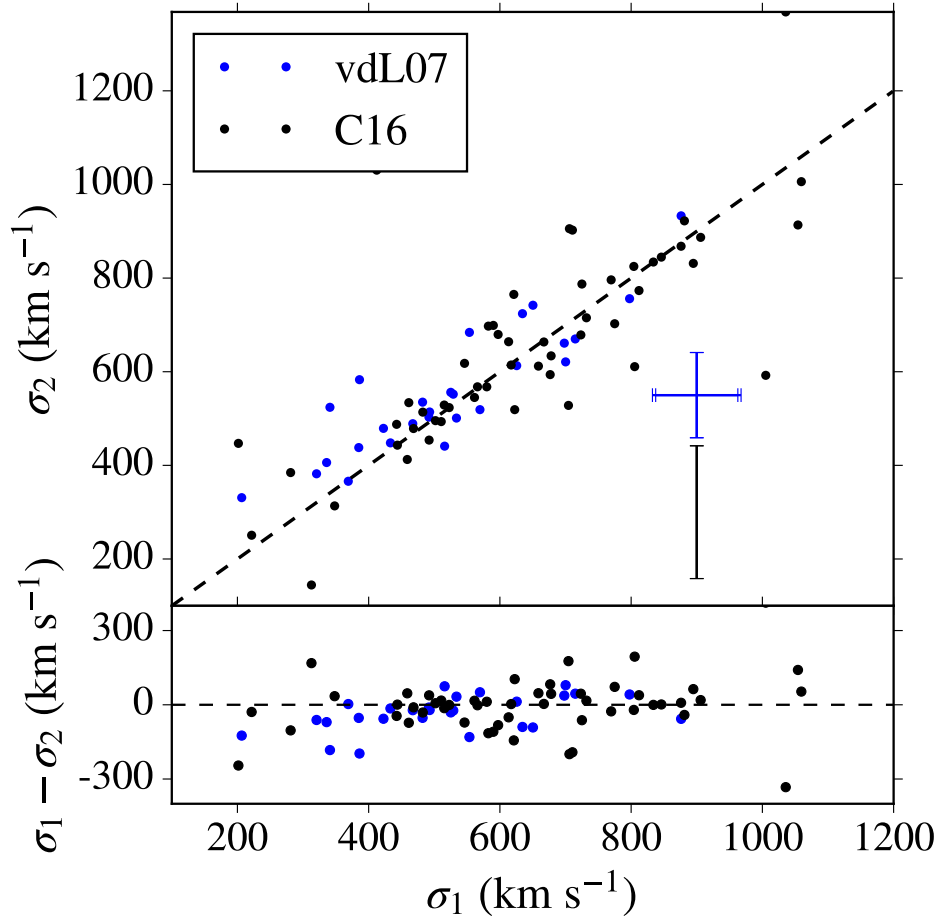


FIGURE 2.7: Comparison plot between 81 velocity dispersion values computed here (y -axis) and those computed by von der Linden et al. (2007) and by Clerc et al. (2016) for 27 and 54 common clusters respectively (the latter did not cite errors in their paper), accounting for duplicates (x -axis). The average 1σ errors for each of the two samples are plotted in the bottom right hand corner.

these clusters were flagged and did not factor into any further analysis. For reference, we present a comparison between σ_{200} estimates for an overlapping sample of 27 and 54 SPIDERS clusters with von der Linden et al. (2007) and Clerc et al. (2016) respectively in figure 2.7; the *rms* is ~ 100 kms⁻¹, with no obvious offset. In an upcoming paper to be released by the SPIDERS collaboration, we attempt to address issues of large scatter through our aforementioned visual screening efforts, with the aim of retrieving more accurate estimates of velocity dispersion (see discussion in Section 2.1).

2.5.2 Profile Modelling using SIGMA

In order to gain information about the morphological properties of our BCGs, we model their light profiles in two dimensions (see [Stott et al. 2011](#) for an example in the context of BCGs). The image data used in this work originate from the SDSS DR12 release ([Alam et al. 2015](#)), which contains all of the photometric data used to form the SPIDERS sample. The data have been scaled, pre-processed and have undergone a global background subtraction following [Blanton et al. \(2011\)](#). The background treatment is much improved over the sigma-clipping method used in releases prior to DR8 (see fig. 12 from [Blanton et al. 2011](#) for comparison), which is known to over-subtract the profile wings of high-Sérsic index objects such as BCGs (e.g. [Bernardi et al. 2007](#), and discussions in part II of this thesis). Here, we choose to use these estimates for the global sky during fitting, which we discuss in Section 2.6.

The BCGs in this work are modelled by a single-Sérsic profile ([Sérsic 1963](#)), which has the form

$$I(R) = I_e \exp \{ b_n [(R/R_e)^{1/n} - 1] \} , \quad (2.8)$$

where $I(R)$ is the surface brightness of an object at radius R , R_e is the effective radius, I_e is the object surface brightness at the effective radius, n is the Sérsic index and b_n is a product of incomplete gamma functions as described in [Ciotti \(1991\)](#). The empirical Sérsic profile is a good description of the light distribution of BCGs, which are predominantly bulge-dominated and ellipsoidal in nature ([Graham & Driver 2005](#) and references therein). The integrated magnitudes produced from Sérsic fitting have the additional advantage that they account for more light than traditional Kron/Petrosian magnitudes for objects with high- n , the latter of which can underestimate the true brightness by as much as 95% ([Graham & Driver 2005](#)).

For the purposes of this study, we opt to fit a single-Sérsic component to each BCG. There is some debate in the literature as to the most appropriate number of components which should be fit to a galaxy in order to accurately estimate galaxy parameters. For example, [Bernardi et al. \(2014\)](#) experimented with fitting single- and double-Sérsic fits to a series of simulated single- and double-Sérsic galaxy images. They found that both the single- and double-Sérsic fits perform well at the bright end ($M_r > -21$) regardless of galaxy type, with both models increasingly ill-suited to their corresponding galaxy

type at fainter magnitudes. It was shown that a single-Sérsic fit to what is, in reality, a double-Sérsic galaxy is as inappropriate a model as applying a double-Sérsic fit to what is, in reality, a single-Sérsic galaxy. On closer inspection of the light profiles for most of our BCGs using the DS9 software, we found no significant evidence for the necessary addition of a secondary component, so we therefore adopt a single-Sérsic as our model type to fit to each BCG.

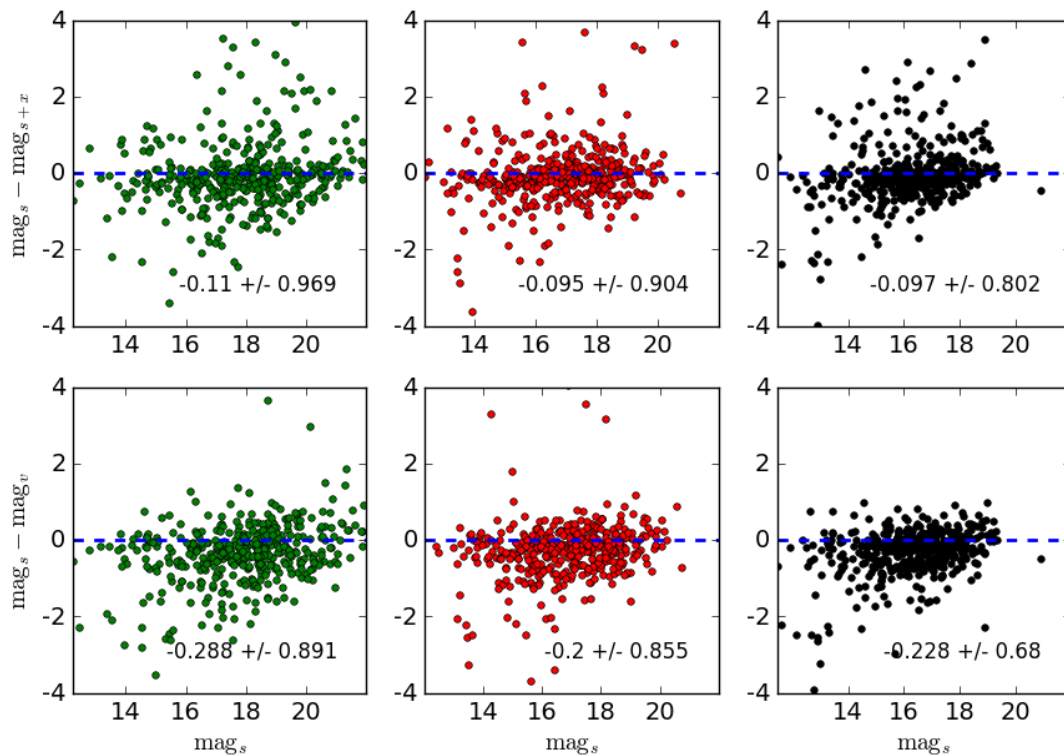


FIGURE 2.8: A comparison between the model magnitude values for the 416 VAC BCGs in Erfanianfar et al., (in review). The subscripts (s , $s+x$, v) indicate the choice of model (Sérsic, Sérsic+Exponential, de Vaucouleurs), while the colour (green, red, black) indicates the band (g , r , i respectively). The zero deviation line is included (blue dashed horizontal line) along with an annotation on each plot providing the median deviation and rms.

As an aside, we do not claim this choice to be necessarily ‘superior’ to a multi-component fit (such as the addition of an extended halo, or a bulge); merely, due to the wide range in apparent surface brightness of the galaxies in our sample, that it is apt to yield more consistent results (Section 2.6.1). As part of our work with the SPIDERS team, we produced a catalogue of fits for BCGs in a similar cluster sample to our own, the results of which we discuss in Chapter 3 (Erfanianfar et al., in review, available at <https://data.sdss.org/sas/dr14/eboss/spiders/analysis>), with 3 model choices per object (Sérsic, Sérsic + Exponential and de Vaucouleurs). A comparison of the integrated model magnitude values for each band (for non-catastrophic fits meeting our basic fit quality cuts, see Section 3.1.1) is shown in figure 2.8 (with the de Vaucouleurs outputs included as a comparison); we see no significant benefit in terms of recovered flux by adding an extra component (i.e. increased scatter, with no large offset in total magnitude).

Numerous profile-fitting codes exist in the literature, such as: GIM2D (Simard 1998), PROFIT (Robotham et al. 2017), IMFIT (Erwin 2015), PYMORPH (Vikram et al. 2010) and GALFIT (GALFIT-3, Peng et al. 2010). Most work on the principle of χ_ν^2 minimisation, computing an optimum model through numerical iteration that follows the real data as closely as possible. The χ_ν^2 parameter is an indicator of the goodness of fit, and is defined as follows:

$$\chi_\nu^2 = \frac{1}{\nu} \sum_{i=0}^i \frac{|O_i - E_i|}{\sigma^2}, \quad (2.9)$$

where O_i are the original data, E_i are the theoretical model values, i is an individual point, σ^2 is the variance within the original data and ν is the total degrees of freedom (DOF). Generally speaking, a χ_ν^2 value of 1 is ‘ideal’, as it infers that the fit residuals are at the noise level of the the data (from Poisson statistics, see Bevington 1969). A $\chi_\nu^2 < 1$ indicates an ‘overfit’, whereas a $\chi_\nu^2 > 1$ indicates an ‘underfit’. Very large reduced χ_ν^2 values indicate poor-quality models, and care should be taken when interpreting them.

Within this study, the GALFIT-3 software is used to model the BCGs (referred to as simply ‘GALFIT’ from this point). Variations of the GALFIT software have been used widely throughout the literature with much success (see Dullo et al. 2016; Guo et al. 2009 & Driver et al. 2011 for recent uses). It relies on a Levenberg-Marquardt χ^2 minimization routine. This method, outlined in Press (1997), is effectively a ‘downhill-gradient’ technique to obtain the maximum likelihood. The algorithm, as utilised in

GALFIT, is as follows:

1. An initial ‘guess’, x , provided prior to fitting is input into the routine.
2. Take a ‘step’ in some random direction δ_1 .
3. Compute the gradient between $x \rightarrow x + \delta_1$.
4. Take another random step, δ_2 .
5. Compare the gradient of $x \rightarrow x + \delta_1$ and $x \rightarrow x + \delta_2$. If $1 > 2$, weight movement towards the direction of δ_1 and vice versa if $2 > 1$ (i.e. the direction of ‘steepest’ descent).
6. Continue until convergence is achieved (i.e. if χ^2 remains the same for five iterations).

This algorithm has the advantage that it is computationally efficient and generally reliable even if initial parameter guesses are poor. However, parameter degeneracies can still occur upon fitting, as GALFIT becomes trapped in local minima. This is especially problematic in the case of objects with large Sérsic indices ($n > 4$) and extensive profile wings, or in crowded environments with many components present (such as PSFs). We attempt to characterise the ability of the algorithm to recover parameters accurately through a suite of simulations, which we discuss at length in Section 2.6.1.

We run GALFIT using the Structural Investigation of Galaxies via Model Analysis code, or SIGMA (Kelvin et al. 2012), which is an R-based pipeline software used with great success in the GAMA survey (Driver et al. 2011) to provide Sérsic model fits to 167,600 galaxies in five optical (SDSS-*ugriz*, Fukugita et al. 1996) and 4 near-infrared (UKIRT-*YJHK*) passbands (see Hill et al. 2011). SIGMA is capable of performing a full fit, including: object extraction through SOURCE EXTRACTOR (SEXTRACTOR; Bertin & Arnouts 1996), creating a model of the field PSF, estimating the local sky about an object, masking external objects and, finally, fitting a profile through GALFIT. Details of our implementation of SIGMA are provided in Section 2.6; more specific information can be found in Kelvin et al. (2012).

2.6 SIGMA Pipeline and Implementation

SIGMA is designed to fit objects in multiple bands in tandem, requiring only the coordinates at which an object is located as an input file alongside any image data corresponding to the desired fitting bands. SIGMA produces an output file containing any relevant SExtractor parameters used in fitting, the background estimate (if requested), and the profile-fitting results from GALFIT. A description of the pipeline is given below, alongside any parameter settings used in this work when running SIGMA.

i. Image Cutout: To begin, SIGMA accesses the WCS information in the header of an image file containing an object. It then converts the celestial RA/DEC coordinates of an object into x/y Cartesian pixel coordinates using the SKY2XY routine in the WCSTOOLS package (Mink 1998). The upper and lower limits of a 1201×1201 pixel region centered on the primary object are determined. This cutout, designated the ‘primary science image’ is used during analysis from this point forward.

ii. Source Extraction: SIGMA then runs SExtractor on the primary science image to detect any objects in the field. During extraction we applied the default SIGMA parameters: DETECT_THRESH = 2σ , DETECT_MINAREA = 10 and SATUR_LEVEL = 25,000. The image is also filtered through a 5×5 pixel Gaussian convolution kernel with FWHM = 2 pixels prior to detection; SExtractor defaults are used everywhere else. Outputs from SExtractor corresponding to the primary object provide initial parameter estimates for the GALFIT algorithm. Any extra object detections about the primary object are designated ‘secondary’ sources. The number of secondaries to be used during fitting is specified by the user prior to running SIGMA; any other objects are designated as ‘tertiaries’ and masked out prior to fitting (see *vi.*).

iii. PSF Extraction: The output catalogue from SExtractor is used to find objects in order to estimate the PSF of the field. The PSF EXTRACTOR software package (PSFEX; Bertin 2013) is applied to create the empirical PSFs used in SIGMA, which are smoothed by fitting the end result with a Moffat profile (Moffat 1969). For an object to qualify for computing the PSF, SIGMA requires a S/N > 10 and an eccentricity, ϵ , of > 0.05. PSFEX then estimates the FWHM of the object, requiring that $2 < \text{FWHM} < 10$ pixels and that the object lies within the central 50% of the distribution. A minimum of 10 objects are required to compute a PSF; if this criterion is not met, SIGMA will loop

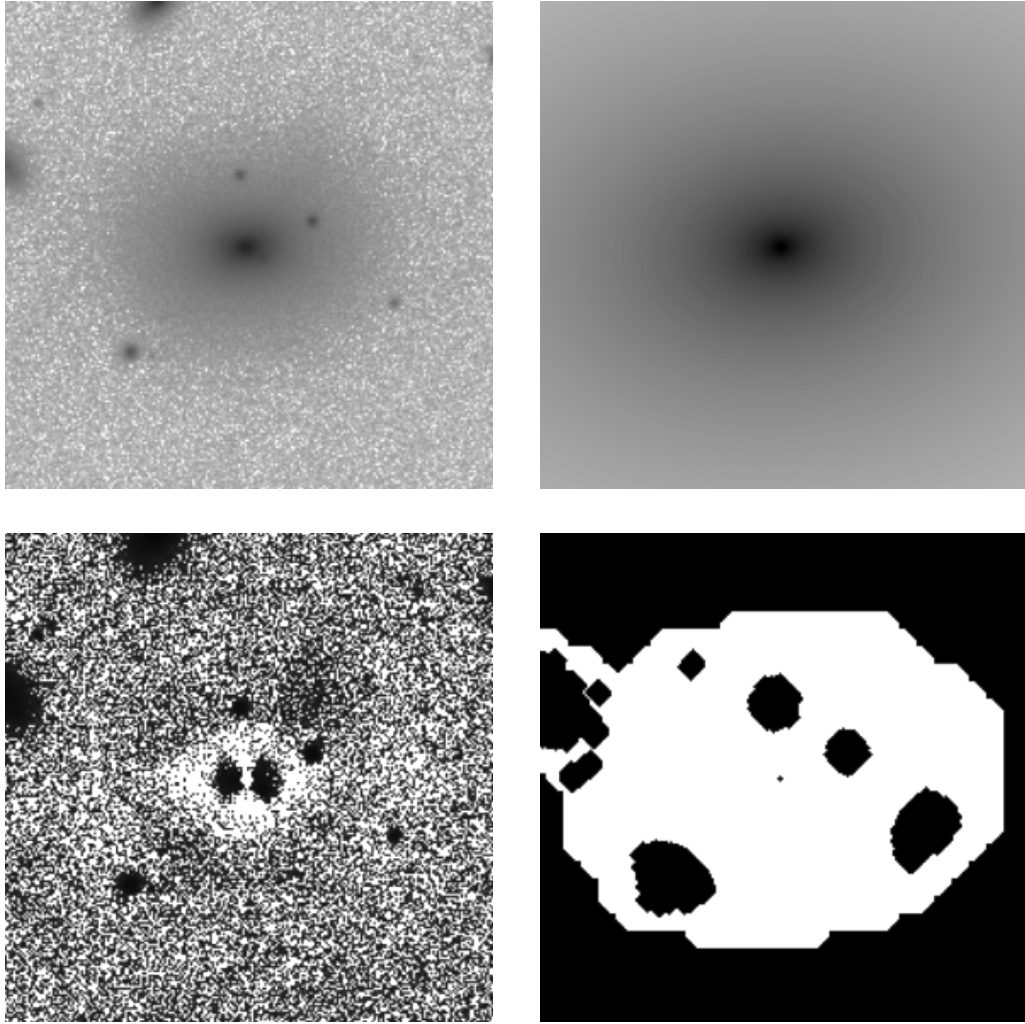


FIGURE 2.9: An example data product from SIGMA for the BCG in SPIDERS cluster 1.1365 (100×100 kpc, $z \sim 0.05$). Clockwise from top left: SDSS r -band image, Sérsic model from GALFIT, image mask, residual (enhanced to bring out faint artifacts). Except for the binary mask, all other quadrants are scaled logarithmically; hence, the high feature contrast in the bottom-left panel for the PSF-sensitive central region of the galaxy.

back and attempt to run PSFEX on a larger cutout area. Upon completion, the final result is a 25×25 pixel PSF estimate, which is used in fitting with GALFIT.

iv. Sky Subtraction: To estimate the local sky about an object, SIGMA uses an adaptive mesh technique dependent on the size of the primary object (see Section 3.3 of [Kelvin et al. 2012](#)). Within each ‘cell’ of the mesh, SIGMA computes the median background level and fits a smooth spline across the frame, subtracting the background estimate from the science image. Although suitable for objects in the field/groups, we prefer not to apply any additional background subtraction to our images due to the nature of the cluster environment. In the cores of clusters, it is often the case that galaxies have

overlapping profile wings. In addition, cluster cores also have a faint ICL component, thought to have formed primarily from stars ejected from galaxies through mergers, tidal stripping, and harassment (Gonzalez et al. 2007; Mihos et al. 2005; Burke et al. 2012 and discussion in Chapters 4 and 5). Therefore, we opt to use the global SDSS estimates when fitting our objects to avoid any sky bias at local scales, primarily as it is known that sky overestimation has a significant impact on the final fit of an object (e.g. Graham & Driver 2005). We explore the impact of field-by-field variations on object fitting in our simulations (Section 2.6.1).

v. Object Masking: SIGMA produces segmentation maps that can be used as object masks; the mask shape and the number of sources to be used during fitting are specified by the user. In this work, we apply inner (to minimise the effect of PSF-sensitive cores on our fits), outer, and tertiary masking to our objects, using a pixel buffer of 5 and a 1 pixel mask to the inner region. We impose a maximum limit of three unmasked secondary sources within 2.5 magnitudes of the primary source; we choose this value primarily as a compromise between computational efficiency and resolving parameter degeneracies at the fitting stage.

vi. Profile Fitting: Prior to fitting, SIGMA creates a further cutout of the science image based on output parameters from SExtractor for the primary object. As aforementioned, initial guesses for both the primary object and secondary objects are taken from SExtractor, including: object magnitude, axis ratio, position angle and effective radius R_e (see Kelvin et al. 2012 for details of the effective radius estimation). The initial estimate of the Sérsic index n is set to a constant value of 2.0; however, changing this value was found by Kelvin et al. (2012) to have little effect on the final result. We modelled our objects with a free Sérsic profile ($1 < n < 20$), imposing no manual constraints beforehand on any output parameters.

In order to impose quality control on the GALFIT output values, SIGMA contains inbuilt constraints which are then applied post-fitting. After running GALFIT on an object, SIGMA analyses the output and refits any objects which are flagged as follows:

1. GALFIT has encountered a serious error that prohibits completion of the fit.
2. The primary object's centre has undergone a migration of $x^2 + y^2 > R_{e,\text{initial}}$.

3. The primary object’s end radius is either exceptionally large ($\log_{10} \left(\frac{R_{e,\text{final}}}{R_{e,\text{initial}}} \right) > 3$) or exceptionally small ($\log_{10} \left(\frac{R_{e,\text{final}}}{R_{e,\text{initial}}} \right) < -3$).
4. The primary object’s final ellipticity is high ($\epsilon > 0.95$).

In total, 326/327 objects were fit with profiles from SIGMA; we discuss the use of the *i*-band model profiles when computing stellar masses in Section 3.1.1 and our choice of the *r*-band for the morphological parameters. Of these, 198 galaxies were used in our subsequent analysis; we discuss in Section 2.6.1 how we arrived at this value. An example of the finished SIGMA data product for a BCG is shown in figure 2.9.

2.6.1 Probing Surface Brightness Limits with Simulated Profiles

As our BCGs encompass a large magnitude range, we decided to investigate any potential structural dependencies that may arise with changes in surface brightness, R_e or n . Little investigation in the literature has been done to understand such biases which arise as a result of fitting (see Guo et al. 2009, Blanton et al. 2011, van der Burg et al. 2017b as examples of studies that attempt to characterise structural biases), with numerous authors content to base their fit quality primarily on the reduced χ^2 estimate (χ_ν^2). These fits are not necessarily representative of a result which is physically meaningful (e.g., Liu et al. 2008 found differing results for their BCGs, dependent on the isophotal level chosen or method of background subtraction). Some studies have even adopted a novel approach to their fitting in order to gain insight into the ‘goodness of fit’ of their objects; a recent example being Lange et al. (2016), who fit their objects with SIGMA using a Monte-Carlo based method, taking the resulting parameters for each fit at the point of convergence.

We therefore tested SIGMA’s ability to recover parameters from BCG-like objects with the fitting criteria specified in Section 2.6 by creating a grid of model profiles with known input parameters, which we then inject into real SDSS fields. The 8 SDSS fields selected for use in the simulations are listed in Table 2.2. Although they were taken from among the fields in the sample, the selection process was effectively at random. The fields contain many features known for causing issues during fitting, such as bright stars and regions of high source density.

ID	α_{2000}	δ_{2000}	RUN	CAMCOL	FIELD
1_1282	133.761	+55.454	1350	2	194
1_14572	352.634	+20.728	8096	6	182
1_2785	143.215	+47.931	2740	6	261
1_2952	163.487	+49.499	2883	1	109
1_3349	202.598	+49.185	3650	5	85
1_4285	146.506	+43.127	2887	4	251
2_11151	11.534	+20.614	7913	5	30
2_2401	126.401	+48.341	1331	4	156

TABLE 2.2: Cluster fields used when inserting mock galaxies. The ID column refers to the corresponding ID string in the SPIDERS catalogues.

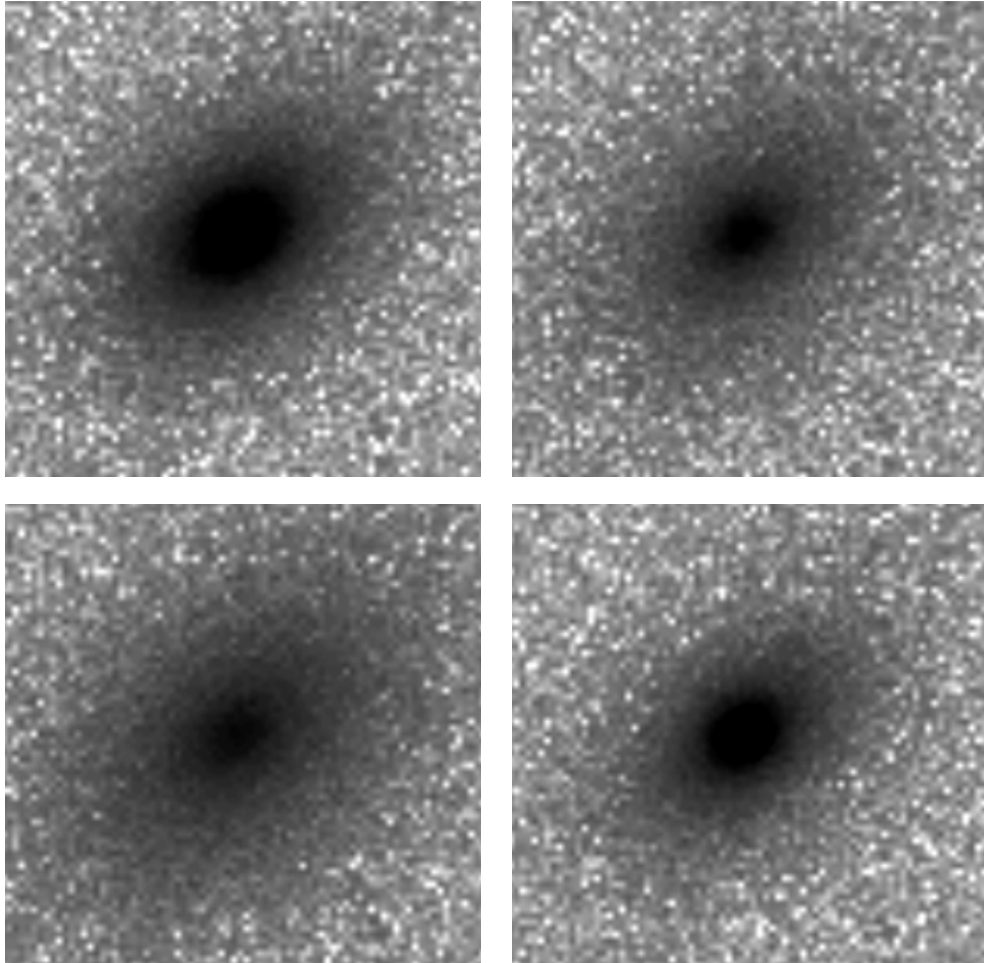


FIGURE 2.10: Example r -band simulated profiles at 15th magnitude (tiles scaled to 100×100 kpc with an assumed redshift of 0.2). Top: for a fixed n of 4, $R_e = 20, 80$ kpc. Bottom: for a fixed R_e of 40 kpc, $n = 2, 8$. Note the change in surface brightness distribution in either case.

The model profiles were generated using GALFIT for consistency, as it was the algorithm of choice used during fitting. The estimated magnitude zeropoints and PSFs (from SIGMA) for these fields were used when generating the model profiles, to account for field-by-field photometric variations. An idealised Poisson noise component was also added, to mimic shot noise. The models were then injected into each of the 8 fields at 8 random, fixed positions and subjected to a full run through the SIGMA pipeline. We chose a range of Sérsic indices from 1 – 10 in steps of 1, apparent magnitude values from 12 – 19 in all three bands and effective radii from 10 – 100 kpc at $z = 0.2$ (equivalent to $0.253''/\text{kpc}$). Therefore, a total of 6,400 model combinations per band were created, or 19,200 in total. We chose this scale for R_e as it represents the approximate peak of the SPIDERS sample, so will correspond to effective radii relevant for our purposes. In addition, we justify our selection of input Sérsic indices by noting that they encompass the bulk of all potentially physically-meaningful outputs; Sérsic indices larger than $n = 10$ represent virtually identical profiles (e.g. [Graham & Driver 2005](#)). Finally, the input axis ratio was held constant at 0.66 (a realistic value for most BCGs; most SPIDERS BCGs have axis ratios between 0.6-0.8 with little variation across bands) and the position angle at 50° (not significant in the context of this study); this was primarily done for the sake of preserving computational resources, so to reduce the number of potential parameter combinations to simulate.

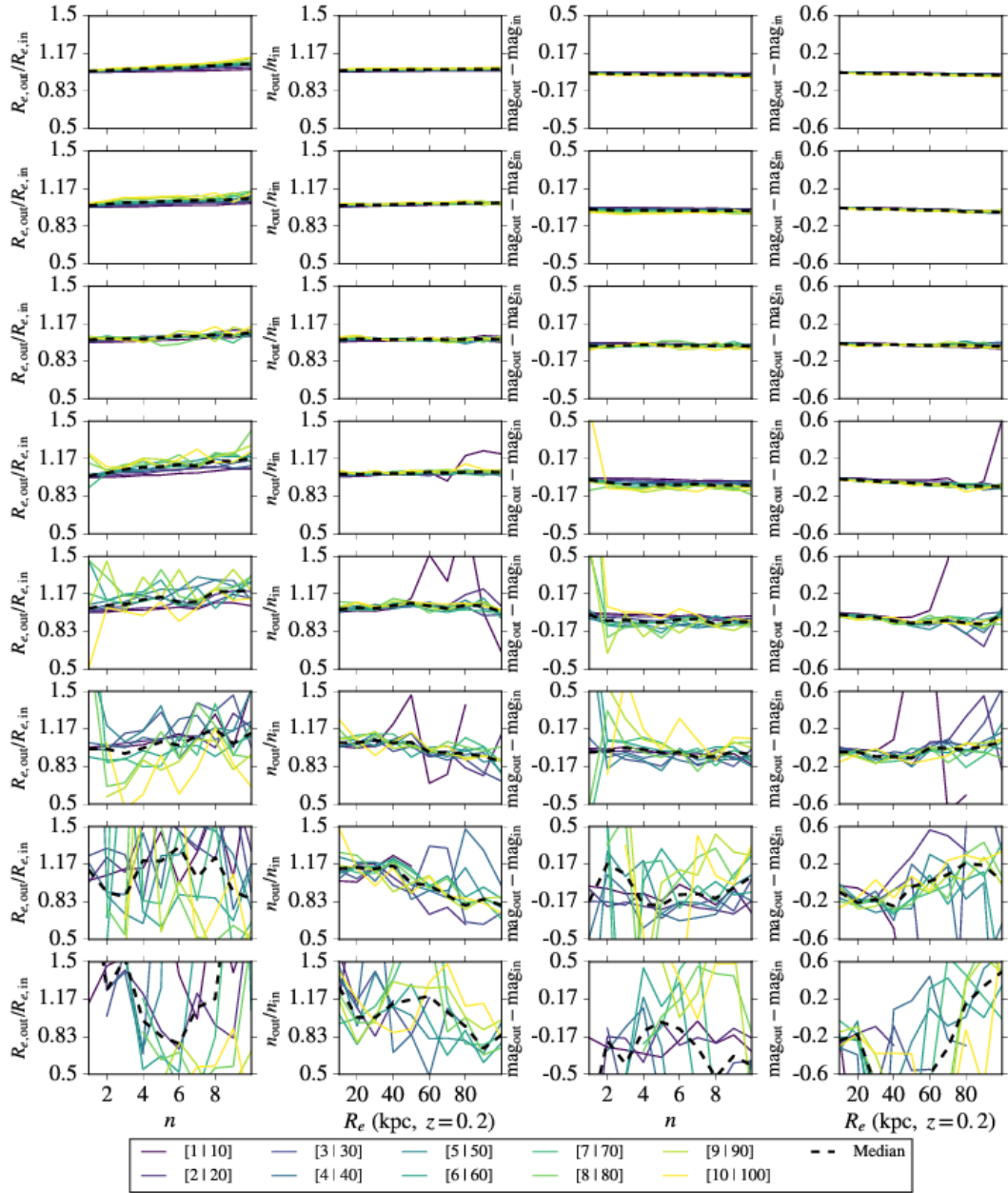
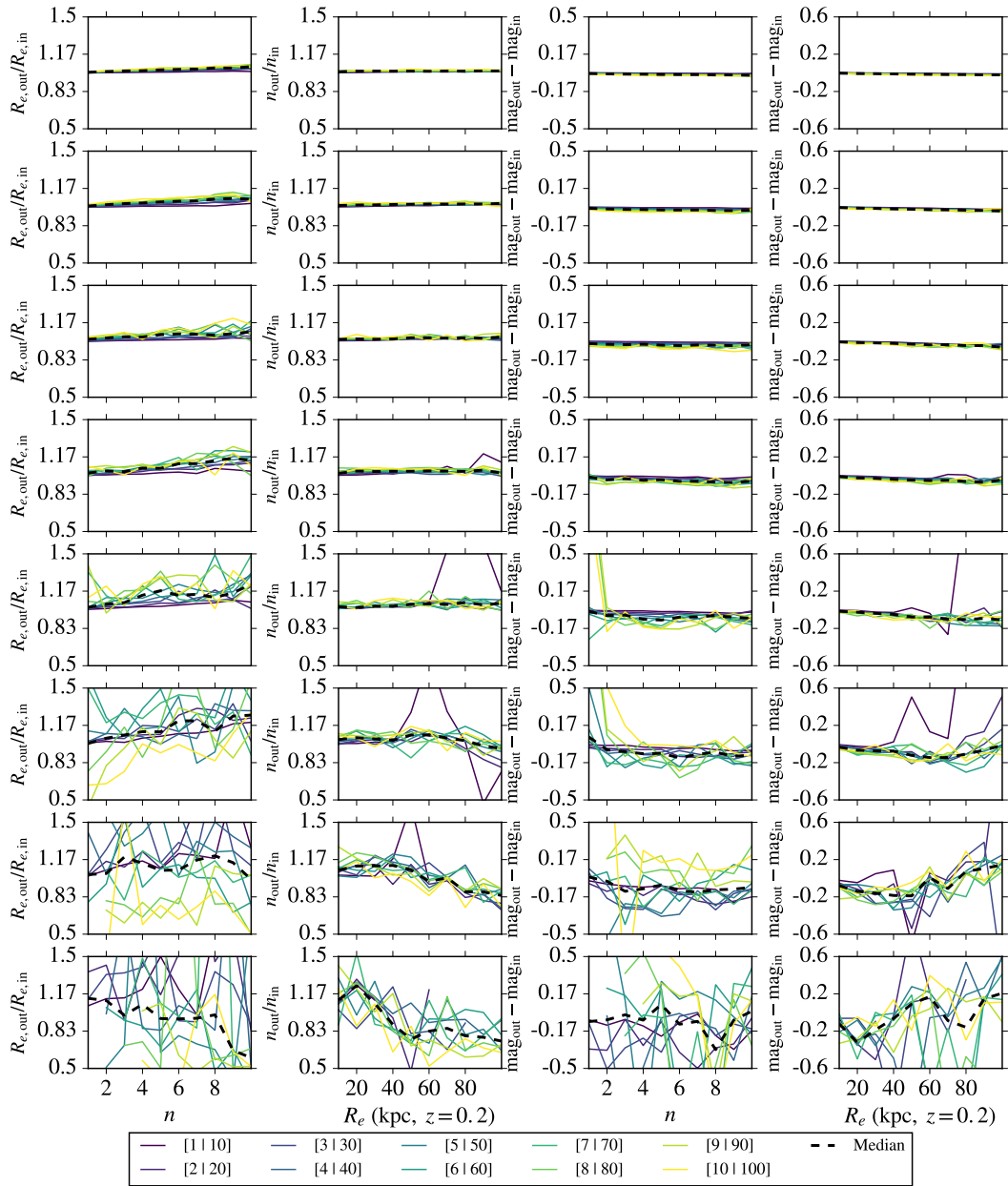
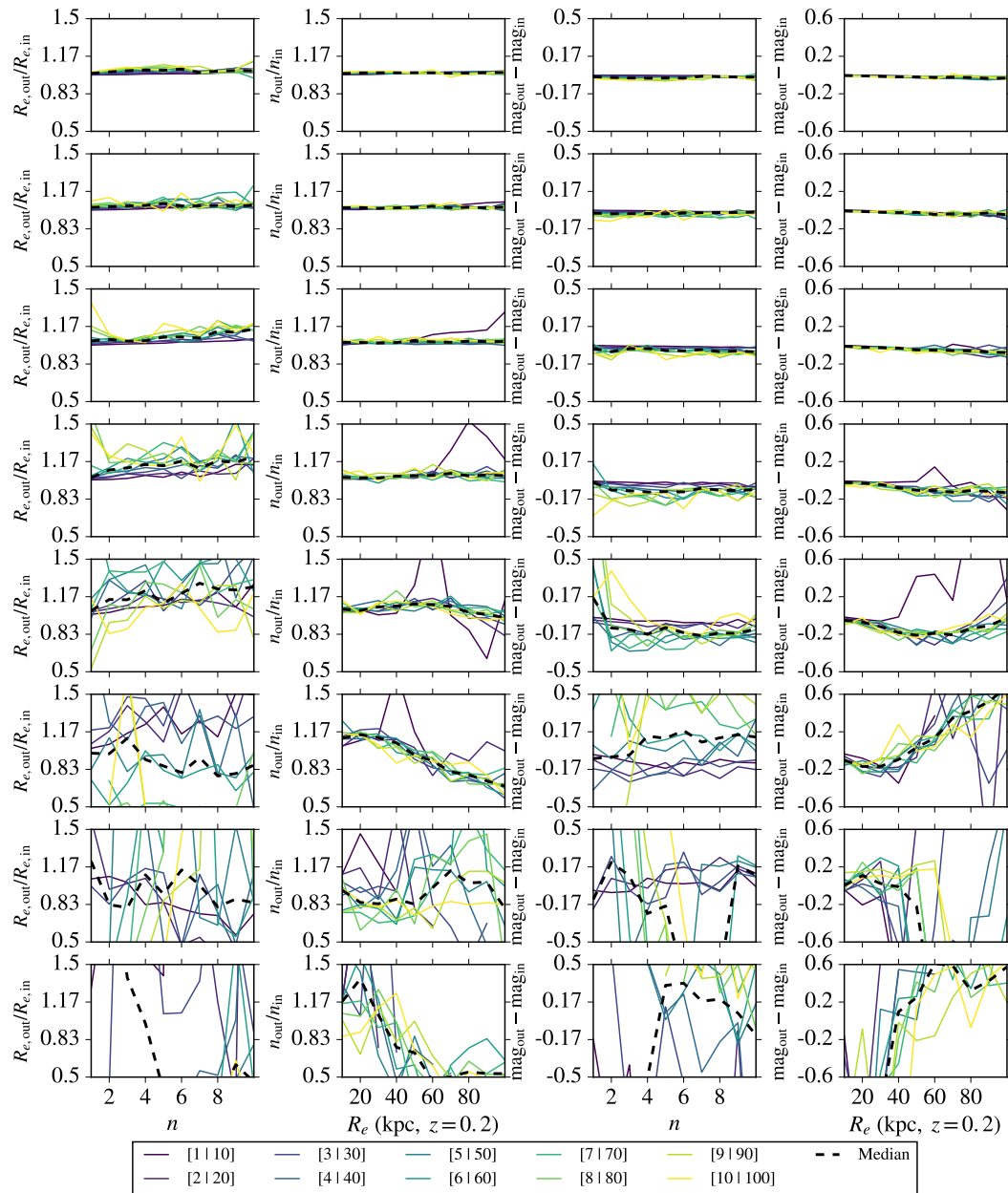


FIGURE 2.11: The results of fitting simulated profiles with SIGMA in the r -band. Each of the four horizontal panels represents the output for one of the eight fixed input magnitudes (12 – 19, descending). The coloured lines represent the biweighted average across the runs (assuming at least 3/8 models at each point were successfully fit; corresponding legend key $[n | R_e]$ for a given colour, interchange for the relevant panel). The black dashed line represents the median $[n | R_e]$ of the coloured lines. There is a clear decline in output-to-input Sérsic index with effective radius at 17th – 19th magnitude (second column).

FIGURE 2.12: As in figure 2.11, but for the g -band.

FIGURE 2.13: As in figure 2.11, but for the i -band.

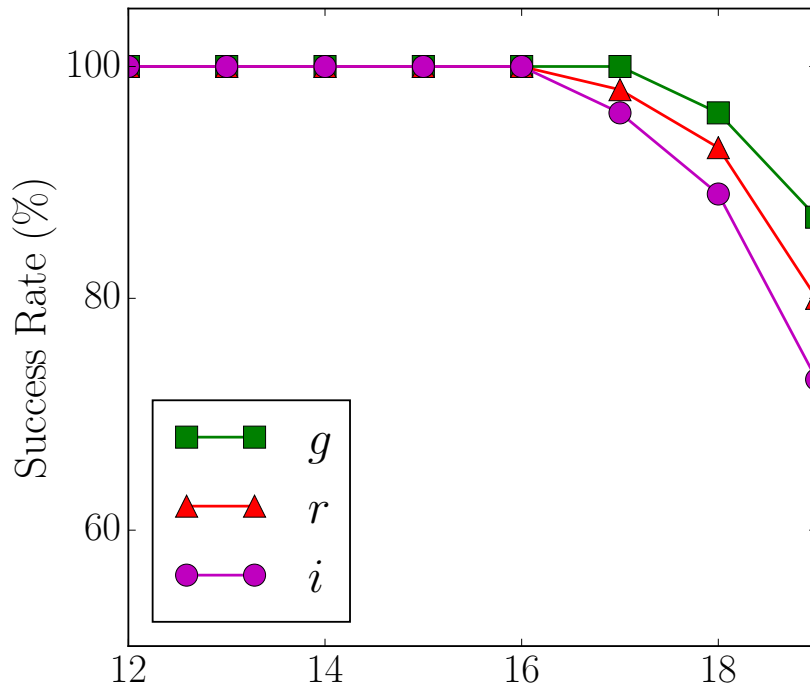


FIGURE 2.14: The fitting ‘success’ rates (i.e. models which completed fitting) from SIGMA fitting of mock profiles. SIGMA’s performance clearly degrades with both wavelength and input magnitude.

Figures 2.12, 2.11 and 2.13 show the results for the g , r and i band simulations respectively; for clarity, however, we will primarily focus on figure 2.11, as it is the r band fits which we use to derive the profile parameters for our BCGs. From figure 2.11, we note several important observations:

1. Firstly, there is an obvious co-dependency between n and R_e ; the outputs are affected if either is changed (e.g., [Graham et al. 1996](#)). Brighter than 17th magnitude, the effect is minimal, with an average scatter about the input of $\sim 5\%$ in Sérsic index for a given stepwise change in effective radius and $\sim 20\%$ vice-versa in effective radius for each incremental change in Sérsic index. In general, magnitude values are accurately recovered; we see an average scatter of ~ 0.1 magnitudes about the input value, regardless of whether n or R_e is changed. As is visible however, the scatter in the values of n and R_e becomes more significant at fainter magnitudes (note the bottom two panels of figure 2.11), with the output scatter well in excess of 50% at 19th magnitude.
2. Secondly, the behaviour of the $n = 1$ profile with R_e is significantly different than for profiles where $n > 1$. At increasing effective radii, it appears that fits to the

profile become ‘chaotic’ at $\sim 14^{\text{th}}$ magnitude, with the scatter exceeding 50% at $\sim 14^{\text{th}}$ magnitude or fainter. Such a profile is exponential by definition and is often used as a model for disc galaxies (e.g. [Freeman 1970](#)); indeed, it is the default model in the SDSS (e.g., [Blanton et al. 2011](#)). The difficulty in fitting such extended, exponential profiles may arise from issues with additional source blending, due to the fact that $n = 1$ profiles are not strongly centrally concentrated (e.g. figure 2.10 shows the effect of changing the Sérsic index). However, this profile is generally not appropriate for galaxies such as BCGs, the majority of which are bulge-dominated and follow a de Vaucouleurs-like profile (e.g., [de Vaucouleurs 1948](#)) where $n \sim 4$. Some studies have modelled cD-type BCGs with a bulge+exponential component, in order to account for their extended stellar halo which is degenerate with the intracluster light (e.g. [Zhao et al. 2015b](#), [Donzelli et al. 2011](#); see also discussion in Chapter 4).

3. Thirdly, we are also able to characterise several important biases, which may have significant consequences if one were to use SDSS data when profile fitting, or when visually-classifying morphologies. There is an obvious bias in Sérsic index with increasing magnitude. At $\geq 17^{\text{th}}$ magnitude, there is a downturn in output Sérsic index with increasing effective radius (second panel from the left, figure 2.11). We strongly suspect this result is due to a surface brightness effect; as the wings of an object become faint with respect to the background level, they become more difficult to detect (surface brightness is dependent on both Sérsic index and effective radius). Therefore, GALFIT underestimates the true slope of the light profile. This effect is consistent regardless of Sérsic index, with all of the output values (bar $n = 1$) showing a similar reduction from input as a trend with effective radius. The effect is also independent of filter; all three bands used for fitting showed a similar bias, albeit to varying degrees of severity (see figures 2.12 and 2.13 in the Appendix, plus discussion below).
4. Finally, it is clear from figures 2.12 & 2.13 that there is a marked decrease in fit robustness moving from the g to the i -band, with the scatter in output values increasing with wavelength (e.g. ~ 0.2 magnitude difference in output g/r band magnitude compared with ~ 0.5 in i at 17^{th} magnitude). This behaviour is also seen in the decreasing success rates of our simulations (with ‘success’ defined as a given combination of fit parameters being modelled by SIGMA to completion),

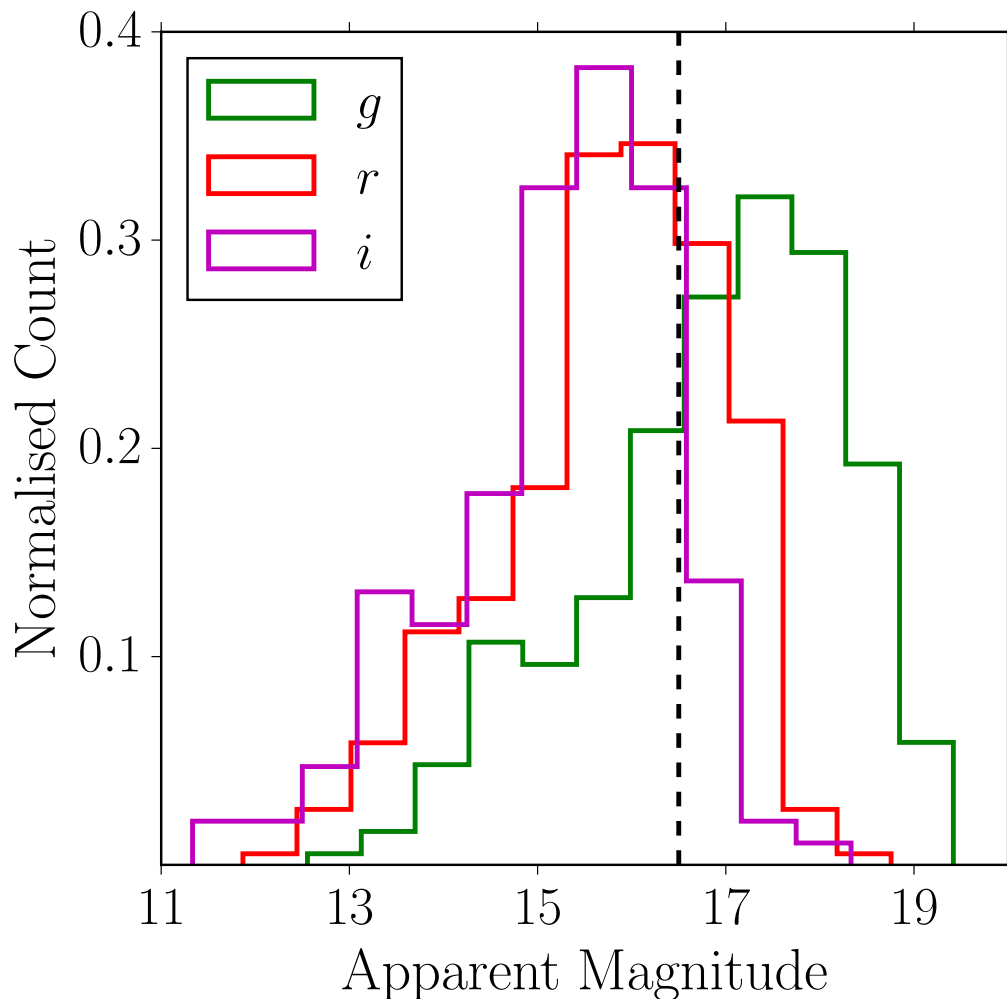


FIGURE 2.15: The raw fit magnitudes for the SPIDERS sample from SIGMA ($N=326$), prior to any k -correction or dust correction. The histograms have been normalised by area.

as presented in figure 2.14. The sky tends to be brighter at redder wavelengths (see [Stoughton et al. 2002](#)), which is reflected in the smaller magnitude limit of the SDSS i -band (21.3 magnitudes, as opposed to 22.2 for g/r). The increased sky brightness in the i -band therefore significantly affects the final fit. We are therefore justified in our selection of the r -band models to characterise our BCGs, as a compromise between both band depth and the amount of k -correction necessary (Section 3.1.1).

For these reasons, we decided to impose a cut on the raw output magnitudes for the SPIDERS BCGs, to minimise potential biases in Sérsic index that may arise as a result of systematics from surface brightness dimming. As we are unsure at the resolution

of our simulations precisely where this effect begins to dominate our fits, we select a magnitude of $m_r = 16.5$ as the faintest magnitude for which to include objects. To place this choice into context with the output magnitudes from SIGMA of the BCGs in our sample, the raw output magnitude distributions are displayed in figure 2.15. The sample peaks at $m_r = 15.8$ (with $m_g = 16.9$ and $m_i = 15.2$), with $\sim 1/3$ of all galaxies lying above our limiting magnitude of 16.5 (99/326). Thus, the total number of objects which we include in our analysis is reduced to 227 (198 after imposing further quality cuts as described in Section 5.2).

Applying this cut in BCG magnitude at $m_r = 16.5$ significantly affects the redshift distribution of our clusters (figure 2.6), in that it reduces the number of intermediate-redshift clusters in the sample (notably, between $0.2 < z < 0.3$; this is also revealed by a K-S test ($\log_{10}[p_{\text{KS}}] = -4.56$). However, we detect no evidence for any differences in the distributions of L_X , M_{200} and λ between the full and magnitude-restricted samples beyond the 1.3σ level ($\log_{10}[p_{\text{KS}}] = -0.772, -0.491$ and -0.077 respectively; see discussions in Chapter 3 about significance).

2.6.2 Consequences of Systematics within Fitting

It is clear from our simulation outputs that not understanding the systematics involved when approaching the surface brightness limit of the parent survey used when modelling data can lead to model results which are either heavily biased, or, due to the sharp rise observed in the scatter of output values (see figures 2.11 to 2.13), nonsensical. This ‘tipping’ point (at least, with respect to integrated magnitude) appears also to be several magnitudes above the survey limit (at least, for the SDSS); it is however unclear at exactly what limiting surface brightness significant degradation of output parameters begins to occur. It is difficult due to the coarseness of our simulations, alongside the fairly limited number of runs for a given parameter combination, to sufficiently probe this here; we base our estimated ‘modelling’ limit at 16.5 magnitudes in r .

There are many factors to consider which may affect the ability of a modelling algorithm such as GALFIT to model a galaxy accurately. For instance, average surface brightness at a fixed apparent magnitude is affected by both profile extent and concentration (hence, the strong correlation in bias between n and R_e) and vice-versa for the output parameters. There is also an influence from the choice of fitting band for three reasons; the influence

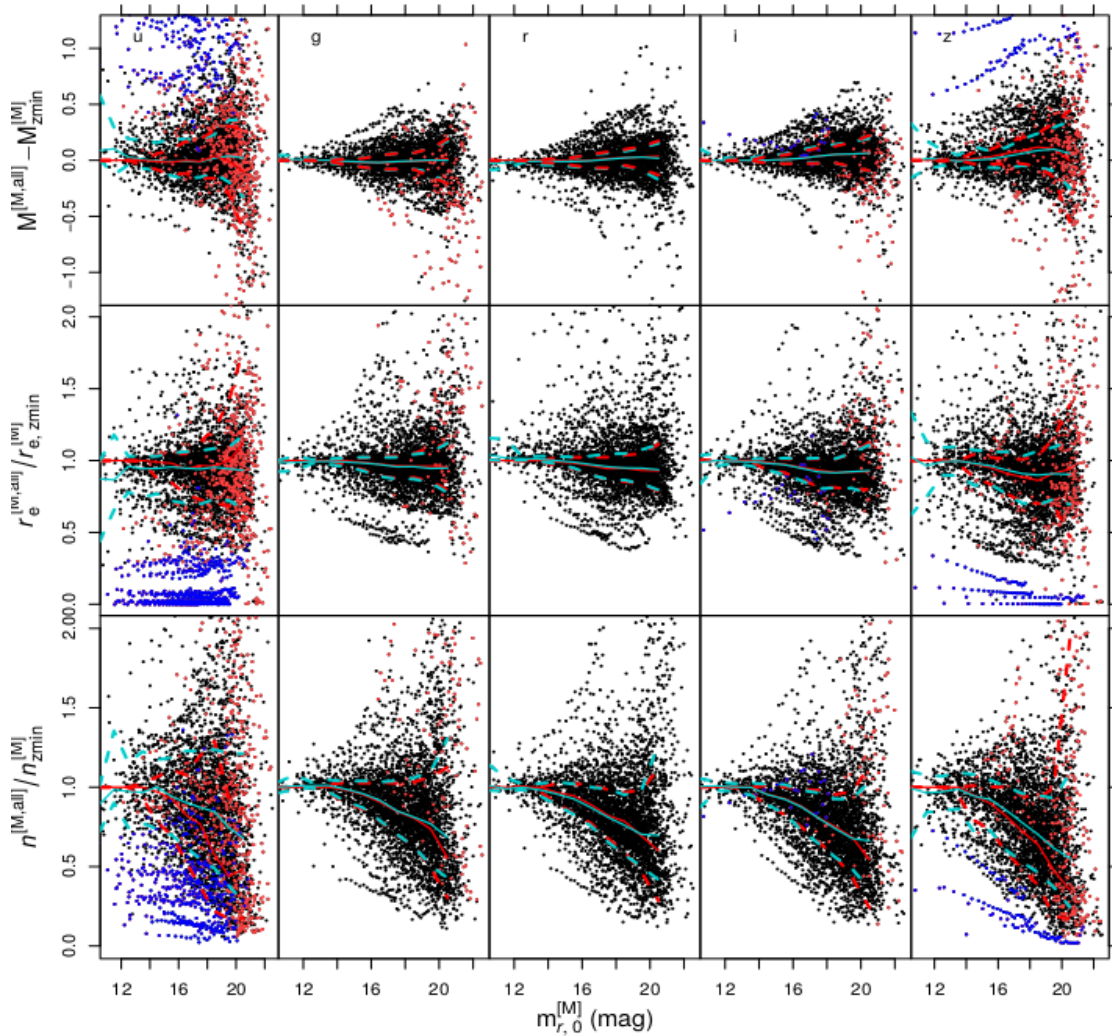


FIGURE 2.16: Outputs from modelling ~ 4000 artificially-redshifted galaxies from [Vika et al. \(2013\)](#) (their figure 13), showing a comparison in output parameters with respect to the lowest artificial redshift ($z = 0.01$). Note the rapid decline in output Sérsic index with increasing redshift in every band.

of k -correction, the depth of the band (e.g. SDSS i is almost a magnitude more shallow than r due to the brightness of the sky) and also, the fact that different bandpasses are more sensitive to certain galaxy features than others (for example, bulges in the centres of late-type galaxies may host older, redder stellar populations than their disks). The latter point has motivated some researchers to consider a band-dependent approach when fitting, and use all photometric data available to better understand the profile shape of a galaxy. For instance, the MEGAMORPH project uses a modified version of GALFIT (known as GALFITM) to perform multi-band fitting of galaxies (e.g. [Häufler et al. 2013](#), [Vika et al. 2013](#) and [Vika et al. 2014](#)).

A similar bias to what we observe through our simulations was reported in [Vika et al. \(2013\)](#) for a sample of ~ 4000 galaxies modelled with artificially-redshifted SDSS photometry. The authors used the FERENGI software ([Barden et al. 2008](#)) to ‘redshift’ galaxies within their sample, where they were reddened and resampled in size on a pixel grid ($0.396''$, the scale of the SDSS). They found that their outputs in Sérsic index, even with the addition of multi-band fitting, were affected significantly by increased redshift, with a downturn in output Sérsic index. The authors concluded that because of the covariance between these parameters (for example, the fact that R_e is inversely proportional to n), an inaccurate Sérsic index measurement would have profound consequences for the rest of the model output parameters (also observed by [Guo et al. 2009](#)).

This conclusion is a fundamental factor for any and all studies which have used profile modelling to analyse any size- or concentration-time relations of galaxies (e.g. [Bernardi et al. 2007](#), [Durret et al. 2019](#)). Quantifying any change in size or shape via a parametric approach becomes next to impossible to do effectively without fully understanding the photometric limitations of the data (or indeed, modelling software) one is using. For BCGs, where a crucial period of ICL and/or halo component formation since $z \sim 1$ is thought to have occurred (around the last 8 Gyr), the approach of profile modelling to quantify this trend, especially in low signal to noise cases, must therefore be used with extreme caution.

2.7 Summary of Chapter

In this chapter, we described the SPIDERS survey, and the nature of the sample, which is based on a hybrid optical (SDSS) and X-ray (RASS) selection process. We outlined how we selected our sample of 329 BCGs, including the quality cuts used and the approach of visual inspection on identifying BCG candidates. We detailed our measures of cluster environment, and our methodology for computing cluster velocity dispersions. We described the fitting methodology used to model the light profiles of our BCGs, and the operation of the GALFIT, SExtractor and PSFEX-based SIGMA pipeline. Finally, we outlined our use of simulated profiles to test the SIGMA pipeline, where we primarily found:

1. the presence of a strong codependency between n , R_e and apparent magnitude,

2. a negative bias in Sérsic index with effective radius, which we concluded occurred as a result of the degeneracy between the background level and profile wings,
3. a significant increase in the scatter of output effective radii at fainter magnitudes, which occurred regardless of band or input Sérsic index or effective radius,
4. a significant difference in behaviour in the case of $n = 1$, which we concluded was due to the lack of profile central concentration, and,
5. a marked decrease in modelling completion rate and overall robustness, dependent on both model surface brightness and the limiting magnitude of the band.

We used the information from our simulations to approximate the fitting magnitude limit of our sample ($m_r = 16.5$), which reduced our sample for analysis to 198 BCGs (after several subsequent quality cuts on the BCG output parameters listed in Section 3.1.1 of Chapter 3). We found, using a K-S test, that although this shifted the distribution of BCGs towards lower redshifts, there were no significant changes in the distributions of the associated environmental parameters of interest for this study.

We concluded that our findings had concerning consequences for galaxy parameter studies (motivation 1 of Section 1.5) not considering systematics related to surface brightness dimming, to which we provided some literature discussion. Due to the coarseness of our simulations, we did not attempt to establish any corrective scaling relations to amend this effect; however, we will discuss a potential future project expanding on this work within the conclusions of this thesis (see Section 6.2, ‘Future Work’).

Chapter 3

Part I - BCG Properties with Respect to Environment

3.1 Overview of Contents

In this chapter, we present the results of our study into the morphological properties of BCGs with respect to the properties of the environment in which they reside, using our primary science sample of 198 BCGs (see current and previous chapter for details). We discuss how we estimate stellar masses for our BCGs, and the various corrections we apply to their colours. We provide a comparison between our stellar masses and stellar masses derived from SED modelling from the MPA-JHU value added catalogue (e.g. [Brinchmann et al. 2004a](#)). We discuss how we quantify our correlations, and how we account for parameter degeneracies through a partial Spearman analysis; we then discuss the consequences of our findings, and their implications for the co-evolution of BCGs with respect to their host haloes as presented in [Furnell et al. \(2018\)](#). Finally, we introduce our work on a Value-Added Catalogue (VAC) released on behalf of the SPIDERS team as a part of SDSS DR14, and discuss results from the corresponding paper (Erfanianfar et al., in press).

This chapter primarily addresses motivation 2: “How do BCGs evolve with respect to their host cluster?”, referenced in Section [1.5](#).

3.1.1 BCG Stellar Masses and Discussion of Systematics

As the Sérsic fits to our BCGs from SIGMA have associated integrated magnitudes, they can be used as a proxy for BCG stellar mass. Firstly, however, in order to ensure the quality of our model fits, we set several criteria which a fit must meet to be included in our analysis (see [Powell et al. 2017](#); [Zhao et al. 2015b](#)). Criteria for exclusion, if exceeded, include: a limit of $\chi_\nu^2 \geq 3$ to remove any BCGs with bad residuals, a limit of $R_e \geq 800''$, $\Delta R_e/R_e \geq 0.8$ (where ΔR_e is the statistical error in R_e from GALFIT, recommended by [Simmons & Urry 2008](#)) and finally, a limit of $n \geq 14$. These parameters remove most fits deemed to be physically unrealistic; in total, approximately $\sim 10\%$ of objects were affected (29/227, see Section 2.6.1), bringing the total number of BCGs included in our primary analysis sample to 198. We have checked and found no significant changes to our conclusions by including the fits which did not meet the stated criteria; for the sake of only adding additional statistical noise, we decided to omit them.

In this work, we adopt the updated scaling relation of [Taylor et al. \(2011\)](#) (see their figure 12), which was used to estimate stellar masses for galaxies in the GAMA survey. They demonstrate that stellar masses can be estimated within ~ 0.1 dex of the SED mass estimates quoted in the MPA-JHU catalogues (<http://wwwmpa.mpa-garching.mpg.de/SDSS/DR7/>; see [Shen et al. 2003](#) for the method used to derive stellar masses). [Taylor et al. \(2011\)](#) also reported that using the i -band as a tracer of galaxy mass produced results of similar quality to using the common proxy of NIR flux. The scaling relation is derived from SED fits to GAMA galaxies using SDSS $ugriz$ photometry, using stellar population synthesis models from the library of [Bruzual & Charlot \(2003\)](#) with a [Chabrier \(2003\)](#) IMF.

From the rest-frame $g - i$ colour of a galaxy and its absolute magnitude M_i , the stellar mass is estimated via the following empirical relation:

$$\log_{10}[M/M_\odot] = 1.15 + 0.70(g - i) - 0.4M_i, \quad (3.1)$$

where M_i are the k - and dust-corrected absolute magnitude values in the i band, derived from the best-fitting Sérsic profile for a given BCG and $g - i$ is its restframe colour. We measure the $g - i$ colours of our objects through fixed 30 kpc apertures, which we do to reduce potential biases which may occur across fits (see Section 2.6.1).

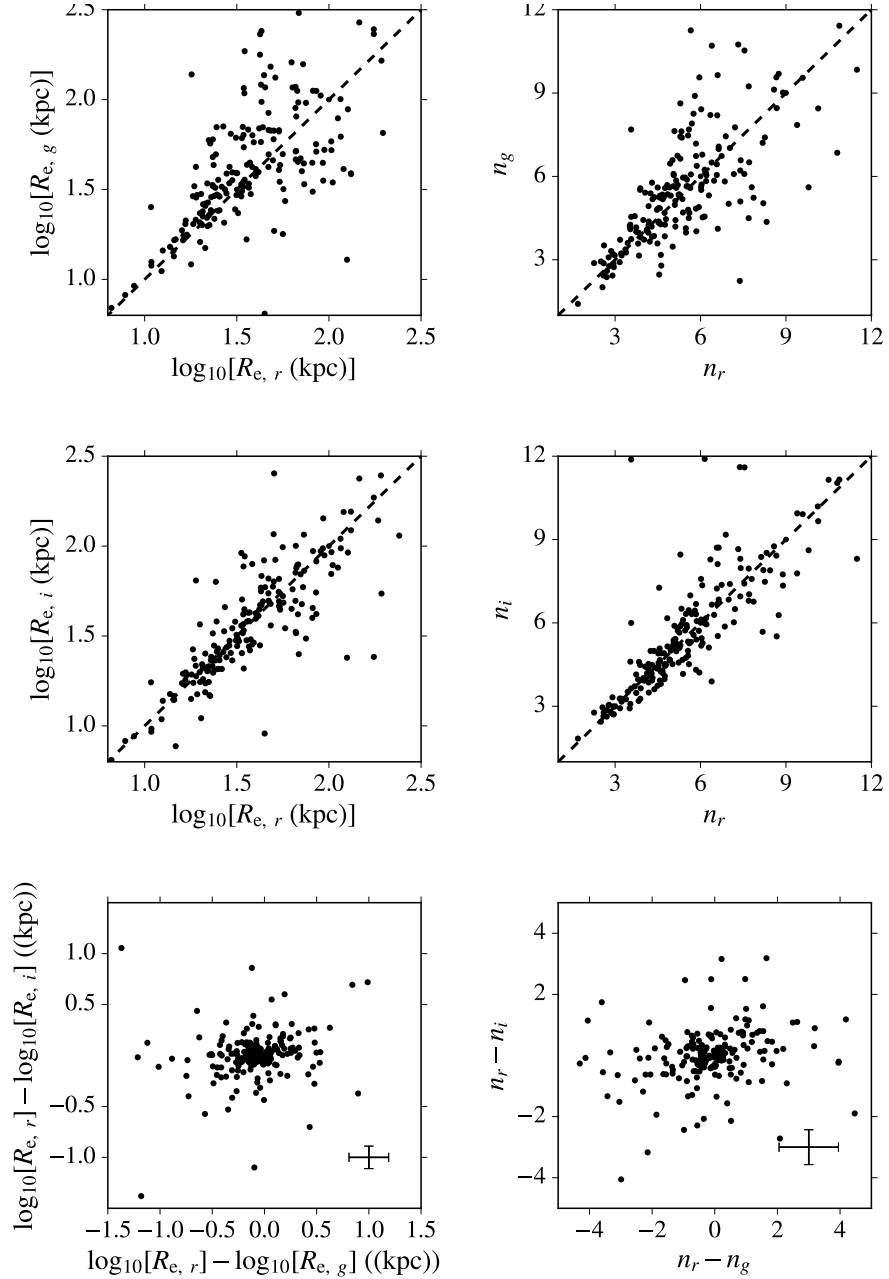


FIGURE 3.1: Comparison between the output structural parameters for the BCG sample ($N=198$) in 3 different passbands (gri). The dashed line represents the 1:1 relation and the crosshairs in the bottom two plots represent the 1σ scatter in x and y . In general, there is a good agreement across bands, albeit with increased scatter at large n and R_e .

This has also been demonstrated in our simulations (Section 2.6.1).

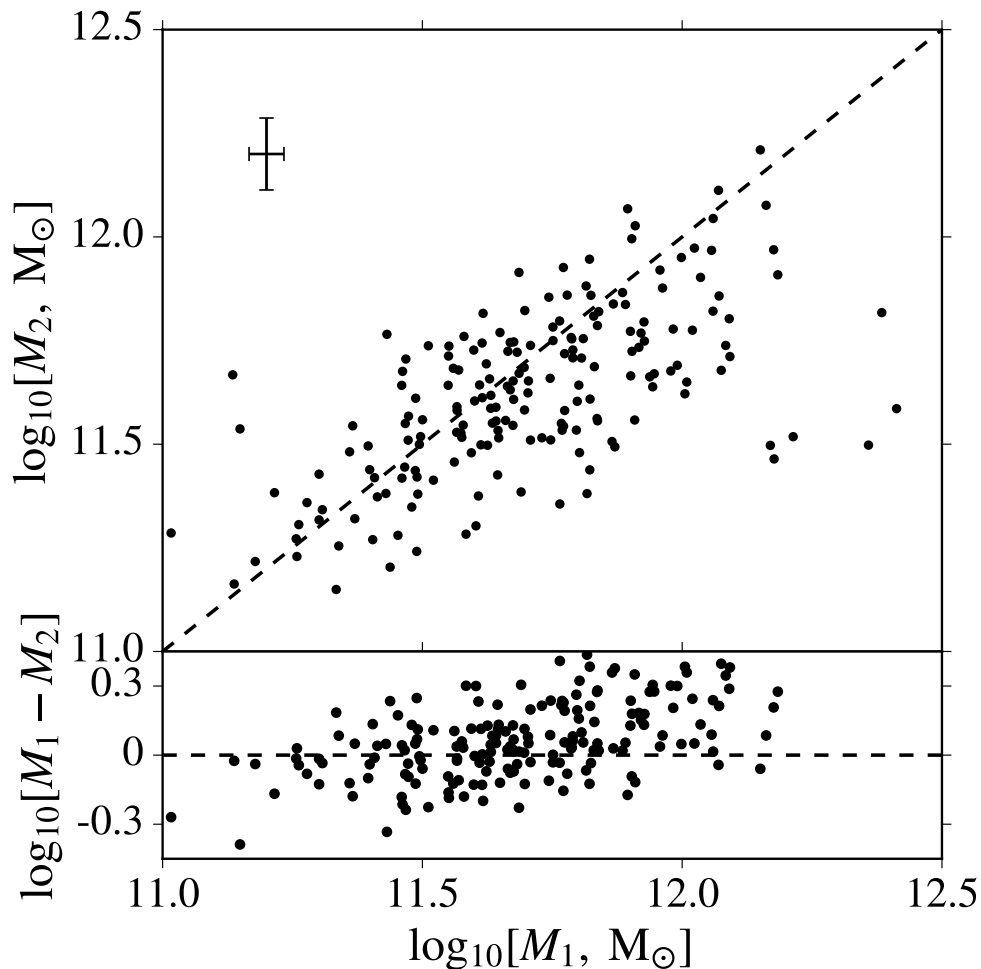


FIGURE 3.2: Comparison between the stellar mass estimates for our BCGs using a scaling relation from [Taylor et al. \(2011\)](#) and those in the MPA-JHU value-added catalogue, for a common sample of 192/198 BCGs (x -axis and y -axis, respectively). The crosshairs give the typical error value in each respective axis (for the MPA-JHU catalogue, drawn from the 16th and 84th percentile estimates).

We correct our objects for extinction from Galactic dust using the standard maps of [Schlegel et al. \(1998\)](#) (updated normalisation in [Schlafly & Finkbeiner 2011](#)), with a [Fitzpatrick \(1999\)](#) reddening law. Typically, this correction is small; the mean values in each band are 0.08, 0.06 and 0.04 magnitudes in g , r and i respectively. We also apply a k -correction to our objects after correcting for dust (see equation 1.11 in the Introduction). The k -corrections are based on the work of [Chilingarian et al. \(2010\)](#) for galaxies up to $z \sim 0.5$ in lieu of multi-band photometry. They are approximated by polynomials (e.g. [Collins & Mann 1998](#)), requiring only a redshift and input color, and produce k -corrections within 0.1 magnitudes of the estimates from the industry-standard KCORRECT software for SDSS data ([Blanton & Roweis 2007](#)). We use our aperture

$g - r$ colors; the average k -corrections are 0.59, 0.19 and 0.10 magnitudes in g , r and i respectively.

We caution the reader that our mass ‘errors’ are drawn from the systematic errors output by the best-fit model from GALFIT; they are therefore likely to be underestimated. Instead, we offer a comparison between the stellar masses of our final sample of objects between a common subsample of 192 with masses drawn from the MPA-JHU value added catalogue in figure 3.2 (Bruzual & Charlot 2003 SP, Kroupa 2001 IMF). The agreement is good, with the average scatter (approximately ± 0.06 dex) similar to that predicted by Taylor et al. (2011). The small, positive offset is predominantly due to our choice of using model magnitude when computing our stellar masses, so as to account for additional mass in the wings of our BCGs; indeed, if we instead compute our magnitudes using a 30 kpc aperture, we see a mean decrease in mass of 0.28 dex. The BCGs span a large range in mass, from $11.0 < \log_{10}[M_{\star}(M_{\odot})] < 12.5$, peaking at $\log_{10}[M_{\star}(M_{\odot})] = 11.5$.

As discussed at length in the previous section, we use the r -band output parameters to characterise our BCGs. There is, however, little variation in the two as both bands pick up light from predominantly the same stellar populations (e.g. Kennedy et al. 2016; Taylor-Mager et al. 2007). We display comparisons between morphological parameter outputs for g and i with r in figure 3.1 to illustrate this point. Moreover, as shown in figure 2.13, the overall scatter in the i -band output at 17th magnitude or brighter compared to input is reasonably small (e.g. $\Delta m_i \sim 0.2$ at $m_i = 17$); this result is also likely to be a worst-case scenario, given that the peak output i -band magnitude for our BCGs is ~ 0.6 magnitudes brighter than for the r -band.

3.1.2 Correlations Between BCG Parameters

To determine which parameters are the primary drivers behind the correlations in our data, we have performed a Spearman rank analysis (referred to in the text as r_s in both the full and partial case, where p_s is the associated p-value) on our main sample (Table 3.1). We have also provided a partial Spearman analysis as well to test the robustness of our results against selection effects for the parameters of interest (Tables A.1-A.7; computed using MATLAB’s ‘PARTIALCORR’ routine), following a similar practice to Collins & Mann (1998). The partial Spearman rank is a means of accounting for degeneracies in

TABLE 3.1: Full Spearman rank analysis for all the variables examined in this study for the r -band morphological parameters. The top half of the table lists the Spearman rank correlation coefficient (r_s), whereas the bottom half of the table provides the log of its corresponding p-value ($\log_{10}[p_s]$).

	R_e	L_X	M_{200}	n	M_\star	λ	z
R_e	-	0.26711	0.11014	0.58263	0.64668	0.12535	0.30716
L_X	-3.8404	–	0.43005	-0.14079	0.39447	0.54933	0.57387
M_{200}	-0.91578	-9.4719	–	-0.14423	0.26984	0.51566	0.29608
n	<-45	-1.3244	-1.3749	–	0.1548	-0.10605	-0.059135
M_\star	<-45	-7.9602	-3.911	-1.536	–	0.24395	0.50075
λ	-1.1095	-16.356	-14.187	-0.86639	-3.2872	–	0.30286
z	-4.9478	<-45	-4.6253	-0.39105	<-45	-4.8622	–

correlations between parameters, and is defined as

$$r_{s,AB|C} = \frac{r_{s,AB} - r_{s,AC}r_{s,BC}}{[(1 - r_{s,AC}^2)(1 - r_{s,BC}^2)]^{1/2}}, \quad (3.2)$$

where A and B are parameters being tested for correlation and C is a third parameter being held constant. The Spearman rank ranges in value from 1 to -1, with 1 being a perfect correlation, 0 implying no correlation and -1 being a perfect anticorrelation. We hold our significance level at the standard value of $p \leq 0.05$ throughout this work ($\log_{10}[p_s] \leq -1.301$).

Figure 3.3 suggests a strong correlation between the effective radius and stellar mass (luminosity) of our objects (Spearman rank coefficient, $r_s = 0.65$, $\log_{10}[p_s] < -45$), which remains largely unchanged when any dependence on the environmental parameters are removed (see Tables A.2, A.3 and A.6 in the Appendix of this thesis). This behaviour is also seen in figure 3.4, which we discuss in detail in the upcoming section (Section 3.1.2). These results indicate that the mass-size relation for BCGs seen here largely appears to exist independently of environment; this was also concluded by Zhao et al. (2015a). These observations support the scenario proposed by Shankar et al. (2014), who provided a semi-analytic model of BCG evolution since $z \sim 0.3$ and found no major environmental dependence on the sizes of early-type central galaxies (see Section 2.3). Indeed, numerous other studies have found this to be true of cluster galaxies in general at $z < 1$. For example, Kelkar et al. (2015) modelled galaxies in a similar way to this work in the ESO distant cluster survey (EDisCS, White et al. 2005), a HST survey of 20 cluster fields from $0.4 < z < 0.8$. Splitting the sample into cluster and field galaxies using a threshold in velocity dispersion, they found no differences in the sizes of galaxies

inside or outside of the cluster. [Huertas-Company et al. \(2013\)](#) reported similar findings in their work, reporting a doubling of massive ellipticals (including BCGs) in size from $z \sim 1$ to present, but no environmental dependence on the mass-size relation.

Comparing with the correlation between mass and effective radius, we also find a weaker correlation between stellar mass and Sérsic index ($r_s = 0.1548$, $\log_{10}[p_s] = -1.536$; see figure 3.3). The correlation remains present for our sample when controlling for the three environmental parameters used to characterise our clusters (M_{200} , λ , L_X ; see Tables A.2, A.3, A.6 in the Appendix), as well as redshift (z ; see Table A.7 in the Appendix). The existence of this correlation has been debated in the literature. Some authors have found correlations between n and M_* , especially in the central regions of BCGs (e.g. [Bai et al. 2014](#)), arguing that it is this correlation that provides evidence for the ‘inside out’ scenario proposed for BCG evolution (e.g. [Guo et al. 2009](#), see also discussion in Section 1.4.1 the Introduction). However, [Zhao et al. \(2015a\)](#) reported that this relation is driven by the strong dependence of n on R_e due to the choice of profile modelling to parametrise their BCGs (rightmost panel of figure 3.3, $r_s = 0.58$, $\log_{10}[p_s] < -45$), finding that this relation disappeared when they chose to use SED-based masses (though their conclusions were otherwise unchanged when they used a scaling relation). They did however find a visual morphological dependence on Sérsic index when they split their sample into E and cD-type BCGs. Here, this weak, positive correlation is removed by accounting for any R_e dependence through applying a partial Spearman rank (Table A.1), indicating that there is a dependence of Sérsic index on effective radius.

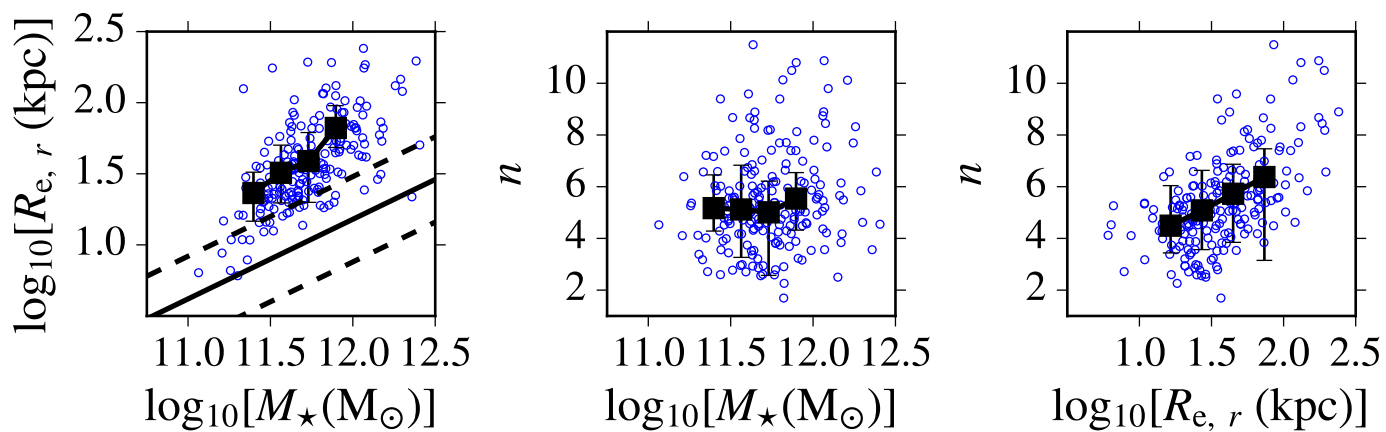


FIGURE 3.3: Correlations between the BCG structural parameters. For clarity, the data have been binned using a Scott's-rule optimised bin width to illustrate structure (omitting bins with fewer than 15 objects). The errorbars mark the 16th and 84th percentiles of each bin. The solid line is the relation for SDSS 'early-type' galaxies ($n > 2.5$) from Shen et al. (2003), with the dashed lines marking the 1σ scatter.

The prominent anti-correlation between n and M_\star that then arises as a result of removing any dependence on R_e ($r_s = -0.3641$, $\log_{10}[p_s] = -6.871$) could therefore arise from two possible effects: evolution, or underestimation of the slope due to surface-brightness effects, as demonstrated by our simulations (figure 2.11). From our simulations in Section 2.6.1, we believe it is more likely that the latter is the cause, due to the likelihood of the cut of 16.5 not being sufficient enough to completely prevent contamination from profiles suffering from this effect. As expected, when fixing for redshift, there is no anti-correlation present (Table A.7, $r_s = 0.2000$, $\log_{10}[p_s] = -2.321$). At the very least underestimating the slope cannot be ruled out as the source of the anti-correlation; nevertheless, although we observe an increased scatter in R_e and magnitude at decreasing surface brightness, we see no evidence for any real change in direction of the correlation (figure 2.11). It is worth noting that Stott et al. (2011) also reported no evidence for any evolutionary dependence on BCG profile slope between $0.25 < z < 1$ from their Sérsic fits; Ascaso et al. (2011) measured a change in size from $0 < z < 0.6$, but also no prominent change in profile slope. In contrast, Bernardi (2009) did find that BCGs are more massive and more extended than field or non-BCG satellite galaxies. Discrepancies between results therefore appear to lie in the method of selection, the method of defining environment and whether to take a single or multiple-component approach when fitting.

3.1.3 How do BCG Parameters Scale with the Cluster Environment?

We compare the properties of our BCGs with those of their host cluster environments in figure 3.4. It is immediately obvious that the masses of our BCGs are significantly correlated with all three environmental properties at the focus of this study; however, the strength of the correlation varies greatly depending on the property of interest (see Table 3.1). The stellar masses of our BCGs are the most strongly correlated with X-ray luminosity ($r_s = 0.394$, $\log_{10}[p_s] = -7.9602$) and are the least correlated with richness ($r_s = 0.244$, $\log_{10}[p_s] = -3.287$).

The corresponding $R_e - M_\star$ relation from Shen et al. (2003) derived for a general population of early-type galaxies independent of environment (defined as $n > 2.5$) has also been included for comparison in figure 3.3. Our BCGs lie significantly above this relation (~ 0.5 dex). Zhao et al. (2015a) came to a similar conclusion in their work, finding that most of their BCGs lay significantly above this relation, especially for BCGs

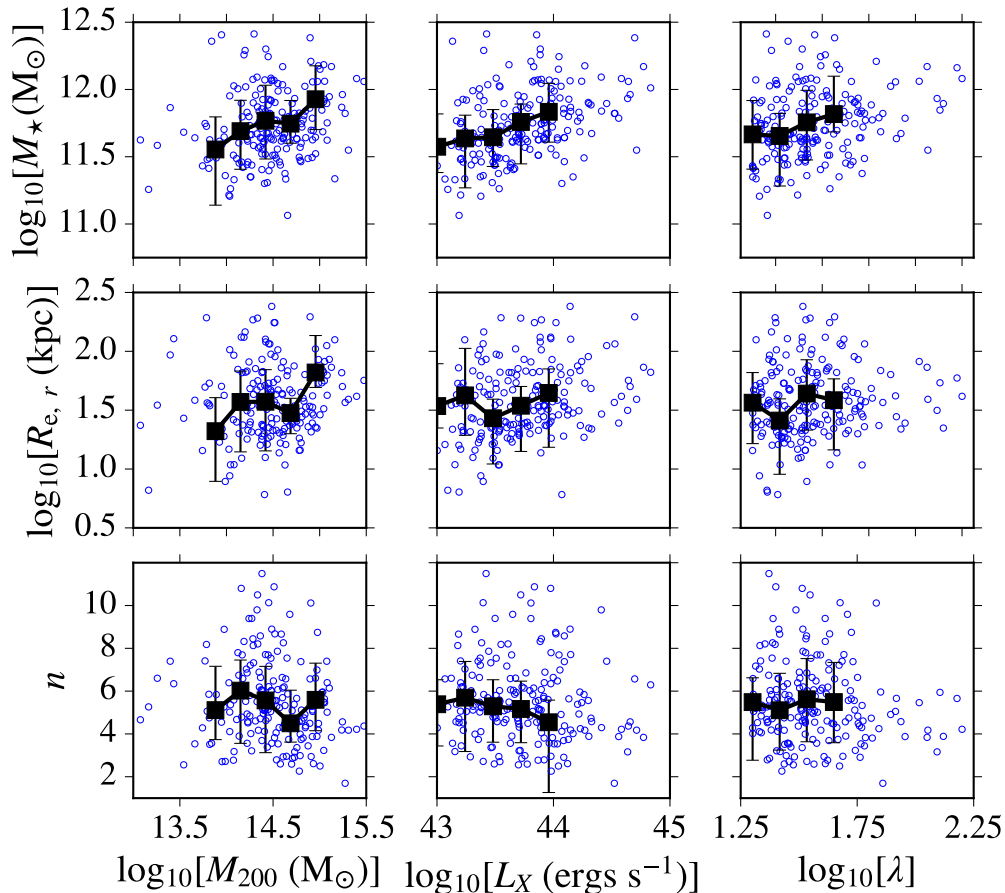


FIGURE 3.4: Correlations between the environmental parameters outlined in this study with BCG structural parameters and stellar mass. Binned medians are shown with $N \geq 15$ objects. The correlation between BCG mass and the properties of the host cluster appear more compelling than with the structural parameters, where we observe few significant correlations (see Table 3.1 and partial Spearman analysis).

which they classified morphologically as ‘cD’ types. The more massive and extended nature of BCGs in comparison to elliptical non-BCGs has been also found by numerous other studies for galaxies at $z \sim 1$ (von der Linden et al. 2007, Vulcani et al. 2014, Bernardi 2009), although some argue that, when matched in colour and mass, there are few differences between BCGs and their satellites (e.g. Guo et al. 2009). The morphological consistency of the BCGs in our sample is likely due to the fact that they all have early-type morphologies and are bulge-dominated (sample median $n = 5.26$, range ± 2.07 ; similar to the sample of Zhao et al. 2015b).

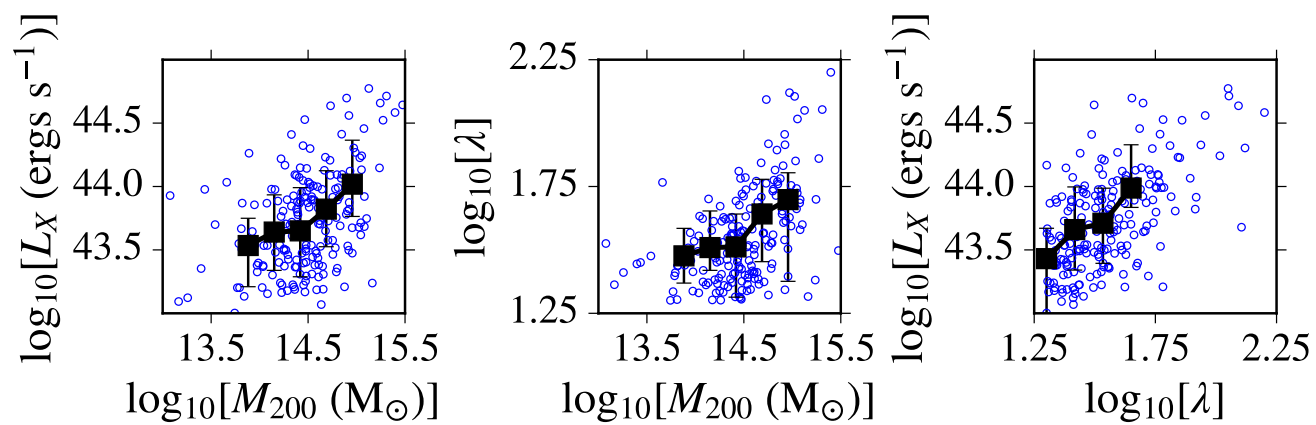


FIGURE 3.5: Correlations between characteristics of the host cluster (binned medians shown with $N \geq 15$ objects). The physical properties of clusters are highly correlated; hence the importance of accounting for selection.

Zhao et al. (2015a) found a similar result with their BCGs, in that they measured a correlation between BCG stellar mass and cluster dynamical mass with large scatter (Pearson rank coefficient = 0.17, see their paper for details). They provided arguments against the correlation being caused due to more massive haloes being populated by more massive BCGs simply by chance, due to the established dominance of BCGs (i.e. their comparably large size and high brightness) in comparison to the general population of cluster galaxies (e.g., von der Linden et al. 2007).

All three environmental parameters, although measured independently, suffer from some degeneracy (more massive haloes are generally more likely to be occupied by a larger number of galaxies and contain a larger amount of bound ICM, e.g., Mehrrens et al. 2016, White et al. 2011, Leauthaud et al. 2010); the relevant environmental correlations are shown for reference in figure 3.5. To address potential selection biases which may arise with redshift (e.g. figure 2.6), we test our correlations independently of redshift (Table A.7) to analyse the robustness of our results. When doing so, we find our correlations remain (albeit at reduced strength) for both X-ray luminosity ($r_s = 0.16$, $\log_{10}[p_s] = -1.61$) and cluster mass ($r_s = 0.14$, $\log_{10}[p_s] = -1.37$), but not for richness, which drops below significance ($r_s = 0.1$, $\log_{10}[p_s] = -0.8$). We discuss our interpretation of the lack of correlation with richness below.

As shown in figure 3.5, the X-ray luminosity of a cluster is clearly dependent on mass and is often used as a proxy for the former. However, depending on the dynamical state of the cluster, such measurements are prone to their own biases (e.g. Nagai et al. 2007). Relaxed, highly-evolved clusters have been found to be more likely to host an X-ray luminous cool core (see Section 1.2 in the Introduction) than clusters out of dynamical relaxation; indeed, the degree of offset of the BCG correlates inversely with the X-ray luminosity of a cluster (e.g. Sanderson et al. 2009, Stott et al. 2012). It would therefore follow that one of the drivers behind the strength of the $L_X - M_\star$ relation is the tendency of more massive BCGs to be located within clusters with a greater degree of dynamical relaxation and structural evolution, potentially where the degree of ‘dominance’ of the BCG is large (e.g., Jones et al. 2003). Of course, there are physical mechanisms that add further complications to this assumption; an increased abundance of radio-loud AGN have been found in BCGs residing in cool core clusters (e.g. Burns 1990, Crawford et al. 1999), the feedback from which are thought to be capable of heating the ICM (e.g. McNamara et al. 2014, Russell et al. 2014, Best et al. 2007).

There is, as previously mentioned in this chapter, little evidence for any independent environmental dependence on the scale sizes of our BCGs from mass. Although there is an apparent correlation with X-ray luminosity on effective radius ($r_s = 0.26711$, $\log_{10}[p_s] = -3.8404$), it entirely disappears at fixed stellar mass ($r_s = 0.028219$, $\log_{10}[p_s] = -0.1592$); suggesting that stellar mass rather than effective radius is the main driver behind the observed correlation. A similar conclusion was reached by [Zhao et al. \(2015a\)](#) who also found, after visually classifying their BCGs into E and cD types (‘bulge only’ versus ‘bulge+envelope’, see [Zhao et al. 2015b](#) for the classification method and [Morgan 1958, 1959](#) for details of the Yerkes classification scheme), that cD types constitute a significantly more massive and more extended population than E-types. [Zhao et al. \(2015a\)](#) also reported a weak environmental dependence on their visual morphologies, with cD-type BCGs generally inhabiting marginally more massive, denser haloes than E-type BCGs. A larger fraction of BCGs with cD-type haloes were found by [Brough et al. \(2005\)](#) to reside in more X-ray luminous clusters. We do not visually classify our BCGs due to the fact we are unlikely to possess the necessary photometric depth, so we cannot provide a direct comparison; nevertheless, it would be interesting to explore large epochs of cosmic history to determine if this morphological dependence holds at higher redshift. Next-generation surveys, such as the Large Synoptic Survey Telescope (LSST) which constitute both large volumes and deep photometry may be the key for solving such problems (e.g., [Ivezic et al. 2008](#)). We explore the ICL using deep Hyper Suprime Cam (HSC) data in Chapters 4 and 5 of this Thesis.

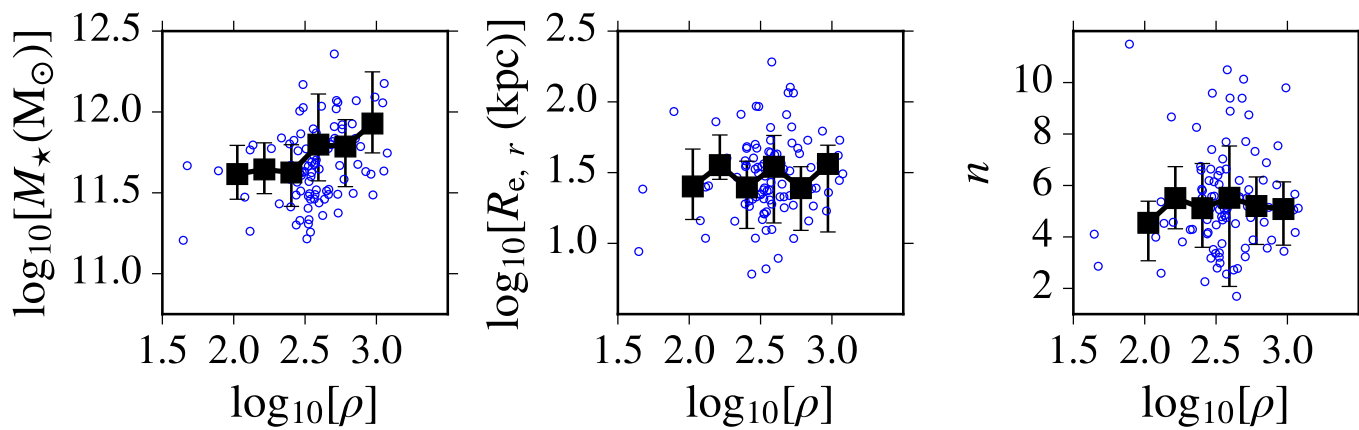


FIGURE 3.6: Correlations between luminosity-weighted environmental density, $\log_{10}[\rho]$, with BCG properties (binned medians shown with $N \geq 5$ objects) for 102 BCGs in common with the catalogues of [Tempel et al. \(2012\)](#). As before, there is a correlation with mass, but no correlation with the structural parameters.

As mentioned previously, cluster richness, of all the properties featured in this work, is the least significantly correlated with BCG properties, with no significant correlation with stellar mass present independently of redshift. This result may arise because richness represents a weaker means of quantifying environment, in that it is simply a proxy for the number of galaxies attributed to a cluster. A richness value provides minimal information about the nature of the cluster galaxies; the influence of several neighbours of comparable mass to a BCG would likely have a larger influence than an equal number of much smaller neighbours, nevertheless the richness estimators in each case would be equivalent (e.g. [Bautz & Morgan 1970](#) provided a basic classification scheme for galaxy clusters with this issue in mind). However, the richness values can be used to provide a robust measure of the total stellar mass of a cluster when coupled with abundance-matching, as demonstrated by [Old et al. \(2015\)](#).

Arguably, a more physically-motivated measure of environment for our purposes than richness would take overall luminosities of galaxies within a cluster into account; this point was also raised by [Zhao et al. \(2015b\)](#). Such a measure is shown in figure 3.6 using the luminosity-weighted environmental density maps of [Tempel et al. \(2012\)](#), smoothed on a scale of 1 Mpc h^{-1} . The environmental ‘density’, ρ , here refers to the luminosity density field of galaxies corrected for selection effects, computed via the methodology described in [Liivamägi et al. \(2012\)](#). The maps are derived from SDSS DR8 data and constitute the largest contiguous region of the SDSS footprint (<http://vizier.u-strasbg.fr/viz-bin/VizieR-3?-source=J/A%2bA/540/A106/dr8gal> for the galaxy properties catalogue used here); we matched the SPIDERS BCGs with galaxies in the catalogues within $3''$, finding 102 common objects which had a corresponding measurement of environmental density. Although we cannot provide a complete comparison as we lack coverage for the full sample of objects, the result appears promising.

In common with figure 3.4, there is a significant correlation between environmental density and BCG stellar mass ($r_s = 0.3233$, $\log_{10}[p_s] = -3.0128$), but no correlation between either effective radius or Sérsic index (Spearman rank correlation coefficients for n and R_e 0.1369 and 0.0117 respectively, with corresponding $\log_{10}[p_s]$ values of -0.6185 and -0.7701). Even after accounting for the strong L_X dependence through our partial Spearman analysis, the correlation between BCG mass and environmental density remains significant ($r_s = 0.2554$, $\log_{10}[p_s] = -2.0023$), as does the $L_X - M_*$ relation when controlling for environmental density ($r_s = 0.3150$, $\log_{10}[p_s] = -2.8811$). This

result suggests that our sample contains a significant fraction of clusters which are mature systems (i.e. self-contained, virialised), having accumulated the majority of their stellar component before $z \sim 0.3$.

3.2 Discussion

At fixed stellar mass, we do not measure any significant anti-correlation between redshift and scale size for our sample (Table A.5); this therefore suggests that there is little overall evolution in the scale size of our BCGs in the ~ 3.4 Gyr since $z = 0.3$. Due to the large number of rich, high-mass clusters in our sample compared with group-level systems, it is likely that many of the clusters in our sample are nearing maturity; this is reflected by the relatively homogeneous properties of the BCGs observed here. Our findings are consistent with [Stott et al. \(2011\)](#), who used a high- z X-ray selected cluster sample alongside a low-redshift comparison sample similar in redshift and cluster X-ray luminosity to the SPIDERS sample. It also appears that any environmental dependence on the size-stellar mass relation for BCGs is minimal for our sample at the redshift and halo mass range of this study (median $M_{200} = 1.4 \times 10^{14} M_{\odot}$). Stellar mass, over the environmental properties featured in this study, arises as the more important factor governing BCG morphology. [Guo et al. \(2009\)](#) reported a similar result in their work. They interpreted the lack of an obvious $n - M_{200}$ relation as indicating that there is no clear mass threshold above which a dark matter halo is capable of producing spheroidal centrals; a threshold which we do not determine due to the fact that we cannot rule out the influence of systematics from modelling (see Section 3.1.3). [Zhao et al. \(2015b\)](#) also found little environmental dependence on the structural parameters of BCGs up to $z \sim 0.1$ when their sample was not split by visual morphology.

Here, in common with [Guo et al. \(2009\)](#), our findings suggest a trend between $n - M_{\star}$; though in general, we make the simplifying assumption due to the higher peak redshift of our BCGs that they are single component objects, and therefore do not attempt to fit a bulge+disc. As we have demonstrated in our simulations in Section 2.6.1, $n = 1$, ‘disk-like’ profiles degenerate more rapidly than ‘bulge-like’, higher- n profiles, as well as an overall degradation in both with surface brightness. It would therefore, at the magnitude range of the BCGs in this study, be difficult to draw any meaningful conclusions from fitting a dual component profile (e.g. Sérsic+exponential) for any but the most luminous

galaxies in our study. As wide surveys with significantly deeper photometry become readily available over the next decade, they would be an ideal testbed at higher redshift to examine the observed dual-component nature of some BCGs seen at $z < 0.1$ (e.g. [Huang et al. 2017](#)), and, by extension, the build-up of the ICL.

It follows that, if the BCGs in our sample display little morphological dependence with environment, any influence of environment on their evolution must have been apparent at an earlier point in the assembly process. Due to the fact that our BCGs are more massive and extended than the general population of $n > 2.5$ elliptical galaxies (Section 3.1.2), the cluster potential well must have had some influence in the past on the formation of BCGs. For example, the work of [von der Linden et al. \(2007\)](#) found BCGs to have a higher dynamical-to-stellar mass ratio, indicating that they contained a larger fraction of dark matter compared to a sample of colour-matched non-BCG galaxies taken from the SDSS.

Various studies have predicted the growth in stellar mass of BCGs with a wide range of results, with some predicting BCGs doubling in size since $z \sim 0.3$ to others predicting size growth of less than 20% since $z \sim 1$ (e.g., [Bernardi 2009](#), [Vulcani et al. 2014](#), [Ascaso et al. 2011](#), [Stott et al. 2011](#)). The discrepancies lie not only in the method of measurement (e.g., single profile-modelling versus dual-profile modelling, to account for the stellar halo seen in BCGs), but also the method of sample selection; an early study, [Collins et al. \(2003\)](#), argued that the growth rates seen in X-ray luminous clusters are modest since $z \sim 1$, with larger rates present in clusters with low X-ray luminosities. The early build-up of stellar mass in BCGs (e.g., [Collins et al. 2009](#)) as well as observations of an established red sequence in clusters at $z > 1.5$ (e.g., [Cooke et al. 2016](#)) still present a challenge to simulations, some of which predict a large mass increase in BCGs between $0 < z < 1$ (e.g., [De Lucia & Blaizot 2007](#) predicted a fourfold increase during this timescale). An improved understanding of the formation of the ICL, such as the stripping of stars from central galaxies during the cluster assembly process, is therefore required to understand the ongoing discrepancies between simulations and observations of BCGs (e.g., [Burke et al. 2012](#)).

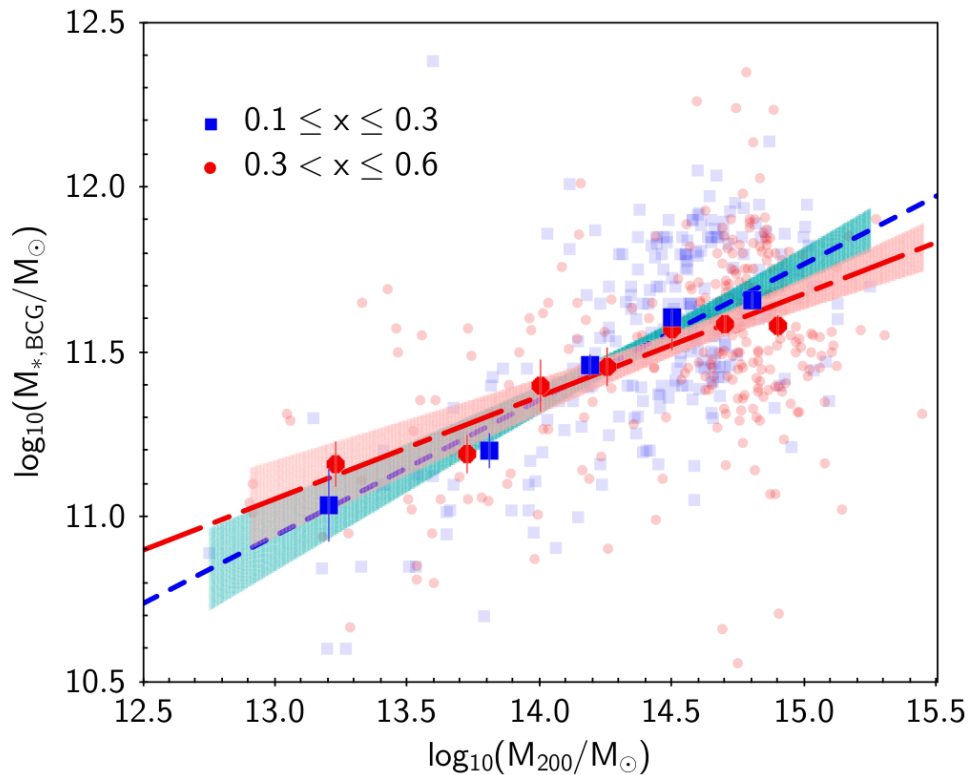


FIGURE 3.7: The $M_\star - M_{200}$ relation for BCGs in Erfanianfar et al., (in press). The solid points represent the medians of the data when binned; the transparent points represent the sample BCGs. The blue dashed and red dot-dashed lines represent the best-fitting power law relations for the low and high redshift bins respectively. There is a typo present in the key of this figure, in that x refers to redshift (z).

3.3 The SPIDERS BCG Value Added-Catalogue

As a result of our collaboration with SPIDERS, we were motivated to produce a large catalogue for public science use of BCG structural parameters. We therefore co-created the SDSS-DR14 ‘The Brightest Cluster Galaxies properties of SPIDERS X-ray galaxy clusters’ (*sic*) VAC (Erfanianfar et al., in press at the time of writing; <https://data.sdss.org/sas/dr14/eboss/spiders/analysis/SpidersXclusterBCGs-v2.0.fits>). Using a similar method to that described here, we provided 3 model fits (free Sérsic, Sérsic+Exponential and de Vaucouleurs) for all 416 BCGs contained within the catalogue, in 3 bands (g, r, i). The BCGs used in Furnell et al. (2018) exist predominantly as a subsample of this catalogue; this is because the selection criteria used in Furnell et al. (2018) are primarily visual and more stringent (see details in Erfanianfar et al., in press).

Our paper centred on the VAC sample predominantly focuses on understanding the $M_\star - M_{200}$ relation between BCGs and their host haloes; the scatter in the relation

provides powerful constraints on the growth of structure in the Universe (i.e. different choices of scatter in abundance matching models can lead to different HODs), and the ratio of the values establishes the star formation efficiency of the baryonic component of a cluster. We model the SEDs of our BCGs using the Le PHARE modelling software (Arnouts et al. 1999, Ilbert et al. 2006), combining SDSS photometry with GALEX photometry (e.g. Morrissey et al. 2007) in the UV and WISE in the infrared (Lang et al. 2016). The halo masses are hydrostatic masses, derived from CODEX data using the scaling relation of Leauthaud et al. (2010), and spectroscopic redshift values are taken from SPIDERS.

Figures 3.7 and 3.8 show the $M_\star - M_{200}$ and $M_\star/M_{200} - M_{200}$ relations respectively; as we combined the SPIDERS catalogue with other known cluster samples (AEGIS, XMM-XXL, COSMOS, XMM-CFHTLS and CDFS, see references within), this relation spans the largest range of halo masses to date ($10^{13} < M_{200} < M^{15.4} M_\odot$) from $0 < z < 0.6$. We find no strong evolution in the relation between M_\star and M_{200} , concluding that the growth of the central galaxy is dominated by the hierarchical growth of the host halo up until at least $z \sim 0.65$ (similar to SPIDERS at $z \sim 0.3$, see Section 3.1.2). We also find a slight evolution in the scatter in the relation with redshift (from 0.21 dex at $0 < z < 0.3$ to 0.25 dex at $0.3 < z < 0.65$) consistent with current predictions from hydrodynamical models (e.g. Yang et al. 2012, Moster et al. 2013), and a consistent $M_\star/M_{200} - M_{200}$ relation. We therefore suggest that the influence of feedback in massive BCGs could be responsible for the ‘decoupling’ of the BCG from the hierarchical growth of the host, which we are currently exploring using RASS-DeCALs data (Erfanianfar et al., in prep).

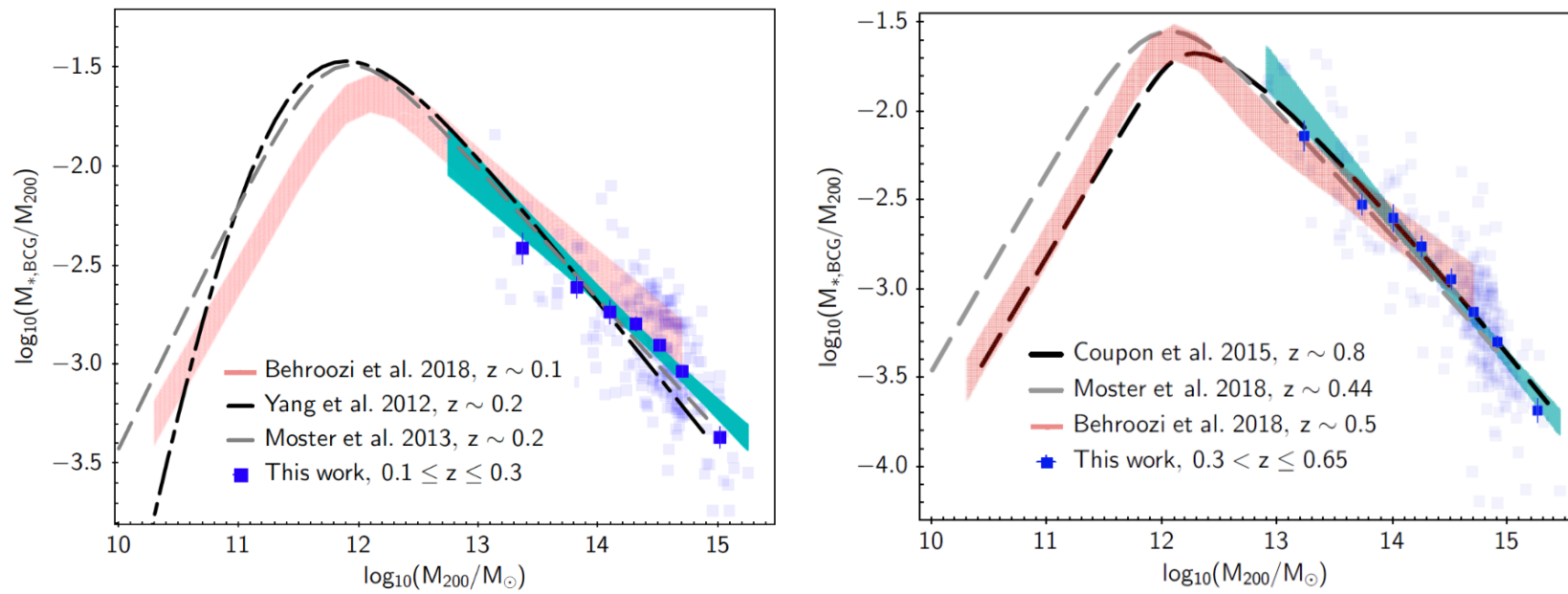


FIGURE 3.8: The stellar mass to halo mass ratio relation from Erfanianfar et al., (in press); as shown, there is good agreement with prior observations of this relation (Behroozi & Silk 2018) and current simulations (Yang et al. 2012, Moster et al. 2013).

3.4 Summary of Chapter

We used the 198/329 BCGs designated as our primary science sample from the X-ray selected SPIDERS clusters survey, and investigated their morphological parameters with respect to three cluster properties of interest: X-ray luminosity, richness and halo mass, the last property of which we estimated through cluster velocity dispersion. Finding the results of our best-fitting parameters to be generally consistent across bands, we derived stellar masses for our BCGs based on [Taylor et al. \(2011\)](#). We conclude the following:

1. There is a weak correlation between BCG mass and Sérsic index (mostly independent of the environmental parameters used here, and redshift; see Section [3.1.1](#)), inferring that more massive BCGs may tend towards having slightly more centrally-concentrated light profiles, e.g. in agreement with [Guo et al. \(2009\)](#) and [Durret et al. \(2019\)](#).
2. Significant correlations exist between the masses of our BCGs and all three of the cluster properties explored in this study (richness, cluster mass and X-ray luminosity), in agreement, for example, with [Guo et al. \(2009\)](#) and [Zhao et al. \(2015a\)](#). However, fixing for redshift dependence, we do not find any significant correlation with richness - indicating that it is likely to be less useful measure of environment in this context (see Section [3.1.3](#)).
3. There is no evidence that environment (L_X , M_{200} , λ ; Section [3.1.3](#)), at the redshift of our clusters, has any influence over the size-stellar mass relation of our BCGs (e.g. [Kelkar et al. 2015](#)), nor is there evidence for any correlation between the profile slopes of our BCGs and the cluster environment (e.g. [Stott et al. 2011](#)).
4. For a reduced sample of 102 BCGs, the environmental density is highly correlated with stellar mass (e.g. [Zhao et al. 2015a](#)), but no correlation is present with either structural parameter. A partial Spearman analysis reveals this correlation to be largely independent of X-ray luminosity (see Section [3.2](#)).

We find therefore that BCGs in rich, X-ray selected clusters appear to have no significant environmental dependence on their structures, independently of their mass, after $z \sim 0.3$. If the primary driver behind growth of BCGs is indeed through multiple mergers (e.g. [Ostriker & Tremaine 1975](#)), it is likely that within the M_{200} range of the clusters explored

here, the mass assembly has predominantly occurred at earlier times, with growth slowing due to the large dynamical friction timescales (τ_{dyn}) associated with massive clusters more commonly present at late times (where $\tau_{dyn} \propto \sigma^2$). We also find, using the VAC, very little redshift evolution in the slope of the BCG $M_\star - M_{200}$ relation, with our halo mass-dependent star-formation efficiency relation for BCGs being consistent with results from recent simulations (see Section 3.3). Our work supports the scenario of the homogeneity presented by BCGs in massive clusters up to intermediate redshifts (e.g. [Collins & Mann 1998](#), [Collins et al. 2009](#), [Whiley et al. 2008](#), [Stott et al. 2011](#)).

The full catalogue of objects used in Chapters 2 and 3 is published electronically (<https://academic.oup.com/mnras/article/478/4/4952/4980953#supplementary-data>); a description of catalogue parameters can be found in [Furnell et al. \(2018\)](#).

Chapter 4

Part II - The ICL in XCS-HSC: Data and Systematics

4.1 Overview of Contents

In this chapter, we introduce our investigation into intracluster light, primarily with a focus on the challenging systematics behind ICL observations. We describe the Hyper Suprime-Cam Subaru Strategic Program (HSC-SSP) and the XMM-Cluster Survey (XCS), alongside our catalogue matching and sample selection methodology. We discuss the systematics behind ICL measurement, describing the HSC pipeline in this context. We outline our threshold-based method of measuring ICL, and how we estimate a $\mu_B = 25$ mag/arcsec² threshold at the rest frame of each cluster. We also cover our contaminant source masking and weighting methods, and outline our methods of estimating both cluster mass $M_{X,500}$ and cluster radius $R_{X,500}$. We then introduce the divot problem, and our use of software developed by Kelvin et al., (in prep) to provide a post-processing correction. Finally, we discuss the results from a suite of simulated ICL-like objects in representative control frames, to understand the level of background contamination at a given surface brightness.

This chapter primarily addresses motivation 3: “How do conventional image-processing methods affect the recovery of ICL?”, referenced in Section 1.5.

4.2 Hyper Suprime-Cam Subaru Strategic Program

4.2.1 Survey Description

In this work, we make use of optical imaging data from the first release of the Hyper Suprime-Cam Subaru Strategic Program (HSC-SSP, e.g. [Aihara et al. 2018](#)); one of the deepest public ground-based optical surveys available (see [Table 4.1](#)). The HSC instrument is a wide-field (1.8 deg^2) imaging camera on the 8.2m Subaru telescope atop Mauna Kea, Hawaii. In total, the survey is scheduled for a run of 300 nights over the course of six years, covering three imaging depths in total: ‘Wide’, ‘Deep’ and ‘Ultra-Deep’ in 5 Sloan-like passbands (*grizy*). In this work, we use imaging from the ‘Deep’ subset; a summary table of the average 5σ limiting depths has been included for reference for the available runs and broad bands ([Table 4.1](#)). The survey footprint overlaps with numerous other surveys, such as the general Sloan footprint and its associated surveys (e.g. [York et al. 2000](#)), Pan-STARRS (e.g. [Chambers et al. 2016](#)), COSMOS (e.g. [Scoville et al. 2007](#)) and DEEP-2 (e.g. [Newman et al. 2013a](#)). The imaging depth of HSC far exceeds that of any current public surveys (e.g. KiDS, [de Jong et al. 2013](#); DES, [The Dark Energy Survey Collaboration 2005](#)), with the exception of the Hubble Frontier Fields (HFF, [Lotz et al. 2017](#)). Current estimates of Deep/Ultra Deep HSC image quality are comparable to those anticipated by the upcoming LSST survey ($r \sim 27.5$ Large Synoptic Survey Telescope, see [Ivezic et al. 2008](#), also [Section 4.2.2](#) for further comments on data reduction).

4.2.2 Data Reduction

For the DR1 release, the HSC-SSP data products have undergone processing through the HSC pipeline prior to download, an adapted version of the so-called ‘LSST Data Management (DM) software stack’ in preparation for LSST data products in the coming decade (first light 2020, see [Jurić et al. 2015](#) for description of the LSST DM stack). The full implementation for HSC is detailed in [Bosch et al. \(2018\)](#) (including a flow diagram of the complete process, see their figure 1) but we include an abridged version here to provide context. The pipeline software itself is open source and licensed for public use under the GNU public license (version 3). The photometric performance of the pipeline on mock objects is described in detail in [Huang et al. \(2018\)](#), who demonstrate

TABLE 4.1: A summary table of the average limiting depths for the HSC-SSP survey. In this work, we use the ‘Deep’ layer in the i band.

Layer	Filter	Lim. mag. (5σ , $2''$)
Wide	g, r	26.5, 26.1
Wide	i	25.9
Wide	z, y	25.1, 24.4
Deep	g, r	27.5, 27.1
Deep	i	26.8
Deep	z	26.3
Deep	y	25.3
Ultra Deep	g, r	28.1, 27.7
Ultra Deep	i	27.4
Ultra Deep	z, y	26.8, 26.3

a strong recovery in input versus output flux even for de Vaucouleurs-like objects (on average $\sim 85\%$ at $m_i = 25$). They acknowledge, however, that the HSC pipeline tends to over-subtract flux around extended, bright objects (which they explore further when studying the faint haloes of elliptical-type galaxies in [Huang et al. 2017](#)). We discuss this issue, along with a proposition of a post-processing ‘fix’, in Section 4.5.4.

In simplified terms, much of the HSC pipeline is built on algorithms and concepts originating from the SDSS *photo* pipeline (see [Lupton et al. 2001](#)), the pipeline which produces the data products for all SDSS data releases. Raw data and coadds can be queried online on the HSC-SSP DR1 release site; alternatively, there are reduced data products (e.g. photometry, best-fit models, photo- z estimates) available which can be downloaded via SQL query.

The HSC pipeline operates in several stages to produce the final scientific data products. The process (with relevant details) is roughly as follows:

1. **CCD processing:** the raw data from each CCD is taken, and basic data corrections and calibrations are applied. Firstly, an Instrument Signature Removal (ISR) is applied, which embodies basic reduction (i.e. flat, bias and dark corrections), brighter-fatter corrections (for source intensity dependence on the measured PSF), corrections for crosstalk and corrections for CCD non-linearity (e.g. [Krick & Bernstein 2007](#) for context as to how this applies to ICL). Pixels flagged as bad or saturated are then detected and masked; with cosmic rays removed at a later stage with the use of the estimated field PSF. The sky is estimated for each image

and subtracted using a variance-weighted 6th order Chebyshev polynomial sampled over 128×128 $3\text{-}\sigma$ clipped average pixel values.

In summary, this stage produces two main data products: calibrated exposure data (i.e. datacubes which contain: a background subtracted, calibrated image; a mask frame containing source detections, pixel flags and star masks; a variance frame, essentially a ‘weight map’ describing the pixel-by-pixel variance of the coadded images) and a ‘source catalogue’, namely a database of detected objects with photometric information as measured by the pipeline.

2. **Joint calibration:** when all CCDs have been processed, their astrometric and photometric calibrations are refined by requiring consistent positional and flux values of sources on repeat visits where they may appear on different regions of the focal plane. This is carried out by matching all overlapping point sources from the raw CCD source catalogues in a given band and ‘tract’ ($\sim 1.5^\circ$ sky regions of HSC observations). The astrometry and photometry are then re-fit with all available information, with the astrometric fit being carried out first.
3. **Image coaddition:** the individual CCD exposures are then coadded to improve the imaging depth. As is widely known in astronomical surveys, co-addition can lead to complications, such as causing data degradation or introduction of systematic errors. Efforts have been made during the HSC pipeline’s construction to avoid these issues wherever possible; as stressed by [Bosch et al. \(2018\)](#), the pipeline is still actively undergoing refinement.
4. **Coadd processing:** after creating the coadds, the pipeline carries out another round of image processing. Objects on the coadds are detected, deblended and measured, creating a catalogue of final object measurements. A final background is then subtracted for each sky ‘patch’ via an average from a $4\text{k} \times 4\text{k}$ bin.

4.3 The XMM Cluster Survey

The XMM Cluster Survey ([Romer et al. 2001](#)) is an all-sky serendipitous search for galaxy clusters using legacy X-ray data from the XMM-Newton space telescope (e.g. [Jansen et al. 2001](#)). The first XCS data release in 2012 ([Mehrtens et al. 2012](#)) contained X-ray and optical confirmations for 503 galaxy clusters, a third of which were entirely

new to the literature. The second XCS public data release (Manolopoulou et al., in collaborative review) increases the number of clusters detected in XCS to ~ 1300 ; overlap with this master catalogue in HSC forms the basis of the sample we use in this work (see Section 2.3). Due to the considerably less biased means of cluster selection in X-rays than optical surveys (see discussion in Introduction) coupled with high angular resolution X-ray imaging ($4.1''$), XCS data is ideal for constructing a representative cluster sample.

At the time of writing, XCS uses a combination approach in order to confirm X-ray detections as true galaxy clusters. Using the XMM Automated Pipeline Algorithm (XAPA, see use in [Mehrtens et al. 2012](#)), X-ray detections are separated into ‘extended’ and ‘point-like’ by comparing the source count distribution in a fitted ellipse similar in extent to the XMM PSF. However, these classifications are not always reliable; for example, clusters may have multiple X-ray peaks, particularly bright sources may have bleed trails (which are often mistaken for extended emission) and AGN which have been misclassified as clusters may all contribute to contamination. Therefore, cluster selection is further refined through the ‘XCS Zoo’; a Zooniverse project open to participation from members of the XCS collaboration (www.zooniverse.org, see [Lintott et al. 2008](#) for details of the prior ‘Galaxy Zoo’ project based on the same principle).

Through the XCS Zoo, participants are able to view images of extended detections in XCS (see Manolopoulou et al., in collaborative review; a subset of experienced participants also classify point-like sources separately): namely the X-ray image (with XAPA detection ellipses), an optical image (in the case of our catalogue, SDSS DR13, but imaging data from other surveys is also being explored, e.g. DES, [Vegeer et al., in prep](#)) and another optical image with overlaid X-ray contours. A ‘classifier’ is provided by the user to indicate the reliability of the detection, the criteria of which are as follows:

- A cluster (1) - a significant overdensity of galaxies associated with an X-ray extended source,
- A ‘possible’ cluster (2) - a moderate overdensity of galaxies associated with an X-ray extended source,
- An object which cannot be confirmed as a cluster, but cannot be ruled conclusively as a contaminant (3),
- An object which is clearly a contaminant (4).

The object’s mean float classifier value (i.e. $1 = 1.0$ and so on) then represents a ‘point score’ indicating the overall consensus on the Zoo participants’ reliability of the object. To be included in the master list, XCS requires at least three classifications by participants, of which the mean classification value must be less than 2.5. If the object in question had a mean classification from 2.0-2.5, it was considered on a case-by-case basis. As an additional check, a small subsample of clusters with significantly deeper optical imaging in the Hyper Suprime-Cam SSP DR1 footprint (see Section 4.2) were put through the XCS Zoo, with comparable classifier results (see figure 10 of Manolopoulou et al., in collaborative review).

In the case of the XCS-DR2 release used in this work (Manolopoulou et al., in collaborative review), XCS detections were cross-matched for spectroscopy with the SDSS DR13, VIPERS PDR2 and DEEP2 surveys (Albareti et al. 2017; Guzzo et al. 2014 and Newman et al. 2013a respectively). Spectroscopic redshifts are assigned to each cluster through application of a biweight location estimator (see Beers et al. 1990) using all galaxies falling within 1.5 arcminutes of the XCS centroid from XAPA; this redshift centroid is then re-calculated after applying a clip of $\Delta v \pm 3000 \text{ kms}^{-1}$ about the initial redshift, within a radius of 1.5 Mpc projected distance from the XAPA centroid (see method described in Hilton et al. 2018).

4.4 Sample Selection

To create our sample of clusters, we cross-matched the XCS-DR2 North (Manolopoulou et al., in prep.) master source list with the entire HSC-SSP DR1 footprint region (Wide, Deep and Ultra-Deep). This produced an initial match of 202 common sources. We required, for robustness, for there to be an available spectroscopic redshift for both the assigned BCG and for the cluster itself; 79 objects met this criterion. The BCGs in this work are assigned through the GMPHoRCC algorithm of Hood & Mann (2017) and then eyeballed individually; here, no reassignments were necessary.

The BCG and red sequence spectroscopic redshifts are then compared - if they deviated significantly from one another beyond a specified velocity space limit ($\Delta v > \pm 5000 \text{ kms}^{-1}$), these objects were discarded (8 objects, leaving 71). We then required that each cluster had X-ray source parameter measurements (e.g. $L_{X,500}$, $T_{X,500}$) from XAPA (53 objects).

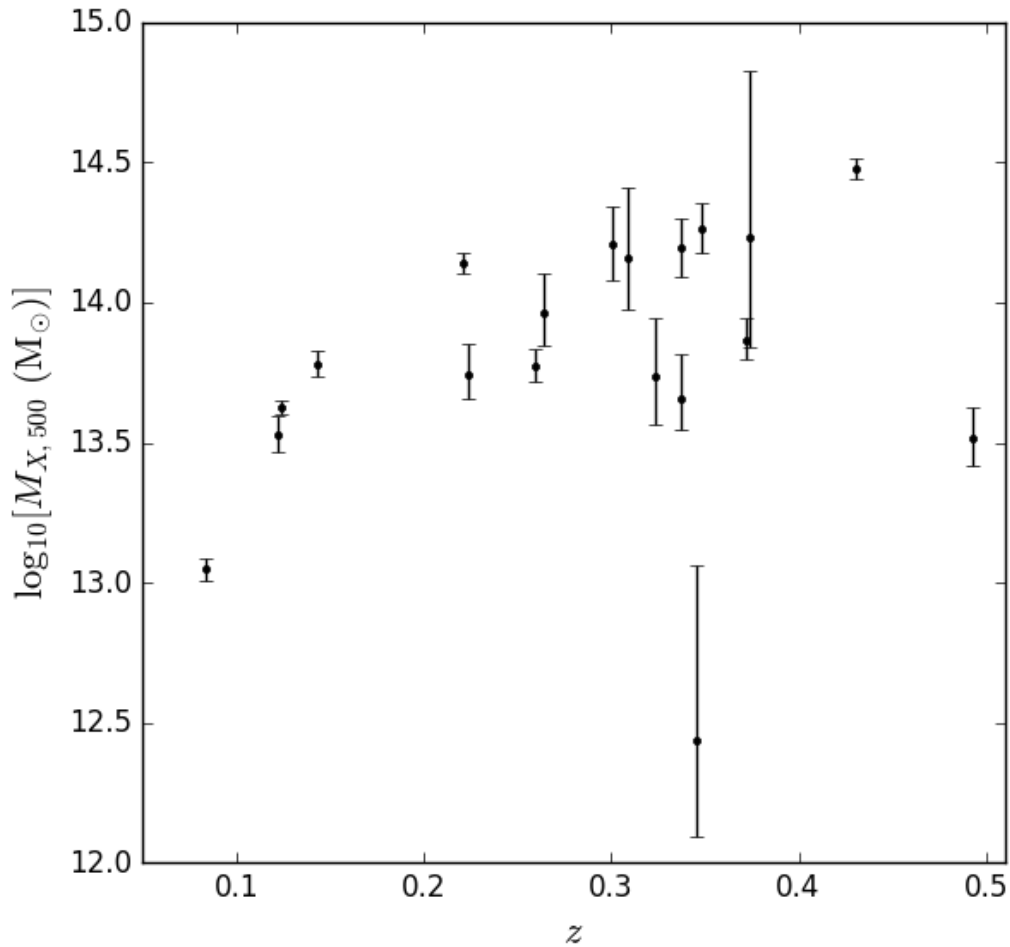


FIGURE 4.1: The $M_{X,500} - z$ relation for the clusters used in this work (see text for details). The redshifts are spectroscopic, with errors $\Delta z \sim 10^{-5}$

Finally, to ensure the depth of our images were approximately consistent, we selected only sources which lay within the HSC-SSP Deep footprint (30 objects).

Image data for each of the fields were then “quarried” (see Section 4.2) using a field size equivalent to 1.5×1.5 Mpc at the spectroscopic redshift of the cluster. These were checked against the $R_{X,500}$ values (see Section 4.5.1) to ensure that the field size encompassed the size of the cluster as estimated by X-rays (see Chapter 2 for further discussion). The quality of the individual fields were checked at this stage, with 7 being discarded due to bright foreground source contamination, or being at the edge of a field. The 7 clusters with rejected image data are shown in figure 4.2. Another 4 clusters were also rejected a posteriori, as they were agreed by the collaboration to be poor candidates. Our final sample therefore consists of 19 clusters (see figure 4.10); the corresponding

$M_{X,500} - z$ relation (see Section 4.5.1) can be seen in figure 4.1. The clusters span a wide range in both redshift ($0.06 < z < 0.5$) and halo mass ($10^{12.5} < M_{X,500} < 10^{14.5}$).

TABLE 4.2: The main parameters of the 19 XCS-HSC clusters used in this work. The BCG rest-frame i -band absolute magnitudes (M_i) are derived from aperture values as described in Section 4.5.2. The relative errors are derived using the HSC variance maps and are typically quite small ($\Delta M_i < 0.01$ mag).

XCS ID	α_{2000}	δ_{2000}	z	M_i	$T_{X,500}$ (keV)	$R_{X,500}$ (Mpc)	$M_{X,500}$ ($10^{14} \times M_{\odot}$)
XMMXCS J022456.1-050802.0	36.234	-5.134	0.0840	-23.023	0.648 ± 0.034	0.331 ± 0.010	0.112 ± 0.010
XMMXCS J161039.2+540604.0	242.664	+54.101	0.339	-23.718	$1.595 \pm^{+0.373}_{-0.227}$	$0.483 \pm^{+0.041}_{-0.062}$	$0.457 \pm^{+0.198}_{-0.105}$
XMMXCS J233137.8+000735.0	352.908	+0.126	0.224	-23.690	$1.719 \pm^{+0.269}_{-0.184}$	$0.537 \pm^{+0.033}_{-0.046}$	$0.553 \pm^{+0.156}_{-0.071}$
XMMXCS J232923.6-004854.7	352.348	-0.815	0.300	-23.882	$3.292 \pm^{+0.677}_{-0.524}$	$0.746 \pm^{+0.070}_{-0.084}$	$1.611 \pm^{+0.608}_{-0.413}$
XMMXCS J161134.1+541640.5	242.892	+54.278	0.337	-24.009	$3.278 \pm^{+0.511}_{-0.429}$	$0.729 \pm^{+0.056}_{-0.063}$	$1.567 \pm^{+0.441}_{-0.334}$
XMMXCS J095902.7+025544.9	149.761	+2.929	0.349	-23.534	$3.609 \pm^{+0.472}_{-0.400}$	$0.765 \pm^{+0.050}_{-0.056}$	$1.836 \pm^{+0.429}_{-0.335}$
XMMXCS J095901.2+024740.4	149.755	+2.794	0.501	-23.587	$1.385 \pm^{+0.223}_{-0.167}$	$0.406 \pm^{+0.029}_{-0.036}$	$0.327 \pm^{+0.095}_{-0.064}$
XMMXCS J100141.6+022538.8	150.424	+2.427	0.124	-23.752	$1.427 \pm^{+0.049}_{-0.045}$	0.509 ± 0.010	$0.424 \pm^{+0.025}_{-0.022}$
XMMXCS J095737.1+023428.9	149.405	+2.575	0.373	-24.652	$3.500 \pm^{+4.291}_{-1.443}$	$0.741 \pm^{+0.194}_{-0.423}$	$1.716 \pm^{+5.027}_{-1.025}$
XMMXCS J022156.8-054521.9	35.487	-5.756	0.259	-23.619	$1.814 \pm^{+0.157}_{-0.129}$	$0.544 \pm^{+0.022}_{-0.026}$	$0.595 \pm^{+0.091}_{-0.071}$
XMMXCS J022148.1-034608.0	35.450	-3.769	0.432	-23.963	$4.949 \pm^{+0.278}_{-0.245}$	$0.873 \pm^{+0.025}_{-0.028}$	$3.001 \pm^{+0.294}_{-0.250}$
XMMXCS J022634.8-040409.2	36.645	-4.069	0.346	-23.887	$0.310 \pm^{+0.408}_{-0.115}$	$0.189 \pm^{+0.044}_{-0.120}$	$0.028 \pm^{+0.088}_{-0.015}$
XMMXCS J022530.8-041421.1	36.378	-4.239	0.143	-23.294	$1.761 \pm^{+0.122}_{-0.103}$	$0.568 \pm^{+0.019}_{-0.022}$	$0.602 \pm^{+0.073}_{-0.059}$
XMMXCS J100047.3+013927.8	150.197	+1.658	0.221	-23.710	$2.933 \pm^{+0.143}_{-0.137}$	$0.730 \pm^{+0.019}_{-0.020}$	$1.382 \pm^{+0.117}_{-0.108}$
XMMXCS J022726.5-043207.1	36.861	-4.535	0.308	-23.662	$3.090 \pm^{+1.273}_{-0.677}$	$0.716 \pm^{+0.100}_{-0.160}$	$1.438 \pm^{+1.156}_{-0.496}$
XMMXCS J022524.8-044043.4	36.353	-4.679	0.264	-23.244	$2.339 \pm^{+0.492}_{-0.343}$	$0.626 \pm^{+0.054}_{-0.072}$	$0.917 \pm^{+0.354}_{-0.218}$
XMMXCS J095951.2+014045.8	149.963	+1.679	0.372	-24.057	$2.128 \pm^{+0.238}_{-0.192}$	$0.557 \pm^{+0.029}_{-0.035}$	$0.734 \pm^{+0.146}_{-0.110}$
XMMXCS J022401.9-050528.4	36.008	-5.091	0.324	-23.206	$1.759 \pm^{+0.576}_{-0.364}$	$0.515 \pm^{+0.064}_{-0.090}$	$0.544 \pm^{+0.339}_{-0.178}$
XMMXCS J095924.7+014614.1	149.853	+1.770	0.124	-22.717	$1.252 \pm^{+0.113}_{-0.098}$	$0.472 \pm^{+0.022}_{-0.024}$	$0.339 \pm^{+0.054}_{-0.044}$

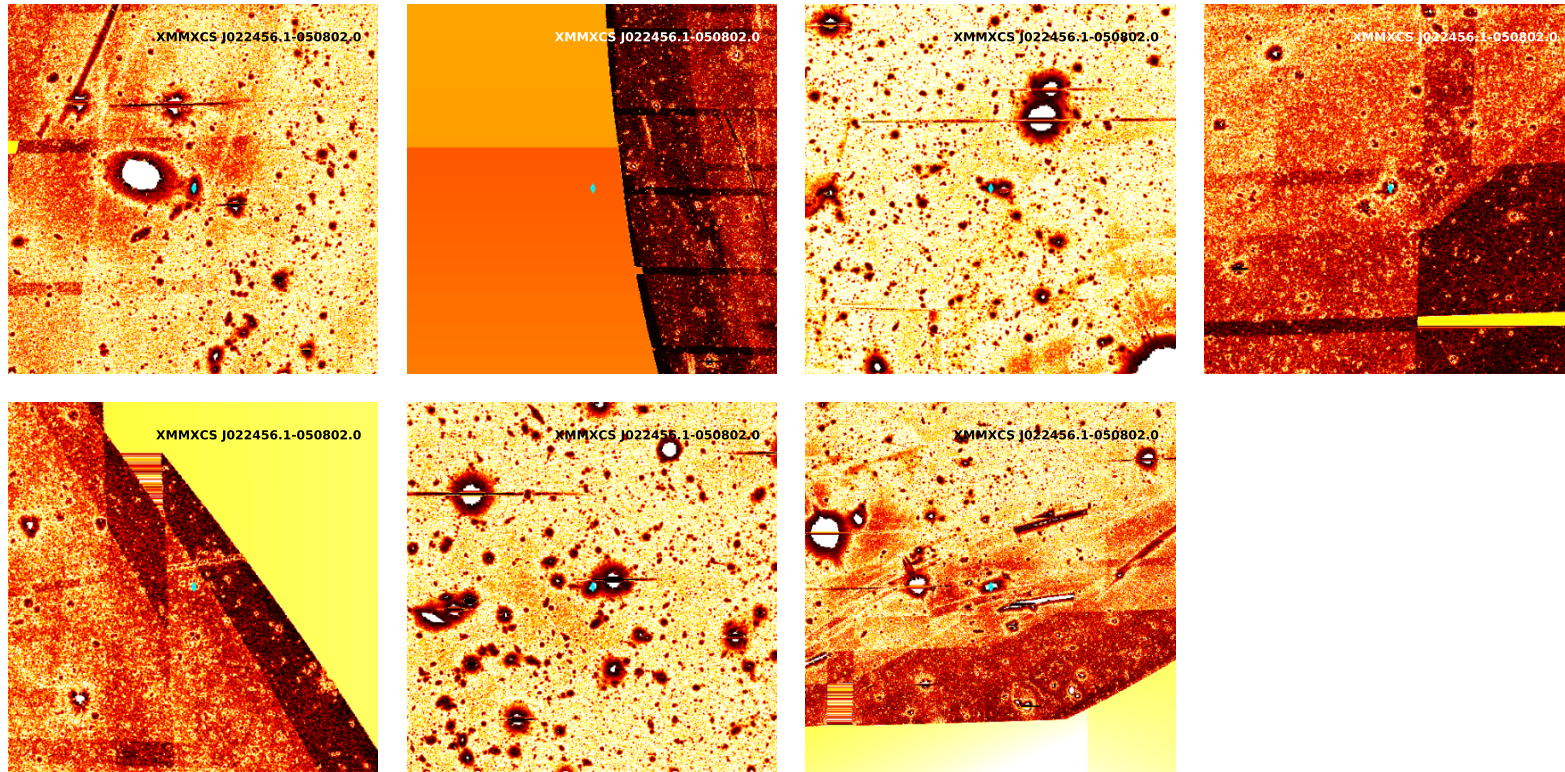


FIGURE 4.2: The 7 clusters (1.5×1.5 Mpc on each frame) omitted from the sample due to poor photometry or bright source contamination. BCGs, if present on the frame, are marked with cyan diamonds. The images have been log-scaled and Gaussian-smoothed to show structure.

4.5 Analysis

4.5.1 Quantifying ICL

Observationally, past studies have generally taken two approaches when quantifying the amount of ICL present in a cluster (see also discussion in Section 1.4.2 in the Introduction): a parametric approach using model fitting (e.g. [Gonzalez et al. 2005, 2007, 2013](#); [Morishita et al. 2017](#)), or by summing up the contribution of ICL below a set (usually isophotal) limit while masking out the BCG and any satellites (e.g. [Burke et al. 2012, 2015](#); [Krick & Bernstein 2005, 2007](#); [Montes & Trujillo 2018](#)). Other approaches looking at either the shape of the BCG+ICL profile (see Chapter 5) or the so-called ‘colour profile’ (see comments in Section 1.4.2) have also measured the relative flux in isophotes or annuli to acquire a 1-D profile (e.g. [Zhang et al. 2019](#); [DeMaio et al. 2018](#); [Burke et al. 2012](#)).

As per our masking methodology outlined in Section 4.5.3, we take an isophotal approach to measuring the ICL in our clusters, which we do for two reasons: simplicity, and to keep our assumptions minimal. When modelling a profile, one must determine a priori; as well as this, exactly the best model to use when describing the BCG+ICL profile varies enormously across studies, with some recommending a double de Vaucouleurs profile (e.g. [Krick & Bernstein 2007](#)), some using a Sérsic+Exponential (e.g. [Lauer et al. 2007](#)) and others still more complicated models (e.g. [Zhang et al. 2019](#)). Choosing the wrong profile can lead to large uncertainties (e.g. [Zhao et al. 2015b](#)); moreover, the degeneracies present when using multiple component fits mean that one cannot readily disentangle individual flux contributions without dynamical information (e.g. [Dolag et al. 2010](#)). While the approach of using a surface brightness limit has limitations (and often leads, according to [Rudick et al. 2011](#), to a lower ICL contribution as opposed to dynamically separating the ICL with the available kinematic information), it is at least model independent. Here, we choose a limit of $\mu_B = 25 \text{ mag/arcsec}^2$ in the rest frame B -band, similar to [Burke et al. \(2015\)](#); we discuss our methodology in Section 4.5.3.

From the X-ray measurements, we estimate $R_{X,500}$ and $M_{X,500}$ using the X-ray temperatures of the remaining clusters in our sample. The $R_{X,500}$ values act as a proxy for the cluster radius and are used as physically-motivated aperture sizes for measuring ICL; $R_{X,500}$ also has the benefit of lower levels of contamination from the background

compared with larger cluster radii (e.g. R_{200}). We do, however, recognise that there is a significant caveat with this method, in that we are assuming the BCG to be a proxy for the centre of the cluster. While this is generally a reasonable assumption at low redshift (e.g. [Lin & Mohr 2004](#)), at higher redshift, there are an increasing number of clusters out of dynamical relaxation (e.g. [Hatch et al. 2011](#)) with multiple BCG candidates. We refer the reader to Section 6.2 in Chapter 6, where we discuss other methodologies.

Both $R_{X,500}$ and $M_{X,500}$ are computed via the scaling relations of [Arnaud et al. \(2005\)](#), modelled as a power laws:

$$E(z)R_{X,500} = 1.104 \left[\frac{kT}{5 \text{ keV}} \right]^{0.57} \text{ Mpc} , \quad (4.1)$$

$$E(z)M_{X,500} = 3.84 \times 10^{14} \left[\frac{kT}{5 \text{ keV}} \right]^{1.71} \text{ M}_{\odot} , \quad (4.2)$$

where $T_{X,500}$ is the X-ray temperature (K) and $E(z)$ here is:

$$E(z) = [\Omega_M(1+z)^3 + \Omega_{\Lambda}]^{-1/2} , \quad (4.3)$$

where z is the cluster redshift and Ω_M and Ω_{Λ} are our concordance cosmology values. The range of $R_{X,500}$ and $M_{X,500}$ values for our clusters are summarised in Table 4.2.

After applying a mask (which includes an isophotal threshold), we sum the weighted flux within an aperture of R_{500} centred on the cluster BCG, and repeat the process without an isophotal limit (Section 4.5.3). We also provide comparisons at the equivalent surface brightness levels of 24 and 26 mag/arcsec² respectively to get a flavour of the effect of changing the selected surface brightness of which to define excess light as ICL. ICL measurement errors, $E(\text{ICL})$, are computed directly from the image variances as follows:

$$E(\text{ICL}) = \sqrt{\left(\frac{\sigma_{\text{ICL}}}{f_{\text{tot}}} \right)^2 + \left(\frac{f_{\text{ICL}} \times \sigma_{\text{tot}}}{f_{\text{tot}}^2} \right)^2} , \quad (4.4)$$

where the subscripts ICL and *tot* refer to the ICL and total flux respectively, f is the flux in counts and σ denotes the standard deviation.

4.5.2 BCG Photometry

We apply three methods of quantifying the flux contribution from our cluster BCGs: total flux within a 50 kpc aperture (e.g. [Whiley et al. 2008](#)) or two parametric models: a single, free Sérsic fit, or a de Vaucouleurs model with a fixed Sérsic index of 4. We choose a 50kpc aperture primarily as other authors have found that this radius corresponds approximately to the region where there is an excess of light in BCGs compared with a de Vaucouleurs profile (e.g. [Presotto et al. 2014](#); see also Section 4.6). As mentioned in Chapter 2, we prefer, given the nature of our data, to take a simplistic approach over attempting to fit multiple components here; we provide the models primarily to give a direct comparison to basic aperture photometry. We take a similar approach as in our previous work in this respect ([Furnell et al. 2018](#)), where we assessed the performance of the pipeline for SDSS data. There are numerous arguments as to the best model to fit; most notably, a two-component model which includes the addition of an exponential halo to a Sérsic profile (e.g. [Donzelli et al. 2011](#); [Zhao et al. 2015b](#); [Bernardi et al. 2013](#)). However, we take the approach in this work that disentangling the BCG from the ICL is non-trivial to achieve, given how much they are closely linked in terms of evolutionary history (e.g. [Burke et al. 2012](#)), so include parametric model fits primarily as a comparative measure. For our results, due to them being non-parametric, we use the aperture values to represent our BCG fluxes.

We model our galaxies using the SIGMA pipeline (Structural Investigation of Galaxies via Model Analysis, see [Kelvin et al. 2012](#)), using a similar implementation as in [Furnell et al. \(2018\)](#). SIGMA is a software wrapper written in R that performs a full model fit of a given object using GALFIT 3 (see [Peng et al. 2010](#)), including an estimate of the field PSF using PSFEx (see [Bertin 2013](#)). The weight maps used in this procedure are those generated by the HSC pipeline. We produce models for our objects pre- and post-divot correction (see Section 4.5.4), and use the post-divot corrected models because of the correction to the profile wings of our objects. Generally, the output parameters are similar in both cases (see figure 4.3), and do not show any obvious biases.

It is important to mention that we do not use the PSFs generated by SIGMA when masking of stars on our images (e.g. to estimate the contamination extent); rather, their sole use is to provide a sufficiently well-approximated model for our BCG model fits. This is primarily because the PSFs generated by SIGMA are not estimated out to large enough

radii to account for the wings of the brightest stars on our frames ($\sim 0.2'$). PSFEx is not optimised for the purposes of producing extended PSFs; indeed, using PSFs with a small angular extent both for the purpose of masking and removal of wings from point source contamination represent two of the most commonly-cited issues regarding the robustness of LSB photometric studies (e.g. [Duc et al. 2015](#), in the context of deep ATLAS-3D survey data). For a more detailed description of the masking process, see Section [4.5.3](#).

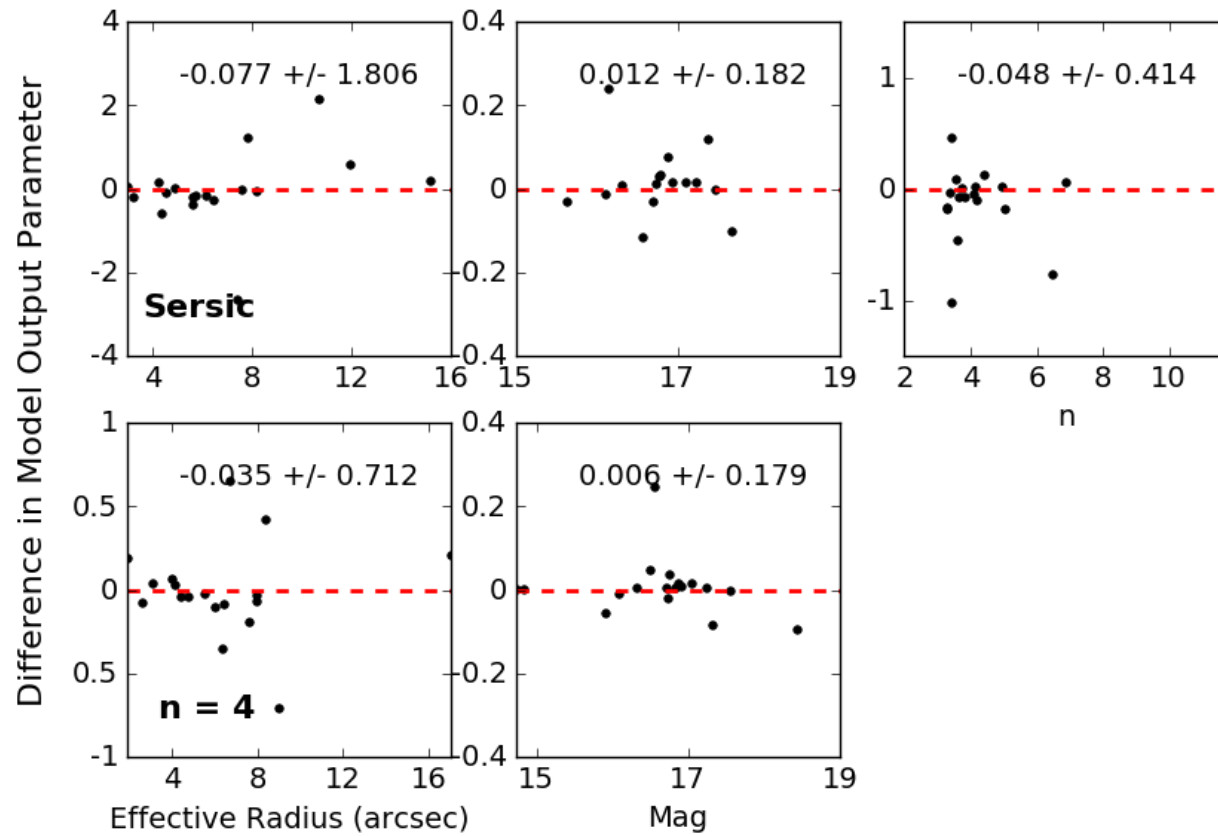


FIGURE 4.3: Differential comparison between the input and output parameters for the cluster BCGs in this sample, with and without an added divot correction. The value at the top of each frame represents the median deviation and rms respectively; the top and bottom panels represent the outputs for a free Sérsic profile and a de Vaucouleurs profile respectively.

We show a histogram of the light contributions for our BCGs (divot corrections included, see 4.5.4 and upcoming Section 4.5.1) to the overall cluster in figure 4.4. In most cases, the three values agree within a few percent, with the aperture values generally yielding slightly lower values due to there being no wing extrapolation (see discussion in Chapter 3). There are, however, a few cases where there is a disagreement between values of $\sim 10\%$ or higher:

1. **XMMXCS J095901.2+024740.4** the highest redshift system in this work ($z = 0.51$; panel 7 of figure 4.10), with the faintest BCG apparent magnitude from an integrated model ($m_i = 18.51$). The BCG fraction for this system doubles using the best Sérsic fit over either the aperture or de Vaucouleurs values (0.34, compared with 0.17 and 0.21 respectively). From our work in Chapter 2, we found that galaxy models tended to degrade with decreasing surface brightness; indeed, of all of the BCGs modelled here, the Sérsic fit for this system has the largest relative error.
2. **XMMXCS J022634.8-040409.2**: the lowest temperature cluster (panel 12 of figure 4.10); consequently, the system with the smallest effective radius ($R_{X,500} = 0.189$ Mpc). Using the aperture value results in an approximate decrease of 20% in the BCG flux contribution, compared with using either of the fitted models (0.52, compared with 0.65 and 0.67 for Sérsic and de Vaucouleurs respectively). As this is likely to be a group-level system, it has a higher sensitivity to any fractional changes in flux than larger systems (due to containing fewer objects and covering a smaller projected area).
3. **XMMXCS J095951.2+014045.8**: closer inspection of the system using the DS9 software revealed it to be a cD-type with an extended halo of stars (panel 14 of figure 4.10); this extra flux may potentially have been missed through using an aperture to measure the BCG, as both fitted models give a larger BCG fraction (0.28 in either case, compared with 0.19 for the aperture estimate). As aforementioned, such cases are testament to the caveats of a non-parametric approach.

4.5.3 Masking

As in every photometric survey, HSC imaging is not free from artifacts. Although the processing algorithm has been optimally designed to avoid such defects wherever possible,

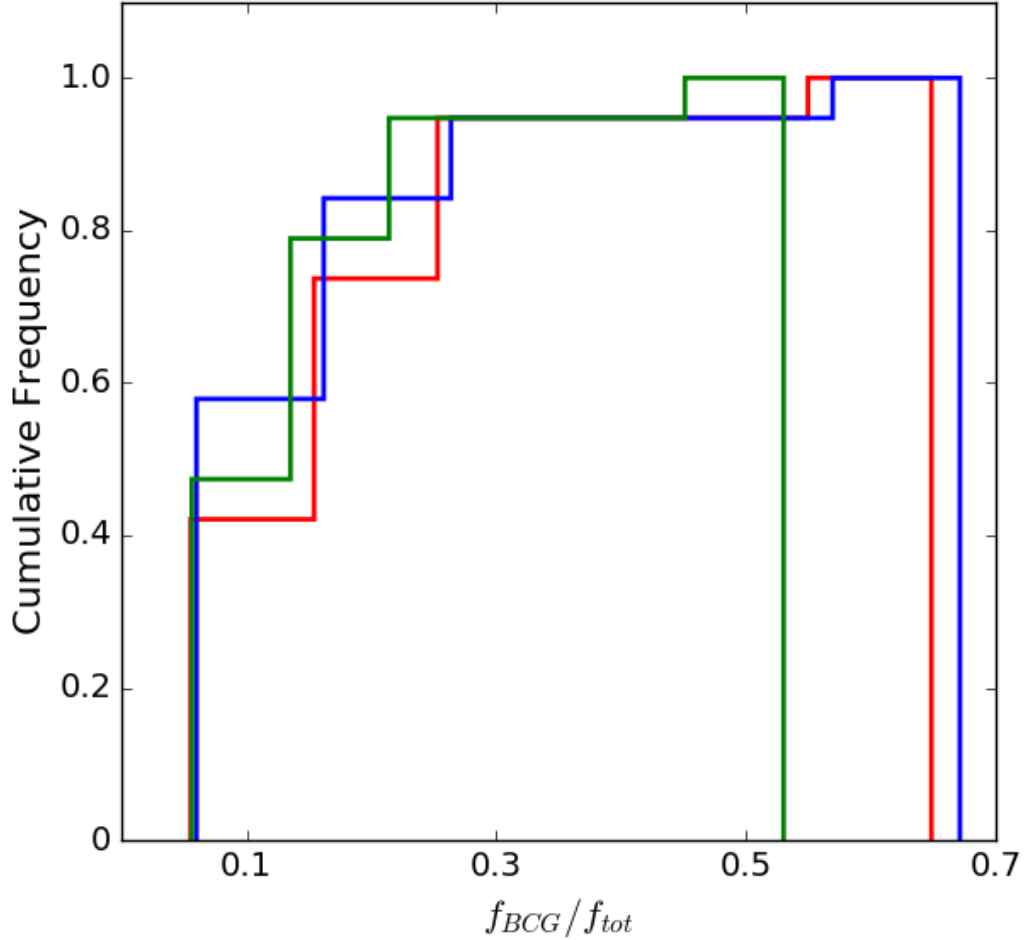


FIGURE 4.4: Cumulative distributions of the BCG flux contributions (plus divot correction) to the overall stellar flux of the clusters (see Table 4.4), where green represents the aperture values, red the de Vaucouleurs values and blue the Sérsic values.

some sources of excess flux remain. These include objects such as ‘bleed trails’ and diffraction spikes from overexposed stars, telescope ghosts, satellite trails and cirrus, to name a few (refer to [Duc et al. 2015](#) for a comprehensive summary). This is shown in figure 4.2, which constitutes examples of clusters in XCS which were not included in the final sample due to heavily contaminated photometry in HSC.

For our sample, we create custom masks in order to minimise the contribution of ICL flux from artifacts. Although the HSC pipeline does produce masks as output, we opt to generate our own, particularly as an attempt to more comprehensively remove artifacts, such as extended diffraction spikes from bright stars which are often not cleanly removed. We refer the reader to [Bosch et al. \(2018\)](#) for more details of the masking method used in the HSC pipeline.

For our custom masks, we begin with the binary masks generated by the HSC pipeline. The binary masks contain numerical identifiers in order to differentiate between different ‘layers’ of the masks - namely artifacts/saturated stars vs. objects. From these, we generate our own mask layers via 4 stages:

1. **Bad Pixel Masking:** we begin by first identifying the ‘bad pixel’ regions thresholded out by the HSC pipeline. These regions are then masked out, and constitute the first mask layer. These include: regions which have been incorrectly weighted by the weight maps, saturated pixels and some of the artifacts generated by bright stars.
2. **Star Masking:** next, we run SExtractor across all of the images. We set a detection threshold for our objects at 10σ ; with other parameters (such as saturation level, etc.) set to roughly the same values as those used during our running of SIGMA. We allow SExtractor to approximate a rough background level using a large mesh size to account for any extended bright sources (128 pixels). The purpose of this step is primarily to identify brighter, more compact objects within the frame, for which we do not require absolutely accurate photometry.

For fainter stars, we query the Gaia DR2 catalogue ([Gaia Collaboration et al. 2018](#)) for both photometry, and astrometry. The Gaia mission aims to collect both photometry and astrometry for $\sim 10^9$ stars in the Milky Way (for science objectives, see [Gaia Collaboration et al. 2016](#)). We produce catalogues of stars within the frames of our images, and mask stars out with $17 < G < 21$ (mean apparent magnitude value in the G -band from Gaia, see technical paper for the filter curve: [Jordi et al. 2010](#); $G \sim 21$ is the survey limit). We then apply the following empirical masking formula used canonically in HSC (<https://hsc-release.mtk.nao.ac.jp/doc/index.php/bright-star-masks/>) to define our exclusion apertures:

$$r = A_0 \times 10^{B_0(C_0-i)} + A_1 \times 10^{B_1(C_1-i)} \quad (4.5)$$

where r is in pixels, i are the HSC i -band magnitudes as measured by SExtractor (Kron aperture, [Kron 1980](#)) and $A_0 = 200$, $B_0 = 0.25$, $C_0 = 7.0$, $A_1 = 12.0$, $B_1 = 0.05$, and $C_1 = 16.0$.

For brighter stars ($G < 17$ in our case), this approach is not recommended. Although some bright stars are masked in HSC already, there are many missing due to the

prior use of the much less complete NOMAD survey (Zacharias et al. 2004) compared with the GAIA survey, which will be used for future releases as detailed in Coupon et al. (2018).

Instead, we create custom masks across all frames by hand for the brightest stars, any other point-like sources missed in our catalogues from Gaia and any visible diffraction spikes (a similar method to that used, for example, in Montes & Trujillo 2018 and Burke et al. 2015). Using the same method, we also mask out all non-cluster galaxies brighter than the BCG, following Burke et al. (2012). We used the SAO DS9 imaging software to view our images, which includes an array of tools for image visualisation ideal for these purposes, including optimised Gaussian smoothing kernels and high contrast scaling (useful for scaling masks to accommodate stellar wings). Masks were then created by hand using the region definition tool in DS9, and subsequently converted to fits format using the open-source MKMASK software (courtesy: Rolf Janssen).

- 3. Isophotal Mask Creation:** we then produce isophotal masks for each of our frames (see discussion in Section 4.5.1); below the isophote value is our definition of ICL for our clusters. To do so, we use an effective surface brightness detection threshold in the rest-frame of 25 mag/arcsec² (an approach similar to that carried out on the CLASH cluster sample by Burke et al. 2015). To compare our results with Burke et al. (2015), we also shift our equivalent surface brightness threshold at which we measure ICL to that of the rest-frame B -band. For the B -band equivalent threshold, we introduce the following modified version of equation 1.9:

$$\mu_{i,obs} = \mu_{B,rest} + 2.5\log_{10}(1+z)^4 + k_{i,B}(z) , \quad (4.6)$$

where $\mu_{i,obs}$ is the limit at which we observe, $\mu_{B,rest}$ is the equivalent rest-frame surface brightness in the B -band, $2.5\log_{10}(1+z)^4$ is the bolometric cosmological surface brightness dimming term and $k_{i,B}(z)$ is the k -correction term, defined here as:

$$k_{i,B}(z) = M_{i,obs}(z) - M_{B,rest}(z) , \quad (4.7)$$

where $M_{i,obs}(z)$ and $M_{B,rest}(z)$ are the pseudo-absolute magnitudes derived for each respective waveband at a given redshift for our choice of stellar population synthesis model. These are computed via the EZGAL software (Mancone &

TABLE 4.3: The k -correction ($k_{i,B}$), cosmological dimming and equivalent B -band surface brightness limits for our clusters below which we consider light as ICL ($\mu_{B,rest} = 25$), used to generate isophotal masks.

XCS ID	$k_{i,B}(z)$	$2.5\log_{10}(1+z)^4$	$\mu_{B,rest} = 25$
XMMXCS J022456.1-050802.0	-1.566	0.350	23.784
XMMXCS J161039.2+540604.0	-1.304	1.263	24.959
XMMXCS J233137.8+000735.0	-1.428	0.877	24.450
XMMXCS J232923.6-004854.7	-1.350	1.142	24.792
XMMXCS J161134.1+541640.5	-1.304	1.263	24.958
XMMXCS J095902.7+025544.9	-1.289	1.299	25.010
XMMXCS J095901.2+024740.4	-1.105	1.741	25.635
XMMXCS J100141.6+022538.8	-1.523	0.508	23.985
XMMXCS J095737.1+023428.9	-1.257	1.378	25.121
XMMXCS J022156.8-054521.9	-1.392	1.001	24.608
XMMXCS J022148.1-034608.0	-1.183	1.556	25.374
XMMXCS J022634.8-040409.2	-1.293	1.289	24.996
XMMXCS J022530.8-041421.1	-1.498	0.580	24.082
XMMXCS J100047.3+013927.8	-1.430	0.865	24.435
XMMXCS J022726.5-043207.1	-1.341	1.168	24.827
XMMXCS J022524.8-044043.4	-1.387	1.018	24.631
XMMXCS J095951.2+014045.8	-1.259	1.374	25.115
XMMXCS J022401.9-050528.4	-1.324	1.218	24.894
XMMXCS J095924.7+014614.1	-1.525	0.500	23.975

[Gonzalez 2012](#)), assuming an old stellar population with a formation redshift of $z_f = 3$, solar metallicity (Z_{\odot}) and passive evolution thereafter, using the models of [Bruzual & Charlot \(2003\)](#) coupled with a [Chabrier \(2003\)](#) IMF (also resembling the methodology of [DeMaio et al. 2018](#)). We list our B -band limits in Table 4.3.

While we appreciate that it is unlikely that the stars contained within our BCGs evolved entirely in situ, most BCGs have shown little evidence for significant growth through star formation activity at $z < 1$ and instead are primarily assumed to gain mass through mergers with satellites containing reasonably similar stellar populations (or even more passive, e.g. [Guo et al. 2009](#)), so we consider this assumption reasonable for simplicity. We show how the choice of metallicity and formation redshift affects our $k_{i,B}(z)$ values in the Appendix of this thesis, for the mean values of our sample split in two bins about the mean redshift ($0 < z < 0.28$ and $0.28 < z < 0.5$ respectively); in short, there is an *rms* of ± 0.3 magnitudes, depending on the model of choice.

4.5.4 Background Over-subtraction - The ‘Divot Correction’ Method

Another major concern regarding the measurement of ICL is not only the *addition* of flux from excess sources (as discussed in Section 4.5.3 and in Section 4.5.5) but also, the *over-subtraction* of flux. For space-based telescopes with low levels of background, this is less of a concern (e.g. HST); in the case of ground based telescopes, however, it provides a significant challenge for LSB science. For extended objects such as galaxies, issues arise due to modern, commonly-used background estimation methods: namely, spline-mesh approaches. Within the galaxy-modelling literature, this issue is long-known and rather notorious (e.g. [Zhao et al. 2015b](#) and references therein); namely, that such approaches produce a ‘dearth’ of flux around extended sources, termed here as a ‘divot’.

Divots occur as we are limited in our background estimation by the size of our chosen mesh; namely, that we cannot accommodate for the differing angular extents of all objects in a frame. Hence, some light in extended object profile wings is often mistaken for background flux and subtracted, due to the sky background about that object being overestimated. Even in surveys such as HSC where background estimation is (more-or-less) state-of-the-art, these features still occur (see figure 4.5). This effect is doubly serious in the case of cluster and ICL science compared with isolated galaxies, as there is often a high source density (i.e. overlapping profile wings), therefore making it nearly impossible to create a ‘one size fits all’ divot correction model.

In an upcoming paper (Kelvin et al., in prep; Lee Kelvin, priv. comm.), we attempt to address these problems, providing survey comparisons and suggesting potential solutions. To do so, we have produced a pipeline to correct for such flux over-subtraction effects. We acknowledge that post-processing is less preferable than an optimised survey strategy; in this case (and in many others), however, this is not an option for either past or present surveys that have not prioritised LSB science in their observational approach. The construction, application and limits of the aforementioned pipeline is not discussed here (Kelvin et al, in prep); we instead provide an abridged description of its operation and use in the context of this work.

The pipeline, which is written in R and is primarily SExtractor and SWARP based, operates on an image in three major steps as follows:

1. **Object detection/modelling:** firstly, SExtractor is run on a given input image weighted by its associated weight map (in the case of HSC-SSP, those provided by the processing pipeline). The settings used are similar to those described in Section 4.5.2.

Since SExtractor version 2.8 (e.g. Bertin 2009), it is possible to fit models to the light profiles of objects detected by the algorithm. There are three model priors available (delta function, exponential profile, Sérsic profile) selected for three primary object types (stars, disk galaxies, spheroidal galaxies). Here, as spheroidals generally constitute most cluster galaxies, we opt for a global Sérsic model (see equation 2.8). All detected objects in the frame are modelled with a Sérsic profile, which are fit through a Levenberg-Marquardt χ^2 minimization algorithm. The result of doing so is an image frame containing the modelled light profiles of all catalogue objects.

2. **Differential inversion:** in order to estimate the flux loss in object profile wings caused during the image processing stage, we then take the difference between the input image and the image containing the object models. The result is then inverted, creating the ‘divot’ image (see centre panel of figure 4.5).

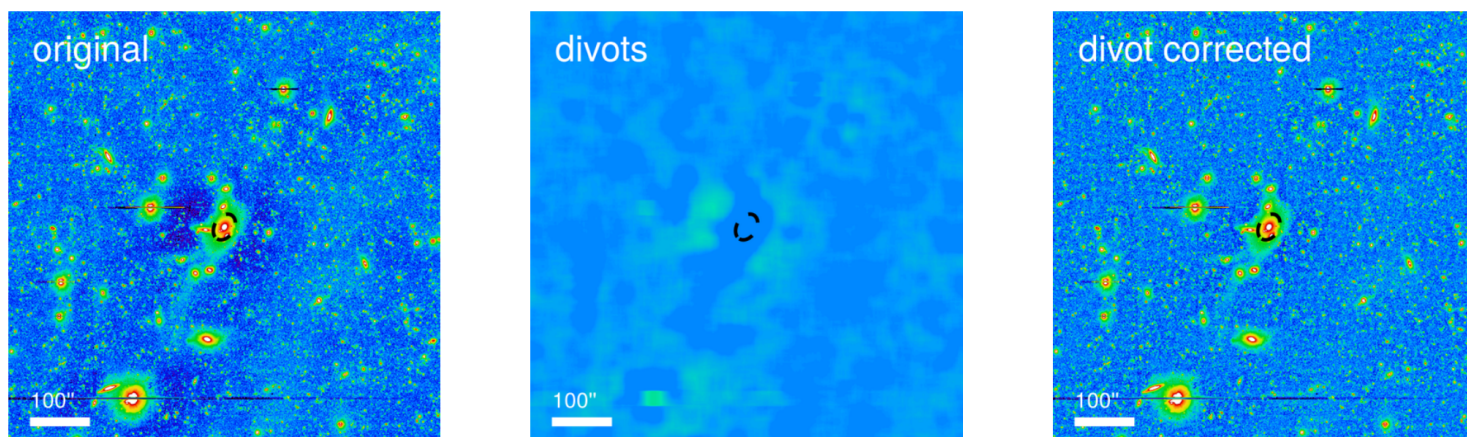


FIGURE 4.5: An example of the 'divot correction' method used in this work (shown here for cluster XMMXCS J232923.6-004854.7); all images have the exact same scaling (from Kelvin et al., in prep). The first image depicts the data prior to correction; as is visible, there is a dearth of flux in the regions around the BCG and its satellites. The second shows the estimated divot correction; the third shows the resultant image after implementation. As is visible, there is a vast improvement, with the sky level varying far more smoothly.

3. **Coaddition:** the divot image is then added on to the original image using SWARP (Lanczos interpolation; this was selected as recommended in the SWARP user manual, but as the resolution of the images is identical, no resampling is necessary), thus providing an approximate flux ‘correction’ (see figure 4.5).

There is an obvious caveat in our approach, namely with our selection of a ‘one type fits all’ Sérsic profile with which we fit to all galaxies in a frame. We therefore assume that object wings will follow those of a Sérsic profile. This estimate is often cuspiest than, for example, the true profiles of BCGs, of which some are thought to be multi-component objects (see, e.g. [Bernardi et al. 2014](#), [Zhao et al. 2015b](#), [Zhang et al. 2018](#); also see Section 4.6). Although we appreciate the simplicity of this approach, the addition of other components to hundreds of models (as well as attempting to accurately morphologically classify all detected objects in a frame), provides not only significant computational cost challenges, but also adds additional free parameters which may not be necessary for all objects and may lead to less reliable fits (see arguments in Chapter 2). We therefore instead caution the reader that our estimates represent, most likely, a lower-limit estimate on the true value of the total wing flux loss during processing (due to having no reliable information regarding additional components which may contribute flux).

4.5.5 Quantifying Systematic Background

In all astronomical image data, a systematic background exists; at visible wavelengths, it is partially caused by faint galaxies below the survey limit, the wings of bright sources such as stars or contaminant galaxies and residual flux from the sky (e.g. [Guglielmetti et al. 2009](#)). In order to better understand this in the context of our image data, we performed a test via applying photometry on injected mock profiles so that we could trace the additional flux contribution at a given surface brightness. We performed this test on ‘control’ frames offset from each of the clusters in this study. The 19 control frames selected were patches of sky within the HSC-SSP footprint, offset at random by 0.5° from the centre of the original frames. We chose to use representative control frames so as to limit any contributions from any ICL that may be present; the control frames were subject to an identical masking method to that used in the cluster frames, were weighted using the HSC-generated weight maps (inverse variance) and were not divot-corrected.

For each of the frames, 10 random positions were selected. To mimic an ICL-like profile, we generated an exponential model ($n = 1$, $R_e = \langle R_{500} \rangle / 4$, $\theta = 50^\circ$, $a/b = 0.8$; Sérsic index, effective radius, position angle and axis ratio respectively; e.g. [Zhang et al. 2019](#)) at 9 average surface brightness levels (24 - 28 mag/arcsec² in steps of 0.5 mag/arcsec²; where ‘average’ refers to the mean surface brightness across a whole profile). The profiles were convolved with the field PSF from SIGMA (as per the modelling process for the BCGs) and an idealised Poisson noise component was added. We injected the models at 10 random positions within each of the control frames, measuring the difference between the input and output flux values using a fixed circular aperture equivalent to the selected effective radius of our models (~ 2000 models in total, for a similar method, see [Burke et al. 2012](#)).

Figure 4.6 shows the bulk output across the fields, with figure 4.7 showing the stacked median for all of the control frames (the deviation is negative due to our convention of input - output). From our mock photometry, we detect a small background at most of around a 5% excess of the input flux on average for an ICL-like profile, with respect to the range of our *B*-band equivalent surface brightness levels (23.74 - 25.63 mag/arcsec²). There is obvious scatter on a case by-case basis (for example, panel 16 of figure 4.6, see also panel 16 of figure 4.10); from eyeballing, the predominant cause of this seems to be due to source-heavy frames (e.g. many/clustered sources, bright sources such as stars present). Moreover, we will show evidence in the upcoming section (Section 4.6) that the flux lost at the range of isophotal levels at which we measure the ICL is approximately $4\times$ the background contribution; hence, we do not correct for it here (see further discussion of systematics in Chapter 5).

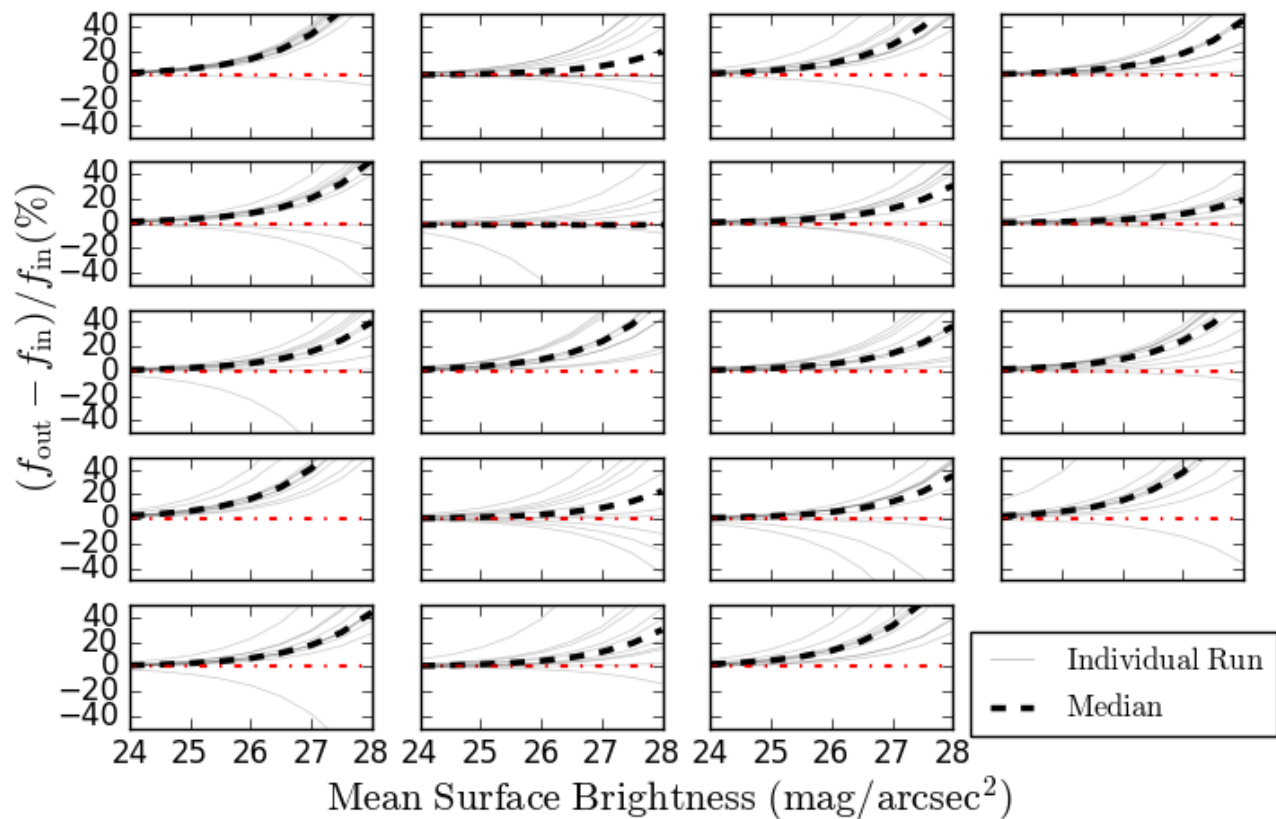


FIGURE 4.6: The results from performing photometry on ~ 2000 mock ICL profiles injected into HSC data (without divot corrections). Each frame in the subplot represents a given control field; each plot shows the relative percentage deviation in flux ($(f_{\text{out}} - f_{\text{in}})/f_{\text{in}}$, where f_{in} is the raw mock profile flux measurement and f_{out} is the flux measurement of the profile after implantation in a HSC control frame) for a given ‘ICL-like’ profile (see text) with respect to mean surface brightness (the average surface brightness across a mock profile).

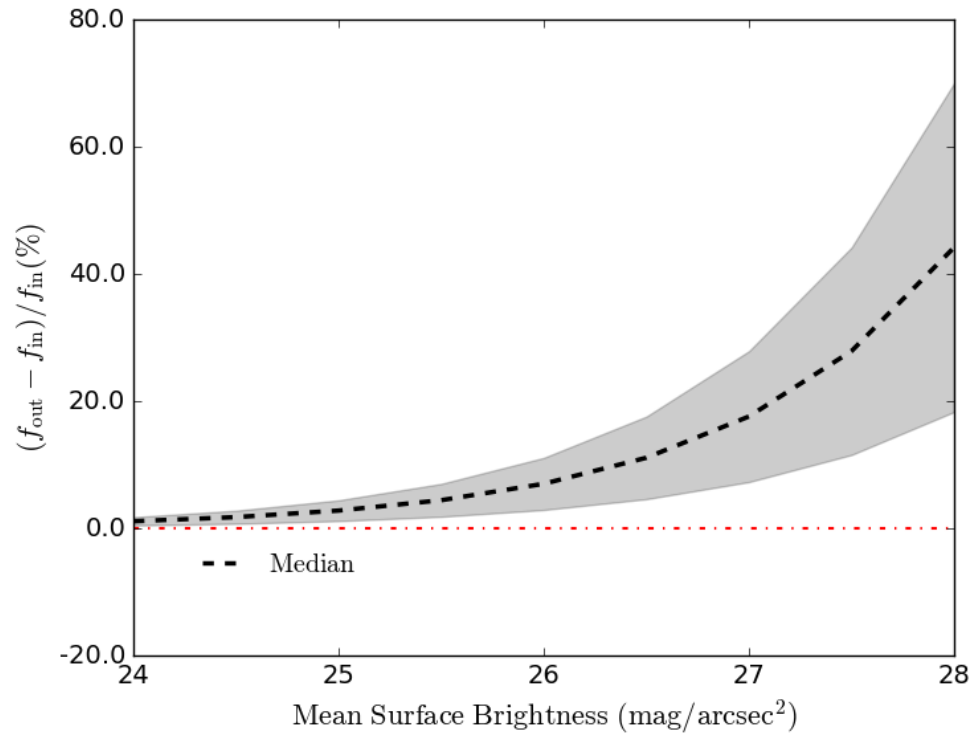


FIGURE 4.7: Stack of median deviations of recovered profiles across all frames with respect to mean surface brightness, with all definitions and conditions the same as in figure 4.6. The grey shaded region indicates the 1σ scatter.

4.6 Results

For comparison, we measure the ICL for our clusters before and after applying a divot correction. The measurements are summarised in Table 4.4. In the upcoming chapter (Chapter 5), we will provide more extensive comments on our results, and the consequences of them for both cosmology and BCG evolution; here, we restrict our commentary towards the inferred *systematics* involved in ICL measurement for ease of comprehension.

For our clusters, with the inclusion of a divot correction, the mean ICL contribution to the overall cluster light at $\mu_{B,rest} = 25 \text{ mag/arcsec}^2$ sits at around 25%. It is immediately clear from Table 4.4 that applying a divot correction has a significant effect on the overall recovered value for the ICL (Δf being the difference in ICL to total cluster light between the divot corrected and uncorrected values); figure 4.8 illustrates this difference, for equivalent surface brightness limits in B from 24 – 26 mag/arcsec^2 in steps of 0.5. On average, we see a recovered flux amount of $\sim 5\%$ for the overall cluster light upon inclusion of a divot correction; $\sim 20\%$ of the mean measured ICL light overall. The final masked, divot-corrected images are shown in figure 4.10.

Our results illustrate exactly how crucial it is to account for the flux over-subtraction problem around objects in surveys. As stated previously, because the divot corrections are modelled with a ‘one-size-fits-all’ Sérsic profile, it is likely that the ‘true’ net flux loss is underestimated due to our choice of Sérsic profile with which to model our divot corrections, with $\sim 50\%$ of BCGs tending to have an additional ‘halo’ as well as a central bulge by $z < 0.1$ (Zhao et al. 2015b). As well as this, we do not account via this method for any stars formed in situ (e.g. Puchwein et al. 2010), assuming instead that any flux which has been lost during processing directly traces the objects in frame (e.g. Burke et al. 2012 demonstrate that this is a fair assumption for the majority of the ICL). Whilst we appreciate that there is a method dependency when measuring ICL (see discussion in Section 1.4.2 of the Introduction), there is still a significant difference upon inclusion of a divot correction when changing the surface brightness limit (figure 4.8).

As a sanity check, to measure the BCG+ICL profile shape, we fit elliptical isophotes using the IRAF ELLIPSE package (Jedrzejewski 1987) centred on each cluster BCG, for both the pre- and post- divot-corrected images. The frames are masked at $\mu_{B,rest} = 24 \text{ mag/arcsec}^2$ using the segmentation maps from SExtractor (plus all star/bad pixel masks), due to

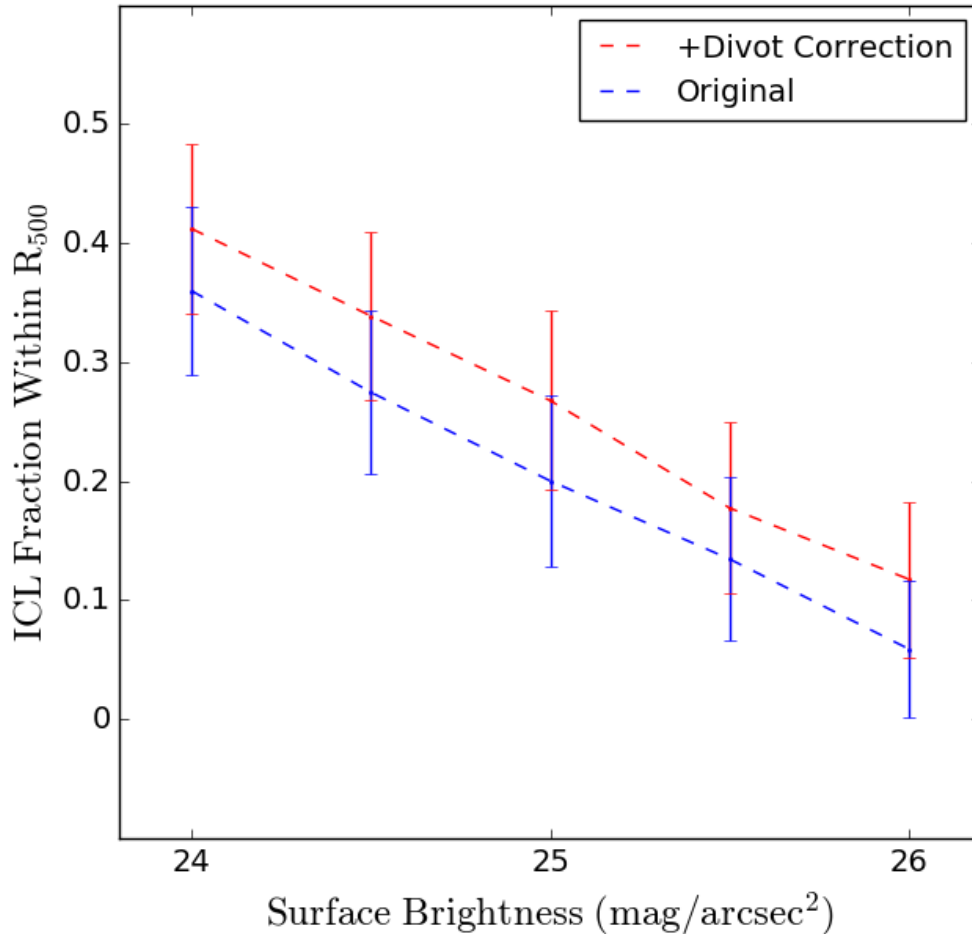


FIGURE 4.8: The stacked ICL fraction to total light fraction at a selection of equivalent surface brightnesses, comparing the divot corrected and uncorrected cases. The errorbars depict the $1\text{-}\sigma$ scatter across all clusters in the sample.

the benefit of the software having an inbuilt de-blending algorithm to separate object fluxes (with the exception of the BCG itself, which is left unmasked during this process). A stack of the resulting profiles is shown in 4.9. The deviation from a Sérsic profile is immediately obvious, in that there is a plateau of light beyond $\sim 40\text{kpc}$, making for an overall profile which is significantly less cuspy; this radius was used by [Presotto et al. \(2014\)](#) beyond which to consider light as ICL, and motivates our choice of 50kpc as an aperture radius when measuring the fluxes of our BCGs. Some aforementioned authors have modelled this flatter, extended component using an exponential model ([Zhang et al. 2019](#) and discussion in Introduction). Interestingly, we do not find much deviation in shape on average when applying a divot correction; within the percentiles of the stacks, they are almost identical; this complements the comparable outputs we obtained through

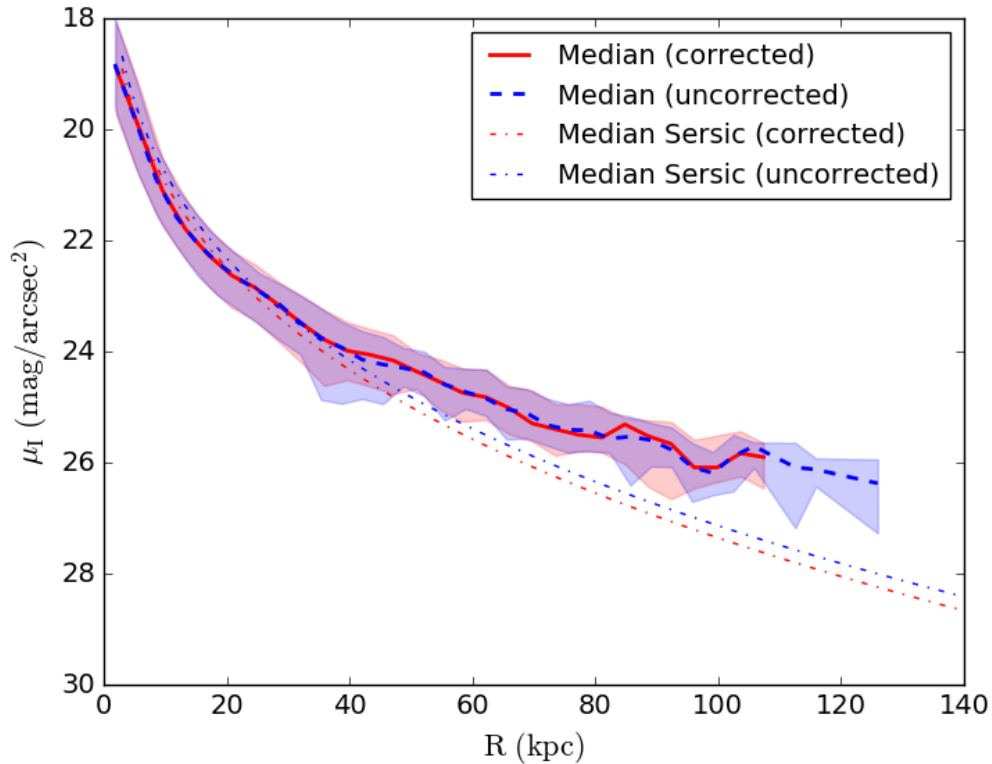


FIGURE 4.9: Comparison between the divot corrected and uncorrected stacks as measured by IRAF ellipse. The shaded region represents the 16th and 84th percentiles of the stacks. The dot-dashed lines are the median Sérsic model from SIGMA in each respective case. It is clear that the Sérsic models miss a great deal of the flux on the outskirts of the BCGs, which previous authors have argued is a plateau of either ICL, or an extended stellar halo. There is little difference in the median n values, with values of 4.65 and 4.57 for the non-corrected and corrected models respectively.

our SIGMA models.

4.7 Summary of Chapter

In this chapter, we introduced our study into the systematics of ICL recovery. We discussed the sample of clusters in XCS used in this work and how they were selected; we also discussed the HSC-SSP survey, the current processing pipeline and the photometry used in this work. We outlined how we measured our ICL, using an equivalent B -band isophotal threshold, measured within an aperture of radius $R_{X,500}$ centred on the brightest cluster galaxy. We introduced the ‘divot’ problem, which arises due to an ‘over-subtraction’ of flux from background estimation during image processing, and our method to correct for this effect. Finally, we introduced a set of basic simulations to allow

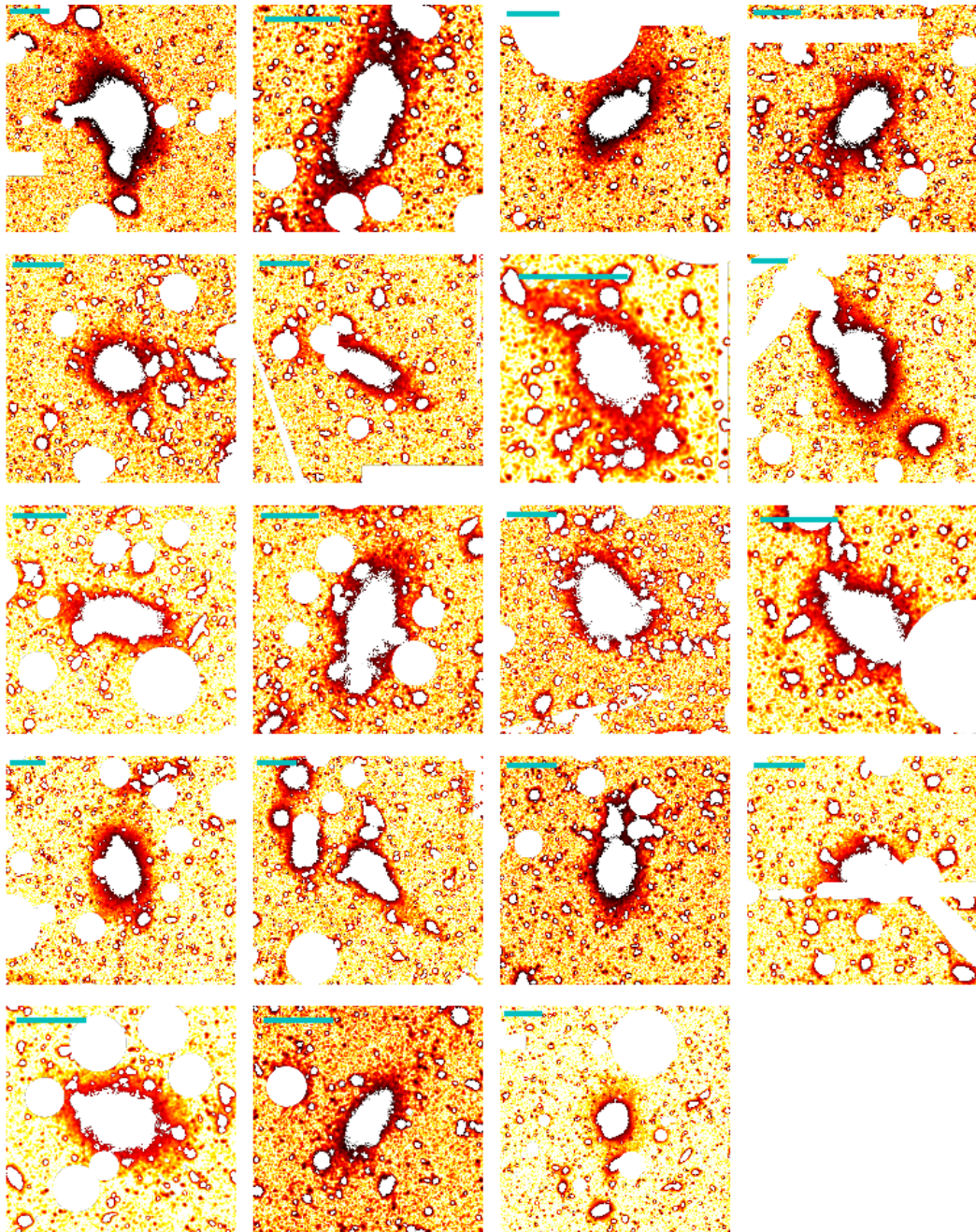


FIGURE 4.10: The final equivalent 25 mag/arcsec^2 masked and divot-corrected images, zoomed to 40% of the R_{500} value of each respective cluster centred on the BCG (with the exception of panel 7). The cyan line at the top left of each panel is equivalent to $30''$. To show structure, the images have been log-scaled and smoothed.

us to understand the flux contribution from the background at a given mean surface brightness for an ICL-like profile; this was done without any divot corrections in place. From this, we conclude the following:

1. there is a contribution from the background of less than 5% at the range of equivalent B -band surface brightness thresholds at which we measure ICL, which increases inversely with decreasing surface brightness,
2. there is a loss in ICL flux of about $4\times$ the estimated background ($\sim 20\%$) from the effects of sky over-subtraction, which remains approximately constant $\pm 1\text{mag/arcsec}^2$ about our chosen threshold. We surmised that this was likely to be an underestimate, given the Sérsic models used when creating the divot corrections,
3. the divot corrections themselves do little to change the overall profile shape (median 4.57 to 4.65 corrected versus uncorrected respectively), with the 1-D profiles and parametric fits from SIGMA respectively yielding very similar results.

Our results illustrate that one must consider their data carefully when attempting to measure ICL; indeed, many authors have recognised this issue and have attempted to overcome it by using novel processing methods of their own, such as implementing less ‘aggressive’ global background subtraction techniques (often, for example, using a larger mesh, e.g. [Huang et al. 2018](#), or, a mean global ‘step’, e.g. [Montes & Trujillo 2019](#)). Our findings therefore contribute to the mandate for an overhaul, as discussed in Section 1.4.2 of the Introduction, of conventional astronomical image processing methods and observational strategies.

We recognise that there are several obvious caveats with our method; for instance, surface-brightness methods of measuring ICL tend to recover less flux than methods more readily available in simulations such as setting a binding energy threshold (e.g. [Rudick et al. 2011](#)). We also assume through our divot corrections that the ICL predominantly traces the cluster galaxies, not accounting for any stars in situ, hence our corrections may underestimate the true extent of the flux loss. Finally, we assume the location of the BCG to be a proxy for the centre of the cluster when measuring the ICL; for local systems, this is often the case (e.g. [Lin & Mohr 2004](#)), however the picture has been known to change at high redshift, with a higher fraction of clusters out of dynamical

relaxation beyond $z \sim 1$ (e.g. [Hatch et al. 2011](#)). We will discuss this issue further in ‘Future Work’ in Chapter 6.

TABLE 4.4: A summary of the results from this work, where f_{ICL}/f_{tot} is the percentage of cluster light that is ICL at $\mu_{B,rest} = 25\text{mag/arcsec}^2$ within $R_{X,500}$ and Δf is the percentage difference in the ICL contribution between the divot corrected and uncorrected cases. The equivalent BCG flux (f_{BCG}) is also included (Sérsic model, de Vaucouleurs model and 50 kpc aperture respectively).

XCS ID	f_{ICL}/f_{tot}	Δf	f_{BCG} (Sérsic)	f_{BCG} (de Vaucouleurs)	f_{BCG} (50 kpc aperture)
XMMXCS J022456.1-050802.0	0.2896 ± 0.0009	0.0473 ± 0.0042	0.2829 ± 0.0007	0.2889 ± 0.0007	0.2653 ± 0.0013
XMMXCS J161039.2+540604.0	0.1877 ± 0.0099	0.0547 ± 0.0091	0.1631 ± 0.0033	0.1704 ± 0.0030	0.1382 ± 0.0010
XMMXCS J233137.8+000735.0	0.2628 ± 0.0010	0.0626 ± 0.0076	0.1731 ± 0.0009	0.1568 ± 0.0006	0.2469 ± 0.0025
XMMXCS J232923.6-004854.7	0.2757 ± 0.0009	0.0495 ± 0.0055	0.1560 ± 0.0011	0.1657 ± 0.0010	0.1201 ± 0.0008
XMMXCS J161134.1+541640.5	0.1540 ± 0.0006	0.0245 ± 0.0060	0.0901 ± 0.0004	0.0871 ± 0.0003	0.0690 ± 0.0007
XMMXCS J095902.7+025544.9	0.2676 ± 0.0012	0.0780 ± 0.0076	0.1178 ± 0.0006	0.1159 ± 0.0005	0.0895 ± 0.0008
XMMXCS J095901.2+024740.4	0.1148 ± 0.0017	0.0441 ± 0.0294	0.3442 ± 0.0159	0.1705 ± 0.0012	0.2058 ± 0.0028
XMMXCS J100141.6+022538.8	0.3121 ± 0.0007	0.0716 ± 0.0036	0.2563 ± 0.0005	0.2535 ± 0.0005	0.2254 ± 0.0013
XMMXCS J095737.1+023428.9	0.1567 ± 0.0007	0.0586 ± 0.0087	0.1244 ± 0.0010	0.1291 ± 0.0009	0.1535 ± 0.0012
XMMXCS J022156.8-054521.9	0.2887 ± 0.0012	0.0652 ± 0.0071	0.2261 ± 0.0026	0.1550 ± 0.0008	0.1269 ± 0.0010
XMMXCS J022148.1-034608.0	0.0972 ± 0.0008	0.0354 ± 0.0170	0.0670 ± 0.0012	0.0700 ± 0.0010	0.0561 ± 0.0004
XMMXCS J022634.8-040409.2	0.1876 ± 0.0014	0.0141 ± 0.0113	0.6481 ± 0.0036	0.6710 ± 0.0033	0.5298 ± 0.0044
XMMXCS J022530.8-041421.1	0.3843 ± 0.0008	0.0335 ± 0.0032	0.1660 ± 0.0007	0.1275 ± 0.0003	0.1506 ± 0.0009
XMMXCS J100047.3+013927.8	0.2385 ± 0.0006	0.0391 ± 0.0041	0.0859 ± 0.0004	0.0852 ± 0.0003	0.0850 ± 0.0007
XMMXCS J022726.5-043207.1	0.2971 ± 0.0009	0.0337 ± 0.0048	0.0551 ± 0.0002	0.0599 ± 0.0002	0.0869 ± 0.0006
XMMXCS J022524.8-044043.4	0.3276 ± 0.0012	0.0627 ± 0.0059	0.1302 ± 0.0008	0.1364 ± 0.0006	0.0977 ± 0.0008
XMMXCS J095951.2+014045.8	0.1985 ± 0.0012	0.0410 ± 0.0100	0.2792 ± 0.0018	0.2839 ± 0.0013	0.1895 ± 0.0016
XMMXCS J022401.9-050528.4	0.2762 ± 0.0024	0.0334 ± 0.0131	0.1860 ± 0.0014	0.1719 ± 0.0007	0.1503 ± 0.0015
XMMXCS J095924.7+014614.1	0.3078 ± 0.0008	0.0542 ± 0.0042	0.1170 ± 0.0003	0.1195 ± 0.0003	0.1342 ± 0.0012

Chapter 5

Part II - The ICL in XCS-HSC: Results and Discussion

5.1 Overview of Contents

In this chapter, we present the results from our study of the ICL within a sample of 19 XCS-HSC clusters (outlined in chapter 4) alongside numerous other studies for comparison, from simulations and observations. Immediately, we note a large degree of scatter in the observed fractional light contribution of ICL, (1-60%, 20-40% for our sample) and theoretically (10-90%), for retrieved ICL fractions; we then discuss at length some of the reasons as to why such discrepancies may exist. While generally finding observational results consistent, our results appear to differ significantly from results from hydrodynamical simulations, even when measured in an observationally consistent way. Results from SAM- and numerical-based simulations however yield results more in line with current observations. Our results yield higher fractions with redshift than comparison studies in this work; we offer observationally motivated reasons as to why this may be the case. While we detect little evidence for evolution in brightness for our BCGs with redshift, we note an ICL growth factor for our sample of $\sim 2-4$, slightly shallower than [Burke et al. \(2015\)](#) (4-5) and similar again to results from SAMs (0.5-4). We also find no clear link between the amount of ICL and the mass of the host cluster; nor do we find a clear link between the relative fractions of ICL and BCG (within 50kpc), indicating a possible decoupling between the two.

This chapter primarily addresses motivation 4: “How does the ICL grow over time? Is its evolution linked to its corresponding BCG, or to the properties of the host cluster?”, referenced in Section 1.5.

5.2 Results

5.2.1 What Drives ICL Growth?

In the previous chapter, we presented the relative fractions of BCG and ICL flux in our clusters in Table 4.4. To enable a more complete interpretation of our results, given the strong selection our clusters exhibit in figure 4.1, we perform a partial Spearman analysis on our sample, the method and formalism of which we describe in chapter 3. The partial Spearman enables us to account statistically for underlying correlations which may be present through the means that we have selected our clusters. Here, we choose four primary parameters of interest; the fractional contribution of the ICL and of the BCG (f_{ICL}/f_{tot} and f_{BCG}/f_{tot} respectively), the cluster redshift (z) and the cluster mass $M_{X,500}$ (which is computed from the X-ray temperature, as detailed in the previous chapter). We also look at correlations between k -corrected BCG absolute magnitude, cluster mass and redshift via a similar means. We require significance, as in chapter 3 and 4, at the standard value of $p \leq 0.05$ throughout ($\log_{10}[p_s] \leq -1.301$). The full Spearman analysis for our clusters is contained in Table 5.1; the partial analysis can be found in Section B.2 in the Appendix.

As in Chapter 4, in the rest-frame B -band, we find a mean ICL flux fraction of around 25%; this slightly exceeds the mean BCG contribution, even when using an Sérsic model (16-19%, see Table 4.4). Qualitatively however, the difference appears to become somewhat more modest with increasing redshift, with a less than 1% difference for 2 of the 4 most distant systems (with XMMXCS J022148.1-034608.0 being the exception at ~ 4 %) and a reversal of the trend for the highest redshift system at $z = 0.501$. This is not a definitive conclusion; we are obviously limited by our small sample size (19 systems), as is the case for most legacy studies of ICL (see discussion in the Introduction), alongside significant caveats with assuming a fixed aperture scale when measuring the fluxes of our BCGs (see discussion in previous chapter). However, it raises interesting questions about

TABLE 5.1: Full Spearman analysis of all the parameters used in this study: the fractional contribution of the ICL and of the BCG (f_{ICL}/f_{tot} and f_{BCG}/f_{tot} respectively), the cluster redshift (z) and the cluster mass $M_{X,500}$. The top half of the table lists the Spearman rank correlation coefficient (r_s), whereas the bottom half of the table provides the log of its corresponding p-value ($\log_{10}[p_s]$).

	f_{ICL}/f_{tot}	f_{BCG}/f_{tot}	z	$\log_{10}M_{X,500}$
f_{ICL}/f_{tot}	–	0.0807	-0.7860	-0.2070
f_{BCG}/f_{tot}	-0.1292	–	-0.1526	-0.7474
z	-4.0174	-0.2746	–	0.3561
$\log_{10}M_{X,500}$	-0.4051	-3.4491	-0.8700	–

the point in time at which the ICL begins to dominate the cluster halo (see upcoming Section 5.2.2).

In common with other authors (e.g. [Burke et al. 2015](#) and upcoming discussion), we detect a significant anti-correlation ($r_s = -0.786$, $\log_{10}[p_s] = -4.017$) between the contribution of ICL with cluster redshift, which remains almost entirely unchanged when accounting for any dependence on cluster mass (see Tab B.6 in the Appendix). This is clearly visible on figures 5.4 and 5.5, which we will discuss in the upcoming Section 5.2.2). This is not the case for the BCG flux fraction, which has no significant correlation with redshift ($r_s = -0.153$, $\log_{10}[p_s] = -0.275$) and remains highly anti-correlated with the cluster mass even after taking redshift dependence into account ($r_s = -0.7504$, $\log_{10}[p_s] = -3.4767$, see Table B.5 in the Appendix). Even if we consider a Sérsic model (which produces almost universally the largest BCG fraction estimates) in place of an aperture magnitude for our BCGs, there is still an anti-correlation present at fixed redshift that remains almost unchanged ($r_s = -0.77506$, $\log_{10}[p_s] = -3.8009$), so it is not strongly related to the flux loss through not accounting for galaxy profile wings. Obviously, as we use $R_{X,500}$ as a proxy for cluster radius, the area which we divide the contributing flux of the BCG over goes as $R_{X,500}^2$; even so, this anti-correlation seems to support the scenario of the relative homogeneity seen in BCGs discussed in chapter 3 up to $z \sim 1$. This result links to our previous work outlined in chapter 3, where we observe a decreasing star-formation efficiency in clusters with increasing halo mass (see figure 3.8).

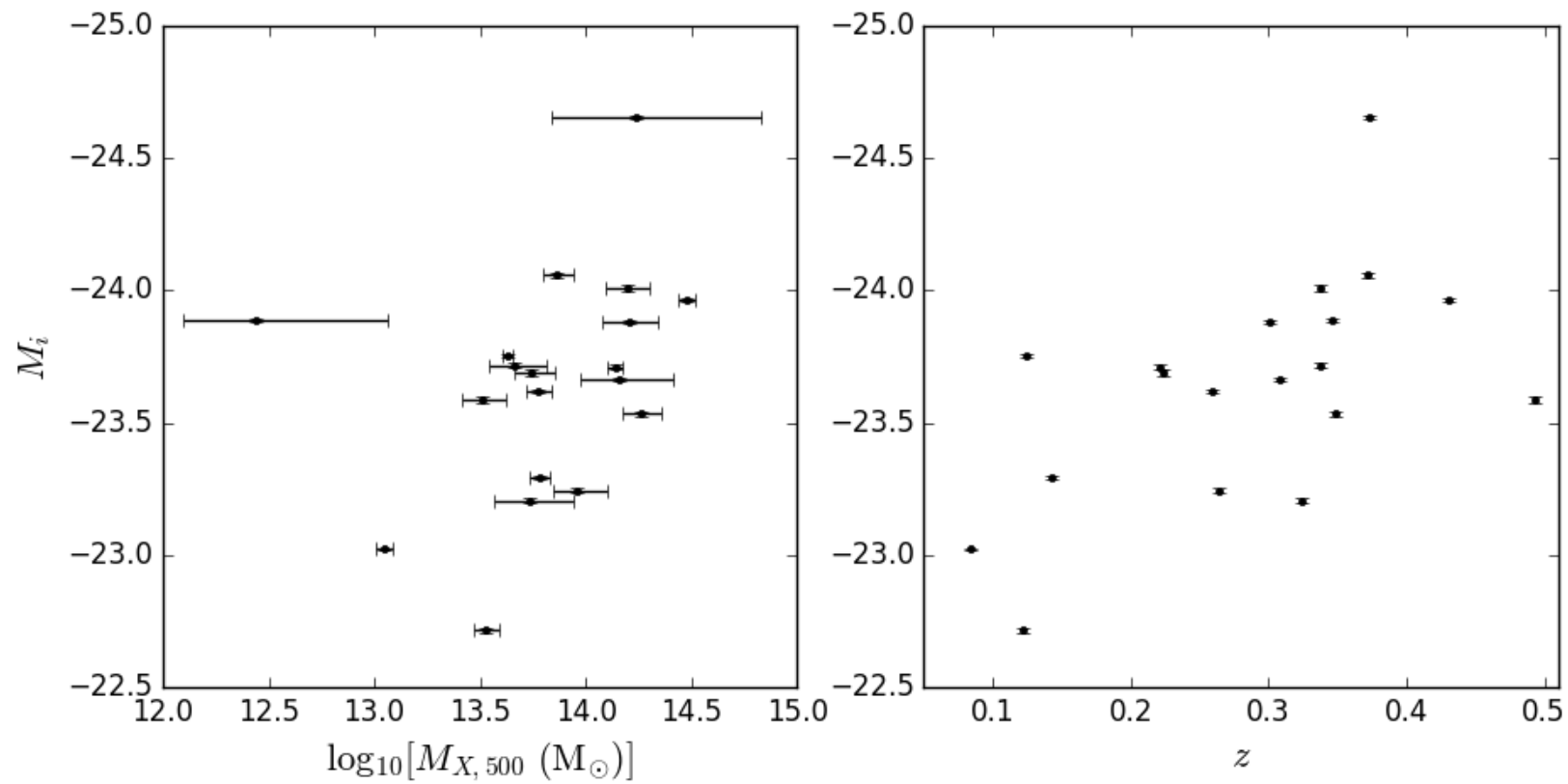


FIGURE 5.1: The rest-frame BCG absolute magnitude (M_i , i -band aperture) versus cluster mass measured in X-rays ($M_{X,500}$, left) and redshift (z , left). For ease of comprehension, we have inverted the y -axis.

There is no strong correlation present, however, between the ICL and the mass of the cluster at fixed redshift ($r_s = 0.126$, $\log_{10}[p_s] =$ from Table B.5). This has an interesting implication; our findings from this thesis (see chapter 3) therefore seem to suggest a much closer dependence between stars within the very central region of the halo (BCG) with the halo properties (such as M_{500}) in comparison to stellar mass distributed further out (ICL). Indeed, with a lack of correlation present between halo mass and ICL mass, there seems to be a ‘decoupling’ between the two components; the ICL, for instance, has been found to exhibit far more growth since $z \sim 1$ than the BCG (e.g. Burke et al. 2012, 2015), with BCG growth rates being much more modest than those predicted from simulations (see discussion in Introduction) and here, also being comparatively homogeneous.

The leftmost panel of figure 5.1 shows the relationship between the k -corrected BCG absolute magnitude (M_i , i -band aperture, see upcoming Section 5.2.2 for discussion) and cluster mass ($M_{X,500}$). Although we detect an anti-correlation between halo mass and absolute magnitude (which is anti-correlated with BCG mass), it is not significant ($r_s = -0.40877$, $\log_{10}[p_s] = -1.0785$); this finding is unchanged if we fix for redshift ($r_s = -0.27456$, $\log_{10}[p_s] = -0.56831$). If we remove the two points with the largest errorbars, it becomes significant by our criteria, but still remains insignificant with redshift ($r_s = -0.48775$, $\log_{10}[p_s] = -1.3094$; $r_s = -0.37136$, $\log_{10}[p_s] = -0.80487$ respectively). We therefore do not find conclusive evidence that our BCG absolute magnitudes (and therefore masses) are strongly governed by halo mass here. This is likely to be as a result of our selection (e.g. Burke et al. 2015) and also due to the fact that our sample size is small (see discussion in upcoming chapter). An obvious point would therefore be to establish whether our result for the BCG flux fraction with halo mass weakens when applying our method a larger sample of clusters with an established $M_{\text{BCG}} - M_{\text{halo}}$ relation (see discussion in Section 4.5.2 in the previous chapter); this was also recognised in Burke et al. (2015).

We find a similar result for absolute magnitude with redshift when fixing for halo mass ($r_s = -0.46034$, $\log_{10}[p_s] = -1.2632$, see rightmost panel of figure 5.1) even having removed the two points with the largest error bars ($r_s = -0.31443$, $\log_{10}[p_s] = -0.62785$); hence, we do not detect any significant change in BCG brightness with redshift either. Although this may also be linked to the way we have selected our BCGs, given numerous authors have found little change in BCG brightnesses since $z \sim 1$ (e.g. Whiley et al.

2008, Collins et al. 2009, Stott et al. 2010), our result acts to confirm trends found by other works using independent data sets.

5.2.2 Comparison with Other Studies

We show the results from a number of other studies of ICL, from both simulations and observations, in figures 5.2–5.5 alongside our results (due to the errorbars on the X-ray temperature being especially large compared with its estimated value, we have omitted the outlier XMMXCS J022634.8-040409.2 from all plots). Where relevant, we have included descriptions giving context to the results presented in the plots. The shorthand for the observational studies shown in the legends of the plots is: Gonzalez et al. (2013) (G13, parametric model) and Burke et al. (2015) (B15, $\mu_B = 25$ mag/arcsec²). Respectively, the shorthand for the simulation-based studies presented in the legends of the plots is: Puchwein et al. (2010) (P10, both with and without an AGN feedback prescription applied), Rudick et al. (2011) (R11, $\mu_V = 25$ mag/arcsec²), Contini et al. (2014) (C14, disruption model only) and Tang et al. (2018) (T18, $\mu_V = 24.7$ mag/arcsec², mock SDSS r -band; closest to our own data). All observational masses have been scaled from X-ray measurements (from either XMM Newton or Chandra in the case of the majority of the CLASH clusters) using the same scaling relation (Arnaud et al. 2005). In the case of the CLASH sample, it is worth noting that clusters with $T > 5$ keV have a $\sim 15\%$ mass increase on average between values computed from Chandra vs XMM-Newton data (see discussion in DeMaio et al. 2018 and Mahdavi et al. 2013), however, scaling the points does little to influence the interpretation of our comparisons (see upcoming discussion). In the case of the theoretical studies, the density contrast was scaled where necessary (e.g. from $\rho_c = 200$ to $\rho_c = 500$) using the method outlined in Hu & Kravtsov (2003), assuming an NFW profile with a concentration of 3.

Figures 5.2 and 5.3 show the relationship between the BCG+ICL fraction and the ICL fraction with cluster mass respectively. In both cases, there is an obvious difference between the results from simulations and observations; in that while the observations qualitatively appear fairly consistent (see upcoming discussion) the simulations appear to predict significantly larger BCG+ICL (or ICL) contributions to the overall cluster light. The exception here is Contini et al. (2014), whose results are consistent with observations (figure 5.3); their simulations are however semi-analytic rather than hydrodynamic, a

point we expand upon later in this chapter. Although not plotted here, larger BCG+ICL fractions than those seen observationally (60-80% compared with 1-60% for literature studies) were also found by [Cui et al. \(2014\)](#), who, using hydrodynamical simulations (for specifics, see [Bonafede et al. 2011](#)), measured the BCG+ICL light using a V -band surface brightness limit, similar to our own approach. [Contini et al. \(2014\)](#) also found that their ICL fractions were also very sensitive to AGN and supernova feedback; this is in contrast to [Puchwein et al. \(2010\)](#), as while the BCG+ICL fractions themselves are similar, there was little difference found between the fractions detected when an AGN model was used (see figure 5.2). [Murante et al. \(2007\)](#), being an exception, found a much lower average fraction of ICL with respect to halo mass ($\sim 22\%$) in a similar mass range to that of the CLASH clusters ($10^{14} - 10^{15} M_{\odot}$); however, they found a positive correlation between halo mass and the fraction of ICL, which has not been seen observationally. In fact, the opposite has increasingly been reported, with lower mass haloes found to be more ‘efficient’ producers of stellar mass than large clusters (e.g. figure 8 of [Tang et al. 2018](#); [DeMaio et al. 2018](#)).

Results from numerical simulations and semi-analytic models (SAMs) appear generally to be more similar to those obtained observationally (e.g. for our work, 20-40%, see [Contini et al. 2014](#), [Rudick et al. 2011](#) for some typical SAM results). [Barai et al. \(2009\)](#), using a numerical prescription, simulated the build-up of intracluster stars using several different cluster mass profiles (e.g. Perseus-like to Virgo-like) while considering the morphology of the galaxies contained within the cluster (e.g. if the BCG was a cD-type). They found mean ICL fractions of $\sim 25\%$ for a Virgo- or Perseus-like system, compared with much higher fractions ($\sim 40\%$) for an NFW model; they also found a dependence of the ICL fraction on the morphology of the BCG (with cD-type BCGs leading to generally more centrally-concentrated ICL profiles). [Henriques & Thomas \(2010\)](#), building on the semi-analytic study of BCG mass growth of [De Lucia & Blaizot \(2007\)](#), included a prescription for ICL (tidal disruption and dynamical friction); they found a mean fraction of ICL at around 18%, with a positive correlation between the ICL fraction and the halo mass of the cluster. [Contini et al. \(2014\)](#) used dark matter haloes from the Millennium simulation, coupled with several simple dynamical models (e.g. mergers, disruption, tidal stripping), finding results similar to observations in [Gonzalez et al. \(2013\)](#) (and indeed, our own), with no correlation with halo mass.

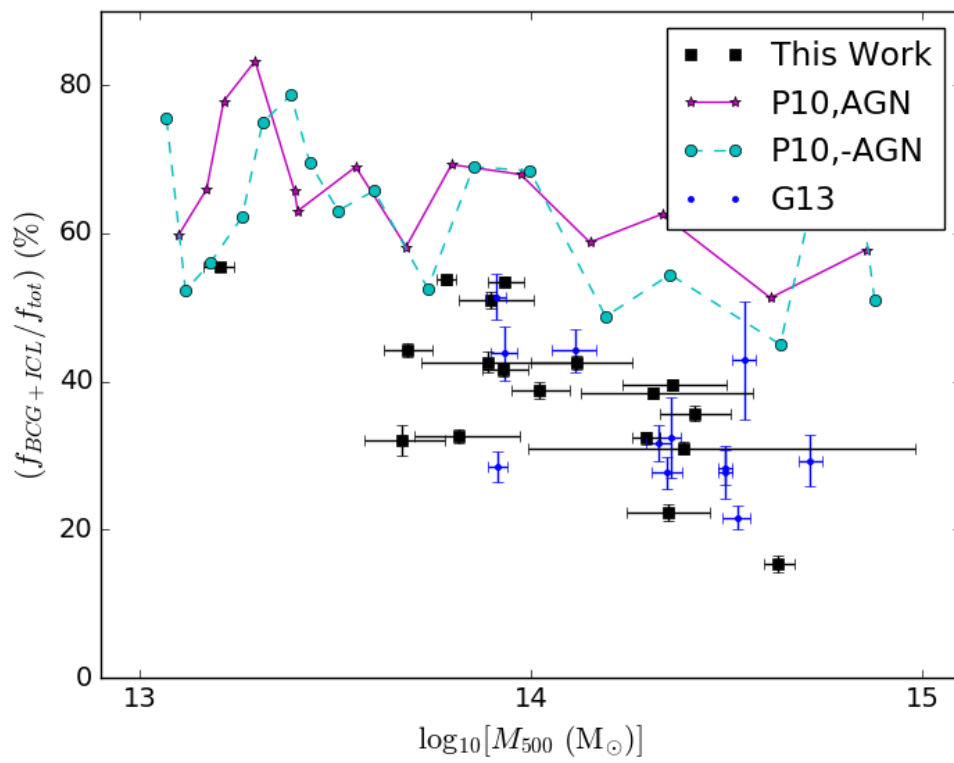


FIGURE 5.2: Comparison of the relative fluxes of ICL+BCG versus halo mass. The legend key is as follows: Puchwein et al. (2010) with/without an AGN prescription (P10, AGN/-AGN) and Gonzalez et al. (2013) (G13).

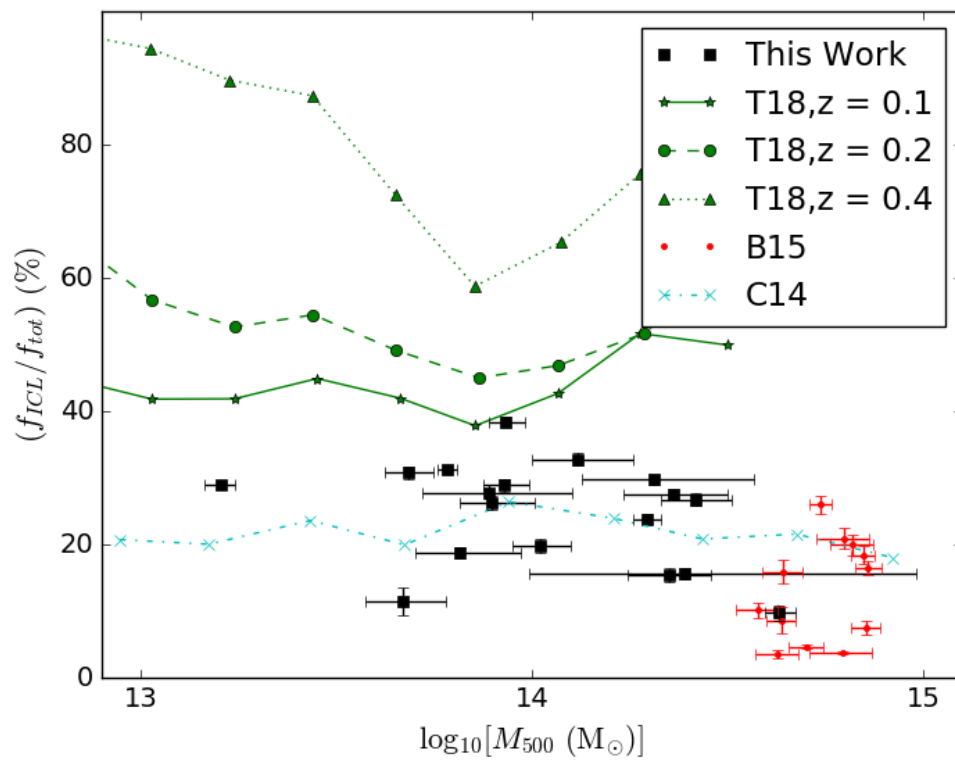


FIGURE 5.3: As in figure 5.2, but for ICL flux only (see text). The legend key is as follows: Tang et al. (2018) at redshift z (T18), Burke et al. (2015) (B15) and Contini et al. (2014) (C14).

Here, we detect no strong trend between halo mass and the fraction of ICL (as was the case in [Burke et al. 2015](#)); it is likely that any gradients present in figure 5.2 are driven by the strong anti-correlation between the fractional flux contribution of the BCG and halo mass established in the previous section (Section 5.2.1), as they are not present with the ICL fraction itself. [Toledo et al. \(2011\)](#) also find little evidence dynamically for any strong correlation between the BCG+ICL fraction with cluster mass at $z \sim 0.3$, acquiring a total fraction of $\sim 70\%$ in line with the low- z ($z < 0.1$) results of [Gonzalez et al. \(2007\)](#), though higher than the latter’s 2013 revisited study ([Gonzalez et al. 2013](#)) and indeed, our own work. Our results with respect to halo mass are fairly consistent observationally with the other studies presented in figures 5.2 and 5.3, with the $\sim 25\%$ ICL fraction and $\sim 41\%$ BCG+ICL fraction seen here comparable with the respective results of [Burke et al. \(2015\)](#) and [Gonzalez et al. \(2013\)](#). As discussed at length however in the Introduction, observational results for ICL dramatically vary in general, with a dependence on the data used and the measurement approach (see figure 8 of [Tang et al. 2018](#)).

To understand such observational differences, [Tang et al. \(2018\)](#), using a set of hydrodynamical simulations (which they themselves stress are imperfect), approached the question of observational variance on ICL measurement in great detail. Although their ICL result differs significantly from our own and that of [Burke et al. \(2015\)](#), their findings on the causes of what effects drive scatter in ICL measurements are arguably far more interesting. Using simulated images of their clusters, they produced mock observations varying numerous parameters, such as band, pixel size, surface brightness limit and PSF size. They found a clear effect from the PSF, finding that large PSFs lead to greater smoothing and a slightly higher ICL fraction (5-10%, see upcoming discussion). They also found a band dependence on the ICL fraction, finding that the r -band yielded a much larger ICL fraction ($\sim 2\times$) even when using the same equivalent V -band surface brightness limit; they attribute this in their discussion to uncertainties in their stellar population model of choice ([Bruzual & Charlot 2003](#) with a [Chabrier 2003](#) IMF). They also found that the surface brightness limit also affected their ICL result, finding a doubling in the amount of ICL detected between $23.0 < \mu_V < 26.5$ for low redshift haloes (also observed in [Cui et al. 2014](#), from whom their method for generating mock images was derived). Finally [Tang et al. \(2018\)](#) also found an *increase* in the relative fraction of ICL up to $z \sim 1$ when accounting for surface brightness dimming (see rightmost

panel of their figure 6). Their results suggest a clear motivation for more studies of this kind, which we discuss in greater detail in the upcoming chapter, as such a result has unexpected consequences regarding the current widely-accepted paradigm of BCG-ICL co-evolution (see Introduction). It is thought that the period $0 < z < 1$ is an era of rapid ICL growth, with little change in the luminosity of the BCG (though, as aforementioned and discussed at length in Chapter 3, there is a dispute about possible changes in BCG scale size).

The theoretical studies presented here also obviously differ enormously in their methodology, with some using methods to estimate ICL that are not observationally feasible (such as tracking star particles). It is, however, curious that despite more complex physical models being included in hydrodynamical simulations, they generally seem to struggle to reproduce ICL fractions with cluster mass in contrast to either a simple numerical or semi-analytic prescription. This therefore presents a challenge to these modern simulation suites and an opportunity for further analysis to better understand the reasons behind these differences, such as the effects of subgrid size and the physical models used (such as the notorious ‘overcooling’ problem, where a larger fraction of the baryons of a simulated cluster is in the form of cold gas and stars than observed, e.g. Nagai 2006).

Figures 5.4 and 5.5 show the trend of our results with redshift, for the BCG+ICL fraction and ICL fraction respectively. Although we appear consistent with Gonzalez et al. (2013) in figure 5.4, there is some deviation present between our results and those presented in figure 5.5 (e.g. Burke et al. 2015), in that our fractions with redshift appear noticeably higher; interestingly, however, there seems to be no clear consensus overall, with the slopes of ICL growth differing clearly across studies. There may be several reasons as to why this may be the case. Firstly, as noted in Tang et al. (2018), observational results are strongly influenced by several factors. The PSF, as aforementioned, was found by Tang et al. (2018) to produce a scatter of 5-10% in the total ICL fraction at a redshift range similar to that explored here ($0 < z < 0.4$ their figure 3, $\mu_V = 26.5$), with a smaller PSF (such as those found using space-based observatories as in CLASH) usually producing smaller results for the ICL fraction. They also found that measuring the ICL in a redder passband (SDSS r) increased the fraction of ICL detected, even when using the same equivalent threshold, by around a factor of 2. They also showed that shifting the surface brightness limit at which they measured the ICL (from $23.0 < \mu_V < 26.5$) also changed the fraction of ICL obtained by a factor of 2.

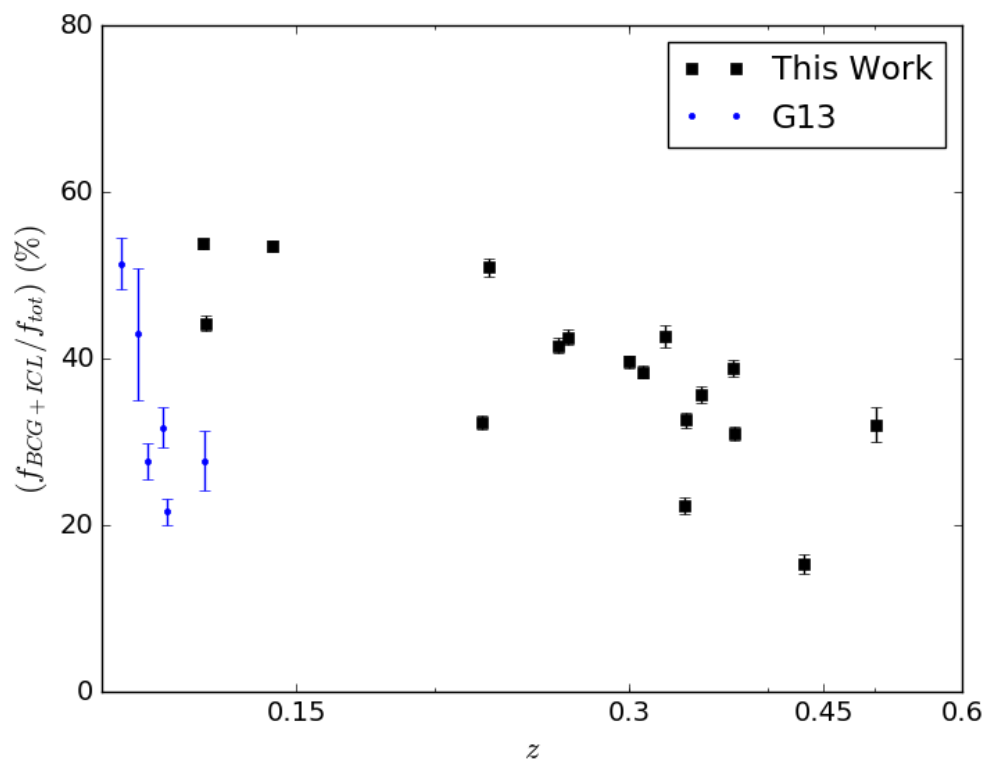


FIGURE 5.4: Comparison of the relative fluxes of ICL+BCG versus redshift, with the points from [Gonzalez et al. \(2013\)](#) (G13).

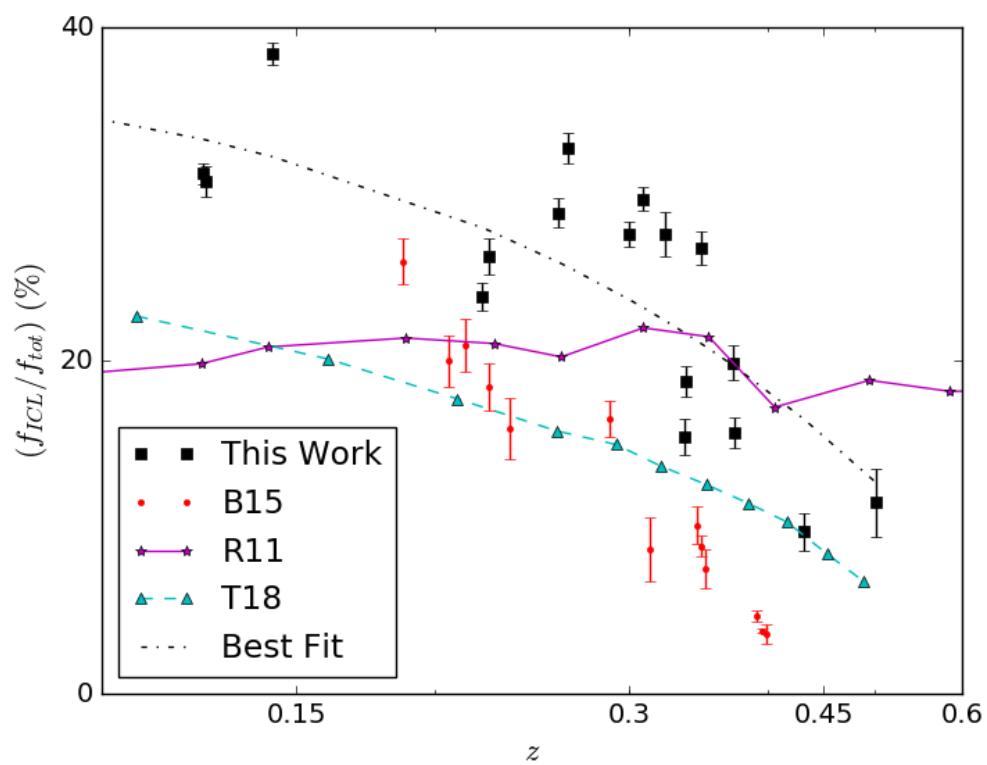


FIGURE 5.5: As in figure 5.4, but for ICL flux only. The legend key is as follows: [Burke et al. \(2015\)](#) (B15), [Rudick et al. \(2011\)](#) (R11) and [Tang et al. \(2018\)](#) (T18). The best least-squares fit has been included for comparison (slope = -54.50, intercept = +40.01).

The results from [Tang et al. \(2018\)](#) presented in figure 5.5 represent an SDSS-like, V -band image with the ICL measured faintward of an isophote of $\mu_V = 24$ mag/arcsec², with cosmological surface brightness dimming not being taken into account; this corresponds to a growth factor of ~ 3 , similar to what we observe. As previously mentioned, [Tang et al. \(2018\)](#) do not actually find any physical growth of the ICL over cosmic time; in fact, they find the ICL contribution to dramatically shrink with decreasing redshift. This result sets them starkly apart from most other theoretical studies, which, within the redshift range explored in this work, find fractional increases in the ICL relatively consistent with our own of 0.5-4 (e.g. [Willman et al. 2004](#); [Murante et al. 2007](#); [Rudick et al. 2011](#); [Contini et al. 2014](#)).

Some of the observational reasons outlined in [Tang et al. \(2018\)](#) may partially account for the difference we see between our results and the results of [Burke et al. \(2015\)](#). We have, for example, larger k -corrections due to our use of a redder band (HSC- i); testing EZGAL using the bands used in CLASH (F606W, F626, F775, F850LP) with an identical stellar evolution model however produced similar results to [Burke et al. \(2015\)](#), with the same trends. Our data is also ground-based with a larger PSF ($\langle \text{FWHM} \rangle \sim 0.5''$ for HSC), which we correct for when fitting profiles (but we do not deconvolve our data when computing ICL); the effect of this on recovering the magnitudes in HSC-SSP-Wide data was investigated in detail by [Huang et al. \(2018\)](#), where they determined a 10-18% margin of error in i -band magnitudes at 25th mag. HSC-SSP-Deep is ~ 1 magnitude deeper than that of CLASH (where, as noted in [Burke et al. 2015](#), a difference in 0.5 magnitudes in survey depth results in a 5-10% reduction in the amount of measured ICL component). Our values are, of course, also divot-corrected. We return to this discussion in Section 6.2 in Chapter 6.

One of the biggest differences we observe is that of the fractional contribution of the BCG, in that ours are far larger than those stated in [Burke et al. \(2015\)](#) ($\sim 19\%$ compared to $\sim 5\%$). It is not clear from [Burke et al. 2015](#) whether the fractions are measured relative to a set absolute cluster radius (here, $R_{X,500}$ in kpc); however, using a radius of R_{500} , similar low BCG fractions are seen in [Burke et al. \(2012\)](#) (2-4% depending on whether a de Vaucouleurs model or 50kpc aperture is used). This differs significantly from numerous other works, with which our BCG fractional contribution to the overall cluster light is more consistent; it is, for example, comparable to [Zibetti et al. \(2005\)](#) at $z \sim 0.25$, who fit de Vaucouleurs profiles and measure the relative fractions contained

within a fixed radius of 500kpc centred on the BCG. A BCG stellar mass contribution to the overall halo of around 15-40% was also noted by [Shan et al. \(2015\)](#), as well as in [Seigar et al. \(2007\)](#). The CLASH sample constitutes especially massive systems, with the range of cluster masses representing the larger end of the cluster population ($\sim 10^{15} M_{\odot}$); very little overlap is present with our sample. As ourselves and other authors have shown (see chapter 3), there appears to be an increasing inefficiency in stellar mass production with increasing halo mass, particularly with respect to the BCG (see figure 3.8 in chapter 3). We found, for example, the BCG stellar mass to halo mass ratio to decrease by approximately a factor of 10 between 10^{14} - $10^{15} M_{\odot}$.

There is also the added issue of how CLASH data was optimised for science; its original focus was specifically to study the lensed and high- z Universe, rather than for LSB science ([Postman et al. 2012](#)). The background subtraction method is generally more aggressive than the ideal to implement in a survey with a focus on LSB observations. In addition, HST’s ACS has a far smaller field of view ($\sim 2.4'$) than HSC ($\sim 1.5^{\circ}$), as well as a very small associated dither pattern in CLASH. The majority of the clusters within CLASH (given their redshift) therefore would fill the majority of a frame (for example, a cluster with a radius of 0.7 Mpc at $z = 0.4$ has an angular extent of $2.2'$, assuming our concordance cosmology in Chapter 1). This infers that it is unlikely that the true background is reached (i.e. that there is little available sky with respect to source), leading to an overestimate. The ‘missing flux’ issue with HST data was explored in detail in [Borlaff et al. \(2019\)](#), who produced a pipeline to re-reduce Hubble Ultra-Deep Field data ([Beckwith et al. 2006](#)); they found, when re-reduced, an integrate magnitude of recovered light of ~ 20 mag, which they state is comparable to the brightest galaxies in the field. Although [Borlaff et al. \(2019\)](#) did not apply their method to the CLASH data, it is likely, given the comparable observational and data-reduction methodology, that it suffers from the same issue. This issue in particular may well be a large factor in the difference between the results of [Burke et al. \(2015\)](#) and our own.

5.3 Summary of Chapter

We presented our results from our study of a sample of XCS-HSC 19 clusters outlined in chapter 5 alongside numerous other studies for comparison, from simulations and observations. We noted a large degree of scatter, observationally (1-60% across all

literature studies, 20-40% for our sample) and theoretically (10-90%) for retrieved ICL fractions; we then discussed at length some of the reasons as to why such discrepancies may exist. We conclude the following for our sample:

1. we detect no significant correlation between BCG absolute magnitude and redshift when fixing for halo mass. We also find the fractional contribution of BCG light to be strongly anti-correlated with halo mass from our partial Spearman analysis, which we determine as evidence for little stellar mass growth in BCGs compared with the overall growth of the halo,
2. we find no strong evidence that the contribution of ICL to the overall stellar content of the cluster is strongly linked to halo mass, in line with most recent simulations,
3. the fraction of ICL light is not strongly linked to the fractional contribution of the BCG, indicating a ‘decoupling’ between the two components (e.g. [DeMaio et al. 2018](#)),
4. while finding generally higher fractions with redshift, we find the ICL to grow by a factor of $\sim 2-4$ between $0.1 < z < 0.5$, slightly more modest than the factor of 4-5 in clusters over a similar range in redshift from [Burke et al. \(2015\)](#) with a higher scatter ($f_{ICL}/f_{tot} \sim 10\%$),
5. we find a significant difference generally between hydrodynamical stellar mass fractions of ICL and BCG+ICL in clusters at a given halo mass, with the simulations almost always over-predicting the contribution (even when measured in an observationally consistent way). Numerical and SAM based simulations, however, yield results closer to our observations.

Our work supports the current scenario of relatively rapid ICL build-up since $z \sim 0.5$, with BCGs remaining relatively unchanged with respect to absolute magnitude. However, we have noted several key systematic caveats. From the evidence presented in this chapter, it seems that a far greater understanding of the observational effects involved is needed (e.g. surface brightness limit used, band used, whether a BCG+ICL model fit is used and PSF size), given that such effects, as noted in [Tang et al. \(2018\)](#), can change the ICL result obtained by a factor of 2.

As sample sizes grow larger and publically-available image data improves in depth with the new generation of telescopes in the coming decade, studies will be more readily able to untangle the degeneracy between a detection of ICL growth and the effect of surface brightness dimming. For now, however, our results support the paradigm of ICL growth being the dominant stellar evolutionary component in galaxy clusters since $z \sim 1$.

Chapter 6

Conclusions and Future Work

6.1 Conclusions

In this thesis, we provide a two-part analysis into the evolution of BCGs and ICL, alongside studies of some of the systematics which may affect them. We did so primarily to gain a deeper understanding into the relationship between the evolution of stellar mass within the cluster halo and how the properties of the host cluster, so as to gain an understanding behind the discrepancy between the observed and simulated growth rates of BCGs (see discussion within the Introduction, Chapters 3 and 5) and ICL. Referring to our science goals in Section 1.5 of the Introduction, this chapter summarises our findings, discusses how successful we have been in our aims and presents some suggestions on how to build on our work in future studies, considering the capabilities of potential future datasets such as those anticipated from, for example, the LSST (e.g. Ivezic et al. 2008), JWST (e.g. Gardner et al. 2006) and E-ELT (e.g. Gilmozzi 2005).

6.1.1 *Motivation 1: How does cosmological dimming affect the recovered structure of BCGs, measured using conventional observational methods in the context of surveys?*

In Chapter 2, we described the SPIDERS survey and the nature of the sample, which is based on a hybrid optical (SDSS) and X-ray (RASS) selection process. We described the fitting methodology used to model the light profiles of our BCGs, and the operation

of the GALFIT, SExtractor and PSFEX-based SIGMA pipeline. Centrally, we outlined our use of simulated profiles to test the SIGMA pipeline and understand any biases which may result from fitting, where we found the following:

1. the presence of a strong codependency between n , R_e and apparent magnitude,
2. a negative bias in Sérsic index with effective radius, which we concluded occurred as a result of the degeneracy between the background level and profile wings,
3. a significant increase in the scatter of output effective radii at fainter magnitudes (well in excess of 50% at $m_r = 18$), which occurred regardless of band or input Sérsic index/effective radius,
4. a significant difference in behaviour in the case of $n = 1$, which we concluded was due to the lack of profile central concentration, and,
5. a marked decrease in modelling completion rate and overall robustness, dependent on both model surface brightness and the limiting magnitude of the band.

We concluded that it was clear that modelling galaxies using conventional methods (such as via a Levenberg-Marquardt algorithm) without understanding the systematics involved at low surface brightnesses can lead to results which are either biased, or deviate significantly from the expected value (e.g. figures 2.11 to 2.13). This ‘tipping’ point appears also to be several orders of magnitude above the estimated survey limit measured for high surface-brightness point-like objects (at least, for the SDSS); it is however unclear at precisely what limiting surface brightness ‘significant’ (e.g. mean deviations of over 20%) degradation of fits begins to occur. Surmising that our simulations were too coarse to probe this accurately (see discussion in ‘Future Work’), we instead set a qualitative limit of 16.5 magnitudes in r at which to count fits in our sample.

We then presented a discussion into the numerous factors as to why this degradation when modelling may take place in a fitting algorithm such as GALFIT (used throughout this thesis), such as: the dependence of morphology on overall surface brightness, influence from the choice of fitting band from the k -correction, the band depth, and the bandpass sensitivity to certain galaxy features (e.g. ‘reddish’ bulges and ‘bluish’ disks). We discussed how the feature sensitivity has led to studies adapting novel approaches to their modelling to compensate (e.g. Häußler et al. 2013, MEGAMORPH). We also

noted a similar result to our work in [Vika et al. \(2013\)](#), modelling artificially redshifted galaxies through the FERENGI software; they noted a downturn in output Sérsic index and effective radius for the galaxies in their sample.

Like [Vika et al. \(2013\)](#), we deduced that this was a fundamental factor for studies which have used profile modelling to analyse any size or concentration relations of galaxies over cosmic time (e.g. [Bernardi et al. 2007](#), [Durret et al. 2019](#)). Quantifying any change in size or shape via a parametric approach becomes next to impossible to do effectively without fully understanding the photometric limitations of the data (or indeed, modelling software) one is using. Critically, we noted that this latter point is especially true for BCGs, where a crucial period of ICL/halo component formation since $z \sim 1$ is thought to have occurred (around the last 8 Gyr). We summarised that the approach of profile modelling to quantify any growth trends with time, especially in low signal to noise cases, must therefore be used with extreme caution.

6.1.2 *Motivation 2: How do BCGs evolve with respect to their host cluster?*

In Chapter 1, we used our primary sample of 198/329 SPIDERS BCGs and investigated their morphological parameters with respect to three cluster properties of interest: X-ray luminosity, richness, and halo mass, the last property of which we estimated through the cluster velocity dispersion. Finding the results of our best-fitting parameters to be generally consistent across bands, we derived stellar masses for our BCGs based on the methods of [Taylor et al. \(2011\)](#). We concluded the following:

1. we found a weak correlation between BCG mass and Sérsic index (mostly independent of the environmental parameters used here, and redshift; see Section 3.1.1), inferring that more massive BCGs may have slightly more centrally-concentrated light profiles, e.g. in agreement with [Guo et al. \(2009\)](#) and [Durret et al. \(2019\)](#),
2. significant correlations were found to exist between the masses of our BCGs and all three of the cluster properties explored in this study (richness, cluster mass and X-ray luminosity), in agreement, for example, with [Guo et al. \(2009\)](#) and [Zhao et al. \(2015a\)](#). However, when accounting for any correlations with redshift, we did not find any significant correlation with richness.

3. there was no evidence that environment (L_X , M_{200} , λ ; Section 3.1.3) at the redshift of our clusters has any influence over the size-stellar mass relation of our BCGs (e.g. Kelkar et al. 2015), nor was there evidence for any correlation between the profile slopes of our BCGs and the cluster environment (e.g. Stott et al. 2011),
4. for a reduced sample of 102 BCGs, the environmental density was found to be highly correlated with stellar mass (e.g. Zhao et al. 2015a), but no correlation was present with either structural parameter. A partial Spearman analysis revealed this correlation to be largely independent of X-ray luminosity (see Section 3.2).

In summary, BCGs in rich, X-ray selected clusters appear to have no significant environmental dependence on their structures, independently of their mass, after $z \sim 0.3$. We concluded that if the primary driver behind growth of BCGs is indeed through multiple mergers (e.g. Ostriker & Tremaine 1975), it is likely that within the M_{200} range of the clusters explored here, the mass assembly has predominantly occurred at earlier times, with growth slowing due to the large dynamical friction timescales (τ_{dyn}) associated with massive clusters more commonly present at late times (where $\tau_{dyn} \propto \sigma^2$). We also found, using the VAC (see Section 3.3), very little redshift evolution in the scatter of the BCG $M_\star - M_{200}$ relation, with our halo mass-dependent star-formation efficiency relation for BCGs being consistent with results from recent simulations (see Section 3.3). We deduced that our findings support the scenario of the homogeneity presented by BCGs in massive clusters up to intermediate redshifts (e.g. Collins & Mann 1998, Collins et al. 2009, Whiley et al. 2008, Stott et al. 2011).

6.1.3 *Motivation 3: How do conventional image-processing methods affect the recovery of ICL?*

In Chapter 4, we presented our study into some of the known systematics of ICL recovery, namely, the issue of conventional processing pipelines mistakenly subtracting ICL as background. We also investigated the relative flux contribution from the background (e.g. faint red galaxies) at a given surface brightness. We discussed the sample of clusters in XCS used in this work and how they were selected; we also discussed the HSC-SSP survey, the current processing pipeline and the photometry. We outlined how we measured the ICL in our clusters, using a 25 mag/arcsec² equivalent B -band isophotal threshold,

measured within an aperture of radius $R_{X,500}$ centred on the brightest cluster galaxy; we then discussed the reasoning behind the methodology used (less contamination, fewer parametric assumptions). We introduced the ‘divot’ problem, which arises due to an ‘over-subtraction’ of flux from background estimation during image processing, and our method to correct for this effect. From our work, we concluded the following:

1. that there was a contribution from the background of less than 5% at the range of equivalent B -band surface brightness thresholds at which we measure ICL, which increased rapidly with the degree of surface brightness dimming,
2. that there was a loss in ICL flux of about $4\times$ the estimated background ($\sim 20\%$) from the effects of sky over-subtraction, which remains approximately constant $\pm 1\text{mag/arcsec}^2$ about our chosen threshold. We surmised that this was likely to be an underestimate, given the Sérsic models used when creating the divot corrections,
3. the divot corrections themselves did little to change the overall mean profile shape, with the 1-D profiles and parametric fits from SIGMA respectively yielding very similar results.

Our results illustrate that one must consider their data carefully when attempting to measure ICL; indeed, many authors have recognised this issue and have attempted to overcome it by using novel processing methods of their own, such as implementing less ‘aggressive’ global background subtraction techniques (often, for example, using a larger mesh, e.g. [Huang et al. 2018](#)). Our findings therefore contribute to the mandate for an overhaul, as discussed in Section 1.4.2 of the Introduction, of conventional astronomical image processing methods and observational strategies (see ‘Future Work’).

We recognised that there were some caveats with our method; for instance, surface-brightness methods of measuring ICL tend to recover less flux than methods, for example, more readily available in simulations such as setting a binding energy threshold (e.g. [Rudick et al. 2011](#)). We also make the assumption through our divot corrections that the ICL predominantly traces the cluster galaxies, not accounting for any stars in situ; hence, our corrections may underestimate the true extent of the flux loss. Finally, we noted that we were making the assumption of the BCG as the centre of the cluster when measuring the ICL. For local systems, this is often the case; however, the picture has

been known to change at high redshift, with higher number of clusters out of dynamical relaxation at $z \sim 1$ and higher (e.g. [Hatch et al. 2011](#)).

6.1.4 *Motivation 4: How does the ICL grow over time? Is its evolution linked to its corresponding BCG, or to the properties of the host cluster?*

We presented our results from our study of a sample of 19 XCS-HSC clusters outlined in Chapter 5 alongside numerous other studies for comparison, from simulations and observations. We concluded the following for our sample:

1. we detected no significant correlation between BCG absolute magnitude and redshift when fixing for halo mass. We also found the fractional contribution of BCG light to be strongly anti-correlated with halo mass, which we determined as evidence for the BCG homogeneity observed up to $z \sim 1$,
2. we found no strong evidence that the contribution of ICL to the overall stellar content of the cluster is strongly linked to halo mass, in line with most recent simulations,
3. the fraction of ICL light was not strongly linked to the fractional contribution of the BCG, indicating a ‘decoupling’ between the two components (e.g. [DeMaio et al. 2018](#)),
4. while finding generally higher fractions with redshift, we found the ICL to grow by a factor of $\sim 2 - 4$ between $0.1 < z < 0.5$, slightly more modest than the factor of $4 - 5$ in clusters over a similar range in redshift from [Burke et al. \(2015\)](#) with a higher scatter (from our work, $\sigma f_{ICL}/f_{tot} \sim 10\%$ compared with $\sim 5\%$ for [Burke et al. 2015](#)),
5. we found a significant difference generally between hydrodynamical stellar mass fractions of ICL and BCG+ICL in clusters at a given halo mass, with the hydro-sims almost always over-predicting the contribution (even when measured in an observationally consistent way). Numerical and SAM based simulations, however, yielded results closer to our observations.

Our work supports the current observational scenario of relatively rapid ICL build-up since $z \sim 0.5$, with BCGs remaining relatively unchanged with respect to absolute magnitude; this is in contrast to simulations (see discussions in Chapter 5). We noted several key systematic caveats in our work (and globally), which we did not address in Chapter 4. We stressed that a consistent method of ICL measurement alongside a far greater understanding of the observational effects involved was needed (e.g. surface brightness limit used, band used, whether a BCG+ICL model fit is used and PSF size). Finally, we noted that larger, deeper samples would be better suited to break the degeneracy between observing ICL growth and surface brightness dimming effects.

6.2 Future Work

At the time of writing, there are many advancements in anticipated observing facilities in the coming decade, which present a great deal of exciting opportunities for progression in understanding the evolution of BCGs and ICL over cosmic time. This section outlines some suggestions for best exploiting these facilities to meet those scientific goals (see discussion in Introduction), as well as suggestions of how to build on the work on systematics carried out in this thesis.

Firstly, and possibly most crucially, we are biased here with respect to our samples, in that both the SPIDERS BCG and XCS-HSC ICL samples have strong selections with respect to X-ray luminosity; our range in masses however is more extensive and arguably more representative of ‘typical’ clusters than the more extreme CLASH sample. We attempt to compensate for this with a partial Spearman analysis (see Appendix A.1 and B.2); ideally however, to study feature evolution of stellar mass within clusters, a deep, volume-limited and highly complete sample of clusters would be the ‘gold-standard’ for such work. Its launch has been delayed to 2020 at the time of writing, but the eROSITA satellite, as discussed in Section 1.3, would potentially be the optimal facility to produce such a sample. In fact, eROSITA observations were behind the initial motivation for this thesis; however, the launch of the satellite has been unfortunately delayed for technical reasons. Coupled with photometry comparable to that of the HSC-SSP from the LSST (which will be an 8m class telescope with a very high observing cadence and unprecedented 9.62° field of view; see Introduction for further discussion) would yield a remarkable look into the evolution of clusters over cosmic time, with minimal sample biases and significantly higher signal to noise (compared with those used within this thesis). In the case of ICL studies, where one is often highly limited by small cluster sample sizes, this is especially crucial in order to get a more complete consensus on its evolution over cosmic time.

Secondly, there needs to be a ready means of assessing datasets as fit for purpose with respect to galaxy parametric modelling. As we have demonstrated in Chapter 2, assuming that data will yield meaningful model results down to the quoted 5σ survey limiting magnitudes is a fallacy; indeed, we find that profile models begin to degrade several magnitudes brighter than the quoted limiting magnitude values, with model-by-model scatter dependent on the average surface brightness. Although we did not test the fitting capabilities of the HSC-SSP data as we were not as focused on acquiring accurate BCG

morphologies (see Chapter 4), we anticipate that it would be prone to the same effect, as indeed would all photometric surveys. A global analysis of all available public photometric datasets using simulated models at a large range of average surface brightnesses would be ideal for solving this problem and provide a useful reference tool. It would enable one to probe more deeply into where systematics begin to dominate the fit, and potentially also allow for the computation of approximate scaling corrections (e.g. [Bernardi et al. 2007](#)). The corrections could be then applied to legacy datasets of galaxy photometric parameters (e.g. in the SDSS, see [Simard 1998](#) for a description of the modelling code) and quality tested against outputs from object models which have photometry from deeper surveys with overlapping footprints (e.g. HSC-SSP).

Thirdly, a standardisation of observational means of measuring ICL is critical, as the variation in current methods hinders an unbiased, consistent approach. In this work, we use a thresholding technique to measure the ICL within our clusters, however, there have been parametric approaches taken in legacy studies (see discussion in Chapters 4 and 5). Although it is clear that there is a large degree of scatter in outputs from simulations (generally that they yield overlarge fractions of ICL even when using observationally-similar methods), they may prove to be an ideal testbed for developing and motivating a standard methodology. At the time of writing, this is being carried out on the C-EAGLE simulations (Kelvin et al., in prep); a state-of-the-art zoomed hydrodynamical simulation of 25 clusters (e.g. [Barnes et al. 2017b](#); $M_{clus} \sim 10^{14} M_{\odot}$). Such investigations may also allow for the development of techniques that are more physically motivated than, for example, an arbitrary threshold; simulation results projected in 2D could also potentially be compared with high signal-to-noise IFU observations of clusters (e.g. [Mahler et al. 2018](#)) to investigate techniques involving dynamical separation. As well as developing ‘gold-standard’ techniques, hydro-sims also allow one to compare and contrast existing methods, which has been explored in limited detail in several studies (e.g. [Tang et al. 2018](#); [Rudick et al. 2011](#)). This could enable an exploration of potential scaling factors between methods, to better understand comparisons of ICL measurements carried out using contrasting techniques, as well as the effect of measuring the ICL in non-relaxed systems with multiple BCG candidates (as recognised in Chapter 4).

Finally, the production of pipelines and observing strategies (e.g. nod-and-shuffle approaches, drift scanning such as in the SDSS) which take ICL (and also, galaxy halo) science into greater consideration will allow for significant strides to be made when

attempting to produce a census of stellar mass in cluster systems. Although from our work it appears possible to estimate this loss using a divot correction which recovers a significant amount of LSB flux (Chapter 4), there are significant caveats to doing so that suggest that an optimised observing strategy and pipeline would be far more desirable (such as assuming a model, and the effect of the divot correction when attempting to fit isophotes). The divot effect has been noted for the LSST stack (on which the HSC pipeline is based) and has led to its continued development with this issue in mind (e.g. Lupton et al., in prep). Some authors have already begun to work on producing more sophisticated sky subtraction methods optimised for photometry on extended or faint objects, with promising results (e.g. Ji et al. 2018). Ideally, this would also include the computation of a field-dependent, robust, more highly-extended PSF (an arcminute or more) than those currently offered by most pipelines (e.g. Duc et al. 2015), which would more robustly quantify any flux contribution present from bright stars within the field of view. One crucial question on the evolution of ICL not examined in this work is the radial variation of its stellar population; two recent observational studies, for example, have concluded that the radial variation of ICL colour suggests that tidal stripping of comparably lower-mass galaxies ($\sim 10^{10.4} M_{\odot}$) has contributed at large cluster radii to its buildup (e.g. Morishita et al. 2017; DeMaio et al. 2018), refuting long-held beliefs about the ICL generally harbouring a similar stellar population to that of the BCG. Any excess flux from stars could potentially bias such measurements and is especially important to consider alongside the increasing contamination level with cluster radius.

We have learned a number of important lessons through the work described in this thesis, particularly the influence of systematics on photometric results. As discussed in the Introduction, there is a wealth of cosmological potential in studying the evolution of stellar mass in cluster cores, from understanding the accumulation of stellar mass and whether it is related to that of the dark matter component (e.g. Erfanianfar et al., in review), and the promising use of the ICL to be used as a more accurate tracer of the dark matter halo over the ICM (e.g. Montes & Trujillo 2019). To acquire a complete picture of the evolution of stellar mass over cosmic time within cluster cores, it is our hope that some of the issues explored here, considered in the context of advanced upcoming observing facilities, will bring forth a new era of cluster science in the 2020s.

Appendix A

Part I - Supplementary Material

A.1 Part I - Partial Spearman Analysis

TABLE A.1: As in table 3.1, but for fixed R_e .

	R_e	L_X	M_{200}	n	M_*	λ	z
R_e	—	—	—	—	—	—	—
L_X	—	—	0.41439	-0.37348	0.3074	0.54307	0.53253
M_{200}	—	-8.8905	—	-0.27916	0.25043	0.48343	0.24611
n	—	-7.2236	-4.1668	—	-0.36407	-0.22452	-0.30248
M_*	—	-4.9761	-3.4282	-6.871	—	0.21417	0.42349
λ	—	-15.858	-12.265	-2.8318	-2.6114	—	0.28225
z	—	-15.17	-3.3243	-4.8288	-9.2931	-4.2512	—

TABLE A.2: As in table 3.1, but for fixed L_X .

	R_e	L_X	M_{200}	n	M_*	λ	z
R_e	—	—	-0.022206	0.64945	0.60292	-0.042913	0.20203
L_X	—	—	—	—	—	—	—
M_{200}	-0.12139	—	—	-0.12644	0.099939	0.33868	0.027848
n	-24.376	—	-1.1198	—	0.22026	-0.049023	0.032956
M_*	-20.257	—	-0.7925	-2.7399	—	0.021243	0.37383
λ	-0.26097	—	-5.9754	-0.30733	-0.11553	—	-0.018234
z	-2.3652	—	-0.15681	-0.19054	-7.2367	-0.097594	—

TABLE A.3: As in table 3.1, but for fixed M_{200} .

	R_e	L_X	M_{200}	n	M_\star	λ	z
R_e	—	0.26515	—	0.61064	0.64182	0.082771	0.30621
L_X	-3.7962	—	—	-0.063337	0.34106	0.43534	0.5292
M_{200}	—	—	—	—	—	—	—
n	-20.894	-0.42555	—	—	0.19977	-0.033542	-0.0023672
M_\star	-23.651	-6.056	—	-2.3209	—	0.13708	0.47805
λ	-0.60848	-9.8358	—	-0.19451	-1.2666	—	0.20791
z	-4.9404	-14.958	—	-0.011621	-11.974	-2.4828	—

TABLE A.4: As in table 3.1, but for fixed n .

	R_e	L_X	M_{200}	n	M_\star	λ	z
R_e	—	0.44098	0.24644	—	0.69269	0.22933	0.42767
L_X	-10.102	—	0.41151	—	0.4339	0.54493	0.57356
M_{200}	-3.3321	-8.766	—	—	0.287	0.48069	0.26014
n	—	—	—	—	—	—	—
M_\star	-28.904	-9.7689	-4.3829	—	—	0.26129	0.52637
λ	-2.9377	-15.981	-12.116	—	-3.6976	—	0.30112
z	-9.4822	-17.987	-3.6684	—	-14.78	-4.7886	—

TABLE A.5: As in table 3.1, but for fixed M_\star .

	R_e	L_X	M_{200}	n	M_\star	λ	z
R_e	—	0.028219	-0.086562	0.6433	—	-0.045577	-0.014766
L_X	-0.1592	—	0.36228	-0.20772	—	0.51141	0.46609
M_{200}	-0.64727	-6.8054	—	-0.21471	—	0.45626	0.16035
n	-23.79	-2.4788	-2.6225	—	—	-0.15252	-0.14405
M_\star	—	—	—	—	—	—	—
λ	-0.28088	-13.863	-10.846	-1.4956	—	—	0.2169
z	-0.077573	-11.345	-1.6193	-1.3676	—	-2.6685	—

TABLE A.6: As in table 3.1, but for fixed λ .

	R_e	L_X	M_{200}	n	M_\star	λ	z
R_e	—	0.25929	0.04714	0.60374	0.63716	—	0.29982
L_X	-3.6471	—	0.21151	-0.080153	0.33863	—	0.51151
M_{200}	-0.29278	-2.5564	—	-0.13082	0.16229	—	0.13857
n	-20.324	-0.58229	-1.1791	—	0.18071	—	-0.0135
M_\star	-23.219	-5.9738	-1.6507	-1.9649	—	—	0.47589
λ	—	—	—	—	—	—	—
z	-4.7505	-13.87	-1.2878	-0.070441	-11.859	—	—

TABLE A.7: As in table 3.1, but for fixed z .

	R_e	L_X	M_{200}	n	M_\star	λ	z
R_e	—	0.1256	0.016817	0.63101	0.58866	0.025858	—
L_X	-1.1086	—	0.34469	-0.12338	0.15958	0.48296	—
M_{200}	-0.089331	-6.1803	—	-0.16127	0.14449	0.44543	—
n	-22.66	-1.0792	-1.6342	—	0.20006	-0.10169	—
M_\star	-19.126	-1.6069	-1.3741	-2.3266	—	0.10323	—
λ	-0.14409	-12.24	-10.315	-0.8125	-0.83019	—	—
z	—	—	—	—	—	—	—

Appendix B

Part II - Supplementary Material

B.1 Part II - Alternative $k_{i,B}$ -correction parameters

TABLE B.1: The mean $k_{i,B}$ correction values for 3 formation redshifts z_f at 3 metallicity values (where $Z_\odot = \text{solar}$) across all BC03 models for all sample clusters within $0 < z < 0.28$. The ones selected for the clusters used in this work sit in the central cell of the table.

	$Z = Z_\odot$	$Z = 0.4Z_\odot$	$Z = 2.5Z_\odot$
$z_f = 2$	-1.4408631	-1.3203344	-1.6470296
$z_f = 3$	-1.4687423	-1.3427639	-1.667927
$z_f = 4$	-1.4810873	-1.3530817	-1.6822027

TABLE B.2: As in table B.1, but for clusters within $0.28 < z < 0.5$.

	$Z = Z_\odot$	$Z = 0.4Z_\odot$	$Z = 2.5Z_\odot$
$z_f = 2$	-1.2494659	-1.1618854	-1.4091853
$z_f = 3$	-1.2735476	-1.1754664	-1.4126995
$z_f = 4$	-1.2865313	-1.1849235	-1.4181291

B.2 Part II - Partial Spearman Analysis

TABLE B.3: Partial Spearman analysis for the parameters discussed in Chapter 5, with f_{ICL}/f_{tot} held constant.

	f_{ICL}/f_{tot}	f_{BCG}/f_{tot}	z	$\log_{10}M_{X,500}$
f_{ICL}/f_{tot}	—	—	—	—
f_{BCG}/f_{tot}	—	—	-0.1448	-0.7493
z	—	-0.2467	—	0.3198
$\log_{10}M_{X,500}$	—	-3.4625	-0.7082	—

TABLE B.4: Partial Spearman analysis for the parameters discussed in Chapter 5, with f_{BCG}/f_{tot} held constant.

	f_{ICL}/f_{tot}	f_{BCG}/f_{tot}	z	$\log_{10}M_{X,500}$
f_{ICL}/f_{tot}	—	—	-0.7854	-0.2215
f_{BCG}/f_{tot}	—	—	—	—
z	-3.9488	—	—	0.3687
$\log_{10}M_{X,500}$	-0.4237	—	-0.8787	—

TABLE B.5: Partial Spearman analysis for the parameters discussed in Chapter 5, with z held constant.

	f_{ICL}/f_{tot}	f_{BCG}/f_{tot}	z	$\log_{10}M_{X,500}$
f_{ICL}/f_{tot}	—	-0.0642	—	0.1262
f_{BCG}/f_{tot}	-0.0969	—	—	-0.7504
z	—	—	—	—
$\log_{10}M_{X,500}$	-0.2091	-3.4767	—	—

TABLE B.6: Partial Spearman analysis for the parameters discussed in Chapter 5, with $\log_{10}M_{X,500}$ held constant.

	f_{ICL}/f_{tot}	f_{BCG}/f_{tot}	z	$\log_{10}M_{X,500}$
f_{ICL}/f_{tot}	—	-0.1139	-0.7791	—
f_{BCG}/f_{tot}	-0.1852	—	0.1829	—
z	-3.8577	-0.3301	—	—
$\log_{10}M_{X,500}$	—	—	—	—

Bibliography

- Abell, G. O. (1958), ‘The Distribution of Rich Clusters of Galaxies.’, *The Astrophysical Journal Supplement Series* **3**, 211.
- Abell, G. O., Corwin, Jr., H. G. & Olowin, R. P. (1989), ‘A catalog of rich clusters of galaxies’, *The Astrophysical Journal Supplement Series* **70**, 1–138.
- Abolfathi, B., Aguado, D. S., Aguilar, G., Allende Prieto, C., Almeida, A., Ananna, T. T., Anders, F., Anderson, S. F., Andrews, B. H., Anguiano, B. & et al. (2018), ‘The Fourteenth Data Release of the Sloan Digital Sky Survey: First Spectroscopic Data from the Extended Baryon Oscillation Spectroscopic Survey and from the Second Phase of the Apache Point Observatory Galactic Evolution Experiment’, *The Astrophysical Journal Supplement Series* **235**, 42.
- Aihara, H., Allende Prieto, C., An, D., Anderson, S. F., Aubourg, É., Balbinot, E., Beers, T. C., Berlind, A. A., Bickerton, S. J., Bizyaev, D., Blanton, M. R., Bochanski, J. J., Bolton, A. S., Bovy, J., Brandt, W. N., Brinkmann, J., Brown, P. J., Brownstein, J. R., Busca, N. G., Campbell, H., Carr, M. A., Chen, Y., Chiappini, C., Comparat, J., Connolly, N., Cortes, M., Croft, R. A. C., Cuesta, A. J., da Costa, L. N., Davenport, J. R. A., Dawson, K., Dhital, S., Ealet, A., Ebelke, G. L., Edmondson, E. M., Eisenstein, D. J., Escoffier, S., Esposito, M., Evans, M. L., Fan, X., Femenía Castellá, B., Font-Ribera, A., Frinchaboy, P. M., Ge, J., Gillespie, B. A., Gilmore, G., González Hernández, J. I., Gott, J. R., Gould, A., Grebel, E. K., Gunn, J. E., Hamilton, J.-C., Harding, P., Harris, D. W., Hawley, S. L., Hearty, F. R., Ho, S., Hogg, D. W., Holtzman, J. A., Honscheid, K., Inada, N., Ivans, I. I., Jiang, L., Johnson, J. A., Jordan, C., Jordan, W. P., Kazin, E. A., Kirkby, D., Klaene, M. A., Knapp, G. R., Kneib, J.-P., Kochanek, C. S., Koesterke, L., Kollmeier, J. A., Kron, R. G., Lampeitl, H., Lang, D., Le Goff, J.-M., Lee, Y. S., Lin, Y.-T., Long, D. C., Loomis, C. P.,

- Lucatello, S., Lundgren, B., Lupton, R. H., Ma, Z., MacDonald, N., Mahadevan, S., Maia, M. A. G., Makler, M., Malanushenko, E., Malanushenko, V., Mandelbaum, R., Maraston, C., Margala, D., Masters, K. L., McBride, C. K., McGehee, P. M., McGreer, I. D., Ménard, B., Miralda-Escudé, J., Morrison, H. L., Mullally, F., Muna, D., Munn, J. A., Murayama, H., Myers, A. D., Naugle, T., Neto, A. F., Nguyen, D. C., Nichol, R. C., O'Connell, R. W., Ogando, R. L. C., Olmstead, M. D., Oravetz, D. J., Padmanabhan, N., Palanque-Delabrouille, N., Pan, K., Pandey, P., Pâris, I., Percival, W. J., Petitjean, P., Pfaffenberger, R., Pforr, J., Phleps, S., Pichon, C., Pieri, M. M., Prada, F., Price-Whelan, A. M., Raddick, M. J., Ramos, B. H. F., Reylé, C., Rich, J., Richards, G. T., Rix, H.-W., Robin, A. C., Rocha-Pinto, H. J., Rockosi, C. M., Roe, N. A., Rollinde, E., Ross, A. J., Ross, N. P., Rossetto, B. M., Sánchez, A. G., Sayres, C., Schlegel, D. J., Schlesinger, K. J., Schmidt, S. J., Schneider, D. P., Sheldon, E., Shu, Y., Simmerer, J., Simmons, A. E., Sivarani, T., Snedden, S. A., Sobeck, J. S., Steinmetz, M., Strauss, M. A., Szalay, A. S., Tanaka, M., Thakar, A. R., Thomas, D., Tinker, J. L., Tofflemire, B. M., Tojeiro, R., Tremonti, C. A., Vandenberg, J., Vargas Magaña, M., Verde, L., Vogt, N. P., Wake, D. A., Wang, J., Weaver, B. A., Weinberg, D. H., White, M., White, S. D. M., Yanny, B., Yasuda, N., Yeche, C. & Zehavi, I. (2011), 'The Eighth Data Release of the Sloan Digital Sky Survey: First Data from SDSS-III', *The Astrophysical Journal Supplement Series* **193**, 29.
- Aihara, H., Arimoto, N., Armstrong, R., Arnouts, S., Bahcall, N. A., Bickerton, S., Bosch, J., Bundy, K., Capak, P. L., Chan, J. H. H., Chiba, M., Coupon, J., Egami, E., Enoki, M., Finet, F., Fujimori, H., Fujimoto, S., Furusawa, H., Furusawa, J., Goto, T., Goulding, A., Greco, J. P., Greene, J. E., Gunn, J. E., Hamana, T., Harikane, Y., Hashimoto, Y., Hattori, T., Hayashi, M., Hayashi, Y., Helminiak, K. G., Higuchi, R., Hikage, C., Ho, P. T. P., Hsieh, B.-C., Huang, K., Huang, S., Ikeda, H., Imanishi, M., Inoue, A. K., Iwasawa, K., Iwata, I., Jaelani, A. T., Jian, H.-Y., Kamata, Y., Karoji, H., Kashikawa, N., Katayama, N., Kawanomoto, S., Kayo, I., Koda, J., Koike, M., Kojima, T., Komiyama, Y., Konno, A., Koshida, S., Koyama, Y., Kusakabe, H., Leauthaud, A., Lee, C.-H., Lin, L., Lin, Y.-T., Lupton, R. H., Mandelbaum, R., Matsuoka, Y., Medezinski, E., Mineo, S., Miyama, S., Miyatake, H., Miyazaki, S., Momose, R., More, A., More, S., Moritani, Y., Moriya, T. J., Morokuma, T., Mukae, S., Murata, R., Murayama, H., Nagao, T., Nakata, F., Niida, M., Niihara, H., Nishizawa, A. J., Obuchi, Y., Oguri, M., Oishi, Y., Okabe, N., Okamoto, S., Okura, Y., Ono, Y.,

- Onodera, M., Onoue, M., Osato, K., Ouchi, M., Price, P. A., Pyo, T.-S., Sako, M., Sawicki, M., Shibuya, T., Shimasaku, K., Shimono, A., Shirasaki, M., Silverman, J. D., Simet, M., Speagle, J., Spergel, D. N., Strauss, M. A., Sugahara, Y., Sugiyama, N., Suto, Y., Suyu, S. H., Suzuki, N., Tait, P. J., Takada, M., Takata, T., Tamura, N., Tanaka, M. M., Tanaka, M., Tanaka, M., Tanaka, Y., Terai, T., Terashima, Y., Toba, Y., Tominaga, N., Toshikawa, J., Turner, E. L., Uchida, T., Uchiyama, H., Umetsu, K., Uraguchi, F., Urata, Y., Usuda, T., Utsumi, Y., Wang, S.-Y., Wang, W.-H., Wong, K. C., Yabe, K., Yamada, Y., Yamanoi, H., Yasuda, N., Yeh, S., Yonehara, A. & Yuma, S. (2018), ‘The Hyper Suprime-Cam SSP Survey: Overview and survey design’, *Publications of the Astronomical Society of Japan* **70**, S4.
- Akerib, D. S., Bai, X., Bedikian, S., Bernard, E., Bernstein, A., Bolozdynya, A., Bradley, A., Byram, D., Cahn, S. B., Camp, C., Carmona-Benitez, M. C., Carr, D., Chapman, J. J., Chiller, A., Chiller, C., Clark, K., Classen, T., Coffey, T., Curioni, A., Dahl, E., Dazeley, S., de Viveiros, L., Dobi, A., Dragowsky, E., Druzskiewicz, E., Edwards, B., Faham, C. H., Fiorucci, S., Gaitskell, R. J., Gibson, K. R., Gilchriese, M., Hall, C., Hanhardt, M., Holbrook, B., Ihm, M., Jacobsen, R. G., Kastens, L., Kazkaz, K., Knoche, R., Kyre, S., Kwong, J., Lander, R., Larsen, N. A., Lee, C., Leonard, D. S., Lesko, K. T., Lindote, A., Lopes, M. I., Lyashenko, A., Malling, D. C., Mannino, R., Marquez, Z., McKinsey, D. N., Mei, D.-M., Mock, J., Moongweluwan, M., Morii, M., Nelson, H., Neves, F., Nikkel, J. A., Pangilinan, M., Parker, P. D., Pease, E. K., Pech, K., Phelps, P., Rodionov, A., Roberts, P., Shei, A., Shutt, T., Silva, C., Skulski, W., Solovov, V. N., Sofka, C. J., Sorensen, P., Spaans, J., Stiegler, T., Stolp, D., Svoboda, R., Sweany, M., Szydagis, M., Taylor, D., Thomson, J., Tripathi, M., Uvarov, S., Verbus, J. R., Walsh, N., Webb, R., White, D., White, J. T., Whitis, T. J., Wlasenko, M., Wolfs, F. L. H., Woods, M. & Zhang, C. (2013), ‘The Large Underground Xenon (LUX) experiment’, *Nuclear Instruments and Methods in Physics Research A* **704**, 111–126.
- Akhlaghi, M. & Ichikawa, T. (2015), ‘Noise-based Detection and Segmentation of Nebulous Objects’, *The Astrophysical Journal Supplement Series* **220**, 1.
- Akritas, M. G. & Bershad, M. A. (1996), ‘Linear Regression for Astronomical Data with Measurement Errors and Intrinsic Scatter’, *The Astrophysical Journal* **470**, 706.

- Alam, S., Albareti, F. D., Allende Prieto, C., Anders, F., Anderson, S. F., Anderton, T., Andrews, B. H., Armengaud, E., Aubourg, É., Bailey, S. & et al. (2015), ‘The Eleventh and Twelfth Data Releases of the Sloan Digital Sky Survey: Final Data from SDSS-III’, *The Astrophysical Journal Supplement Series* **219**, 12.
- Albareti, F. D., Allende Prieto, C., Almeida, A., Anders, F., Anderson, S., Andrews, B. H., Aragón-Salamanca, A., Argudo-Fernández, M., Armengaud, E., Aubourg, E. & et al. (2017), ‘The 13th Data Release of the Sloan Digital Sky Survey: First Spectroscopic Data from the SDSS-IV Survey Mapping Nearby Galaxies at Apache Point Observatory’, *The Astrophysical Journal Supplement Series* **233**, 25.
- Alpaslan, M., Driver, S., Robotham, A. S. G., Obreschkow, D., Andrae, E., Cluver, M., Kelvin, L. S., Lange, R., Owers, M., Taylor, E. N., Andrews, S. K., Bamford, S., Bland-Hawthorn, J., Brough, S., Brown, M. J. I., Colless, M., Davies, L. J. M., Eardley, E., Grootes, M. W., Hopkins, A. M., Kennedy, R., Liske, J., Lara-López, M. A., López-Sánchez, Á. R., Loveday, J., Madore, B. F., Mahajan, S., Meyer, M., Moffett, A., Norberg, P., Penny, S., Pimblet, K. A., Popescu, C. C., Seibert, M. & Tuffs, R. (2015), ‘Galaxy And Mass Assembly (GAMA): trends in galaxy colours, morphology, and stellar populations with large-scale structure, group, and pair environments’, *Monthly Notices of the Royal Astronomical Society* **451**, 3249–3268.
- Aragon-Salamanca, A., Baugh, C. M. & Kauffmann, G. (1998), ‘The K-band Hubble diagram for the brightest cluster galaxies: a test of hierarchical galaxy formation models’, *Monthly Notices of the Royal Astronomical Society* **297**, 427–434.
- Arnaud, M., Pointecouteau, E. & Pratt, G. W. (2005), ‘The structural and scaling properties of nearby galaxy clusters. II. The M-T relation’, *Astronomy & Astrophysics* **441**, 893–903.
- Arnouts, S., Cristiani, S., Moscardini, L., Matarrese, S., Lucchin, F., Fontana, A. & Giallongo, E. (1999), ‘Measuring and modelling the redshift evolution of clustering: the Hubble Deep Field North’, *Monthly Notices of the Royal Astronomical Society* **310**, 540–556.
- Ascaso, B., Aguerri, J. A. L., Varela, J., Cava, A., Bettoni, D., Moles, M. & D’Onofrio, M. (2011), ‘Evolution of Brightest Cluster Galaxy Structural Parameters in the Last ~6 Gyr: Feedback Processes Versus Merger Events’, *The Astrophysical Journal* **726**, 69.

- Bai, L., Yee, H. K. C., Yan, R., Lee, E., Gilbank, D. G., Ellingson, E., Barrientos, L. F., Gladders, M. D., Hsieh, B. C. & Li, I. H. (2014), ‘The Inside-out Growth of the Most Massive Galaxies at $0.3 < z < 0.9$ ’, *The Astrophysical Journal* **789**(2), 134.
- Baldry, I. K., Balogh, M. L., Bower, R. G., Glazebrook, K., Nichol, R. C., Bamford, S. P. & Budavari, T. (2006), ‘Galaxy bimodality versus stellar mass and environment’, *Monthly Notices of the Royal Astronomical Society* **373**, 469–483.
- Baldry, I. K., Driver, S. P., Loveday, J., Taylor, E. N., Kelvin, L. S., Liske, J., Norberg, P., Robotham, A. S. G., Brough, S., Hopkins, A. M., Bamford, S. P., Peacock, J. A., Bland-Hawthorn, J., Conselice, C. J., Croom, S. M., Jones, D. H., Parkinson, H. R., Popescu, C. C., Prescott, M., Sharp, R. G. & Tuffs, R. J. (2012), ‘Galaxy And Mass Assembly (GAMA): the galaxy stellar mass function at $z < 0.06$ ’, *Monthly Notices of the Royal Astronomical Society* **421**, 621–634.
- Balogh, M. L., Mazzotta, P., Bower, R. G., Eke, V., Bourdin, H., Lu, T. & Theuns, T. (2011), ‘The stellar and hot gas content of low-mass galaxy clusters’, *Monthly Notices of the Royal Astronomical Society* **412**, 947–959.
- Bamford, S. P., Häußler, B., Rojas, A. & Borch, A. (2011), Measuring the Physical Properties of Galaxy Components Using Modern Surveys, in I. N. Evans, A. Accomazzi, D. J. Mink & A. H. Rots, eds, ‘Astronomical Data Analysis Software and Systems XX’, Vol. 442 of *Astronomical Society of the Pacific Conference Series*, p. 479.
- Barai, P., Brito, W. & Martel, H. (2009), ‘The Fate of Dwarf Galaxies in Clusters and the Origin of Intracluster Stars’, *Journal of Astrophysics and Astronomy* **30**(1), 1–36.
- Barden, M., Häußler, B., Peng, C. Y., McIntosh, D. H. & Guo, Y. (2012), ‘GALAPAGOS: from pixels to parameters’, *Monthly Notices of the Royal Astronomical Society* **422**, 449–468.
- Barden, M., Jahnke, K. & Häußler, B. (2008), ‘FERENGI: Redshifting Galaxies from SDSS to GEMS, STAGES, and COSMOS’, *The Astrophysical Journal Supplement Series* **175**, 105–115.
- Barnes, D. J., Kay, S. T., Bahé, Y. M., Dalla Vecchia, C., McCarthy, I. G., Schaye, J., Bower, R. G., Jenkins, A., Thomas, P. A., Schaller, M., Crain, R. A., Theuns, T. & White, S. D. M. (2017b), ‘The Cluster-EAGLE project: global properties of simulated

- clusters with resolved galaxies', *Monthly Notices of the Royal Astronomical Society* **471**, 1088–1106.
- Barnes, D. J., Kay, S. T., Henson, M. A., McCarthy, I. G., Schaye, J. & Jenkins, A. (2017a), 'The redshift evolution of massive galaxy clusters in the MACSIS simulations', *Monthly Notices of the Royal Astronomical Society* **465**, 213–233.
- Bautz, L. P. & Morgan, W. W. (1970), 'On the Classification of the Forms of Clusters of Galaxies', *The Astrophysical Journal Letters* **162**, L149.
- Beckwith, S. V. W., Stiavelli, M., Koekemoer, A. M., Caldwell, J. A. R., Ferguson, H. C., Hook, R., Lucas, R. A., Bergeron, L. E., Corbin, M., Jogee, S., Panagia, N., Robberto, M., Royle, P., Somerville, R. S. & Sosey, M. (2006), 'The Hubble Ultra Deep Field', *The Astronomical Journal* **132**, 1729–1755.
- Beers, T. C., Flynn, K. & Gebhardt, K. (1990), 'Measures of location and scale for velocities in clusters of galaxies - A robust approach', *The Astronomical Journal* **100**, 32–46.
- Behroozi, P. & Silk, J. (2018), 'The most massive galaxies and black holes allowed by Λ CDM', *Monthly Notices of the Royal Astronomical Society* **477**, 5382–5387.
- Bell, E. F., McIntosh, D. H., Katz, N. & Weinberg, M. D. (2003), 'The Optical and Near-Infrared Properties of Galaxies. I. Luminosity and Stellar Mass Functions', *The Astrophysical Journal Supplement Series* **149**, 289–312.
- Bennett, C. L., Bay, M., Halpern, M., Hinshaw, G., Jackson, C., Jarosik, N., Kogut, A., Limon, M., Meyer, S. S., Page, L., Spergel, D. N., Tucker, G. S., Wilkinson, D. T., Wollack, E. & Wright, E. L. (2003), 'The Microwave Anisotropy Probe Mission', *The Astrophysical Journal* **583**, 1–23.
- Bernardi, M. (2009), 'Evolution in the structural properties of early-type brightest cluster galaxies at small lookback time and dependence on the environment', *Monthly Notices of the Royal Astronomical Society* **395**, 1491–1506.
- Bernardi, M., Fischer, J.-L., Sheth, R. K., Meert, A., Huertas-Company, M., Shankar, F. & Vikram, V. (2017), 'Comparing pzmorph and SDSS photometry - II. The differences are more than semantics and are not dominated by intracluster light', *Monthly Notices of the Royal Astronomical Society* **468**, 2569–2581.

- Bernardi, M., Hyde, J. B., Sheth, R. K., Miller, C. J. & Nichol, R. C. (2007), ‘The Luminosities, Sizes, and Velocity Dispersions of Brightest Cluster Galaxies: Implications for Formation History’, *The Astronomical Journal* **133**, 1741–1755.
- Bernardi, M., Meert, A., Sheth, R. K., Vikram, V., Huertas-Company, M., Mei, S. & Shankar, F. (2013), ‘The massive end of the luminosity and stellar mass functions: dependence on the fit to the light profile’, *Monthly Notices of the Royal Astronomical Society* **436**, 697–704.
- Bernardi, M., Meert, A., Vikram, V., Huertas-Company, M., Mei, S., Shankar, F. & Sheth, R. K. (2014), ‘Systematic effects on the size-luminosity relations of early- and late-type galaxies: dependence on model fitting and morphology’, *Monthly Notices of the Royal Astronomical Society* **443**, 874–897.
- Bertin, E. (2009), ‘SkyMaker: astronomical image simulations made easy.’, *Memorie della Societa Astronomica Italiana* **80**, 422.
- Bertin, E. (2010), ‘SWarp: Resampling and Co-adding FITS Images Together’, Astrophysics Source Code Library.
- Bertin, E. (2013), ‘PSFEx: Point Spread Function Extractor’, Astrophysics Source Code Library.
- Bertin, E. & Arnouts, S. (1996), ‘SExtractor: Software for source extraction.’, *Astronomy & Astrophysics Supplement Series* **117**, 393–404.
- Best, P. N., von der Linden, A., Kauffmann, G., Heckman, T. M. & Kaiser, C. R. (2007), ‘On the prevalence of radio-loud active galactic nuclei in brightest cluster galaxies: implications for AGN heating of cooling flows’, *Monthly Notices of the Royal Astronomical Society* **379**, 894–908.
- Bevington, P. R. (1969), *Data reduction and error analysis for the physical sciences*.
- Beygu, B., Kreckel, K., van der Hulst, J. M., Jarrett, T. H., Peletier, R., van de Weygaert, R., van Gorkom, J. H. & Aragon-Calvo, M. A. (2016), ‘The void galaxy survey: Star formation properties’, *Monthly Notices of the Royal Astronomical Society* **458**, 394–409.
- Bhavsar, S. P. & Barrow, J. D. (1985), ‘First ranked galaxies in groups and clusters’, *Monthly Notices of the Royal Astronomical Society* **213**, 857–869.

- Bianchi, L. & the GALEX Team (1999), ‘The Galaxy Evolution Explorer (GALEX): an All Sky Ultraviolet Survey’, *Memorie della Societa Astronomica Italiana* **70**.
- Birkhoff, G. D. & Langer, R. E. (1923), *Relativity and modern physics*.
- Birkinshaw, M. (1999), ‘The Sunyaev-Zel’dovich effect’, *Physics Reports* **310**, 97–195.
- Biviano, A. & Salucci, P. (2006), ‘The radial profiles of the different mass components in galaxy clusters’, *Astronomy & Astrophysics* **452**, 75–81.
- Blanton, M. R., Bershad, M. A., Abolfathi, B., Albareti, F. D., Allende Prieto, C., Almeida, A., Alonso-García, J., Anders, F., Anderson, S. F., Andrews, B. & et al. (2017), ‘Sloan Digital Sky Survey IV: Mapping the Milky Way, Nearby Galaxies, and the Distant Universe’, *The Astronomical Journal* **154**, 28.
- Blanton, M. R., Kazin, E., Muna, D., Weaver, B. A. & Price-Whelan, A. (2011), ‘Improved Background Subtraction for the Sloan Digital Sky Survey Images’, *The Astronomical Journal* **142**, 31.
- Blanton, M. R., Lin, H., Lupton, R. H., Maley, F. M., Young, N., Zehavi, I. & Loveday, J. (2003), ‘An Efficient Targeting Strategy for Multiobject Spectrograph Surveys: the Sloan Digital Sky Survey “Tiling” Algorithm’, *The Astronomical Journal* **125**, 2276–2286.
- Blanton, M. R. & Roweis, S. (2007), ‘K-Corrections and Filter Transformations in the Ultraviolet, Optical, and Near-Infrared’, *The Astronomical Journal* **133**, 734–754.
- Bocquet, S., Saro, A., Mohr, J. J., Aird, K. A., Ashby, M. L. N., Bautz, M., Bayliss, M., Bazin, G., Benson, B. A., Bleem, L. E., Brodwin, M., Carlstrom, J. E., Chang, C. L., Chiu, I., Cho, H. M., Clocchiatti, A., Crawford, T. M., Crites, A. T., Desai, S., de Haan, T., Dietrich, J. P., Dobbs, M. A., Foley, R. J., Forman, W. R., Gangkofner, D., George, E. M., Gladders, M. D., Gonzalez, A. H., Halverson, N. W., Hennig, C., Hlavacek-Larrondo, J., Holder, G. P., Holzzapfel, W. L., Hrubes, J. D., Jones, C., Keisler, R., Knox, L., Lee, A. T., Leitch, E. M., Liu, J., Lueker, M., Luong-Van, D., Marrone, D. P., McDonald, M., McMahon, J. J., Meyer, S. S., Mocuano, L., Murray, S. S., Padin, S., Pryke, C., Reichardt, C. L., Rest, A., Ruel, J., Ruhl, J. E., Saliwanchik, B. R., Sayre, J. T., Schaffer, K. K., Shirokoff, E., Spieler, H. G., Stalder, B., Stanford, S. A., Staniszewski, Z., Stark, A. A., Story, K., Stubbs, C. W., Vanderlinde, K.,

- Vieira, J. D., Vikhlinin, A., Williamson, R., Zahn, O. & Zenteno, A. (2015), ‘Mass Calibration and Cosmological Analysis of the SPT-SZ Galaxy Cluster Sample Using Velocity Dispersion σ_v and X-Ray Y_X Measurements’, *The Astrophysical Journal* **799**, 214.
- Böhringer, H., Chon, G., Bristow, M. & Collins, C. A. (2015), ‘The extended ROSAT-ESO Flux-Limited X-ray Galaxy Cluster Survey (REFLEX II). V. Exploring a local underdensity in the southern sky’, *Astronomy & Astrophysics* **574**, A26.
- Böhringer, H., Schuecker, P., Guzzo, L., Collins, C. A., Voges, W., Schindler, S., Neumann, D. M., Cruddace, R. G., De Grandi, S., Chincarini, G., Edge, A. C., MacGillivray, H. T. & Shaver, P. (2001), ‘The ROSAT-ESO flux limited X-ray (REFLEX) galaxy cluster survey. I. The construction of the cluster sample’, *Astronomy & Astrophysics* **369**, 826–850.
- Böhringer, H., Schuecker, P., Pratt, G. W., Arnaud, M., Ponman, T. J., Croston, J. H., Borgani, S., Bower, R. G., Briel, U. G., Collins, C. A., Donahue, M., Forman, W. R., Finoguenov, A., Geller, M. J., Guzzo, L., Henry, J. P., Kneissl, R., Mohr, J. J., Matsushita, K., Mullis, C. R., Ohashi, T., Pedersen, K., Pierini, D., Quintana, H., Raychaudhury, S., Reiprich, T. H., Romer, A. K., Rosati, P., Sabirli, K., Temple, R. F., Viana, P. T. P., Vikhlinin, A., Voit, G. M. & Zhang, Y. Y. (2007), ‘The representative XMM-Newton cluster structure survey (REXCESS) of an X-ray luminosity selected galaxy cluster sample’, *Astronomy & Astrophysics* **469**(1), 363–377.
- Bolton, A. S., Schlegel, D. J., Aubourg, É., Bailey, S., Bhardwaj, V., Brownstein, J. R., Burles, S., Chen, Y.-M., Dawson, K., Eisenstein, D. J., Gunn, J. E., Knapp, G. R., Loomis, C. P., Lupton, R. H., Maraston, C., Muna, D., Myers, A. D., Olmstead, M. D., Padmanabhan, N., Pâris, I., Percival, W. J., Petitjean, P., Rockosi, C. M., Ross, N. P., Schneider, D. P., Shu, Y., Strauss, M. A., Thomas, D., Tremonti, C. A., Wake, D. A., Weaver, B. A. & Wood-Vasey, W. M. (2012), ‘Spectral Classification and Redshift Measurement for the SDSS-III Baryon Oscillation Spectroscopic Survey’, *The Astronomical Journal* **144**, 144.
- Bonafede, A., Dolag, K., Stasyszyn, F., Murante, G. & Borgani, S. (2011), ‘A non-ideal magnetohydrodynamic GADGET: simulating massive galaxy clusters’, *Monthly Notices of the Royal Astronomical Society* **418**, 2234–2250.

- Borgani, S., Dolag, K., Murante, G., Cheng, L.-M., Springel, V., Diaferio, A., Moscardini, L., Tormen, G., Tornatore, L. & Tozzi, P. (2006), ‘Hot and cooled baryons in smoothed particle hydrodynamic simulations of galaxy clusters: physics and numerics’, *Monthly Notices of the Royal Astronomical Society* **367**, 1641–1654.
- Borgani, S., Murante, G., Springel, V., Diaferio, A., Dolag, K., Moscardini, L., Tormen, G., Tornatore, L. & Tozzi, P. (2004), ‘X-ray properties of galaxy clusters and groups from a cosmological hydrodynamical simulation’, *Monthly Notices of the Royal Astronomical Society* **348**, 1078–1096.
- Borlaff, A., Trujillo, I., Román, J., Beckman, J. E., Eliche-Moral, M. C., Infante-Sáinz, R., Lumbreras-Calle, A., de Almagro, R. T. S. M., Gómez-Guijarro, C., Cebrián, M., Dorta, A., Cardiel, N., Akhlaghi, M. & Martínez-Lombilla, C. (2019), ‘The missing light of the Hubble Ultra Deep Field’, *Astronomy & Astrophysics* **621**, A133.
- Bosch, J., Armstrong, R., Bickerton, S., Furusawa, H., Ikeda, H., Koike, M., Lupton, R., Mineo, S., Price, P., Takata, T., Tanaka, M., Yasuda, N., AlSayyad, Y., Becker, A. C., Coulton, W., Coupon, J., Garmilla, J., Huang, S., Krughoff, K. S., Lang, D., Leauthaud, A., Lim, K.-T., Lust, N. B., MacArthur, L. A., Mandelbaum, R., Miyatake, H., Miyazaki, S., Murata, R., More, S., Okura, Y., Owen, R., Swinbank, J. D., Strauss, M. A., Yamada, Y. & Yamanoi, H. (2018), ‘The Hyper Suprime-Cam software pipeline’, *Publications of the Astronomical Society of Japan* **70**, S5.
- Brinchmann, J., Charlot, S., Heckman, T. M., Kauffmann, G., Tremonti, C. & White, S. D. M. (2004a), ‘Stellar masses, star formation rates, metallicities and AGN properties for 200,000 galaxies in the SDSS Data Release Two (DR2)’, *arXiv Astrophysics e-prints* .
- Brinchmann, J., Charlot, S., White, S. D. M., Tremonti, C., Kauffmann, G., Heckman, T. & Brinkmann, J. (2004b), ‘The physical properties of star-forming galaxies in the low-redshift Universe’, *Monthly Notices of the Royal Astronomical Society* **351**, 1151–1179.
- Brough, S., Collins, C. A., Burke, D. J., Lynam, P. D. & Mann, R. G. (2005), ‘Environmental dependence of the structure of brightest cluster galaxies’, *Monthly Notices of the Royal Astronomical Society* **364**, 1354–1362.

- Brough, S., Tran, K.-V., Sharp, R. G., von der Linden, A. & Couch, W. J. (2011), ‘Spatial kinematics of Brightest Cluster Galaxies and their close companions from Integral Field Unit spectroscopy’, *Monthly Notices of the Royal Astronomical Society* **414**, L80–L84.
- Bruzual, G. & Charlot, S. (2003), ‘Stellar population synthesis at the resolution of 2003’, *Monthly Notices of the Royal Astronomical Society* **344**, 1000–1028.
- Burke, C. & Collins, C. A. (2013), ‘Growth of brightest cluster galaxies via mergers since $z=1$ ’, *Monthly Notices of the Royal Astronomical Society* **434**, 2856–2865.
- Burke, C., Collins, C. A., Stott, J. P. & Hilton, M. (2012), ‘Measurement of the intracluster light at $z \sim 1$ ’, *Monthly Notices of the Royal Astronomical Society* **425**, 2058–2068.
- Burke, C., Hilton, M. & Collins, C. (2015), ‘Coevolution of brightest cluster galaxies and intracluster light using CLASH’, *Monthly Notices of the Royal Astronomical Society* **449**, 2353–2367.
- Burke, D. J., Collins, C. A. & Mann, R. G. (2000), ‘Cluster Selection and the Evolution of Brightest Cluster Galaxies’, *The Astrophysical Journal Letters* **532**, L105–L108.
- Burns, J. O. (1990), ‘The radio properties of cD galaxies in Abell clusters. I - an X-ray selected sample’, *The Astronomical Journal* **99**, 14–30.
- Caldwell, C. E., McCarthy, I. G., Baldry, I. K., Collins, C. A., Schaye, J. & Bird, S. (2016), ‘Cosmology with velocity dispersion counts: an alternative to measuring cluster halo masses’, *Monthly Notices of the Royal Astronomical Society* **462**, 4117–4129.
- Carlberg, R. G., Yee, H. K. C., Ellingson, E., Abraham, R., Gravel, P., Morris, S. & Pritchet, C. J. (1996), ‘Galaxy Cluster Virial Masses and Omega’, *The Astrophysical Journal* **462**, 32.
- Carlstrom, J. E., Ade, P. A. R., Aird, K. A., Benson, B. A., Bleem, L. E., Busetti, S., Chang, C. L., Chauvin, E., Cho, H.-M., Crawford, T. M., Crites, A. T., Dobbs, M. A., Halverson, N. W., Heimsath, S., Holzzapfel, W. L., Hrubes, J. D., Joy, M., Keisler, R., Lanting, T. M., Lee, A. T., Leitch, E. M., Leong, J., Lu, W., Lueker, M., Luong-Van, D., McMahon, J. J., Mehl, J., Meyer, S. S., Mohr, J. J., Montroy, T. E., Padin, S., Plagge, T., Pryke, C., Ruhl, J. E., Schaffer, K. K., Schwan, D., Shirokoff, E., Spieler, H. G., Staniszewski, Z., Stark, A. A., Tucker, C., Vanderlinde, K., Vieira,

- J. D. & Williamson, R. (2011), ‘The 10 Meter South Pole Telescope’, *Publications of the Astronomical Society of the Pacific* **123**, 568.
- Carr, B. J., Kohri, K., Sendouda, Y. & Yokoyama, J. (2010), ‘New cosmological constraints on primordial black holes’, *Phys. Rev. D* **81**, 104019.
URL: <https://link.aps.org/doi/10.1103/PhysRevD.81.104019>
- Chabrier, G. (2003), ‘Galactic Stellar and Substellar Initial Mass Function’, *Publications of the Astronomical Society of the Pacific* **115**, 763–795.
- Chambers, K. C., Magnier, E. A., Metcalfe, N., Flewelling, H. A., Huber, M. E., Waters, C. Z., Denneau, L., Draper, P. W., Farrow, D., Finkbeiner, D. P., Holmberg, C., Koppenhoefer, J., Price, P. A., Saglia, R. P., Schlafly, E. F., Smartt, S. J., Sweeney, W., Wainscoat, R. J., Burgett, W. S., Grav, T., Heasley, J. N., Hodapp, K. W., Jedicke, R., Kaiser, N., Kudritzki, R.-P., Luppino, G. A., Lupton, R. H., Monet, D. G., Morgan, J. S., Onaka, P. M., Stubbs, C. W., Tonry, J. L., Banados, E., Bell, E. F., Bender, R., Bernard, E. J., Botticella, M. T., Casertano, S., Chastel, S., Chen, W.-P., Chen, X., Cole, S., Deacon, N., Frenk, C., Fitzsimmons, A., Gezari, S., Goessl, C., Goggia, T., Goldman, B., Grebel, E. K., Hambly, N. C., Hasinger, G., Heavens, A. F., Heckman, T. M., Henderson, R., Henning, T., Holman, M., Hopp, U., Ip, W.-H., Isani, S., Keyes, C. D., Koekemoer, A., Kotak, R., Long, K. S., Lucey, J. R., Liu, M., Martin, N. F., McLean, B., Morganson, E., Murphy, D. N. A., Nieto-Santisteban, M. A., Norberg, P., Peacock, J. A., Pier, E. A., Postman, M., Primak, N., Rae, C., Rest, A., Riess, A., Riffeser, A., Rix, H. W., Roser, S., Schilbach, E., Schultz, A. S. B., Scolnic, D., Szalay, A., Seitz, S., Shiao, B., Small, E., Smith, K. W., Soderblom, D., Taylor, A. N., Thakar, A. R., Thiel, J., Thilker, D., Urata, Y., Valenti, J., Walter, F., Watters, S. P., Werner, S., White, R., Wood-Vasey, W. M. & Wyse, R. (2016), ‘The Pan-STARRS1 Surveys’, *ArXiv e-prints* .
- Chan, M. C. & Stott, J. P. (2019), ‘Deep-CEE I: Fishing for Galaxy Clusters with Deep Neural Nets’, *arXiv e-prints* p. arXiv:1906.08784.
- Chilingarian, I. V., Melchior, A.-L. & Zolotukhin, I. Y. (2010), ‘Analytical approximations of K-corrections in optical and near-infrared bands’, *Monthly Notices of the Royal Astronomical Society* **405**, 1409–1420.

- Cibirka, N., Cypriano, E. S., Brimiouille, F., Gruen, D., Erben, T., van Waerbeke, L., Miller, L., Finoguenov, A., Kirkpatrick, C., Henry, J. P., Rykoff, E., Rozo, E., Dupke, R., Kneib, J.-P., Shan, H. & Spinelli, P. (2017), ‘CODEX weak lensing: concentration of galaxy clusters at $z \sim 0.5$ ’, *Monthly Notices of the Royal Astronomical Society* **468**, 1092–1116.
- Ciotti, L. (1991), ‘Stellar systems following the $R \propto 1/m$ luminosity law’, *Astronomy & Astrophysics* **249**, 99–106.
- Clerc, N., Merloni, A., Zhang, Y.-Y., Finoguenov, A., Dwelly, T., Nandra, K., Collins, C., Dawson, K., Kneib, J.-P., Rozo, E., Rykoff, E., Sadibekova, T., Brownstein, J., Lin, Y.-T., Ridl, J., Salvato, M., Schwobe, A., Steinmetz, M., Seo, H.-J. & Tinker, J. (2016), ‘SPIDERS: the spectroscopic follow-up of X-ray selected clusters of galaxies in SDSS-IV’, *Monthly Notices of the Royal Astronomical Society* **463**, 4490–4515.
- Clerc, N., Sadibekova, T., Pierre, M., Pacaud, F., Le Fèvre, J.-P., Adami, C., Altieri, B. & Valtchanov, I. (2012), ‘The cosmological analysis of X-ray cluster surveys - II. Application of the CR-HR method to the XMM archive’, *Monthly Notices of the Royal Astronomical Society* **423**, 3561–3583.
- Colless, M., Dalton, G., Maddox, S., Sutherland, W., Norberg, P., Cole, S., Bland-Hawthorn, J., Bridges, T., Cannon, R., Collins, C., Couch, W., Cross, N., Deeley, K., De Propriis, R., Driver, S. P., Efstathiou, G., Ellis, R. S., Frenk, C. S., Glazebrook, K., Jackson, C., Lahav, O., Lewis, I., Lumsden, S., Madgwick, D., Peacock, J. A., Peterson, B. A., Price, I., Seaborne, M. & Taylor, K. (2001), ‘The 2dF Galaxy Redshift Survey: spectra and redshifts’, *Monthly Notices of the Royal Astronomical Society* **328**, 1039–1063.
- Collins, C. A., Guzzo, L., Nichol, R. C. & Lumsden, S. L. (1995), ‘The Edinburgh-Durham Southern Galaxy Catalogue - VII. The Edinburgh-Milano cluster redshift survey’, *Monthly Notices of the Royal Astronomical Society* **274**, 1071–1092.
- Collins, C. A. & Mann, R. G. (1998), ‘The K-band Hubble diagram for brightest cluster galaxies in X-ray clusters’, *Monthly Notices of the Royal Astronomical Society* **297**, 128–142.
- Collins, C. A., Stott, J. P., Hilton, M., Kay, S. T., Stanford, S. A., Davidson, M., Hosmer, M., Hoyle, B., Liddle, A., Lloyd-Davies, E., Mann, R. G., Mehrtens, N., Miller, C. J.,

- Nichol, R. C., Romer, A. K., Sahlén, M., Viana, P. T. P. & West, M. J. (2009), ‘Early assembly of the most massive galaxies’, *Nature* **458**, 603–606.
- Collins, C., Brough, S., Burke, D., Mann, R. & Lynam, P. (2003), ‘The Evolution of Brightest Cluster Galaxies’, *Astrophysics & Space Science* **285**, 51–60.
- Contini, E., De Lucia, G., Villalobos, Á. & Borgani, S. (2014), ‘On the formation and physical properties of the intracluster light in hierarchical galaxy formation models’, *Monthly Notices of the Royal Astronomical Society* **437**, 3787–3802.
- Cooke, E. A., Hatch, N. A., Muldrew, S. I., Rigby, E. E. & Kurk, J. D. (2014), ‘A $z = 2.5$ protocluster associated with the radio galaxy MRC 2104-242: star formation and differing mass functions in dense environments’, *Monthly Notices of the Royal Astronomical Society* **440**, 3262–3274.
- Cooke, E. A., Hatch, N. A., Stern, D., Rettura, A., Brodwin, M., Galametz, A., Wylezalek, D., Bridge, C., Conselice, C. J., De Breuck, C., Gonzalez, A. H. & Jarvis, M. (2016), ‘A Mature Galaxy Cluster at $z=1.58$ around the Radio Galaxy 7C1753+6311’, *The Astrophysical Journal* **816**, 83.
- Cooper, M. C., Griffith, R. L., Newman, J. A., Coil, A. L., Davis, M., Dutton, A. A., Faber, S. M., Guhathakurta, P., Koo, D. C., Lotz, J. M., Weiner, B. J., Willmer, C. N. A. & Yan, R. (2012), ‘The DEEP3 Galaxy Redshift Survey: the impact of environment on the size evolution of massive early-type galaxies at intermediate redshift’, *Monthly Notices of the Royal Astronomical Society* **419**, 3018–3027.
- Correa, C. A., Schaye, J., Clauwens, B., Bower, R. G., Crain, R. A., Schaller, M., Theuns, T. & Thob, A. C. R. (2017), ‘The relation between galaxy morphology and colour in the EAGLE simulation’, *Monthly Notices of the Royal Astronomical Society* **472**, L45–L49.
- Coupon, J., Czakon, N., Bosch, J., Komiyama, Y., Medezinski, E., Miyazaki, S. & Oguri, M. (2018), ‘The bright-star masks for the HSC-SSP survey’, *Publications of the Astronomical Society of Japan* **70**, S7.
- Crawford, C. S., Allen, S. W., Ebeling, H., Edge, A. C. & Fabian, A. C. (1999), ‘The ROSAT Brightest Cluster Sample - III. Optical spectra of the central cluster galaxies’, *Monthly Notices of the Royal Astronomical Society* **306**, 857–896.

- Cui, W., Murante, G., Monaco, P., Borgani, S., Granato, G. L., Killedar, M., De Lucia, G., Presotto, V. & Dolag, K. (2014), ‘Characterizing diffused stellar light in simulated galaxy clusters’, *Monthly Notices of the Royal Astronomical Society* **437**(1), 816–830.
- Curtis, M. & Sijacki, D. (2016), ‘Resolving flows around black holes: the impact of gas angular momentum’, *Monthly Notices of the Royal Astronomical Society* **463**, 63–77.
- Dawson, K. S., Kneib, J.-P., Percival, W. J., Alam, S., Albareti, F. D., Anderson, S. F., Armengaud, E., Aubourg, É., Bailey, S., Bautista, J. E., Berlind, A. A., Bershad, M. A., Beutler, F., Bizyaev, D., Blanton, M. R., Blomqvist, M., Bolton, A. S., Bovy, J., Brandt, W. N., Brinkmann, J., Brownstein, J. R., Burtin, E., Busca, N. G., Cai, Z., Chuang, C.-H., Clerc, N., Comparat, J., Cope, F., Croft, R. A. C., Cruz-Gonzalez, I., da Costa, L. N., Cousinou, M.-C., Darling, J., de la Macorra, A., de la Torre, S., Delubac, T., du Mas des Bourboux, H., Dwelly, T., Ealet, A., Eisenstein, D. J., Eracleous, M., Escoffier, S., Fan, X., Finoguenov, A., Font-Ribera, A., Frinchaboy, P., Gaulme, P., Georgakakis, A., Green, P., Guo, H., Guy, J., Ho, S., Holder, D., Huehnerhoff, J., Hutchinson, T., Jing, Y., Jullo, E., Kamble, V., Kinemuchi, K., Kirkby, D., Kitaura, F.-S., Klaene, M. A., Laher, R. R., Lang, D., Laurent, P., Le Goff, J.-M., Li, C., Liang, Y., Lima, M., Lin, Q., Lin, W., Lin, Y.-T., Long, D. C., Lundgren, B., MacDonald, N., Geimba Maia, M. A., Malanushenko, E., Malanushenko, V., Mariappan, V., McBride, C. K., McGreer, I. D., Ménard, B., Merloni, A., Meza, A., Montero-Dorta, A. D., Muna, D., Myers, A. D., Nandra, K., Naugle, T., Newman, J. A., Noterdaeme, P., Nugent, P., Ogando, R., Olmstead, M. D., Oravetz, A., Oravetz, D. J., Padmanabhan, N., Palanque-Delabrouille, N., Pan, K., Parejko, J. K., Pâris, I., Peacock, J. A., Petitjean, P., Pieri, M. M., Pisani, A., Prada, F., Prakash, A., Raichoor, A., Reid, B., Rich, J., Ridl, J., Rodriguez-Torres, S., Carnero Rosell, A., Ross, A. J., Rossi, G., Ruan, J., Salvato, M., Sayres, C., Schneider, D. P., Schlegel, D. J., Seljak, U., Seo, H.-J., Sesar, B., Shandera, S., Shu, Y., Slosar, A., Sobreira, F., Streblyanska, A., Suzuki, N., Taylor, D., Tao, C., Tinker, J. L., Tojeiro, R., Vargas-Magaña, M., Wang, Y., Weaver, B. A., Weinberg, D. H., White, M., Wood-Vasey, W. M., Yeche, C., Zhai, Z., Zhao, C., Zhao, G.-b., Zheng, Z., Ben Zhu, G. & Zou, H. (2016), ‘The SDSS-IV Extended Baryon Oscillation Spectroscopic Survey: Overview and Early Data’, *The Astronomical Journal* **151**, 44.
- Dawson, K. S., Schlegel, D. J., Ahn, C. P., Anderson, S. F., Aubourg, É., Bailey, S., Barkhouser, R. H., Bautista, J. E., Beifiori, A., Berlind, A. A., Bhardwaj, V., Bizyaev,

- D., Blake, C. H., Blanton, M. R., Blomqvist, M., Bolton, A. S., Borde, A., Bovy, J., Brandt, W. N., Brewington, H., Brinkmann, J., Brown, P. J., Brownstein, J. R., Bundy, K., Busca, N. G., Carithers, W., Carnero, A. R., Carr, M. A., Chen, Y., Comparat, J., Connolly, N., Cope, F., Croft, R. A. C., Cuesta, A. J., da Costa, L. N., Davenport, J. R. A., Delubac, T., de Putter, R., Dhital, S., Ealet, A., Ebelke, G. L., Eisenstein, D. J., Escoffier, S., Fan, X., Filiz Ak, N., Finley, H., Font-Ribera, A., Génova-Santos, R., Gunn, J. E., Guo, H., Haggard, D., Hall, P. B., Hamilton, J.-C., Harris, B., Harris, D. W., Ho, S., Hogg, D. W., Holder, D., Honscheid, K., Huehnerhoff, J., Jordan, B., Jordan, W. P., Kauffmann, G., Kazin, E. A., Kirkby, D., Klaene, M. A., Kneib, J.-P., Le Goff, J.-M., Lee, K.-G., Long, D. C., Loomis, C. P., Lundgren, B., Lupton, R. H., Maia, M. A. G., Makler, M., Malanushenko, E., Malanushenko, V., Mandelbaum, R., Manera, M., Maraston, C., Margala, D., Masters, K. L., McBride, C. K., McDonald, P., McGreer, I. D., McMahon, R. G., Mena, O., Miralda-Escudé, J., Montero-Dorta, A. D., Montesano, F., Muna, D., Myers, A. D., Naugle, T., Nichol, R. C., Noterdaeme, P., Nuza, S. E., Olmstead, M. D., Oravetz, A., Oravetz, D. J., Owen, R., Padmanabhan, N., Palanque-Delabrouille, N., Pan, K., Parejko, J. K., Pâris, I., Percival, W. J., Pérez-Fournon, I., Pérez-Ràfols, I., Petitjean, P., Pfaffenberger, R., Pforr, J., Pieri, M. M., Prada, F., Price-Whelan, A. M., Raddick, M. J., Rebolo, R., Rich, J., Richards, G. T., Rockosi, C. M., Roe, N. A., Ross, A. J., Ross, N. P., Rossi, G., Rubiño-Martín, J. A., Samushia, L., Sánchez, A. G., Sayres, C., Schmidt, S. J., Schneider, D. P., Scóccola, C. G., Seo, H.-J., Sheldon, A., Sheldon, E., Shen, Y., Shu, Y., Slosar, A., Smee, S. A., Snedden, S. A., Stauffer, F., Steele, O., Strauss, M. A., Streblyanska, A., Suzuki, N., Swanson, M. E. C., Tal, T., Tanaka, M., Thomas, D., Tinker, J. L., Tojeiro, R., Tremonti, C. A., Vargas Magaña, M., Verde, L., Viel, M., Wake, D. A., Watson, M., Weaver, B. A., Weinberg, D. H., Weiner, B. J., West, A. A., White, M., Wood-Vasey, W. M., Yeche, C., Zehavi, I., Zhao, G.-B. & Zheng, Z. (2013), ‘The Baryon Oscillation Spectroscopic Survey of SDSS-III’, *The Astronomical Journal* **145**, 10.
- de Blok, W. J. G. (2010), ‘The Core-Cusp Problem’, *Advances in Astronomy* **2010**, 789293.
- de Jong, J. T. A., Verdoes Kleijn, G. A., Kuijken, K. H. & Valentijn, E. A. (2013), ‘The Kilo-Degree Survey’, *Experimental Astronomy* **35**, 25–44.

- De Lucia, G. & Blaizot, J. (2007), ‘The hierarchical formation of the brightest cluster galaxies’, *Monthly Notices of the Royal Astronomical Society* **375**, 2–14.
- de Souza, R. E., Gadotti, D. A. & dos Anjos, S. (2004), ‘BUDDA: A New Two-dimensional Bulge/Disk Decomposition Code for Detailed Structural Analysis of Galaxies’, *The Astrophysical Journal Supplement Series* **153**, 411–427.
- de Swart, J. G., Bertone, G. & van Dongen, J. (2017), ‘How dark matter came to matter’, *Nature Astronomy* **1**, 0059.
- de Vaucouleurs, G. (1948), ‘Recherches sur les Nebuleuses Extragalactiques’, *Annales d’Astrophysique* **11**, 247.
- de Vaucouleurs, G. (1960), ‘The Apparent Density of Matter in Groups and Clusters of Galaxies.’, *The Astrophysical Journal* **131**, 585.
- Dekel, A. & Silk, J. (1986), ‘The origin of dwarf galaxies, cold dark matter, and biased galaxy formation’, *The Astrophysical Journal* **303**, 39–55.
- DeMaio, T., Gonzalez, A. H., Zabludoff, A., Zaritsky, D., Connor, T., Donahue, M. & Mulchaey, J. S. (2018), ‘Lost but not forgotten: intracluster light in galaxy groups and clusters’, *Monthly Notices of the Royal Astronomical Society* **474**, 3009–3031.
- Deshev, B., Finoguenov, A., Verdugo, M., Ziegler, B., Park, C., Hwang, H. S., Haines, C., Kamphuis, P., Tamm, A., Einasto, M., Hwang, N. & Park, B.-G. (2017), ‘Galaxy evolution in merging clusters: The passive core of the “Train Wreck” cluster of galaxies, $z_{\text{ASTROBJ}_i\text{A } 520_i/\text{ASTROBJ}_i}$ ’, *Astronomy & Astrophysics* **607**, A131.
- Djorgovski, S. & Davis, M. (1987), ‘Fundamental properties of elliptical galaxies’, *The Astrophysical Journal* **313**, 59–68.
- Dolag, K., Murante, G. & Borgani, S. (2010), ‘Dynamical difference between the cD galaxy and the diffuse, stellar component in simulated galaxy clusters’, *Monthly Notices of the Royal Astronomical Society* **405**, 1544–1559.
- Donzelli, C. J., Muriel, H. & Madrid, J. P. (2011), ‘The Luminosity Profiles of Brightest Cluster Galaxies’, *The Astrophysical Journal Supplement Series* **195**, 15.
- Dries, M., Trager, S. C. & Koopmans, L. V. E. (2016), ‘A hierarchical Bayesian approach for reconstructing the initial mass function of single stellar populations’, *Monthly Notices of the Royal Astronomical Society* **463**, 886–912.

- Driver, S. P., Hill, D. T., Kelvin, L. S., Robotham, A. S. G., Liske, J., Norberg, P., Baldry, I. K., Bamford, S. P., Hopkins, A. M., Loveday, J., Peacock, J. A., Andrae, E., Bland-Hawthorn, J., Brough, S., Brown, M. J. I., Cameron, E., Ching, J. H. Y., Colless, M., Conselice, C. J., Croom, S. M., Cross, N. J. G., de Propris, R., Dye, S., Drinkwater, M. J., Ellis, S., Graham, A. W., Grootes, M. W., Gunawardhana, M., Jones, D. H., van Kampen, E., Maraston, C., Nichol, R. C., Parkinson, H. R., Phillipps, S., Pimblet, K., Popescu, C. C., Prescott, M., Roseboom, I. G., Sadler, E. M., Sansom, A. E., Sharp, R. G., Smith, D. J. B., Taylor, E., Thomas, D., Tuffs, R. J., Wijesinghe, D., Dunne, L., Frenk, C. S., Jarvis, M. J., Madore, B. F., Meyer, M. J., Seibert, M., Staveley-Smith, L., Sutherland, W. J. & Warren, S. J. (2011), ‘Galaxy and Mass Assembly (GAMA): survey diagnostics and core data release’, *Monthly Notices of the Royal Astronomical Society* **413**, 971–995.
- Driver, S. P., Norberg, P., Baldry, I. K., Bamford, S. P., Hopkins, A. M., Liske, J., Loveday, J., Peacock, J. A., Hill, D. T., Kelvin, L. S., Robotham, A. S. G., Cross, N. J. G., Parkinson, H. R., Prescott, M., Conselice, C. J., Dunne, L., Brough, S., Jones, H., Sharp, R. G., van Kampen, E., Oliver, S., Roseboom, I. G., Bland-Hawthorn, J., Croom, S. M., Ellis, S., Cameron, E., Cole, S., Frenk, C. S., Couch, W. J., Graham, A. W., Proctor, R., De Propris, R., Doyle, I. F., Edmondson, E. M., Nichol, R. C., Thomas, D., Eales, S. A., Jarvis, M. J., Kuijken, K., Lahav, O., Madore, B. F., Seibert, M., Meyer, M. J., Staveley-Smith, L., Phillipps, S., Popescu, C. C., Sansom, A. E., Sutherland, W. J., Tuffs, R. J. & Warren, S. J. (2009), ‘GAMA: towards a physical understanding of galaxy formation’, *Astronomy and Geophysics* **50**(5), 5.12–5.19.
- Duc, P.-A., Cuillandre, J.-C., Karabal, E., Cappellari, M., Alatalo, K., Blitz, L., Bournaud, F., Bureau, M., Crocker, A. F., Davies, R. L., Davis, T. A., de Zeeuw, P. T., Emsellem, E., Khochfar, S., Krajnović, D., Kuntschner, H., McDermid, R. M., Michel-Dansac, L., Morganti, R., Naab, T., Oosterloo, T., Paudel, S., Sarzi, M., Scott, N., Serra, P., Weijmans, A.-M. & Young, L. M. (2015), ‘The ATLAS^{3D} project - XXIX. The new look of early-type galaxies and surrounding fields disclosed by extremely deep optical images’, *Monthly Notices of the Royal Astronomical Society* **446**, 120–143.
- Dullo, B. T., Martínez-Lombilla, C. & Knapen, J. H. (2016), ‘Complex central structures suggest complex evolutionary paths for barred S0 galaxies’, *Monthly Notices of the Royal Astronomical Society* **462**, 3800–3811.

- Durret, F., Tarricq, Y., Márquez, I., Ashkar, H. & Adami, C. (2019), ‘Link between brightest cluster galaxy properties and large scale extensions of 38 DAFT/FADA and CLASH clusters in the redshift range $0.2 < z < 0.9$ ’, *Astronomy & Astrophysics* **622**, A78.
- Dwelly, T., Salvato, M., Merloni, A., Brusa, M., Buchner, J., Anderson, S. F., Boller, T., Brandt, W. N., Budavári, T., Clerc, N., Coffey, D., Del Moro, A., Georgakakis, A., Green, P. J., Jin, C., Menzel, M.-L., Myers, A. D., Nandra, K., Nichol, R. C., Ridl, J., Schwobe, A. D. & Simm, T. (2017), ‘SPIDERS: selection of spectroscopic targets using AGN candidates detected in all-sky X-ray surveys’, *Monthly Notices of the Royal Astronomical Society* **469**, 1065–1095.
- Eckert, D., Molendi, S. & Paltani, S. (2011), ‘The cool-core bias in X-ray galaxy cluster samples. I. Method and application to HIFLUGCS’, *Astronomy & Astrophysics* **526**, A79.
- Edge, A. C. (2001), ‘The detection of molecular gas in the central galaxies of cooling flow clusters’, *Monthly Notices of the Royal Astronomical Society* **328**, 762–782.
- Efron, B. (1979), ‘Bootstrap methods: Another look at the jackknife’, *Ann. Statist.* **7**(1), 1–26.
URL: <https://doi.org/10.1214/aos/1176344552>
- Einstein, A. (1915), ‘Die Feldgleichungen der Gravitation’, *Sitzungsberichte der Königlich Preussischen Akademie der Wissenschaften (Berlin)*, Seite 844-847. .
- Einstein, A. (1919), ‘Prüfung der allgemeinen Relativitätstheorie’, *die Naturwissenschaften* **7**, 776–776.
- Einstein, A. & de Sitter, W. (1932), ‘On the Relation between the Expansion and the Mean Density of the Universe’, *Proceedings of the National Academy of Science* **18**, 213–214.
- Ellis, J., Flores, R. A., Freese, K., Ritz, S., Seckel, D. & Silk, J. (1988), ‘Cosmic ray constraints on the annihilations of relic particles in the galactic halo’, *Physics Letters B* **214**, 403–412.
- Erwin, P. (2015), ‘IMFIT: A Fast, Flexible New Program for Astronomical Image Fitting’, *The Astrophysical Journal* **799**, 226.

- Fabian, A. C., Crawford, C. S., Edge, A. C. & Mushotzky, R. F. (1994), ‘Cooling flows and the X-ray luminosity-temperature relation for clusters’, *Monthly Notices of the Royal Astronomical Society* **267**, 779.
- Fabian, A. C. & Nulsen, P. E. J. (1977), ‘Subsonic accretion of cooling gas in clusters of galaxies’, *Monthly Notices of the Royal Astronomical Society* **180**, 479–484.
- Fabian, A. C., Sanders, J. S., Allen, S. W., Crawford, C. S., Iwasawa, K., Johnstone, R. M., Schmidt, R. W. & Taylor, G. B. (2003), ‘A deep Chandra observation of the Perseus cluster: shocks and ripples’, *Monthly Notices of the Royal Astronomical Society* **344**, L43–L47.
- Finn, R. A., Zaritsky, D., McCarthy, Jr., D. W., Poggianti, B., Rudnick, G., Halliday, C., Milvang-Jensen, B., Pelló, R. & Simard, L. (2005), ‘H α -derived Star Formation Rates for Three $z \sim 0.75$ EDisCS Galaxy Clusters’, *The Astrophysical Journal* **630**, 206–227.
- Finoguenov, A., Guzzo, L., Hasinger, G., Scoville, N. Z., Aussel, H., Böhringer, H., Brusa, M., Capak, P., Cappelluti, N., Comastri, A., Giodini, S., Griffiths, R. E., Impey, C., Koekemoer, A. M., Kneib, J.-P., Leauthaud, A., Le Fèvre, O., Lilly, S., Mainieri, V., Massey, R., McCracken, H. J., Mobasher, B., Murayama, T., Peacock, J. A., Sakelliou, I., Schinnerer, E., Silverman, J. D., Smolčić, V., Taniguchi, Y., Tasca, L., Taylor, J. E., Trump, J. R. & Zamorani, G. (2007), ‘The XMM-Newton Wide-Field Survey in the COSMOS Field: Statistical Properties of Clusters of Galaxies’, *The Astrophysical Journal Supplement Series* **172**, 182–195.
- Finoguenov, A., Reiprich, T. H. & Böhringer, H. (2001), ‘Details of the mass-temperature relation for clusters of galaxies’, *Astronomy & Astrophysics* **368**, 749–759.
- Fitzpatrick, E. L. (1999), ‘Correcting for the Effects of Interstellar Extinction’, *Publications of the Astronomical Society of the Pacific* **111**, 63–75.
- Forman, W. & Jones, C. (1982), ‘X-ray-imaging observations of clusters of galaxies’, *Annual Review of Astronomy and Astrophysics* **20**, 547–585.
- Forman, W., Kellogg, E., Gursky, H., Tananbaum, H. & Giacconi, R. (1972), ‘Observations of the Extended X-Ray Sources in the Perseus and Coma Clusters from UHURU’, *The Astrophysical Journal* **178**, 309–316.

- Forrest, B., Tran, K.-V. H., Tomczak, A. R., Broussard, A., Labbé, I., Papovich, C., Kriek, M., Allen, R. J., Cowley, M., Dickinson, M., Glazebrook, K., van Houdt, J., Inami, H., Kacprzak, G. G., Kawinwanichakij, L., Kelson, D., McCarthy, P. J., Monson, A., Morrison, G., Nanayakkara, T., Persson, S. E., Quadri, R. F., Spitler, L. R., Straatman, C. & Tilvi, V. (2016), ‘UV to IR Luminosities and Dust Attenuation Determined from ~ 4000 K-selected Galaxies at $1 < z < 3$ in the ZFOURGE Survey’, *The Astrophysical Journal Letters* **818**, L26.
- Freeman, K. C. (1970), ‘On the Disks of Spiral and S0 Galaxies’, *The Astrophysical Journal* **160**, 811.
- Friedmann, A. (1922), ‘Über die Krümmung des Raumes’, *Zeitschrift für Physik* **10**, 377–386.
- Fukugita, M., Ichikawa, T., Gunn, J. E., Doi, M., Shimasaku, K. & Schneider, D. P. (1996), ‘The Sloan Digital Sky Survey Photometric System’, *The Astronomical Journal* **111**, 1748.
- Fukugita, M., Shimasaku, K. & Ichikawa, T. (1995), ‘Galaxy Colors in Various Photometric Band Systems’, *Publications of the Astronomical Society of the Pacific* **107**, 945.
- Furnell, K. E., Collins, C. A., Kelvin, L. S., Clerc, N., Baldry, I. K., Finoguenov, A., Erfanianfar, G., Comparat, J. & Schneider, D. P. (2018), ‘Exploring relations between BCG and cluster properties in the SPectroscopic IDentification of eROSITA Sources survey from $0.05 < z < 0.3$ ’, *Monthly Notices of the Royal Astronomical Society* **478**, 4952–4973.
- Gaia Collaboration, Brown, A. G. A., Vallenari, A., Prusti, T., de Bruijne, J. H. J., Babusiaux, C., Bailer-Jones, C. A. L., Biermann, M., Evans, D. W., Eyer, L., Jansen, F., Jordi, C., Klioner, S. A., Lammers, U., Lindegren, L., Luri, X., Mignard, F., Panem, C., Pourbaix, D., Randich, S., Sartoretti, P., Siddiqui, H. I., Soubiran, C., van Leeuwen, F., Walton, N. A., Arenou, F., Bastian, U., Cropper, M., Drimmel, R., Katz, D., Lattanzi, M. G., Bakker, J., Cacciari, C., Castañeda, J., Chaoul, L., Cheek, N., De Angeli, F., Fabricius, C., Guerra, R., Holl, B., Masana, E., Messineo, R., Mowlavi, N., Nienartowicz, K., Panuzzo, P., Portell, J., Riello, M., Seabroke, G. M., Tanga, P., Thévenin, F., Gracia-Abril, G., Comoretto, G., Garcia-Reinaldos, M., Teyssier, D., Altmann, M., Andrae, R., Audard, M., Bellas-Velidis, I., Benson, K.,

Berthier, J., Blomme, R., Burgess, P., Busso, G., Carry, B., Cellino, A., Clementini, G., Clotet, M., Creevey, O., Davidson, M., De Ridder, J., Delchambre, L., Dell'Oro, A., Ducourant, C., Fernández- Hernández, J., Fouesneau, M., Frémat, Y., Galluccio, L., García-Torres, M., González-Núñez, J., González-Vidal, J. J., Gosset, E., Guy, L. P., Halbwachs, J. L., Hambly, N. C., Harrison, D. L., Hernández, J., Hestroffer, D., Hodgkin, S. T., Hutton, A., Jasniewicz, G., Jean-Antoine-Piccolo, A., Jordan, S., Korn, A. J., Krone-Martins, A., Lanzafame, A. C., Lebzelter, T., Löffler, W., Manteiga, M., Marrese, P. M., Martín-Fleitas, J. M., Moitinho, A., Mora, A., Muinonen, K., Osinde, J., Pancino, E., Pauwels, T., Petit, J. M., Recio-Blanco, A., Richards, P. J., Rimoldini, L., Robin, A. C., Sarro, L. M., Siopis, C., Smith, M., Sozzetti, A., Süveges, M., Torra, J., van Reeve, W., Abbas, U., Abreu Aramburu, A., Accart, S., Aerts, C., Altavilla, G., Álvarez, M. A., Alvarez, R., Alves, J., Anderson, R. I., Andrei, A. H., Anglada Varela, E., Antiche, E., Antoja, T., Arcay, B., Astraatmadja, T. L., Bach, N., Baker, S. G., Balaguer-Núñez, L., Balm, P., Barache, C., Barata, C., Barbato, D., Barblan, F., Barklem, P. S., Barrado, D., Barros, M., Barstow, M. A., Bartholomé Muñoz, S., Bassilana, J. L., Becciani, U., Bellazzini, M., Berihuete, A., Bertone, S., Bianchi, L., Bienaymé, O., Blanco-Cuaresma, S., Boch, T., Boeche, C., Bombrun, A., Borrachero, R., Bossini, D., Bouquillon, S., Bourda, G., Bragaglia, A., Bramante, L., Breddels, M. A., Bressan, A., Brouillet, N., Brüsemeister, T., Brugaletta, E., Bucciarelli, B., Burlacu, A., Busonero, D., Butkevich, A. G., Buzzi, R., Caffau, E., Cancelliere, R., Cannizzaro, G., Cantat-Gaudin, T., Carballo, R., Carlucci, T., Carrasco, J. M., Casamiquela, L., Castellani, M., Castro-Ginard, A., Charlot, P., Chemin, L., Chiavassa, A., Cocozza, G., Costigan, G., Cowell, S., Crifo, F., Crosta, M., Crowley, C., Cuyppers, J., Dafonte, C., Damerdji, Y., Dapergolas, A., David, P., David, M., de Laverny, P., De Luise, F., De March, R., de Martino, D., de Souza, R., de Torres, A., Debosscher, J., del Pozo, E., Delbo, M., Delgado, A., Delgado, H. E., Di Matteo, P., Diakite, S., Diener, C., Distefano, E., Dolding, C., Drazinos, P., Durán, J., Edvardsson, B., Enke, H., Eriksson, K., Esquej, P., Eynard Bontemps, G., Fabre, C., Fabrizio, M., Faigler, S., Falcão, A. J., Farràs Casas, M., Federici, L., Fedorets, G., Fernique, P., Figueras, F., Filippi, F., Findeisen, K., Fonti, A., Fraile, E., Fraser, M., Frézouls, B., Gai, M., Galleti, S., Garabato, D., García-Sedano, F., Garofalo, A., Garralda, N., Gavel, A., Gavras, P., Gerssen, J., Geyer, R., Giacobbe, P., Gilmore, G., Girona, S., Giuffrida, G., Glass, F., Gomes, M., Granvik, M., Gueguen, A., Guerrier, A., Guiraud, J., Gutiérrez-Sánchez, R., Haigron, R., Hatzidimitriou,

D., Hauser, M., Haywood, M., Heiter, U., Helmi, A., Heu, J., Hilger, T., Hobbs, D., Hofmann, W., Holland, G., Huckle, H. E., Hypki, A., Icardi, V., Janßen, K., Jevardat de Fombelle, G., Jonker, P. G., Juhász, Á. L., Julbe, F., Karampelas, A., Kewley, A., Klar, J., Kochoska, A., Kohley, R., Kolenberg, K., Kontizas, M., Kontizas, E., Koposov, S. E., Kordopatis, G., Kostrzewa-Rutkowska, Z., Koubsky, P., Lambert, S., Lanza, A. F., Lasne, Y., Lavigne, J. B., Le Fustec, Y., Le Poncin-Lafitte, C., Lebreton, Y., Leccia, S., Leclerc, N., Lecoœur-Taibi, I., Lenhardt, H., Leroux, F., Liao, S., Licata, E., Lindstrøm, H. E. P., Lister, T. A., Livanou, E., Lobel, A., López, M., Managau, S., Mann, R. G., Mantelet, G., Marchal, O., Marchant, J. M., Marconi, M., Marinoni, S., Marschalkó, G., Marshall, D. J., Martino, M., Marton, G., Mary, N., Massari, D., Matijević, G., Mazeh, T., McMillan, P. J., Messina, S., Michalik, D., Millar, N. R., Molina, D., Molinaro, R., Molnár, L., Montegriffo, P., Mor, R., Morbidelli, R., Morel, T., Morris, D., Mulone, A. F., Muraveva, T., Musella, I., Nelemans, G., Nicastrò, L., Noval, L., O'Mullane, W., Ordénovic, C., Ordóñez-Blanco, D., Osborne, P., Pagani, C., Pagano, I., Pailer, F., Palacin, H., Palaversa, L., Panahi, A., Pawlak, M., Piersimoni, A. M., Pineau, F. X., Plachy, E., Plum, G., Poggio, E., Poujoulet, E., Prša, A., Pulone, L., Racero, E., Ragaini, S., Rambaux, N., Ramos-Lerate, M., Regibo, S., Reylé, C., Rielet, F., Ripepi, V., Riva, A., Rivard, A., Rixon, G., Roegiers, T., Roelens, M., Romero-Gómez, M., Rowell, N., Royer, F., Ruiz-Dern, L., Sadowski, G., Sagristà Sellés, T., Sahlmann, J., Salgado, J., Salguero, E., Sanna, N., Santana-Ros, T., Sarasso, M., Savietto, H., Schultheis, M., Sciacca, E., Segol, M., Segovia, J. C., Ségransan, D., Shih, I. C., Siltala, L., Silva, A. F., Smart, R. L., Smith, K. W., Solano, E., Solitro, F., Sordo, R., Soria Nieto, S., Souchay, J., Spagna, A., Spoto, F., Stampa, U., Steele, I. A., Steidelmüller, H., Stephenson, C. A., Stoev, H., Suess, F. F., Surdej, J., Szabados, L., Szegedi-Elek, E., Tapiador, D., Taris, F., Tauran, G., Taylor, M. B., Teixeira, R., Terrett, D., Teyssandier, P., Thuillot, W., Titarenko, A., Torra Clotet, F., Turon, C., Ulla, A., Utrilla, E., Uzzi, S., Vaillant, M., Valentini, G., Valette, V., van Elteren, A., Van Hemelryck, E., van Leeuwen, M., Vaschetto, M., Vecchiato, A., Veljanoski, J., Viala, Y., Vicente, D., Vogt, S., von Essen, C., Voss, H., Votruba, V., Voutsinas, S., Walmsley, G., Weiler, M., Wertz, O., Wevers, T., Wyrzykowski, Ł., Yoldas, A., Žerjal, M., Ziaeeppour, H., Zorec, J., Zschocke, S., Zucker, S., Zurbach, C. & Zwitter, T. (2018), 'Gaia Data Release 2. Summary of the contents and survey properties', *Astronomy & Astrophysics* **616**, A1.

Gaia Collaboration, Prusti, T., de Bruijne, J. H. J., Brown, A. G. A., Vallenari, A., Babusiaux, C., Bailer-Jones, C. A. L., Bastian, U., Biermann, M., Evans, D. W., Eyer, L., Jansen, F., Jordi, C., Klioner, S. A., Lammers, U., Lindegren, L., Luri, X., Mignard, F., Milligan, D. J., Panem, C., Poinsignon, V., Pourbaix, D., Randich, S., Sarri, G., Sartoretti, P., Siddiqui, H. I., Soubiran, C., Valette, V., van Leeuwen, F., Walton, N. A., Aerts, C., Arenou, F., Cropper, M., Drimmel, R., Høg, E., Katz, D., Lattanzi, M. G., O'Mullane, W., Grebel, E. K., Holland, A. D., Huc, C., Passot, X., Bramante, L., Cacciari, C., Castañeda, J., Chaoul, L., Cheek, N., De Angeli, F., Fabricius, C., Guerra, R., Hernández, J., Jean-Antoine-Piccolo, A., Masana, E., Messineo, R., Mowlavi, N., Nienartowicz, K., Ordóñez-Blanco, D., Panuzzo, P., Portell, J., Richards, P. J., Riello, M., Seabroke, G. M., Tanga, P., Thévenin, F., Torra, J., Els, S. G., Gracia-Abril, G., Comoretto, G., Garcia-Reinaldos, M., Lock, T., Mercier, E., Altmann, M., Andrae, R., Astraatmadja, T. L., Bellas-Velidis, I., Benson, K., Berthier, J., Blomme, R., Busso, G., Carry, B., Cellino, A., Clementini, G., Cowell, S., Creevey, O., Cuypers, J., Davidson, M., De Ridder, J., de Torres, A., Delchambre, L., Dell'Oro, A., Ducourant, C., Frémat, Y., García-Torres, M., Gosset, E., Halbwachs, J. L., Hambly, N. C., Harrison, D. L., Hauser, M., Hestroffer, D., Hodgkin, S. T., Huckle, H. E., Hutton, A., Jasniewicz, G., Jordan, S., Kontizas, M., Korn, A. J., Lanzafame, A. C., Manteiga, M., Moitinho, A., Muinonen, K., Osinde, J., Pancino, E., Pauwels, T., Petit, J. M., Recio-Blanco, A., Robin, A. C., Sarro, L. M., Siopis, C., Smith, M., Smith, K. W., Sozzetti, A., Thuillot, W., van Reeven, W., Viala, Y., Abbas, U., Abreu Aramburu, A., Accart, S., Aguado, J. J., Allan, P. M., Allasia, W., Altavilla, G., Álvarez, M. A., Alves, J., Anderson, R. I., Andrei, A. H., Anglada Varela, E., Antiche, E., Antoja, T., Antón, S., Arcay, B., Atzei, A., Ayache, L., Bach, N., Baker, S. G., Balaguer-Núñez, L., Barache, C., Barata, C., Barbier, A., Barblan, F., Baroni, M., Barrado y Navascués, D., Barros, M., Barstow, M. A., Becciani, U., Bellazzini, M., Bellei, G., Bello García, A., Belokurov, V., Bendjoya, P., Berihuete, A., Bianchi, L., Bienaymé, O., Billebaud, F., Blagorodnova, N., Blanco-Cuaresma, S., Boch, T., Bombrun, A., Borrachero, R., Bouquillon, S., Bourda, G., Bouy, H., Bragaglia, A., Breddels, M. A., Brouillet, N., Brüsemeister, T., Bucciarelli, B., Budnik, F., Burgess, P., Burgon, R., Burlacu, A., Busonero, D., Buzzi, R., Caffau, E., Cambras, J., Campbell, H., Cancelliere, R., Cantat-Gaudin, T., Carlucci, T., Carrasco, J. M., Castellani, M., Charlot, P., Charnas, J., Charvet, P., Chassat, F., Chiavassa, A., Clotet, M., Coccozza, G., Collins, R. S., Collins, P., Costigan, G., Crifo, F., Cross, N. J. G.,

Crosta, M., Crowley, C., Dafonte, C., Damerdji, Y., Dapergolas, A., David, P., David, M., De Cat, P., de Felice, F., de Laverny, P., De Luise, F., De March, R., de Martino, D., de Souza, R., Debosscher, J., del Pozo, E., Delbo, M., Delgado, A., Delgado, H. E., di Marco, F., Di Matteo, P., Diakite, S., Distefano, E., Dolding, C., Dos Anjos, S., Drazinos, P., Durán, J., Dzigan, Y., Ecale, E., Edvardsson, B., Enke, H., Erdmann, M., Escolar, D., Espina, M., Evans, N. W., Eynard Bontemps, G., Fabre, C., Fabrizio, M., Faigler, S., Falcão, A. J., Farràs Casas, M., Faye, F., Federici, L., Fedorets, G., Fernández-Hernández, J., Fernique, P., Fienga, A., Figueras, F., Filippi, F., Findeisen, K., Fonti, A., Fouesneau, M., Fraile, E., Fraser, M., Fuchs, J., Furnell, R., Gai, M., Galleti, S., Galluccio, L., Garabato, D., García-Sedano, F., Garé, P., Garofalo, A., Garralda, N., Gavras, P., Gerssen, J., Geyer, R., Gilmore, G., Girona, S., Giuffrida, G., Gomes, M., González-Marcos, A., González-Núñez, J., González-Vidal, J. J., Granvik, M., Guerrier, A., Guillout, P., Guiraud, J., Gúrpide, A., Gutiérrez-Sánchez, R., Guy, L. P., Haigron, R., Hatzidimitriou, D., Haywood, M., Heiter, U., Helmi, A., Hobbs, D., Hofmann, W., Holl, B., Holland, G., Hunt, J. A. S., Hypki, A., Icardi, V., Irwin, M., Jevardat de Fombelle, G., Jofré, P., Jonker, P. G., Jorissen, A., Julbe, F., Karampelas, A., Kochoska, A., Kohley, R., Kolenberg, K., Kontizas, E., Koposov, S. E., Kordopatis, G., Koubsky, P., Kowalczyk, A., Krone-Martins, A., Kudryashova, M., Kull, I., Bachchan, R. K., Lacoste-Seris, F., Lanza, A. F., Lavigne, J. B., Le Poncin-Lafitte, C., Lebreton, Y., Lebzelter, T., Leccia, S., Leclerc, N., Lecoeur-Taibi, I., Lemaitre, V., Lenhardt, H., Leroux, F., Liao, S., Licata, E., Lindstrøm, H. E. P., Lister, T. A., Livanou, E., Lobel, A., Löffler, W., López, M., Lopez-Lozano, A., Lorenz, D., Loureiro, T., MacDonald, I., Magalhães Fernandes, T., Managau, S., Mann, R. G., Mantelet, G., Marchal, O., Marchant, J. M., Marconi, M., Marie, J., Marinoni, S., Marrese, P. M., Marschalkó, G., Marshall, D. J., Martín-Fleitas, J. M., Martino, M., Mary, N., Matijević, G., Mazeh, T., McMillan, P. J., Messina, S., Mestre, A., Michalik, D., Millar, N. R., Miranda, B. M. H., Molina, D., Molinaro, R., Molinaro, M., Molnár, L., Moniez, M., Montegriffo, P., Monteiro, D., Mor, R., Mora, A., Morbidelli, R., Morel, T., Morgenthaler, S., Morley, T., Morris, D., Mulone, A. F., Muraveva, T., Musella, I., Narbonne, J., Nelemans, G., Nicastro, L., Noval, L., Ordénovic, C., Ordieres-Meré, J., Osborne, P., Pagani, C., Pagano, I., Pailler, F., Palacin, H., Palaversa, L., Parsons, P., Paulsen, T., Pecoraro, M., Pedrosa, R., Pentikäinen, H., Pereira, J., Pichon, B., Piersimoni, A. M., Pineau, F. X., Plachy, E., Plum, G., Poujoulet, E., Prša, A., Pulone, L., Ragaini, S., Rago, S., Rambaux, N., Ramos-Lerate, M., Ranalli, P., Rauw, G., Read,

A., Regibo, S., Renk, F., Reylé, C., Ribeiro, R. A., Rimoldini, L., Ripepi, V., Riva, A., Rixon, G., Roelens, M., Romero-Gómez, M., Rowell, N., Royer, F., Rudolph, A., Ruiz-Dern, L., Sadowski, G., Sagristà Sellés, T., Sahlmann, J., Salgado, J., Salguero, E., Sarasso, M., Savietto, H., Schnorhk, A., Schultheis, M., Sciacca, E., Segol, M., Segovia, J. C., Segransan, D., Serpell, E., Shih, I. C., Smareglia, R., Smart, R. L., Smith, C., Solano, E., Solitro, F., Sordo, R., Soria Nieto, S., Souchay, J., Spagna, A., Spoto, F., Stampa, U., Steele, I. A., Steidelmüller, H., Stephenson, C. A., Stoev, H., Suess, F. F., Süveges, M., Surdej, J., Szabados, L., Szegedi-Elek, E., Tapiador, D., Taris, F., Tauran, G., Taylor, M. B., Teixeira, R., Terrett, D., Tingley, B., Trager, S. C., Turon, C., Ulla, A., Utrilla, E., Valentini, G., van Elteren, A., Van Hemelryck, E., van Leeuwen, M., Varadi, M., Vecchiato, A., Veljanoski, J., Via, T., Vicente, D., Vogt, S., Voss, H., Votruba, V., Voutsinas, S., Walmsley, G., Weiler, M., Weingrill, K., Werner, D., Wevers, T., Whitehead, G., Wyrzykowski, L., Yoldas, A., Žerjal, M., Zucker, S., Zurbach, C., Zwitter, T., Alecu, A., Allen, M., Allende Prieto, C., Amorim, A., Anglada-Escudé, G., Arsenijevic, V., Azaz, S., Balm, P., Beck, M., Bernstein, H. H., Bigot, L., Bijaoui, A., Blasco, C., Bonfigli, M., Bono, G., Boudreault, S., Bressan, A., Brown, S., Brunet, P. M., Bunclark, P., Buonanno, R., Butkevich, A. G., Carret, C., Carrion, C., Chemin, L., Chéreau, F., Corcione, L., Darmigny, E., de Boer, K. S., de Teodoro, P., de Zeeuw, P. T., Delle Luche, C., Domingues, C. D., Dubath, P., Fodor, F., Frézouls, B., Fries, A., Fustes, D., Fyfe, D., Gallardo, E., Gallegos, J., Gardiol, D., Gebran, M., Gomboc, A., Gómez, A., Grux, E., Gueguen, A., Heyrovsky, A., Hoar, J., Iannicola, G., Isasi Parache, Y., Janotto, A. M., Joliet, E., Jonckheere, A., Keil, R., Kim, D. W., Klagyivik, P., Klar, J., Knude, J., Kochukhov, O., Kolka, I., Kos, J., Kutka, A., Lainey, V., LeBouquin, D., Liu, C., Loreggia, D., Makarov, V. V., Marseille, M. G., Martayan, C., Martinez-Rubi, O., Massart, B., Meynadier, F., Mignot, S., Munari, U., Nguyen, A. T., Nordlander, T., Ocvirk, P., O'Flaherty, K. S., Olias Sanz, A., Ortiz, P., Osorio, J., Oszkiewicz, D., Ouzounis, A., Palmer, M., Park, P., Pasquato, E., Peltzer, C., Peralta, J., Péturaud, F., Pieniluoma, T., Pigozzi, E., Poels, J., Prat, G., Prod'homme, T., Raison, F., Rebordao, J. M., Risquez, D., Rocca-Volmerange, B., Rosen, S., Ruiz-Fuertes, M. I., Russo, F., Sembay, S., Serraller Vizcaino, I., Short, A., Siebert, A., Silva, H., Sinachopoulos, D., Slezak, E., Soffel, M., Sosnowska, D., Straižys, V., ter Linden, M., Terrell, D., Theil, S., Tiede, C., Troisi, L., Tsalmantza, P., Tur, D., Vaccari, M., Vachier, F., Valles, P., Van Hamme, W., Veltz, L., Virtanen, J., Wallut, J. M., Wichmann, R., Wilkinson, M. I., Ziaepour, H. & Zschocke, S. (2016),

- ‘The Gaia mission’, *Astronomy & Astrophysics* **595**, A1.
- Gamow, G. (1948), ‘The Origin of Elements and the Separation of Galaxies’, *Physical Review* **74**, 505–506.
- Gardner, J. P., Mather, J. C., Clampin, M., Doyon, R., Greenhouse, M. A., Hammel, H. B., Hutchings, J. B., Jakobsen, P., Lilly, S. J., Long, K. S., Lunine, J. I., McCaughrean, M. J., Mountain, M., Nella, J., Rieke, G. H., Rieke, M. J., Rix, H.-W., Smith, E. P., Sonneborn, G., Stiavelli, M., Stockman, H. S., Windhorst, R. A. & Wright, G. S. (2006), ‘The James Webb Space Telescope’, *Space Science Reviews* **123**(4), 485–606.
- George, M. R., Leauthaud, A., Bundy, K., Finoguenov, A., Ma, C.-P., Rykoff, E. S., Tinker, J. L., Wechsler, R. H., Massey, R. & Mei, S. (2012), ‘Galaxies in X-Ray Groups. II. A Weak Lensing Study of Halo Centering’, *The Astrophysical Journal* **757**, 2.
- Gilmozzi, R. (2005), ‘Science, Technology and Detectors for Extremely Large Telescopes’, *Experimental Astronomy* **19**, 5–13.
- Gladders, M. D., López-Cruz, O., Yee, H. K. C. & Kodama, T. (1998), ‘The Slope of the Cluster Elliptical Red Sequence: A Probe of Cluster Evolution’, *The Astrophysical Journal* **501**, 571–577.
- Gladders, M. D. & Yee, H. K. C. (2000), ‘A New Method For Galaxy Cluster Detection. I. The Algorithm’, *The Astronomical Journal* **120**, 2148–2162.
- Gonzalez, A. H., Sivanandam, S., Zabludoff, A. I. & Zaritsky, D. (2013), ‘Galaxy Cluster Baryon Fractions Revisited’, *The Astrophysical Journal* **778**(1), 14.
- Gonzalez, A. H., Zabludoff, A. I. & Zaritsky, D. (2005), ‘Intracluster Light in Nearby Galaxy Clusters: Relationship to the Halos of Brightest Cluster Galaxies’, *The Astrophysical Journal* **618**, 195–213.
- Gonzalez, A. H., Zaritsky, D. & Zabludoff, A. I. (2007), ‘A Census of Baryons in Galaxy Clusters and Groups’, *The Astrophysical Journal* **666**, 147–155.
- Graham, A., Lauer, T. R., Colless, M. & Postman, M. (1996), ‘Brightest Cluster Galaxy Profile Shapes’, *The Astrophysical Journal* **465**, 534.
- Graham, A. W. & Driver, S. P. (2005), ‘A Concise Reference to (Projected) Sérsic $R^{1/n}$ Quantities, Including Concentration, Profile Slopes, Petrosian Indices, and Kron Magnitudes’, *Publications of the Astronomical Society of Australia* **22**, 118–127.

- Graham, A. W., Erwin, P., Trujillo, I. & Asensio Ramos, A. (2003), ‘A New Empirical Model for the Structural Analysis of Early-Type Galaxies, and A Critical Review of the Nuker Model’, *The Astronomical Journal* **125**, 2951–2963.
- Gray, M. E., Wolf, C., Barden, M., Peng, C. Y., Häußler, B., Bell, E. F., McIntosh, D. H., Guo, Y., Caldwell, J. A. R., Bacon, D., Balogh, M., Barazza, F. D., Böhm, A., Heymans, C., Jahnke, K., Jogee, S., van Kampen, E., Lane, K., Meisenheimer, K., Sánchez, S. F., Taylor, A., Wisotzki, L., Zheng, X., Green, D. A., Beswick, R. J., Saikia, D. J., Gilmour, R., Johnson, B. D. & Papovich, C. (2009), ‘STAGES: the Space Telescope A901/2 Galaxy Evolution Survey’, *Monthly Notices of the Royal Astronomical Society* **393**, 1275–1301.
- Green, T. S., Edge, A. C., Stott, J. P., Ebeling, H., Burgett, W. S., Chambers, K. C., Draper, P. W., Metcalfe, N., Kaiser, N., Wainscoat, R. J. & Waters, C. (2016), ‘A multiwavelength photometric census of AGN and star formation activity in the brightest cluster galaxies of X-ray selected clusters’, *Monthly Notices of the Royal Astronomical Society* **461**, 560–577.
- Gregg, M. D., Holden, B. P. & West, M. J. (2003), ‘Cluster–Galaxy Interactions in Coma’, *ArXiv Astrophysics e-prints* .
- Guglielmetti, F., Fischer, R. & Dose, V. (2009), ‘Backgroundsource separation in astronomical images with Bayesian probability theory I. The method’, *Monthly Notices of the Royal Astronomical Society* **396**(1), 165–190.
URL: <https://doi.org/10.1111/j.1365-2966.2009.14739.x>
- Gunn, J. E. & Gott, III, J. R. (1972), ‘On the Infall of Matter Into Clusters of Galaxies and Some Effects on Their Evolution’, *The Astrophysical Journal* **176**, 1.
- Gunn, J. E., Siegmund, W. A., Mannery, E. J., Owen, R. E., Hull, C. L., Leger, R. F., Carey, L. N., Knapp, G. R., York, D. G., Boroski, W. N., Kent, S. M., Lupton, R. H., Rockosi, C. M., Evans, M. L., Waddell, P., Anderson, J. E., Annis, J., Barentine, J. C., Bartoszek, L. M., Bastian, S., Bracker, S. B., Brewington, H. J., Briegel, C. I., Brinkmann, J., Brown, Y. J., Carr, M. A., Czarapata, P. C., Drennan, C. C., Dombeck, T., Federwitz, G. R., Gillespie, B. A., Gonzales, C., Hansen, S. U., Harvanek, M., Hayes, J., Jordan, W., Kinney, E., Klaene, M., Kleinman, S. J., Kron, R. G., Kresinski, J., Lee, G., Limmongkol, S., Lindenmeyer, C. W., Long, D. C., Loomis, C. L., McGehee,

- P. M., Mantsch, P. M., Neilsen, Jr., E. H., Neswold, R. M., Newman, P. R., Nitta, A., Peoples, Jr., J., Pier, J. R., Prieto, P. S., Prosapio, A., Rivetta, C., Schneider, D. P., Snedden, S. & Wang, S.-i. (2006), ‘The 2.5 m Telescope of the Sloan Digital Sky Survey’, *The Astronomical Journal* **131**, 2332–2359.
- Guo, Y., McIntosh, D. H., Mo, H. J., Katz, N., van den Bosch, F. C., Weinberg, M., Weinmann, S. M., Pasquali, A. & Yang, X. (2009), ‘Structural properties of central galaxies in groups and clusters’, *Monthly Notices of the Royal Astronomical Society* **398**, 1129–1149.
- Gursky, H., Kellogg, E., Murray, S., Leong, C., Tananbaum, H. & Giacconi, R. (1971), ‘A Strong X-Ray Source in the Coma Cluster Observed by UHURU’, *The Astrophysical Journal Letters* **167**, L81.
- Gursky, H. & Schwartz, D. A. (1977), ‘Extragalactic X-ray sources’, *Annual Review of Astronomy and Astrophysics* **15**, 541–568.
- Guth, A. H. (1981), ‘Inflationary universe: A possible solution to the horizon and flatness problems’, *Physical Review D* **23**, 347–356.
- Guzzo, L., Scodreggio, M., Garilli, B., Granett, B. R., Fritz, A., Abbas, U., Adami, C., Arnouts, S., Bel, J., Bolzonella, M., Bottini, D., Branchini, E., Cappi, A., Coupon, J., Cucciati, O., Davidzon, I., De Lucia, G., de la Torre, S., Franzetti, P., Fumana, M., Hudelot, P., Ilbert, O., Iovino, A., Krywult, J., Le Brun, V., Le Fèvre, O., Maccagni, D., Małek, K., Marulli, F., McCracken, H. J., Paioro, L., Peacock, J. A., Polletta, M., Pollo, A., Schlagenhauser, H., Tasca, L. A. M., Tojeiro, R., Vergani, D., Zamorani, G., Zanichelli, A., Burden, A., Di Porto, C., Marchetti, A., Marinoni, C., Mellier, Y., Moscardini, L., Nichol, R. C., Percival, W. J., Phleps, S. & Wolk, M. (2014), ‘The VIMOS Public Extragalactic Redshift Survey (VIPERS). An unprecedented view of galaxies and large-scale structure at $0.5 < z < 1.2$ ’, *Astronomy & Astrophysics* **566**, A108.
- Haines, C. P., Finoguenov, A., Smith, G. P., Babul, A., Egami, E., Mazzotta, P., Okabe, N., Pereira, M. J., Bianconi, M., McGee, S. L., Ziparo, F., Campusano, L. E. & Loyola, C. (2018), ‘LoCuSS: The infall of X-ray groups on to massive clusters’, *Monthly Notices of the Royal Astronomical Society* **477**, 4931–4950.

- Harvey, D., Courbin, F., Kneib, J. P. & McCarthy, I. G. (2017), ‘A detection of wobbling brightest cluster galaxies within massive galaxy clusters’, *Monthly Notices of the Royal Astronomical Society* **472**, 1972–1980.
- Hasselfield, M., Hilton, M., Marriage, T. A., Addison, G. E., Barrientos, L. F., Battaglia, N., Battistelli, E. S., Bond, J. R., Crichton, D., Das, S., Devlin, M. J., Dicker, S. R., Dunkley, J., Dünner, R., Fowler, J. W., Gralla, M. B., Hajian, A., Halpern, M., Hincks, A. D., Hlozek, R., Hughes, J. P., Infante, L., Irwin, K. D., Kosowsky, A., Marsden, D., Menanteau, F., Moodley, K., Niemack, M. D., Nolta, M. R., Page, L. A., Partridge, B., Reese, E. D., Schmitt, B. L., Sehgal, N., Sherwin, B. D., Sievers, J., Sifón, C., Spergel, D. N., Staggs, S. T., Swetz, D. S., Switzer, E. R., Thornton, R., Trac, H. & Wollack, E. J. (2013), ‘The Atacama Cosmology Telescope: Sunyaev-Zel’dovich selected galaxy clusters at 148 GHz from three seasons of data’, *Journal of Cosmology and Astroparticle Physics* **7**, 008.
- Hatch, N. A., De Breuck, C., Galametz, A., Miley, G. K., Overzier, R. A., Röttgering, H. J. A., Doherty, M., Kodama, T., Kurk, J. D., Seymour, N., Venemans, B. P., Vernet, J. & Zirm, A. W. (2011), ‘Galaxy protocluster candidates around $z \sim 2.4$ radio galaxies’, *Monthly Notices of the Royal Astronomical Society* **410**, 1537–1549.
- Häufler, B., Bamford, S. P., Vika, M., Rojas, A. L., Barden, M., Kelvin, L. S., Alpaslan, M., Robotham, A. S. G., Driver, S. P., Baldry, I. K., Brough, S., Hopkins, A. M., Liske, J., Nichol, R. C., Popescu, C. C. & Tuffs, R. J. (2013), ‘MegaMorph - multiwavelength measurement of galaxy structure: complete Sérsic profile information from modern surveys’, *Monthly Notices of the Royal Astronomical Society* **430**, 330–369.
- Häussler, B., McIntosh, D. H., Barden, M., Bell, E. F., Rix, H.-W., Borch, A., Beckwith, S. V. W., Caldwell, J. A. R., Heymans, C., Jahnke, K., Jogee, S., Kopesov, S. E., Meisenheimer, K., Sánchez, S. F., Somerville, R. S., Wisotzki, L. & Wolf, C. (2007), ‘GEMS: Galaxy Fitting Catalogs and Testing Parametric Galaxy Fitting Codes: GALFIT and GIM2D’, *The Astrophysical Journal Supplement Series* **172**, 615–633.
- Hawkins, M. R. S. (2011), ‘The case for primordial black holes as dark matter’, *Monthly Notices of the Royal Astronomical Society* **415**, 2744–2757.

- Henriques, B. M. B. & Thomas, P. A. (2010), ‘Tidal disruption of satellite galaxies in a semi-analytic model of galaxy formation’, *Monthly Notices of the Royal Astronomical Society* **403**, 768–779.
- Hikage, C., Mandelbaum, R., Leauthaud, A., Rozo, E. & Rykoff, E. S. (2017), ‘Testing redMaPPer Centering Probabilities using Galaxy Clustering and Galaxy-Galaxy Lensing’, *ArXiv e-prints* .
- Hill, D. T., Kelvin, L. S., Driver, S. P., Robotham, A. S. G., Cameron, E., Cross, N., Andrae, E., Baldry, I. K., Bamford, S. P., Bland-Hawthorn, J., Brough, S., Conselice, C. J., Dye, S., Hopkins, A. M., Liske, J., Loveday, J., Norberg, P., Peacock, J. A., Croom, S. M., Frenk, C. S., Graham, A. W., Jones, D. H., Kuijken, K., Madore, B. F., Nichol, R. C., Parkinson, H. R., Phillipps, S., Pimblet, K. A., Popescu, C. C., Prescott, M., Seibert, M., Sharp, R. G., Sutherland, W. J., Thomas, D., Tuffs, R. J. & van Kampen, E. (2011), ‘Galaxy and Mass Assembly: FUV, NUV, ugrizYJHK Petrosian, Kron and Sérsic photometry’, *Monthly Notices of the Royal Astronomical Society* **412**, 765–799.
- Hilton, M., Hasselfield, M., Sifón, C., Battaglia, N., Aiola, S., Bharadwaj, V., Bond, J. R., Choi, S. K., Crichton, D., Datta, R., Devlin, M. J., Dunkley, J., Dünner, R., Gallardo, P. A., Gralla, M., Hincks, A. D., Ho, S.-P. P., Hubmayr, J., Huppenberger, K. M., Hughes, J. P., Koopman, B. J., Kosowsky, A., Louis, T., Madhavacheril, M. S., Marriage, T. A., Maurin, L., McMahon, J., Miyatake, H., Moodley, K., Naess, S., Nati, F., Newburgh, L., Niemack, M. D., Oguri, M., Page, L. A., Partridge, B., Schmitt, B. L., Sievers, J., Spergel, D. N., Staggs, S. T., Trac, H., van Engelen, A., Vavagiakis, E. M. & Wollack, E. J. (2018), ‘The Atacama Cosmology Telescope: The Two-season ACTPol Sunyaev-Zeldovich Effect Selected Cluster Catalog’, *The Astrophysical Journal Supplement Series* **235**, 20.
- Hogg, D. W., Baldry, I. K., Blanton, M. R. & Eisenstein, D. J. (2002), ‘The K correction’, *ArXiv Astrophysics e-prints* .
- Holland, J. G., Bhringer, H., Chon, G. & Pierini, D. (2015), ‘Optical and X-ray profiles in the REXCESS sample of galaxy clusters*’, *Monthly Notices of the Royal Astronomical Society* **448**(3), 2644–2664.
- URL:** <https://doi.org/10.1093/mnras/stv097>

- Hood, R. J. & Mann, R. G. (2017), ‘Characterizing the optical properties of galaxy clusters with GMPhoRCC’, *Monthly Notices of the Royal Astronomical Society* **469**, 3851–3871.
- Hu, W. & Kravtsov, A. V. (2003), ‘Sample Variance Considerations for Cluster Surveys’, *The Astrophysical Journal* **584**(2), 702–715.
- Huang, S., Leauthaud, A., Greene, J., Bundy, K., Lin, Y.-T., Tanaka, M., Miyazaki, S. & Komiyama, Y. (2017), ‘Individual Stellar Halos of Massive Galaxies Measured to 100 kpc at $0.3 < z < 0.5$ using Hyper Suprime-Cam’, *ArXiv e-prints*.
- Huang, S., Leauthaud, A., Murata, R., Bosch, J., Price, P., Lupton, R., Mandelbaum, R., Lackner, C., Bickerton, S., Miyazaki, S., Coupon, J. & Tanaka, M. (2018), ‘Characterization and photometric performance of the Hyper Suprime-Cam Software Pipeline’, *Publications of the Astronomical Society of Japan* **70**, S6.
- Hubble, E. (1929), ‘A Relation between Distance and Radial Velocity among Extra-Galactic Nebulae’, *Proceedings of the National Academy of Science* **15**, 168–173.
- Hubble, E. & Humason, M. L. (1931), ‘The Velocity-Distance Relation among Extra-Galactic Nebulae’, *The Astrophysical Journal* **74**, 43.
- Hudson, D. S., Mittal, R., Reiprich, T. H., Nulsen, P. E. J., Andernach, H. & Sarazin, C. L. (2010), ‘What is a cool-core cluster? a detailed analysis of the cores of the X-ray flux-limited HIFLUGCS cluster sample’, *Astronomy & Astrophysics* **513**, A37.
- Huertas-Company, M., Aguerri, J. A. L., Bernardi, M., Mei, S. & Sánchez Almeida, J. (2011), ‘Revisiting the Hubble sequence in the SDSS DR7 spectroscopic sample: a publicly available Bayesian automated classification’, *Astronomy & Astrophysics* **525**, A157.
- Huertas-Company, M., Mei, S., Shankar, F., Delaye, L., Raichoor, A., Covone, G., Finoguenov, A., Kneib, J. P., Le, F. O. & Povic, M. (2013), ‘The evolution of the mass-size relation for early-type galaxies from $z \sim 1$ to the present: dependence on environment, mass range and detailed morphology’, *Monthly Notices of the Royal Astronomical Society* **428**, 1715–1742.
- Ilbert, O., Arnouts, S., McCracken, H. J., Bolzonella, M., Bertin, E., Le Fèvre, O., Mellier, Y., Zamorani, G., Pellò, R., Iovino, A., Tresse, L., Le Brun, V., Bottini, D., Garilli, B., Maccagni, D., Picat, J. P., Scaramella, R., Scodreggio, M., Vettolani, G.,

- Zanichelli, A., Adami, C., Bardelli, S., Cappi, A., Charlot, S., Ciliegi, P., Contini, T., Cucciati, O., Foucaud, S., Franzetti, P., Gavignaud, I., Guzzo, L., Marano, B., Marinoni, C., Mazure, A., Meneux, B., Merighi, R., Paltani, S., Pollo, A., Pozzetti, L., Radovich, M., Zucca, E., Bondi, M., Bongiorno, A., Busarello, G., de La Torre, S., Gregorini, L., Lamareille, F., Mathez, G., Merluzzi, P., Ripepi, V., Rizzo, D. & Vergani, D. (2006), ‘Accurate photometric redshifts for the CFHT legacy survey calibrated using the VIMOS VLT deep survey’, *Astronomy & Astrophysics* **457**, 841–856.
- Ivezic, Z., Tyson, J. A., Abel, B., Acosta, E., Allsman, R., AlSayyad, Y., Anderson, S. F., Andrew, J., Angel, R., Angeli, G., Ansari, R., Antilogus, P., Arndt, K. T., Astier, P., Aubourg, E., Axelrod, T., Bard, D. J., Barr, J. D., Barrau, A., Bartlett, J. G., Bauman, B. J., Beaumont, S., Becker, A. C., Becla, J., Beldica, C., Bellavia, S., Blanc, G., Blandford, R. D., Bloom, J. S., Bogart, J., Borne, K., Bosch, J. F., Boutigny, D., Brandt, W. N., Brown, M. E., Bullock, J. S., Burchat, P., Burke, D. L., Cagnoli, G., Calabrese, D., Chandrasekharan, S., Chesley, S., Cheu, E. C., Chiang, J., Claver, C. F., Connolly, A. J., Cook, K. H., Cooray, A., Covey, K. R., Cribbs, C., Cui, W., Cutri, R., Daubard, G., Daues, G., Delgado, F., Digel, S., Doherty, P., Dubois, R., Dubois-Felsmann, G. P., Durech, J., Eracleous, M., Ferguson, H., Frank, J., Freemon, M., Gangler, E., Gawiser, E., Geary, J. C., Gee, P., Geha, M., Gibson, R. R., Gilmore, D. K., Glanzman, T., Goodenow, I., Gressler, W. J., Gris, P., Guyonnet, A., Hascall, P. A., Haupt, J., Hernandez, F., Hogan, C., Huang, D., Huffer, M. E., Innes, W. R., Jacoby, S. H., Jain, B., Jee, J., Jernigan, J. G., Jevremovic, D., Johns, K., Jones, R. L., Juramy-Gilles, C., Juric, M., Kahn, S. M., Kalirai, J. S., Kallivayalil, N., Kalmbach, B., Kantor, J. P., Kasliwal, M. M., Kessler, R., Kirkby, D., Knox, L., Kotov, I., Krabbendam, V. L., Krughoff, S., Kubanek, P., Kuczewski, J., Kulkarni, S., Lambert, R., Le Guillou, L., Levine, D., Liang, M., Lim, K., Lintott, C., Lupton, R. H., Mahabal, A., Marshall, P., Marshall, S., May, M., McKercher, R., Migliore, M., Miller, M., Mills, D. J., Monet, D. G., Moniez, M., Neill, D. R., Nief, J., Nomerotski, A., Nordby, M., O’Connor, P., Oliver, J., Olivier, S. S., Olsen, K., Ortiz, S., Owen, R. E., Pain, R., Peterson, J. R., Petry, C. E., Pierfederici, F., Pietrowicz, S., Pike, R., Pinto, P. A., Plante, R., Plate, S., Price, P. A., Prouza, M., Radeka, V., Rajagopal, J., Rasmussen, A., Regnault, N., Ridgway, S. T., Ritz, S., Rosing, W., Roucelle, C., Rumore, M. R., Russo, S., Saha, A., Sassolas, B., Schalk, T. L., Schindler, R. H., Schneider, D. P., Schumacher, G., Sebag, J., Sembroski, G. H., Seppala, L. G., Shipsey,

- I., Silvestri, N., Smith, J. A., Smith, R. C., Strauss, M. A., Stubbs, C. W., Sweeney, D., Szalay, A., Takacs, P., Thaler, J. J., Van Berg, R., Vanden Berk, D., Vetter, K., Virieux, F., Xin, B., Walkowicz, L., Walter, C. W., Wang, D. L., Warner, M., Willman, B., Wittman, D., Wolff, S. C., Wood-Vasey, W. M., Yoachim, P., Zhan, H. & for the LSST Collaboration (2008), ‘LSST: from Science Drivers to Reference Design and Anticipated Data Products’, *ArXiv e-prints* .
- Jansen, F., Lumb, D., Altieri, B., Clavel, J., Ehle, M., Erd, C., Gabriel, C., Guainazzi, M., Gondoin, P., Much, R., Munoz, R., Santos, M., Schartel, N., Texier, D. & Vacanti, G. (2001), ‘XMM-Newton observatory. I. The spacecraft and operations’, *Astronomy & Astrophysics* **365**, L1–L6.
- Jauzac, M., Clément, B., Limousin, M., Richard, J., Jullo, E., Ebeling, H., Atek, H., Kneib, J.-P., Knowles, K., Natarajan, P., Eckert, D., Egami, E., Massey, R. & Rexroth, M. (2014), ‘Hubble Frontier Fields: a high-precision strong-lensing analysis of galaxy cluster MACSJ0416.1-2403 using ~ 200 multiple images’, *Monthly Notices of the Royal Astronomical Society* **443**, 1549–1554.
- Jedrzejewski, R. I. (1987), ‘CCD surface photometry of elliptical galaxies. I - Observations, reduction and results’, *Monthly Notices of the Royal Astronomical Society* **226**, 747–768.
- Ji, I., Hasan, I., Schmidt, S. J. & Tyson, J. A. (2018), ‘Estimating Sky Level’, *Publications of the Astronomical Society of the Pacific* **130**(8), 084504.
- Johansson, P. H., Naab, T. & Ostriker, J. P. (2012), ‘Forming Early-type Galaxies in Λ CDM Simulations. I. Assembly Histories’, *The Astrophysical Journal* **754**, 115.
- Johnson, H. L. & Morgan, W. W. (1953), ‘Fundamental stellar photometry for standards of spectral type on the revised system of the Yerkes spectral atlas’, *The Astrophysical Journal* **117**, 313.
- Jones, L. R., Ponman, T. J., Horton, A., Babul, A., Ebeling, H. & Burke, D. J. (2003), ‘The nature and space density of fossil groups of galaxies’, *Monthly Notices of the Royal Astronomical Society* **343**, 627–638.
- Jordán, A., Blakeslee, J. P., Côté, P., Ferrarese, L., Infante, L., Mei, S., Merritt, D., Peng, E. W., Tonry, J. L. & West, M. J. (2007), ‘The ACS Fornax Cluster Survey. I. Introduction to the Survey and Data Reduction Procedures’, *The Astrophysical Journal Supplement Series* **169**, 213–224.

- Jordi, C., Gebran, M., Carrasco, J. M., de Bruijne, J., Voss, H., Fabricius, C., Knude, J., Vallenari, A., Kohley, R. & Mora, A. (2010), ‘Gaia broad band photometry’, *Astronomy & Astrophysics* **523**, A48.
- Jurić, M., Kantor, J., Lim, K., Lupton, R. H., Dubois-Felsmann, G., Jenness, T., Axelrod, T. S., Aleksić, J., Allsman, R. A., AlSayyad, Y., Alt, J., Armstrong, R., Basney, J., Becker, A. C., Becla, J., Bickerton, S. J., Biswas, R., Bosch, J., Boutigny, D., Carrasco Kind, M., Ciardi, D. R., Connolly, A. J., Daniel, S. F., Daues, G. E., Economou, F., Chiang, H.-F., Fausti, A., Fisher-Levine, M., Freemon, D. M., Gee, P., Gris, P., Hernandez, F., Hoblitt, J., Ivezić, Ž., Jammes, F., Jevremović, D., Jones, R. L., Bryce Kalmbach, J., Kasliwal, V. P., Krughoff, K. S., Lang, D., Lurie, J., Lust, N. B., Mullally, F., MacArthur, L. A., Melchior, P., Moeyens, J., Nidever, D. L., Owen, R., Parejko, J. K., Peterson, J. M., Petravick, D., Pietrowicz, S. R., Price, P. A., Reiss, D. J., Shaw, R. A., Sick, J., Slater, C. T., Strauss, M. A., Sullivan, I. S., Swinbank, J. D., Van Dyk, S., Vujčić, V., Withers, A., Yoachim, P. & LSST Project, f. t. (2015), ‘The LSST Data Management System’, *ArXiv e-prints* .
- Karman, W., Caputi, K. I., Grillo, C., Balestra, I., Rosati, P., Vanzella, E., Coe, D., Christensen, L., Koekemoer, A. M., Krühler, T., Lombardi, M., Mercurio, A., Nonino, M. & van der Wel, A. (2015), ‘MUSE integral-field spectroscopy towards the Frontier Fields cluster Abell S1063. I. Data products and redshift identifications’, *Astronomy & Astrophysics* **574**, A11.
- Kelkar, K., Aragón-Salamanca, A., Gray, M. E., Maltby, D., Vulcani, B., De Lucia, G., Poggianti, B. M. & Zaritsky, D. (2015), ‘Galaxy sizes as a function of environment at intermediate redshift from the ESO Distant Cluster Survey’, *Monthly Notices of the Royal Astronomical Society* **450**, 1246–1255.
- Kelvin, L. S., Driver, S. P., Robotham, A. S. G., Hill, D. T., Alpaslan, M., Baldry, I. K., Bamford, S. P., Bland-Hawthorn, J., Brough, S., Graham, A. W., Häußler, B., Hopkins, A. M., Liske, J., Loveday, J., Norberg, P., Phillipps, S., Popescu, C. C., Prescott, M., Taylor, E. N. & Tuffs, R. J. (2012), ‘Galaxy And Mass Assembly (GAMA): Structural Investigation of Galaxies via Model Analysis’, *Monthly Notices of the Royal Astronomical Society* **421**, 1007–1039.
- Kennedy, R., Bamford, S. P., Häußler, B., Baldry, I., Bremer, M., Brough, S., Brown, M. J. I., Driver, S., Duncan, K., Graham, A. W., Holwerda, B. W., Hopkins, A. M.,

- Kelvin, L. S., Lange, R., Phillipps, S., Vika, M. & Vulcani, B. (2016), ‘Galaxy And Mass Assembly (GAMA): understanding the wavelength dependence of galaxy structure with bulge-disc decompositions’, *Monthly Notices of the Royal Astronomical Society* **460**, 3458–3471.
- Klypin, A., Kravtsov, A. V., Valenzuela, O. & Prada, F. (1999), ‘Where Are the Missing Galactic Satellites?’, *The Astrophysical Journal* **522**, 82–92.
- Knuth, K. H. (2006), ‘Optimal Data-Based Binning for Histograms’, *ArXiv Physics e-prints* .
- Koposov, S. E., Belokurov, V. & Torrealba, G. (2017), ‘Gaia 1 and 2. A pair of new Galactic star clusters’, *Monthly Notices of the Royal Astronomical Society* **470**, 2702–2709.
- Kowal, C. T. (1968), ‘Absolute magnitudes of supernovae.’, *The Astronomical Journal* **73**, 1021–1024.
- Krick, J., Desai, V., Murphy, E., Bridge, C., Mihos, C., Rudick, C., Neill, J., Surace, J., Kenney, J., van Gorkom, J. & Carlberg, R. (2010), A Full Census of Intracluster Light in the Virgo Cluster, *in* ‘American Astronomical Society Meeting Abstracts #215’, Vol. 215 of *American Astronomical Society Meeting Abstracts*, p. 378.04.
- Krick, J. E. & Bernstein, R. A. (2005), Intracluster stellar population in 10 galaxy clusters, *in* ‘American Astronomical Society Meeting Abstracts’, Vol. 207, p. 177.14.
- Krick, J. E. & Bernstein, R. A. (2007), ‘Diffuse Optical Light in Galaxy Clusters. II. Correlations with Cluster Properties’, *The Astronomical Journal* **134**(2), 466–493.
- Kron, R. G. (1980), ‘Photometry of a complete sample of faint galaxies’, *The Astrophysical Journal Supplement Series* **43**, 305–325.
- Kroupa, P. (2001), ‘On the variation of the initial mass function’, *Monthly Notices of the Royal Astronomical Society* **322**, 231–246.
- Lacey, C. & Cole, S. (1993), ‘Merger rates in hierarchical models of galaxy formation’, *Monthly Notices of the Royal Astronomical Society* **262**, 627–649.
- Lang, D., Hogg, D. W. & Schlegel, D. J. (2016), ‘WISE Photometry for 400 Million SDSS Sources’, *The Astronomical Journal* **151**, 36.

- Lange, R., Moffett, A. J., Driver, S. P., Robotham, A. S. G., Lagos, C. d. P., Kelvin, L. S., Conselice, C., Margalef-Bentabol, B., Alpaslan, M., Baldry, I., Bland-Hawthorn, J., Bremer, M., Brough, S., Cluver, M., Colless, M., Davies, L. J. M., Häußler, B., Holwerda, B. W., Hopkins, A. M., Kafle, P. R., Kennedy, R., Liske, J., Phillipps, S., Popescu, C. C., Taylor, E. N., Tuffs, R., van Kampen, E. & Wright, A. H. (2016), ‘Galaxy And Mass Assembly (GAMA): $M_{\text{star}} - R_e$ relations of $z = 0$ bulges, discs and spheroids’, *Monthly Notices of the Royal Astronomical Society* **462**, 1470–1500.
- Laporte, C. F. P. & White, S. D. M. (2015), ‘The redistribution of matter in the cores of galaxy clusters’, *Monthly Notices of the Royal Astronomical Society* **451**, 1177–1189.
- Lauer, T. R. (1988), ‘The morphology of multiple-nucleus brightest cluster galaxies’, *The Astrophysical Journal* **325**, 49–73.
- Lauer, T. R., Gebhardt, K., Faber, S. M., Richstone, D., Tremaine, S., Kormendy, J., Aller, M. C., Bender, R., Dressler, A., Filippenko, A. V., Green, R. & Ho, L. C. (2007), ‘The Centers of Early-Type Galaxies with Hubble Space Telescope. VI. Bimodal Central Surface Brightness Profiles’, *The Astrophysical Journal* **664**(1), 226–256.
- Lauer, T. R., Postman, M., Strauss, M. A., Graves, G. J. & Chisari, N. E. (2014), ‘Brightest Cluster Galaxies at the Present Epoch’, *The Astrophysical Journal* **797**, 82.
- Lea, S. M., Silk, J., Kellogg, E. & Murray, S. (1973), ‘Thermal-Bremsstrahlung Interpretation of Cluster X-Ray Sources’, *The Astrophysical Journal Letters* **184**, L105.
- Leauthaud, A., Finoguenov, A., Kneib, J.-P., Taylor, J. E., Massey, R., Rhodes, J., Ilbert, O., Bundy, K., Tinker, J., George, M. R., Capak, P., Koekemoer, A. M., Johnston, D. E., Zhang, Y.-Y., Cappelluti, N., Ellis, R. S., Elvis, M., Giodini, S., Heymans, C., Le Fèvre, O., Lilly, S., McCracken, H. J., Mellier, Y., Réfrégier, A., Salvato, M., Scoville, N., Smoot, G., Tanaka, M., Van Waerbeke, L. & Wolk, M. (2010), ‘A Weak Lensing Study of X-ray Groups in the Cosmos Survey: Form and Evolution of the Mass-Luminosity Relation’, *The Astrophysical Journal* **709**, 97–114.
- Lemaître, G. (1927), ‘Un Univers homogène de masse constante et de rayon croissant rendant compte de la vitesse radiale des nébuleuses extra-galactiques’, *Annales de la Société Scientifique de Bruxelles* **47**, 49–59.
- Liivamägi, L. J., Tempel, E. & Saar, E. (2012), ‘SDSS DR7 superclusters. The catalogues’, *Astronomy & Astrophysics* **539**, A80.

- Lilly, S. J., Le Fèvre, O., Renzini, A., Zamorani, G., Scodreggio, M., Contini, T., Carollo, C. M., Hasinger, G., Kneib, J.-P., Iovino, A., Le Brun, V., Maier, C., Mainieri, V., Mignoli, M., Silverman, J., Tasca, L. A. M., Bolzonella, M., Bongiorno, A., Bottini, D., Capak, P., Caputi, K., Cimatti, A., Cucciati, O., Daddi, E., Feldmann, R., Franzetti, P., Garilli, B., Guzzo, L., Ilbert, O., Kampczyk, P., Kovac, K., Lamareille, F., Leauthaud, A., Borgne, J.-F. L., McCracken, H. J., Marinoni, C., Pello, R., Ricciardelli, E., Scarlata, C., Vergani, D., Sanders, D. B., Schinnerer, E., Scoville, N., Taniguchi, Y., Arnouts, S., Aussel, H., Bardelli, S., Brusa, M., Cappi, A., Ciliegi, P., Finoguenov, A., Foucaud, S., Franceschini, A., Halliday, C., Impey, C., Knobel, C., Koekemoer, A., Kurk, J., Maccagni, D., Maddox, S., Marano, B., Marconi, G., Meneux, B., Mobasher, B., Moreau, C., Peacock, J. A., Porciani, C., Pozzetti, L., Scaramella, R., Schiminovich, D., Shopbell, P., Smail, I., Thompson, D., Tresse, L., Vettolani, G., Zanichelli, A. & Zucca, E. (2007), ‘zCOSMOS: A Large VLT/VIMOS Redshift Survey Covering $0 < z < 3$ in the COSMOS Field’, *The Astrophysical Journal Supplement Series* **172**, 70–85.
- Lin, Y.-T. & Mohr, J. J. (2004), ‘K-band Properties of Galaxy Clusters and Groups: Brightest Cluster Galaxies and Intracluster Light’, *The Astrophysical Journal* **617**, 879–895.
- Lintott, C. J., Schawinski, K., Slosar, A., Land, K., Bamford, S., Thomas, D., Raddick, M. J., Nichol, R. C., Szalay, A., Andreescu, D., Murray, P. & Vandenberg, J. (2008), ‘Galaxy Zoo: morphologies derived from visual inspection of galaxies from the Sloan Digital Sky Survey’, *Monthly Notices of the Royal Astronomical Society* **389**, 1179–1189.
- Lintott, C., Schawinski, K., Bamford, S., Slosar, A., Land, K., Thomas, D., Edmondson, E., Masters, K., Nichol, R. C., Raddick, M. J., Szalay, A., Andreescu, D., Murray, P. & Vandenberg, J. (2011), ‘Galaxy Zoo 1: data release of morphological classifications for nearly 900 000 galaxies’, *Monthly Notices of the Royal Astronomical Society* **410**, 166–178.
- Liu, F. S., Xia, X. Y., Mao, S., Wu, H. & Deng, Z. G. (2008), ‘Photometric properties and scaling relations of early-type Brightest Cluster Galaxies’, *Monthly Notices of the Royal Astronomical Society* **385**, 23–39.
- Lloyd-Davies, E. J., Romer, A. K., Mehrrens, N., Hosmer, M., Davidson, M., Sabirli, K., Mann, R. G., Hilton, M., Liddle, A. R., Viana, P. T. P., Campbell, H. C., Collins, C. A., Dubois, E. N., Freeman, P., Harrison, C. D., Hoyle, B., Kay, S. T., Kuwertz, E.,

- Miller, C. J., Nichol, R. C., Sahlén, M., Stanford, S. A. & Stott, J. P. (2011), ‘The XMM Cluster Survey: X-ray analysis methodology’, *Monthly Notices of the Royal Astronomical Society* **418**, 14–53.
- Lotz, J. M., Koekemoer, A., Coe, D., Grogin, N., Capak, P., Mack, J., Anderson, J., Avila, R., Barker, E. A., Borncamp, D., Brammer, G., Durbin, M., Gunning, H., Hilbert, B., Jenkner, H., Khandrika, H., Levay, Z., Lucas, R. A., MacKenty, J., Ogaz, S., Porterfield, B., Reid, N., Robberto, M., Royle, P., Smith, L. J., Storrie-Lombardi, L. J., Sunnquist, B., Surace, J., Taylor, D. C., Williams, R., Bullock, J., Dickinson, M., Finkelstein, S., Natarajan, P., Richard, J., Robertson, B., Tumlinson, J., Zitrin, A., Flanagan, K., Sembach, K., Soifer, B. T. & Mountain, M. (2017), ‘The Frontier Fields: Survey Design and Initial Results’, *The Astrophysical Journal* **837**, 97.
- Loubser, S. I., Sánchez-Blázquez, P., Sansom, A. E. & Soechting, I. K. (2009), ‘Stellar populations in the centres of brightest cluster galaxies’, *Monthly Notices of the Royal Astronomical Society* **398**, 133–156.
- Lubin, L. M., Mulchaey, J. S. & Postman, M. (2004), ‘The First Detailed X-Ray Observations of High-Redshift, Optically Selected Clusters: XMM-Newton Results for Cl 1324+3011 at $z = 0.76$ and Cl 1604+4304 at $z = 0.90$ ’, *The Astrophysical Journal Letters* **601**, L9–L12.
- Lund, J. M. & Dixon, R. S. (1973), ‘A User’s Guide to the Palomar Sky Survey’, *Publications of the Astronomical Society of the Pacific* **85**, 230.
- Lupton, R., Gunn, J. E., Ivezić, Z., Knapp, G. R. & Kent, S. (2001), The SDSS Imaging Pipelines, in F. R. Harnden, Jr., F. A. Primini & H. E. Payne, eds, ‘Astronomical Data Analysis Software and Systems X’, Vol. 238 of *Astronomical Society of the Pacific Conference Series*, p. 269.
- MacGillivray, H. T. & Stobie, R. S. (1984), ‘New results with the COSMOS machine’, *Vistas in Astronomy* **27**, 433–475.
- Mahdavi, A., Hoekstra, H., Babul, A., Bildfell, C., Jeltema, T. & Henry, J. P. (2013), ‘Joint Analysis of Cluster Observations. II. Chandra/XMM-Newton X-Ray and Weak Lensing Scaling Relations for a Sample of 50 Rich Clusters of Galaxies’, *The Astrophysical Journal* **767**, 116.

- Mahler, G., Richard, J., Clément, B., Lagattuta, D., Schmidt, K., Patrício, V., Soucail, G., Bacon, R., Pello, R., Bouwens, R., Maseda, M., Martinez, J., Carollo, M., Inami, H., Leclercq, F. & Wisotzki, L. (2018), ‘Strong-lensing analysis of A2744 with MUSE and Hubble Frontier Fields images’, *Monthly Notices of the Royal Astronomical Society* **473**, 663–692.
- Maltby, D. T., Aragón-Salamanca, A., Gray, M. E., Barden, M., Häußler, B., Wolf, C., Peng, C. Y., Jahnke, K., McIntosh, D. H., Böhm, A. & van Kampen, E. (2010), ‘The environmental dependence of the stellar-mass-size relation in STAGES galaxies’, *Monthly Notices of the Royal Astronomical Society* **402**, 282–294.
- Mancone, C. L. & Gonzalez, A. H. (2012), ‘EzGal: A Flexible Interface for Stellar Population Synthesis Models’, *Publications of the Astronomical Society of the Pacific* **124**, 606.
- Markevitch, M., Gonzalez, A. H., David, L., Vikhlinin, A., Murray, S., Forman, W., Jones, C. & Tucker, W. (2002), ‘A Textbook Example of a Bow Shock in the Merging Galaxy Cluster 1E 0657-56’, *The Astrophysical Journal Letters* **567**, L27–L31.
- Martocchia, S., Cabrera-Ziri, I., Lardo, C., Dalessandro, E., Bastian, N., Kozhurina-Platais, V., Usher, C., Niederhofer, F., Cordero, M., Geisler, D., Hollyhead, K., Kacharov, N., Larsen, S., Li, C., Mackey, D., Hilker, M., Mucciarelli, A., Platais, I. & Salaris, M. (2018), ‘Age as a major factor in the onset of multiple populations in stellar clusters’, *Monthly Notices of the Royal Astronomical Society* **473**, 2688–2700.
- Maughan, B. J., Giles, P. A., Rines, K. J., Diaferio, A., Geller, M. J., Van Der Pyl, N. & Bonamente, M. (2016), ‘Hydrostatic and caustic mass profiles of galaxy clusters’, *Monthly Notices of the Royal Astronomical Society* **461**, 4182–4191.
- McCarthy, I. G., Schaye, J., Bird, S. & Le Brun, A. M. C. (2016), ‘The BAHAMAS project: Calibrated hydrodynamical simulations for large-scale structure cosmology’, *ArXiv e-prints*.
- McConnachie, A. W., Irwin, M. J., Ibata, R. A., Dubinski, J., Widrow, L. M., Martin, N. F., Côté, P., Dotter, A. L., Navarro, J. F., Ferguson, A. M. N., Puzia, T. H., Lewis, G. F., Babul, A., Barmby, P., Bienaymé, O., Chapman, S. C., Cockcroft, R., Collins, M. L. M., Fardal, M. A., Harris, W. E., Huxor, A., Mackey, A. D., Peñarrubia, J., Rich, R. M., Richer, H. B., Siebert, A., Tanvir, N., Valls-Gabaud, D. & Venn, K. A.

- (2009), ‘The remnants of galaxy formation from a panoramic survey of the region around M31’, *Nature* **461**, 66–69.
- McNamara, B. R., Russell, H. R., Nulsen, P. E. J., Edge, A. C., Murray, N. W., Main, R. A., Vantyghem, A. N., Combes, F., Fabian, A. C., Salome, P., Kirkpatrick, C. C., Baum, S. A., Bregman, J. N., Donahue, M., Egami, E., Hamer, S., O’Dea, C. P., Oonk, J. B. R., Tremblay, G. & Voit, G. M. (2014), ‘A 10^{10} Solar Mass Flow of Molecular Gas in the A1835 Brightest Cluster Galaxy’, *The Astrophysical Journal* **785**, 44.
- Mehrtens, N., Romer, A. K., Hilton, M., Lloyd-Davies, E. J., Miller, C. J., Stanford, S. A., Hosmer, M., Hoyle, B., Collins, C. A., Liddle, A. R., Viana, P. T. P., Nichol, R. C., Stott, J. P., Dubois, E. N., Kay, S. T., Sahlén, M., Young, O., Short, C. J., Christodoulou, L., Watson, W. A., Davidson, M., Harrison, C. D., Baruah, L., Smith, M., Burke, C., Mayers, J. A., Deadman, P.-J., Rooney, P. J., Edmondson, E. M., West, M., Campbell, H. C., Edge, A. C., Mann, R. G., Sabirli, K., Wake, D., Benoist, C., da Costa, L., Maia, M. A. G. & Ogando, R. (2012), ‘The XMM Cluster Survey: optical analysis methodology and the first data release’, *Monthly Notices of the Royal Astronomical Society* **423**, 1024–1052.
- Mehrtens, N., Romer, A. K., Nichol, R. C., Collins, C. A., Sahlén, M., Rooney, P. J., Mayers, J. A., Bermeo-Hernandez, A., Bristow, M., Capozzi, D., Christodoulou, L., Comparat, J., Hilton, M., Hoyle, B., Kay, S. T., Liddle, A. R., Mann, R. G., Masters, K., Miller, C. J., Parejko, J. K., Prada, F., Ross, A. J., Schneider, D. P., Stott, J. P., Streblyanska, A., Viana, P. T. P., White, M., Wilcox, H. & Zehavi, I. (2016), ‘The XMM Cluster Survey: the halo occupation number of BOSS galaxies in X-ray clusters’, *Monthly Notices of the Royal Astronomical Society* **463**, 1929–1943.
- Merloni, A., Predehl, P., Becker, W., Böhringer, H., Boller, T., Brunner, H., Brusa, M., Dennerl, K., Freyberg, M., Friedrich, P., Georgakakis, A., Haberl, F., Hasinger, G., Meidinger, N., Mohr, J., Nandra, K., Rau, A., Reiprich, T. H., Robrade, J., Salvato, M., Santangelo, A., Sasaki, M., Schwobe, A., Wilms, J. & German eROSITA Consortium, t. (2012), ‘eROSITA Science Book: Mapping the Structure of the Energetic Universe’, *ArXiv e-prints*.
- Merritt, D. (1985), ‘Relaxation and tidal stripping in rich clusters of galaxies. III - Growth of a massive central galaxy’, *The Astrophysical Journal* **289**, 18–32.

- Mihos, J. C., Harding, P., Feldmeier, J. & Morrison, H. (2005), ‘Diffuse Light in the Virgo Cluster’, *The Astrophysical Journal Letters* **631**, L41–L44.
- Miller, C. J., Nichol, R. C., Reichart, D., Wechsler, R. H., Evrard, A. E., Annis, J., McKay, T. A., Bahcall, N. A., Bernardi, M., Boehringer, H., Connolly, A. J., Goto, T., Kniazev, A., Lamb, D., Postman, M., Schneider, D. P., Sheth, R. K. & Voges, W. (2005), ‘The C4 Clustering Algorithm: Clusters of Galaxies in the Sloan Digital Sky Survey’, *The Astronomical Journal* **130**, 968–1001.
- Mink, D. J. (1998), WCSTools: an Image Astrometry Toolkit, in ‘AAS/Division of Dynamical Astronomy Meeting’, Vol. 30 of *Bulletin of the American Astronomical Society*, p. 1144.
- Minkowski, R. (1941), ‘Spectra of Supernovae’, *Publications of the Astronomical Society of the Pacific* **53**, 224.
- Moffat, A. F. J. (1969), ‘A Theoretical Investigation of Focal Stellar Images in the Photographic Emulsion and Application to Photographic Photometry’, *Astronomy & Astrophysics* **3**, 455.
- Montes, M. & Trujillo, I. (2018), ‘Intracluster light at the Frontier - II. The Frontier Fields Clusters’, *Monthly Notices of the Royal Astronomical Society* **474**, 917–932.
- Montes, M. & Trujillo, I. (2019), ‘Intracluster light: a luminous tracer for dark matter in clusters of galaxies’, *Monthly Notices of the Royal Astronomical Society* **482**(2), 2838–2851.
- More, S., Kravtsov, A. V., Dalal, N. & Gottlöber, S. (2011), ‘The Overdensity and Masses of the Friends-of-friends Halos and Universality of Halo Mass Function’, *The Astrophysical Journal Supplement Series* **195**, 4.
- Morgan, W. W. (1958), ‘A Preliminary Classification of the Forms of Galaxies According to Their Stellar Population’, *Publications of the Astronomical Society of the Pacific* **70**, 364.
- Morgan, W. W. (1959), ‘Preliminary Classification of the Forms of Galaxies According to Their Stellar Population. II’, *Publications of the Astronomical Society of the Pacific* **71**, 394.

- Morgan, W. W. & Lesh, J. R. (1965), ‘The Supergiant Galaxies.’, *The Astrophysical Journal* **142**, 1364.
- Morishita, T., Abramson, L. E., Treu, T., Schmidt, K. B., Vulcani, B. & Wang, X. (2017), ‘Characterizing Intracluster Light in the Hubble Frontier Fields’, *The Astrophysical Journal* **846**(2), 139.
- Morrissey, P., Conrow, T., Barlow, T. A., Small, T., Seibert, M., Wyder, T. K., Budavári, T., Arnouts, S., Friedman, P. G., Forster, K., Martin, D. C., Neff, S. G., Schiminovich, D., Bianchi, L., Donas, J., Heckman, T. M., Lee, Y.-W., Madore, B. F., Milliard, B., Rich, R. M., Szalay, A. S., Welsh, B. Y. & Yi, S. K. (2007), ‘The Calibration and Data Products of GALEX’, *The Astrophysical Journal Supplement Series* **173**, 682–697.
- Moster, B. P., Naab, T. & White, S. D. M. (2013), ‘Galactic star formation and accretion histories from matching galaxies to dark matter haloes’, *Monthly Notices of the Royal Astronomical Society* **428**, 3121–3138.
- Muñoz-Cuartas, J. C. & Müller, V. (2012), ‘Galaxy groups and haloes in the seventh data release of the Sloan Digital Sky Survey’, *Monthly Notices of the Royal Astronomical Society* **423**, 1583–1595.
- Murante, G., Giovalli, M., Gerhard, O., Arnaboldi, M., Borgani, S. & Dolag, K. (2007), ‘The importance of mergers for the origin of intracluster stars in cosmological simulations of galaxy clusters’, *Monthly Notices of the Royal Astronomical Society* **377**, 2–16.
- Muzzin, A., Marchesini, D., Stefanon, M., Franx, M., McCracken, H. J., Milvang-Jensen, B., Dunlop, J. S., Fynbo, J. P. U., Brammer, G., Labbé, I. & van Dokkum, P. G. (2013), ‘The Evolution of the Stellar Mass Functions of Star-forming and Quiescent Galaxies to $z = 4$ from the COSMOS/UltraVISTA Survey’, *The Astrophysical Journal* **777**, 18.
- Nagai, D. (2006), ‘The Impact of Galaxy Formation on the Sunyaev-Zel’dovich Effect of Galaxy Clusters’, *The Astrophysical Journal* **650**, 538–549.
- Nagai, D., Vikhlinin, A. & Kravtsov, A. V. (2007), ‘Testing X-Ray Measurements of Galaxy Clusters with Cosmological Simulations’, *The Astrophysical Journal* **655**, 98–108.

- Navarro, J. F., Frenk, C. S. & White, S. D. M. (1996), ‘The Structure of Cold Dark Matter Halos’, *The Astrophysical Journal* **462**, 563.
- Newman, A. B., Treu, T., Ellis, R. S. & Sand, D. J. (2013b), ‘The Density Profiles of Massive, Relaxed Galaxy Clusters. II. Separating Luminous and Dark Matter in Cluster Cores’, *The Astrophysical Journal* **765**, 25.
- Newman, J. A., Cooper, M. C., Davis, M., Faber, S. M., Coil, A. L., Guhathakurta, P., Koo, D. C., Phillips, A. C., Conroy, C., Dutton, A. A., Finkbeiner, D. P., Gerke, B. F., Rosario, D. J., Weiner, B. J., Willmer, C. N. A., Yan, R., Harker, J. J., Kassin, S. A., Konidaris, N. P., Lai, K., Madgwick, D. S., Noeske, K. G., Wirth, G. D., Connolly, A. J., Kaiser, N., Kirby, E. N., Lemaux, B. C., Lin, L., Lotz, J. M., Luppino, G. A., Marinoni, C., Matthews, D. J., Metevier, A. & Schiavon, R. P. (2013a), ‘The DEEP2 Galaxy Redshift Survey: Design, Observations, Data Reduction, and Redshifts’, *The Astrophysical Journal Supplement Series* **208**, 5.
- O’Dea, C. P., Baum, S. A., Privon, G., Noel-Storr, J., Quillen, A. C., Zufelt, N., Park, J., Edge, A., Russell, H., Fabian, A. C., Donahue, M., Sarazin, C. L., McNamara, B., Bregman, J. N. & Egami, E. (2008), ‘An Infrared Survey of Brightest Cluster Galaxies. II. Why are Some Brightest Cluster Galaxies Forming Stars?’, *The Astrophysical Journal* **681**, 1035–1045.
- Oemler, A. (1973), ‘The cluster of galaxies Abell 2670.’, *The Astrophysical Journal* **180**.
- Oemler, Jr., A. (1976), ‘The structure of elliptical and cD galaxies.’, *The Astrophysical Journal* **209**, 693–709.
- Oke, J. B. & Sandage, A. (1968), ‘Energy Distributions, K Corrections, and the Stebbins-Whitford Effect for Giant Elliptical Galaxies’, *The Astrophysical Journal* **154**, 21.
- Old, L., Wojtak, R., Mamon, G. A., Skibba, R. A., Pearce, F. R., Croton, D., Bamford, S., Behroozi, P., de Carvalho, R., Muñoz-Cuartas, J. C., Gifford, D., Gray, M. E., von der Linden, A., Merrifield, M. R., Muldrew, S. I., Müller, V., Pearson, R. J., Ponman, T. J., Rozo, E., Rykoff, E., Saro, A., Sepp, T., Sifón, C. & Tempel, E. (2015), ‘Galaxy Cluster Mass Reconstruction Project - II. Quantifying scatter and bias using contrasting mock catalogues’, *Monthly Notices of the Royal Astronomical Society* **449**, 1897–1920.

- Oliva-Altamirano, P., Brough, S., Lidman, C., Couch, W. J., Hopkins, A. M., Colless, M., Taylor, E., Robotham, A. S. G., Gunawardhana, M. L. P., Ponman, T., Baldry, I., Bauer, A. E., Bland-Hawthorn, J., Cluver, M., Cameron, E., Conselice, C. J., Driver, S., Edge, A. C., Graham, A. W., van Kampen, E., Lara-López, M. A., Liske, J., López-Sánchez, A. R., Loveday, J., Mahajan, S., Peacock, J., Phillipps, S., Pimbblet, K. A. & Sharp, R. G. (2014), ‘Galaxy And Mass Assembly (GAMA): testing galaxy formation models through the most massive galaxies in the Universe’, *Monthly Notices of the Royal Astronomical Society* **440**, 762–775.
- Oliva-Altamirano, P., Brough, S., Tran, K.-V., Jimmy, Miller, C., Bremer, M. N., Phillipps, S., Sharp, R., Colless, M., Lara-López, M. A., López-Sánchez, Á. R., Pimbblet, K., Kafle, P. R. & Couch, W. J. (2017), ‘A Study of Central Galaxy Rotation with Stellar Mass and Environment’, *The Astronomical Journal* **153**, 89.
- Ostriker, J. P. & Tremaine, S. D. (1975), ‘Another evolutionary correction to the luminosity of giant galaxies’, *The Astrophysical Journal Letters* **202**, L113–L117.
- Peebles, P. J. E. & Yu, J. T. (1970), ‘Primeval Adiabatic Perturbation in an Expanding Universe’, *The Astrophysical Journal* **162**, 815.
- Peng, C. Y., Ho, L. C., Impey, C. D. & Rix, H.-W. (2010), ‘Detailed Decomposition of Galaxy Images. II. Beyond Axisymmetric Models’, *The Astronomical Journal* **139**, 2097–2129.
- Penzias, A. A. & Wilson, R. W. (1965), ‘A Measurement of Excess Antenna Temperature at 4080 Mc/s.’, *The Astrophysical Journal* **142**, 419–421.
- Perlmutter, S., Gabi, S., Goldhaber, G., Goobar, A., Groom, D. E., Hook, I. M., Kim, A. G., Kim, M. Y., Lee, J. C., Pain, R., Pennypacker, C. R., Small, I. A., Ellis, R. S., McMahon, R. G., Boyle, B. J., Bunclark, P. S., Carter, D., Irwin, M. J., Glazebrook, K., Newberg, H. J. M., Filippenko, A. V., Matheson, T., Dopita, M. & Couch, W. J. (1997), ‘Measurements of the Cosmological Parameters Ω and Λ from the First Seven Supernovae at $z \geq 0.35$ ’, *The Astrophysical Journal* **483**, 565–581.
- Peterson, J. R. & Fabian, A. C. (2006), ‘X-ray spectroscopy of cooling clusters’, *Physics Reports* **427**, 1–39.
- Petrosian, V. (1976), ‘Surface brightness and evolution of galaxies’, *The Astrophysical Journal Letters* **209**, L1–L5.

- Pillepich, A., Porciani, C. & Reiprich, T. H. (2012), ‘The X-ray cluster survey with eRosita: forecasts for cosmology, cluster physics and primordial non-Gaussianity’, *Monthly Notices of the Royal Astronomical Society* **422**, 44–69.
- Planck Collaboration, Ade, P. A. R., Aghanim, N., Alves, M. I. R., Armitage-Caplan, C., Arnaud, M., Ashdown, M., Atrio-Barandela, F., Aumont, J., Aussel, H. & et al. (2014), ‘Planck 2013 results. I. Overview of products and scientific results’, *Astronomy & Astrophysics* **571**, A1.
- Planck Collaboration, Ade, P. A. R., Aghanim, N., Arnaud, M., Ashdown, M., Aumont, J., Baccigalupi, C., Banday, A. J., Barreiro, R. B., Bartlett, J. G., Bartolo, N., Battaner, E., Battye, R., Benabed, K., Benoît, A., Benoit-Lévy, A., Bernard, J. P., Bersanelli, M., Bielewicz, P., Bock, J. J., Bonaldi, A., Bonavera, L., Bond, J. R., Borrill, J., Bouchet, F. R., Bucher, M., Burigana, C., Butler, R. C., Calabrese, E., Cardoso, J. F., Catalano, A., Challinor, A., Chamballu, A., Chary, R. R., Chiang, H. C., Christensen, P. R., Church, S., Clements, D. L., Colombi, S., Colombo, L. P. L., Combet, C., Comis, B., Couchot, F., Coulais, A., Crill, B. P., Curto, A., Cuttaia, F., Danese, L., Davies, R. D., Davis, R. J., de Bernardis, P., de Rosa, A., de Zotti, G., Delabrouille, J., Désert, F. X., Diego, J. M., Dolag, K., Dole, H., Donzelli, S., Doré, O., Douspis, M., Ducout, A., Dupac, X., Efstathiou, G., Elsner, F., Enßlin, T. A., Eriksen, H. K., Falgarone, E., Fergusson, J., Finelli, F., Forni, O., Frailis, M., Fraisse, A. A., Franceschi, E., Frejsel, A., Galeotta, S., Galli, S., Ganga, K., Giard, M., Giraud-Héraud, Y., Gjerløw, E., González-Nuevo, J., Górski, K. M., Gratton, S., Gregorio, A., Gruppuso, A., Gudmundsson, J. E., Hansen, F. K., Hanson, D., Harrison, D. L., Henrot-Versillé, S., Hernández-Monteagudo, C., Herranz, D., Hildebrandt, S. R., Hivon, E., Hobson, M., Holmes, W. A., Hornstrup, A., Hovest, W., Huppenberger, K. M., Hurier, G., Jaffe, A. H., Jaffe, T. R., Jones, W. C., Juvela, M., Keihänen, E., Keskitalo, R., Kisner, T. S., Kneissl, R., Knoche, J., Kunz, M., Kurki-Suonio, H., Lagache, G., Lähteenmäki, A., Lamarre, J. M., Lasenby, A., Lattanzi, M., Lawrence, C. R., Leonardi, R., Lesgourgues, J., Levrier, F., Liguori, M., Lilje, P. B., Linden-Vørnle, M., López-Caniego, M., Lubin, P. M., Macías-Pérez, J. F., Maggio, G., Maino, D., Mandolese, N., Mangilli, A., Maris, M., Martin, P. G., Martínez-González, E., Masi, S., Matarrese, S., McGehee, P., Meinhold, P. R., Melchiorri, A., Melin, J. B., Mendes, L., Mennella, A., Migliaccio, M., Mitra, S., Miville-Deschênes, M. A., Moneti, A., Montier, L., Morgante, G., Mortlock, D., Moss, A., Munshi, D., Murphy, J. A.,

- Naselsky, P., Nati, F., Natoli, P., Netterfield, C. B., Nørgaard-Nielsen, H. U., Noviello, F., Novikov, D., Novikov, I., Oxborrow, C. A., Paci, F., Pagano, L., Pajot, F., Paoletti, D., Partridge, B., Pasian, F., Patanchon, G., Pearson, T. J., Perdureau, O., Perotto, L., Perrotta, F., Pettorino, V., Piacentini, F., Piat, M., Pierpaoli, E., Pietrobon, D., Plaszczynski, S., Pointecouteau, E., Polenta, G., Popa, L., Pratt, G. W., Prézeau, G., Prunet, S., Puget, J. L., Rachen, J. P., Rebolo, R., Reinecke, M., Remazeilles, M., Renault, C., Renzi, A., Ristorcelli, I., Rocha, G., Roman, M., Rosset, C., Rossetti, M., Roudier, G., Rubiño-Martín, J. A., Rusholme, B., Sandri, M., Santos, D., Savelainen, M., Savini, G., Scott, D., Seiffert, M. D., Shellard, E. P. S., Spencer, L. D., Stolyarov, V., Stompor, R., Sudiwala, R., Sunyaev, R., Sutton, D., Suur-Uski, A. S., Sygnet, J. F., Tauber, J. A., Terenzi, L., Toffolatti, L., Tomasi, M., Tristram, M., Tucci, M., Tuovinen, J., Türler, M., Umama, G., Valenziano, L., Valiviita, J., Van Tent, B., Vielva, P., Villa, F., Wade, L. A., Wandelt, B. D., Wehus, I. K., Weller, J., White, S. D. M., Yvon, D., Zacchei, A. & Zonca, A. (2016b), ‘Planck 2015 results. XXIV. Cosmology from Sunyaev-Zeldovich cluster counts’, *Astronomy & Astrophysics* **594**, A24.
- Planck Collaboration, Ade, P. A. R., Aghanim, N., Arnaud, M., Ashdown, M., Aumont, J., Baccigalupi, C., Banday, A. J., Barreiro, R. B., Bartlett, J. G. & et al. (2016a), ‘Planck 2015 results. XIII. Cosmological parameters’, *Astronomy & Astrophysics* **594**, A13.
- Popesso, P., Biviano, A., Böhringer, H. & Romaniello, M. (2007), ‘RASS-SDSS galaxy cluster survey. VII. On the cluster mass-to-light ratio and the halo occupation distribution’, *Astronomy & Astrophysics* **464**, 451–464.
- Popper, K. R. (1959), *The Logic of Scientific Discovery*, Routledge.
- Postman, M., Coe, D., Benítez, N., Bradley, L., Broadhurst, T., Donahue, M., Ford, H., Graur, O., Graves, G., Jouvel, S., Koekemoer, A., Lemze, D., Medezinski, E., Molino, A., Moustakas, L., Ogaz, S., Riess, A., Rodney, S., Rosati, P., Umetsu, K., Zheng, W., Zitrin, A., Bartelmann, M., Bouwens, R., Czakon, N., Golwala, S., Host, O., Infante, L., Jha, S., Jimenez-Teja, Y., Kelson, D., Lahav, O., Lazkoz, R., Maoz, D., McCully, C., Melchior, P., Meneghetti, M., Merten, J., Moustakas, J., Nonino, M., Patel, B., Regös, E., Sayers, J., Seitz, S. & Van der Wel, A. (2012), ‘The Cluster Lensing and Supernova Survey with Hubble: An Overview’, *The Astrophysical Journal Supplement Series* **199**, 25.

- Powell, M. C., Urry, C. M., Cardamone, C. N., Simmons, B. D., Schawinski, K., Young, S. & Kawakatsu, M. (2017), ‘Morphology and the Color-mass Diagram as Clues to Galaxy Evolution at $z \sim 1$ ’, *The Astrophysical Journal* **835**, 22.
- Presotto, V., Girardi, M., Nonino, M., Mercurio, A., Grillo, C., Rosati, P., Biviano, A., Annunziatella, M., Balestra, I., Cui, W., Sartoris, B., Lemze, D., Ascaso, B., Moustakas, J., Ford, H., Fritz, A., Czoske, O., Ettori, S., Kuchner, U., Lombardi, M., Maier, C., Medezinski, E., Molino, A., Scodreggio, M., Strazzullo, V., Tozzi, P., Ziegler, B., Bartelmann, M., Benitez, N., Bradley, L., Brescia, M., Broadhurst, T., Coe, D., Donahue, M., Gobat, R., Graves, G., Kelson, D., Koekemoer, A., Melchior, P., Meneghetti, M., Merten, J., Moustakas, L. A., Munari, E., Postman, M., Regős, E., Seitz, S., Umetsu, K., Zheng, W. & Zitrin, A. (2014), ‘Intracluster light properties in the CLASH-VLT cluster MACS J1206.2-0847’, *Astronomy & Astrophysics* **565**, A126.
- Press, W. H. (1997), Understanding data better with Bayesian and global statistical methods., in J. N. Bahcall & J. P. Ostriker, eds, ‘Unsolved Problems in Astrophysics’, pp. 49–60.
- Press, W. H. & Davis, M. (1982), ‘How to identify and weigh virialized clusters of galaxies in a complete redshift catalog’, *The Astrophysical Journal* **259**, 449–473.
- Press, W. H. & Schechter, P. (1974), ‘Formation of Galaxies and Clusters of Galaxies by Self-Similar Gravitational Condensation’, *The Astrophysical Journal* **187**, 425–438.
- Puchwein, E., Springel, V., Sijacki, D. & Dolag, K. (2010), ‘Intracluster stars in simulations with active galactic nucleus feedback’, *Monthly Notices of the Royal Astronomical Society* **406**, 936–951.
- Purcell, C. W., Bullock, J. S. & Zentner, A. R. (2007), ‘Shredded Galaxies as the Source of Diffuse Intrahalo Light on Varying Scales’, *The Astrophysical Journal* **666**, 20–33.
- Ragone-Figueroa, C., Granato, G. L., Murante, G., Borgani, S. & Cui, W. (2013), ‘Brightest cluster galaxies in cosmological simulations: achievements and limitations of active galactic nuclei feedback models’, *Monthly Notices of the Royal Astronomical Society* **436**, 1750–1764.
- Ramsay, S., D’Odorico, S., Casali, M., González, J. C., Hubin, N., Kasper, M., Käufl, H. U., Kissler-Patig, M., Marchetti, E., Pauflique, J., Pasquini, L., Siebenmorgen, R.,

- Richichi, A., Vernet, J. & Zerbi, F. M. (2010), An overview of the E-ELT instrumentation programme, *in* ‘Ground-based and Airborne Instrumentation for Astronomy III’, Vol. 7735 of *SPIE Conference Proceedings*, p. 773524.
- Reiprich, T. H. & Böhringer, H. (2002), ‘The Mass Function of an X-Ray Flux-limited Sample of Galaxy Clusters’, *The Astrophysical Journal* **567**, 716–740.
- Rettura, A., Rosati, P., Nonino, M., Fosbury, R. A. E., Gobat, R., Menci, N., Strazzullo, V., Mei, S., Demarco, R. & Ford, H. C. (2010), ‘Formation Epochs, Star Formation Histories, and Sizes of Massive Early-Type Galaxies in Cluster and Field Environments at $z = 1.2$: Insights from the Rest-Frame Ultraviolet’, *The Astrophysical Journal* **709**, 512–524.
- Riess, A. G., Davis, M., Baker, J. & Kirshner, R. P. (1997), ‘The Velocity Field from Type IA Supernovae Matches the Gravity Field from Galaxy Surveys’, *The Astrophysical Journal Letters* **488**, L1–L5.
- Robertson, H. P. (1932), ‘The Expanding Universe’, *Science* **76**, 221–226.
- Robotham, A. S. G., Norberg, P., Driver, S. P., Baldry, I. K., Bamford, S. P., Hopkins, A. M., Liske, J., Loveday, J., Merson, A., Peacock, J. A., Brough, S., Cameron, E., Conselice, C. J., Croom, S. M., Frenk, C. S., Gunawardhana, M., Hill, D. T., Jones, D. H., Kelvin, L. S., Kuijken, K., Nichol, R. C., Parkinson, H. R., Pimbblet, K. A., Phillipps, S., Popescu, C. C., Prescott, M., Sharp, R. G., Sutherland, W. J., Taylor, E. N., Thomas, D., Tuffs, R. J., van Kampen, E. & Wijesinghe, D. (2011), ‘Galaxy and Mass Assembly (GAMA): the GAMA galaxy group catalogue (G^3Cv1)’, *Monthly Notices of the Royal Astronomical Society* **416**, 2640–2668.
- Robotham, A. S. G., Taranu, D. S., Tobar, R., Moffett, A. & Driver, S. P. (2017), ‘PROFIT: Bayesian profile fitting of galaxy images’, *Monthly Notices of the Royal Astronomical Society* **466**, 1513–1541.
- Romer, A. K., Viana, P. T. P., Liddle, A. R. & Mann, R. G. (2001), ‘A Serendipitous Galaxy Cluster Survey with XMM: Expected Catalog Properties and Scientific Applications’, *The Astrophysical Journal* **547**, 594–608.
- Rubin, V. C. & Ford, Jr., W. K. (1970), ‘Rotation of the Andromeda Nebula from a Spectroscopic Survey of Emission Regions’, *The Astrophysical Journal* **159**, 379.

- Rudick, C. S., Mihos, J. C., Harding, P., Feldmeier, J. J., Janowiecki, S. & Morrison, H. L. (2010), ‘Optical Colors of Intracluster Light in the Virgo Cluster Core’, *The Astrophysical Journal* **720**, 569–580.
- Rudick, C. S., Mihos, J. C. & McBride, C. (2006), ‘The Formation and Evolution of Intracluster Light’, *The Astrophysical Journal* **648**, 936–946.
- Rudick, C. S., Mihos, J. C. & McBride, C. K. (2011), ‘The Quantity of Intracluster Light: Comparing Theoretical and Observational Measurement Techniques using Simulated Clusters’, *The Astrophysical Journal* **732**, 48.
- Ruel, J., Bazin, G., Bayliss, M., Brodwin, M., Foley, R. J., Stalder, B., Aird, K. A., Armstrong, R., Ashby, M. L. N., Bautz, M., Benson, B. A., Bleem, L. E., Bocquet, S., Carlstrom, J. E., Chang, C. L., Chapman, S. C., Cho, H. M., Clocchiatti, A., Crawford, T. M., Crites, A. T., de Haan, T., Desai, S., Dobbs, M. A., Dudley, J. P., Forman, W. R., George, E. M., Gladders, M. D., Gonzalez, A. H., Halverson, N. W., Harrington, N. L., High, F. W., Holder, G. P., Holzzapfel, W. L., Hrubes, J. D., Jones, C., Joy, M., Keisler, R., Knox, L., Lee, A. T., Leitch, E. M., Liu, J., Lueker, M., Luong-Van, D., Mantz, A., Marrone, D. P., McDonald, M., McMahon, J. J., Mehl, J., Meyer, S. S., Mocuano, L., Mohr, J. J., Montroy, T. E., Murray, S. S., Natoli, T., Nurgaliev, D., Padin, S., Plagge, T., Pryke, C., Reichardt, C. L., Rest, A., Ruhl, J. E., Saliwanchik, B. R., Saro, A., Sayre, J. T., Schaffer, K. K., Shaw, L., Shirokoff, E., Song, J., Šuhada, R., Spieler, H. G., Stanford, S. A., Staniszewski, Z., Starsk, A. A., Story, K., Stubbs, C. W., van Engelen, A., Vanderlinde, K., Vieira, J. D., Vikhlinin, A., Williamson, R., Zahn, O. & Zenteno, A. (2014), ‘Optical Spectroscopy and Velocity Dispersions of Galaxy Clusters from the SPT-SZ Survey’, *The Astrophysical Journal* **792**, 45.
- Russell, H. R., McNamara, B. R., Edge, A. C., Nulsen, P. E. J., Main, R. A., Vantyghem, A. N., Combes, F., Fabian, A. C., Murray, N., Salomé, P., Wilman, R. J., Baum, S. A., Donahue, M., O’Dea, C. P., Oonk, J. B. R., Tremblay, G. R. & Voit, G. M. (2014), ‘Massive Molecular Gas Flows in the A1664 Brightest Cluster Galaxy’, *The Astrophysical Journal* **784**, 78.
- Russell, H. R., McNamara, B. R., Fabian, A. C., Nulsen, P. E. J., Combes, F., Edge, A. C., Hogan, M. T., McDonald, M., Salomé, P., Tremblay, G. & Vantyghem, A. N. (2017), ‘Close entrainment of massive molecular gas flows by radio bubbles in the

- central galaxy of Abell 1795', *Monthly Notices of the Royal Astronomical Society* **472**, 4024–4037.
- Rykoff, E. S., Koester, B. P., Rozo, E., Annis, J., Evrard, A. E., Hansen, S. M., Hao, J., Johnston, D. E., McKay, T. A. & Wechsler, R. H. (2012), 'Robust Optical Richness Estimation with Reduced Scatter', *The Astrophysical Journal* **746**, 178.
- Rykoff, E. S., Rozo, E., Busha, M. T., Cunha, C. E., Finoguenov, A., Evrard, A., Hao, J., Koester, B. P., Leauthaud, A., Nord, B., Pierre, M., Reddick, R., Sadibekova, T., Sheldon, E. S. & Wechsler, R. H. (2014), 'redMaPPer. I. Algorithm and SDSS DR8 Catalog', *The Astrophysical Journal* **785**, 104.
- Rykoff, E. S., Rozo, E., Hollowood, D., Bermeo-Hernandez, A., Jeltama, T., Mayers, J., Romer, A. K., Rooney, P., Saro, A., Vergara Cervantes, C., Wechsler, R. H., Wilcox, H., Abbott, T. M. C., Abdalla, F. B., Allam, S., Annis, J., Benoit-Lévy, A., Bernstein, G. M., Bertin, E., Brooks, D., Burke, D. L., Capozzi, D., Carnero Rosell, A., Carrasco Kind, M., Castander, F. J., Childress, M., Collins, C. A., Cunha, C. E., D'Andrea, C. B., da Costa, L. N., Davis, T. M., Desai, S., Diehl, H. T., Dietrich, J. P., Doel, P., Evrard, A. E., Finley, D. A., Flaughner, B., Fosalba, P., Frieman, J., Glazebrook, K., Goldstein, D. A., Gruen, D., Gruendl, R. A., Gutierrez, G., Hilton, M., Honscheid, K., Hoyle, B., James, D. J., Kay, S. T., Kuehn, K., Kuropatkin, N., Lahav, O., Lewis, G. F., Lidman, C., Lima, M., Maia, M. A. G., Mann, R. G., Marshall, J. L., Martini, P., Melchior, P., Miller, C. J., Miquel, R., Mohr, J. J., Nichol, R. C., Nord, B., Ogando, R., Plazas, A. A., Reil, K., Sahlén, M., Sanchez, E., Santiago, B., Scarpine, V., Schubnell, M., Sevilla-Noarbe, I., Smith, R. C., Soares-Santos, M., Sobreira, F., Stott, J. P., Suchyta, E., Swanson, M. E. C., Tarle, G., Thomas, D., Tucker, D., Uddin, S., Viana, P. T. P., Vikram, V., Walker, A. R., Zhang, Y. & DES Collaboration (2016), 'The RedMaPPer Galaxy Cluster Catalog From DES Science Verification Data', *The Astrophysical Journal Supplement Series* **224**, 1.
- Sadibekova, T., Pierre, M., Clerc, N., Faccioli, L., Gastaud, R., Le Fevre, J.-P., Rozo, E. & Rykoff, E. (2014), 'The X-CLASS-redMaPPer galaxy cluster comparison. I. Identification procedures', *Astronomy & Astrophysics* **571**, A87.
- Sandage, A. (1972), 'The redshift-distance relation. II. The Hubble diagram and its scatter for first-ranked cluster galaxies: A formal value for q_0 .', *The Astrophysical Journal* **178**, 1–24.

- Sandage, A. (1976), ‘The Absolute Magnitude of First-Ranked Cluster Galaxies as a Function of Cluster Richness’, *The Astrophysical Journal* **205**, 6–12.
- Sanderson, A. J. R., Edge, A. C. & Smith, G. P. (2009), ‘LoCuSS: the connection between brightest cluster galaxy activity, gas cooling and dynamical disturbance of X-ray cluster cores’, *Monthly Notices of the Royal Astronomical Society* **398**, 1698–1705.
- Schaye, J., Crain, R. A., Bower, R. G., Furlong, M., Schaller, M., Theuns, T., Dalla Vecchia, C., Frenk, C. S., McCarthy, I. G., Helly, J. C., Jenkins, A., Rosas-Guevara, Y. M., White, S. D. M., Baes, M., Booth, C. M., Camps, P., Navarro, J. F., Qu, Y., Rahmati, A., Sawala, T., Thomas, P. A. & Trayford, J. (2015), ‘The EAGLE project: simulating the evolution and assembly of galaxies and their environments’, *Monthly Notices of the Royal Astronomical Society* **446**, 521–554.
- Schlafly, E. F. & Finkbeiner, D. P. (2011), ‘Measuring Reddening with Sloan Digital Sky Survey Stellar Spectra and Recalibrating SFD’, *The Astrophysical Journal* **737**, 103.
- Schlegel, D. J., Finkbeiner, D. P. & Davis, M. (1998), ‘Maps of Dust Infrared Emission for Use in Estimation of Reddening and Cosmic Microwave Background Radiation Foregrounds’, *The Astrophysical Journal* **500**, 525–553.
- Schmidt, B. P., Suntzeff, N. B., Phillips, M. M., Schommer, R. A., Clocchiatti, A., Kirshner, R. P., Garnavich, P., Challis, P., Leibundgut, B., Spyromilio, J., Riess, A. G., Filippenko, A. V., Hamuy, M., Smith, R. C., Hogan, C., Stubbs, C., Diercks, A., Reiss, D., Gilliland, R., Tonry, J., Maza, J., Dressler, A., Walsh, J. & Ciardullo, R. (1998), ‘The High-Z Supernova Search: Measuring Cosmic Deceleration and Global Curvature of the Universe Using Type IA Supernovae’, *The Astrophysical Journal* **507**, 46–63.
- Schneider, D. P., Gunn, J. E. & Hoessel, J. G. (1983), ‘CCD photometry of Abell clusters. I - Magnitudes and redshifts for 84 brightest cluster galaxies’, *The Astrophysical Journal* **264**, 337–355.
- Schombert, J. M. (1986), ‘The structure of brightest cluster members. I - Surface photometry’, *The Astrophysical Journal Supplement Series* **60**, 603–693.
- Scoville, N., Aussel, H., Brusa, M., Capak, P., Carollo, C. M., Elvis, M., Giavalisco, M., Guzzo, L., Hasinger, G., Impey, C., Kneib, J.-P., LeFevre, O., Lilly, S. J., Mobasher, B., Renzini, A., Rich, R. M., Sanders, D. B., Schinnerer, E., Schminovich, D., Shopbell,

- P., Taniguchi, Y. & Tyson, N. D. (2007), ‘The Cosmic Evolution Survey (COSMOS): Overview’, *The Astrophysical Journal Supplement Series* **172**, 1–8.
- Seigar, M. S., Graham, A. W. & Jerjen, H. (2007), ‘Intracluster light and the extended stellar envelopes of cD galaxies: an analytical description’, *Monthly Notices of the Royal Astronomical Society* **378**(4), 1575–1588.
- Sérsic, J. L. (1963), ‘Influence of the atmospheric and instrumental dispersion on the brightness distribution in a galaxy’, *Boletín de la Asociación Argentina de Astronomía La Plata Argentina* **6**, 41.
- Shan, Y., McDonald, M. & Courteau, S. (2015), ‘Revised Mass-to-light Ratios for Nearby Galaxy Groups and Clusters’, *The Astrophysical Journal* **800**(2), 122.
- Shankar, F., Mei, S., Huertas-Company, M., Moreno, J., Fontanot, F., Monaco, P., Bernardi, M., Cattaneo, A., Sheth, R., Licitra, R., Delaye, L. & Raichoor, A. (2014), ‘Environmental dependence of bulge-dominated galaxy sizes in hierarchical models of galaxy formation. Comparison with the local Universe’, *Monthly Notices of the Royal Astronomical Society* **439**, 3189–3212.
- Shen, S., Mo, H. J., White, S. D. M., Blanton, M. R., Kauffmann, G., Voges, W., Brinkmann, J. & Csabai, I. (2003), ‘The size distribution of galaxies in the Sloan Digital Sky Survey’, *Monthly Notices of the Royal Astronomical Society* **343**, 978–994.
- Silk, J. (1968), ‘Cosmic Black-Body Radiation and Galaxy Formation’, *The Astrophysical Journal* **151**, 459.
- Simard, L. (1998), GIM2D: an IRAF package for the Quantitative Morphology Analysis of Distant Galaxies, in R. Albrecht, R. N. Hook & H. A. Bushouse, eds, ‘Astronomical Data Analysis Software and Systems VII’, Vol. 145 of *Astronomical Society of the Pacific Conference Series*, p. 108.
- Simard, L., Willmer, C. N. A., Vogt, N. P., Sarajedini, V. L., Phillips, A. C., Weiner, B. J., Koo, D. C., Im, M., Illingworth, G. D. & Faber, S. M. (2002), ‘The DEEP Groth Strip Survey. II. Hubble Space Telescope Structural Parameters of Galaxies in the Groth Strip’, *The Astrophysical Journal Supplement Series* **142**, 1–33.
- Simmons, B. D. & Urry, C. M. (2008), ‘The Accuracy of Morphological Decomposition of Active Galactic Nucleus Host Galaxies’, *The Astrophysical Journal* **683**, 644–658.

- Skidmore, W., TMT International Science Development Teams & Science Advisory Committee, T. (2015), ‘Thirty Meter Telescope Detailed Science Case: 2015’, *Research in Astronomy and Astrophysics* **15**, 1945.
- Smee, S. A., Gunn, J. E., Uomoto, A., Roe, N., Schlegel, D., Rockosi, C. M., Carr, M. A., Leger, F., Dawson, K. S., Olmstead, M. D., Brinkmann, J., Owen, R., Barkhouser, R. H., Honscheid, K., Harding, P., Long, D., Lupton, R. H., Loomis, C., Anderson, L., Annis, J., Bernardi, M., Bhardwaj, V., Bizyaev, D., Bolton, A. S., Brewington, H., Briggs, J. W., Burles, S., Burns, J. G., Castander, F. J., Connolly, A., Davenport, J. R. A., Ebelke, G., Epps, H., Feldman, P. D., Friedman, S. D., Frieman, J., Heckman, T., Hull, C. L., Knapp, G. R., Lawrence, D. M., Loveday, J., Mannery, E. J., Malanushenko, E., Malanushenko, V., Merrelli, A. J., Muna, D., Newman, P. R., Nichol, R. C., Oravetz, D., Pan, K., Pope, A. C., Ricketts, P. G., Shelden, A., Sandford, D., Siegmund, W., Simmons, A., Smith, D. S., Snedden, S., Schneider, D. P., SubbaRao, M., Tremonti, C., Waddell, P. & York, D. G. (2013), ‘The Multi-object, Fiber-fed Spectrographs for the Sloan Digital Sky Survey and the Baryon Oscillation Spectroscopic Survey’, *The Astronomical Journal* **146**, 32.
- Smoot, G., Bennett, C., Weber, R., Maruschak, J., Ratliff, R., Janssen, M., Chitwood, J., Hilliard, L., Lecha, M., Mills, R., Patschke, R., Richards, C., Backus, C., Mather, J., Hauser, M., Weiss, R., Wilkinson, D., Gulkis, S., Boggess, N., Cheng, E., Kelsall, T., Lubin, P., Meyer, S., Moseley, H., Murdock, T., Shafer, R., Silverberg, R. & Wright, E. (1990), ‘COBE Differential Microwave Radiometers - Instrument design and implementation’, *The Astrophysical Journal* **360**, 685–695.
- Somerville, R. S. & Primack, J. R. (1999), ‘Semi-analytic modelling of galaxy formation: the local Universe’, *Monthly Notices of the Royal Astronomical Society* **310**(4), 1087–1110.
URL: <https://dx.doi.org/10.1046/j.1365-8711.1999.03032.x>
- Sommer-Larsen, J., Romeo, A. D. & Portinari, L. (2005), ‘Simulating galaxy clusters - III. Properties of the intracluster stars’, *Monthly Notices of the Royal Astronomical Society* **357**, 478–488.
- Springel, V. (2005), ‘The cosmological simulation code GADGET-2’, *Monthly Notices of the Royal Astronomical Society* **364**, 1105–1134.

- Springel, V. & Hernquist, L. (2003), ‘Cosmological smoothed particle hydrodynamics simulations: a hybrid multiphase model for star formation’, *Monthly Notices of the Royal Astronomical Society* **339**, 289–311.
- Springel, V., White, S. D. M., Jenkins, A., Frenk, C. S., Yoshida, N., Gao, L., Navarro, J., Thacker, R., Croton, D., Helly, J., Peacock, J. A., Cole, S., Thomas, P., Couchman, H., Evrard, A., Colberg, J. & Pearce, F. (2005), ‘Simulations of the formation, evolution and clustering of galaxies and quasars’, *Nature* **435**, 629–636.
- Steinhauser, D., Schindler, S. & Springel, V. (2016), ‘Simulations of ram-pressure stripping in galaxy-cluster interactions’, *Astronomy & Astrophysics* **591**, A51.
- Stott, J. P., Collins, C. A., Burke, C., Hamilton-Morris, V. & Smith, G. P. (2011), ‘Little change in the sizes of the most massive galaxies since $z = 1$ ’, *Monthly Notices of the Royal Astronomical Society* **414**, 445–457.
- Stott, J. P., Collins, C. A., Sahlén, M., Hilton, M., Lloyd-Davies, E., Capozzi, D., Hosmer, M., Liddle, A. R., Mehrrens, N., Miller, C. J., Romer, A. K., Stanford, S. A., Viana, P. T. P., Davidson, M., Hoyle, B., Kay, S. T. & Nichol, R. C. (2010), ‘The XMM Cluster Survey: The Build-up of Stellar Mass in Brightest Cluster Galaxies at High Redshift’, *The Astrophysical Journal* **718**, 23–30.
- Stott, J. P., Edge, A. C., Smith, G. P., Swinbank, A. M. & Ebeling, H. (2008), ‘Near-infrared evolution of brightest cluster galaxies in the most X-ray luminous clusters since $z = 1$ ’, *Monthly Notices of the Royal Astronomical Society* **384**, 1502–1510.
- Stott, J. P., Hickox, R. C., Edge, A. C., Collins, C. A., Hilton, M., Harrison, C. D., Romer, A. K., Rooney, P. J., Kay, S. T., Miller, C. J., Sahlén, M., Lloyd-Davies, E. J., Mehrrens, N., Hoyle, B., Liddle, A. R., Viana, P. T. P., McCarthy, I. G., Schaye, J. & Booth, C. M. (2012), ‘The XMM Cluster Survey: the interplay between the brightest cluster galaxy and the intracluster medium via AGN feedback’, *Monthly Notices of the Royal Astronomical Society* **422**, 2213–2229.
- Stoughton, C., Lupton, R. H., Bernardi, M., Blanton, M. R., Burles, S., Castander, F. J., Connolly, A. J., Eisenstein, D. J., Frieman, J. A., Hennessey, G. S., Hindsley, R. B., Ivezić, Ž., Kent, S., Kunszt, P. Z., Lee, B. C., Meiksin, A., Munn, J. A., Newberg, H. J., Nichol, R. C., Nicinski, T., Pier, J. R., Richards, G. T., Richmond, M. W., Schlegel, D. J., Smith, J. A., Strauss, M. A., SubbaRao, M., Szalay, A. S., Thakar, A. R.,

- Tucker, D. L., Vanden Berk, D. E., Yanny, B., Adelman, J. K., Anderson, Jr., J. E., Anderson, S. F., Annis, J., Bahcall, N. A., Bakken, J. A., Bartelmann, M., Bastian, S., Bauer, A., Berman, E., Böhringer, H., Boroski, W. N., Bracker, S., Briegel, C., Briggs, J. W., Brinkmann, J., Brunner, R., Carey, L., Carr, M. A., Chen, B., Christian, D., Colestock, P. L., Crocker, J. H., Csabai, I., Czarapata, P. C., Dalcanton, J., Davidsen, A. F., Davis, J. E., Dehnen, W., Dodelson, S., Doi, M., Dombeck, T., Donahue, M., Ellman, N., Elms, B. R., Evans, M. L., Eyer, L., Fan, X., Federwitz, G. R., Friedman, S., Fukugita, M., Gal, R., Gillespie, B., Glazebrook, K., Gray, J., Grebel, E. K., Greenawalt, B., Greene, G., Gunn, J. E., de Haas, E., Haiman, Z., Haldeman, M., Hall, P. B., Hamabe, M., Hansen, B., Harris, F. H., Harris, H., Harvanek, M., Hawley, S. L., Hayes, J. J. E., Heckman, T. M., Helmi, A., Henden, A., Hogan, C. J., Hogg, D. W., Holmgren, D. J., Holtzman, J., Huang, C.-H., Hull, C., Ichikawa, S.-I., Ichikawa, T., Johnston, D. E., Kauffmann, G., Kim, R. S. J., Kimball, T., Kinney, E., Klaene, M., Kleinman, S. J., Klypin, A., Knapp, G. R., Korienek, J., Krolik, J., Kron, R. G., Krzesiński, J., Lamb, D. Q., Leger, R. F., Limmongkol, S., Lindenmeyer, C., Long, D. C., Loomis, C., Loveday, J., MacKinnon, B., Mannery, E. J., Mantsch, P. M., Margon, B., McGehee, P., McKay, T. A., McLean, B., Menou, K., Merelli, A., Mo, H. J., Monet, D. G., Nakamura, O., Narayanan, V. K., Nash, T., Neilsen, Jr., E. H., Newman, P. R., Nitta, A., Odenkirchen, M., Okada, N., Okamura, S., Ostriker, J. P., Owen, R., Pauls, A. G., Peoples, J., Peterson, R. S., Petravick, D., Pope, A., Pordes, R., Postman, M., Prosapio, A., Quinn, T. R., Rechenmacher, R., Rivetta, C. H., Rix, H.-W., Rockosi, C. M., Rosner, R., Ruthmansdorfer, K., Sandford, D., Schneider, D. P., Scranton, R., Sekiguchi, M., Sergey, G., Sheth, R., Shimasaku, K., Smee, S., Snedden, S. A., Stebbins, A., Stubbs, C., Szapudi, I., Szkody, P., Szokoly, G. P., Tabachnik, S., Tsvetanov, Z., Uomoto, A., Vogeley, M. S., Voges, W., Waddell, P., Walterbos, R., Wang, S.-i., Watanabe, M., Weinberg, D. H., White, R. L., White, S. D. M., Wilhite, B., Wolfe, D., Yasuda, N., York, D. G., Zehavi, I. & Zheng, W. (2002), 'Sloan Digital Sky Survey: Early Data Release', *The Astronomical Journal* **123**, 485–548.
- Sunyaev, R. A. & Zeldovich, Y. B. (1972), 'The Observations of Relic Radiation as a Test of the Nature of X-Ray Radiation from the Clusters of Galaxies', *Comments on Astrophysics and Space Physics* **4**, 173.
- Swetz, D. S., Ade, P. A. R., Amiri, M., Appel, J. W., Battistelli, E. S., Burger, B.,

- Chervenak, J., Devlin, M. J., Dicker, S. R., Doriese, W. B., Dünner, R., Essinger-Hileman, T., Fisher, R. P., Fowler, J. W., Halpern, M., Hasselfield, M., Hilton, G. C., Hincks, A. D., Irwin, K. D., Jarosik, N., Kaul, M., Klein, J., Lau, J. M., Limon, M., Marriage, T. A., Marsden, D., Martocci, K., Mauskopf, P., Moseley, H., Netterfield, C. B., Niemack, M. D., Nolta, M. R., Page, L. A., Parker, L., Staggs, S. T., Stryzak, O., Switzer, E. R., Thornton, R., Tucker, C., Wollack, E. & Zhao, Y. (2011), ‘Overview of the Atacama Cosmology Telescope: Receiver, Instrumentation, and Telescope Systems’, *The Astrophysical Journal Supplement Series* **194**, 41.
- Tang, L., Lin, W., Cui, W., Kang, X., Wang, Y., Contini, E. & Yu, Y. (2018), ‘An Investigation of Intracluster Light Evolution Using Cosmological Hydrodynamical Simulations’, *The Astrophysical Journal* **859**, 85.
- Taylor, E. N., Hopkins, A. M., Baldry, I. K., Bland-Hawthorn, J., Brown, M. J. I., Colless, M., Driver, S., Norberg, P., Robotham, A. S. G., Alpaslan, M., Brough, S., Cluver, M. E., Gunawardhana, M., Kelvin, L. S., Liske, J., Conselice, C. J., Croom, S., Foster, C., Jarrett, T. H., Lara-Lopez, M. & Loveday, J. (2015), ‘Galaxy And Mass Assembly (GAMA): deconstructing bimodality - I. Red ones and blue ones’, *Monthly Notices of the Royal Astronomical Society* **446**, 2144–2185.
- Taylor, E. N., Hopkins, A. M., Baldry, I. K., Brown, M. J. I., Driver, S. P., Kelvin, L. S., Hill, D. T., Robotham, A. S. G., Bland-Hawthorn, J., Jones, D. H., Sharp, R. G., Thomas, D., Liske, J., Loveday, J., Norberg, P., Peacock, J. A., Bamford, S. P., Brough, S., Colless, M., Cameron, E., Conselice, C. J., Croom, S. M., Frenk, C. S., Gunawardhana, M., Kuijken, K., Nichol, R. C., Parkinson, H. R., Phillipps, S., Pimblet, K. A., Popescu, C. C., Prescott, M., Sutherland, W. J., Tuffs, R. J., van Kampen, E. & Wijesinghe, D. (2011), ‘Galaxy And Mass Assembly (GAMA): stellar mass estimates’, *Monthly Notices of the Royal Astronomical Society* **418**, 1587–1620.
- Taylor-Mager, V. A., Conselice, C. J., Windhorst, R. A. & Jansen, R. A. (2007), ‘Dependence of Galaxy Structure on Rest-Frame Wavelength and Galaxy Type’, *The Astrophysical Journal* **659**, 162–187.
- Tempel, E., Tago, E. & Liivamägi, L. J. (2012), ‘Groups and clusters of galaxies in the SDSS DR8. Value-added catalogues’, *Astronomy & Astrophysics* **540**, A106.

- Teyssier, R., Chièze, J.-P. & Alimi, J.-M. (1997), ‘Self-similar Spherical Collapse Revisited: A Comparison between Gas and Dark Matter Dynamics’, *The Astrophysical Journal* **480**, 36–42.
- The Dark Energy Survey Collaboration (2005), ‘The Dark Energy Survey’, *ArXiv Astrophysics e-prints*.
- Tinker, J., Kravtsov, A. V., Klypin, A., Abazajian, K., Warren, M., Yepes, G., Gottlöber, S. & Holz, D. E. (2008), ‘Toward a Halo Mass Function for Precision Cosmology: The Limits of Universality’, *The Astrophysical Journal* **688**, 709–728.
- Tinker, J. L., Sheldon, E. S., Wechsler, R. H., Becker, M. R., Rozo, E., Zu, Y., Weinberg, D. H., Zehavi, I., Blanton, M. R., Busha, M. T. & Koester, B. P. (2012), ‘Cosmological Constraints from Galaxy Clustering and the Mass-to-number Ratio of Galaxy Clusters’, *The Astrophysical Journal* **745**, 16.
- Toledo, I., Melnick, J., Selman, F., Quintana, H., Giraud, E. & Zelaya, P. (2011), ‘Diffuse intracluster light at intermediate redshifts: intracluster light observations in an X-ray cluster at $z=0.29$ ’, *Monthly Notices of the Royal Astronomical Society* **414**, 602–614.
- Tonini, C., Bernyk, M., Croton, D., Maraston, C. & Thomas, D. (2012), ‘The Evolution of Brightest Cluster Galaxies in a Hierarchical Universe’, *The Astrophysical Journal* **759**, 43.
- Tovmassian, H. M. & Andernach, H. (2012), ‘On the formation of cD galaxies and their parent clusters’, *Monthly Notices of the Royal Astronomical Society* **427**, 2047–2056.
- Tremaine, S. D. & Richstone, D. O. (1977), ‘A test of a statistical model for the luminosities of bright cluster galaxies’, *The Astrophysical Journal* **212**, 311–316.
- Trimble, V. (1987), ‘Existence and nature of dark matter in the universe’, *Annual Review of Astronomy and Astrophysics* **25**, 425–472.
- Trujillo, I. & Fliri, J. (2016), ‘Beyond 31 mag arcsec⁻²: The Frontier of Low Surface Brightness Imaging with the Largest Optical Telescopes’, *The Astrophysical Journal* **823**, 123.
- Tyson, J. A., Valdes, F. & Wenk, R. A. (1990), ‘Detection of systematic gravitational lens galaxy image alignments - Mapping dark matter in galaxy clusters’, *The Astrophysical Journal Letters* **349**, L1–L4.

- Uson, J. M., Boughn, S. P. & Kuhn, J. R. (1991), ‘Diffuse light in dense clusters of galaxies. I - R-band observations of Abell 2029’, *The Astrophysical Journal* **369**, 46–53.
- van der Burg, R. F. J., Hoekstra, H., Muzzin, A., Sifón, C., Viola, M., Bremer, M. N., Brough, S., Driver, S. P., Erben, T., Heymans, C., Hildebrandt, H., Holwerda, B. W., Klaes, D., Kuijken, K., McGee, S., Nakajima, R., Napolitano, N., Norberg, P., Taylor, E. N. & Valentijn, E. (2017a), ‘The abundance of ultra-diffuse galaxies from groups to clusters. UDGs are relatively more common in more massive haloes’, *Astronomy & Astrophysics* **607**, A79.
- van der Burg, R. F. J., Hoekstra, H., Muzzin, A., Sifon, C., Viola, M., Bremer, M. N., Brough, S., Driver, S. P., Erben, T., Heymans, C., Hildebrandt, H., Holwerda, B. W., Klaes, D., Kuijken, K., McGee, S., Nakajima, R., Napolitano, N., Norberg, P., Taylor, E. N. & Valentijn, E. (2017b), ‘The abundance of ultra-diffuse galaxies from groups to clusters: UDGs are relatively more common in more massive haloes’, *ArXiv e-prints* .
- van der Wel, A., Holden, B. P., Zirm, A. W., Franx, M., Rettura, A., Illingworth, G. D. & Ford, H. C. (2008), ‘Recent Structural Evolution of Early-Type Galaxies: Size Growth from $z = 1$ to $z = 0$ ’, *The Astrophysical Journal* **688**, 48–58.
- van Dokkum, P. G., Franx, M., Kriek, M., Holden, B., Illingworth, G. D., Magee, D., Bouwens, R., Marchesini, D., Quadri, R., Rudnick, G., Taylor, E. N. & Toft, S. (2008), ‘Confirmation of the Remarkable Compactness of Massive Quiescent Galaxies at $z \sim 2.3$: Early-Type Galaxies Did not Form in a Simple Monolithic Collapse’, *The Astrophysical Journal Letters* **677**, L5.
- van Waerbeke, L. & Zhitnitsky, A. (2018), ‘Fast Radio Bursts and the Axion Quark Nugget Dark Matter Model’, *ArXiv e-prints* .
- Vika, M., Bamford, S. P., Häußler, B. & Rojas, A. L. (2014), ‘MegaMorph - multiwavelength measurement of galaxy structure: physically meaningful bulge-disc decomposition of galaxies near and far’, *Monthly Notices of the Royal Astronomical Society* **444**, 3603–3621.
- Vika, M., Bamford, S. P., Häußler, B., Rojas, A. L., Borch, A. & Nichol, R. C. (2013), ‘MegaMorph - multiwavelength measurement of galaxy structure. Sérsic profile fits to galaxies near and far’, *Monthly Notices of the Royal Astronomical Society* **435**, 623–649.

- Vikram, V., Wadadekar, Y., Kembhavi, A. K. & Vijayagovindan, G. V. (2010), ‘PY-MORPH: automated galaxy structural parameter estimation using PYTHON’, *Monthly Notices of the Royal Astronomical Society* **409**, 1379–1392.
- Vílchez-Gómez, R. (1999), Optical diffuse light in clusters of galaxies, in J. I. Davies, C. Impey & S. Phillips, eds, ‘The Low Surface Brightness Universe’, Vol. 170 of *Astronomical Society of the Pacific Conference Series*, p. 349.
- Vogelsberger, M., Genel, S., Springel, V., Torrey, P., Sijacki, D., Xu, D., Snyder, G., Nelson, D. & Hernquist, L. (2014), ‘Introducing the Illustris Project: simulating the coevolution of dark and visible matter in the Universe’, *Monthly Notices of the Royal Astronomical Society* **444**, 1518–1547.
- Voges, W. (1992), The ROSAT all-sky X ray survey, Technical report.
- Voges, W., Aschenbach, B., Boller, T., Bräuninger, H., Briel, U., Burkert, W., Dennerl, K., Englhauser, J., Gruber, R., Haberl, F., Hartner, G., Hasinger, G., Kürster, M., Pfeffermann, E., Pietsch, W., Predehl, P., Rosso, C., Schmitt, J. H. M. M., Trümper, J. & Zimmermann, H. U. (1999), ‘The ROSAT all-sky survey bright source catalogue’, *Astronomy & Astrophysics* **349**, 389–405.
- Voit, G. M., Meece, G., Li, Y., O’Shea, B. W., Bryan, G. L. & Donahue, M. (2016), ‘A Global Model For Circumgalactic and Cluster-Core Precipitation’, *ArXiv e-prints* .
- von der Linden, A., Allen, M. T., Applegate, D. E., Kelly, P. L., Allen, S. W., Ebeling, H., Burchat, P. R., Burke, D. L., Donovan, D., Morris, R. G., Blandford, R., Erben, T. & Mantz, A. (2014), ‘Weighing the Giants - I. Weak-lensing masses for 51 massive galaxy clusters: project overview, data analysis methods and cluster images’, *Monthly Notices of the Royal Astronomical Society* **439**, 2–27.
- von der Linden, A., Best, P. N., Kauffmann, G. & White, S. D. M. (2007), ‘How special are brightest group and cluster galaxies?’, *Monthly Notices of the Royal Astronomical Society* **379**, 867–893.
- Vulcani, B., Bundy, K., Lackner, C., Leauthaud, A., Treu, T., Mei, S., Coccato, L., Kneib, J. P., Auger, M. & Nipoti, C. (2014), ‘Understanding the Unique Assembly History of Central Group Galaxies’, *The Astrophysical Journal* **797**, 62.

- Wainer, H. & Thissen, D. (1976), ‘Three steps towards robust regression’, *Psychometrika* **41**(1), 9–34.
URL: <https://EconPapers.repec.org/RePEc:spr:psycho:v:41:y:1976:i:1:p:9-34>
- Walcher, J., Groves, B., Budavári, T. & Dale, D. (2011), ‘Fitting the integrated spectral energy distributions of galaxies’, *Astrophysics & Space Science* **331**, 1–52.
- Walker, A. G. (1933), ‘Distance in an expanding universe’, *Monthly Notices of the Royal Astronomical Society* **94**, 159.
- Walker, S. A., Hlavacek-Larrondo, J., Gendron-Marsolais, M., Fabian, A. C., Intema, H., Sanders, J. S., Bamford, J. T. & van Weeren, R. (2017), ‘Is there a giant Kelvin-Helmholtz instability in the sloshing cold front of the Perseus cluster?’, *Monthly Notices of the Royal Astronomical Society* **468**, 2506–2516.
- Weinmann, S. M., Kauffmann, G., van den Bosch, F. C., Pasquali, A., McIntosh, D. H., Mo, H., Yang, X. & Guo, Y. (2009), ‘Environmental effects on satellite galaxies: the link between concentration, size and colour profile’, *Monthly Notices of the Royal Astronomical Society* **394**, 1213–1228.
- Weisskopf, M. C., Tananbaum, H. D., Van Speybroeck, L. P. & O’Dell, S. L. (2000), Chandra X-ray Observatory (CXO): overview, in J. E. Truemper & B. Aschenbach, eds, ‘X-Ray Optics, Instruments, and Missions III’, Vol. 4012 of *SPIE Conference Proceedings*, pp. 2–16.
- Whiley, I. M., Aragón-Salamanca, A., De Lucia, G., von der Linden, A., Bamford, S. P., Best, P., Bremer, M. N., Jablonka, P., Johnson, O., Milvang-Jensen, B., Noll, S., Poggianti, B. M., Rudnick, G., Saglia, R., White, S. & Zaritsky, D. (2008), ‘The evolution of the brightest cluster galaxies since $z \sim 1$ from the ESO Distant Cluster Survey (EDisCS)’, *Monthly Notices of the Royal Astronomical Society* **387**, 1253–1263.
- White, M., Blanton, M., Bolton, A., Schlegel, D., Tinker, J., Berlind, A., da Costa, L., Kazin, E., Lin, Y.-T., Maia, M., McBride, C. K., Padmanabhan, N., Parejko, J., Percival, W., Prada, F., Ramos, B., Sheldon, E., de Simoni, F., Skibba, R., Thomas, D., Wake, D., Zehavi, I., Zheng, Z., Nichol, R., Schneider, D. P., Strauss, M. A., Weaver, B. A. & Weinberg, D. H. (2011), ‘The Clustering of Massive Galaxies at $z \sim 0.5$ from the First Semester of BOSS Data’, *The Astrophysical Journal* **728**, 126.

- White, N. E. & Peacock, A. (1988), ‘The EXOSAT observatory’, *Memorie della Societa Astronomica Italiana* **59**, 7–31.
- White, S. D. M. (1976), ‘The dynamics of rich clusters of galaxies’, *Monthly Notices of the Royal Astronomical Society* **177**, 717–733.
- White, S. D. M., Clowe, D. I., Simard, L., Rudnick, G., De Lucia, G., Aragón-Salamanca, A., Bender, R., Best, P., Bremer, M., Charlot, S., Dalcanton, J., Dantel, M., Desai, V., Fort, B., Halliday, C., Jablonka, P., Kauffmann, G., Mellier, Y., Milvang-Jensen, B., Pelló, R., Poggianti, B., Poirier, S., Rottgering, H., Saglia, R., Schneider, P. & Zaritsky, D. (2005), ‘EDisCS - the ESO distant cluster survey. Sample definition and optical photometry’, *Astronomy & Astrophysics* **444**, 365–379.
- White, S. D. M. & Frenk, C. S. (1991), ‘Galaxy formation through hierarchical clustering’, *The Astrophysical Journal* **379**, 52–79.
- White, S. D. M., Frenk, C. S., Davis, M. & Efstathiou, G. (1987), ‘Clusters, filaments, and voids in a universe dominated by cold dark matter’, *The Astrophysical Journal* **313**, 505–516.
- Williams, R. P., Baldry, I. K., Kelvin, L. S., James, P. A., Driver, S. P., Prescott, M., Brough, S., Brown, M. J. I., Davies, L. J. M., Holwerda, B. W., Liske, J., Norberg, P., Moffett, A. J. & Wright, A. H. (2016), ‘Galaxy And Mass Assembly (GAMA): detection of low-surface-brightness galaxies from SDSS data’, *Monthly Notices of the Royal Astronomical Society* **463**, 2746–2755.
- Willman, B., Governato, F., Wadsley, J. & Quinn, T. (2004), ‘The origin and properties of intracluster stars in a rich cluster’, *Monthly Notices of the Royal Astronomical Society* **355**, 159–168.
- Wolf, M. (1906), ‘Über einen Nebelfleck-Haufen im Perseus’, *Astronomische Nachrichten* **170**, 211.
- Wright, E. L., Eisenhardt, P. R. M., Mainzer, A. K., Ressler, M. E., Cutri, R. M., Jarrett, T., Kirkpatrick, J. D., Padgett, D., McMillan, R. S., Skrutskie, M., Stanford, S. A., Cohen, M., Walker, R. G., Mather, J. C., Leisawitz, D., Gautier, III, T. N., McLean, I., Benford, D., Lonsdale, C. J., Blain, A., Mendez, B., Irace, W. R., Duval, V., Liu, F., Royer, D., Heinrichsen, I., Howard, J., Shannon, M., Kendall, M., Walsh, A. L., Larsen,

- M., Cardon, J. G., Schick, S., Schwalm, M., Abid, M., Fabinsky, B., Naes, L. & Tsai, C.-W. (2010), ‘The Wide-field Infrared Survey Explorer (WISE): Mission Description and Initial On-orbit Performance’, *The Astronomical Journal* **140**, 1868–1881.
- Wylezalek, D., Galametz, A., Stern, D., Vernet, J., De Breuck, C., Seymour, N., Brodwin, M., Eisenhardt, P. R. M., Gonzalez, A. H., Hatch, N., Jarvis, M., Rettura, A., Stanford, S. A. & Stevens, J. A. (2013), ‘Galaxy Clusters around Radio-loud Active Galactic Nuclei at $1.3 < z < 3.2$ as Seen by Spitzer’, *The Astrophysical Journal* **769**, 79.
- Yang, X., Mo, H. J., van den Bosch, F. C. & Jing, Y. P. (2005), ‘A halo-based galaxy group finder: calibration and application to the 2dFGRS’, *Monthly Notices of the Royal Astronomical Society* **356**, 1293–1307.
- Yang, X., Mo, H. J., van den Bosch, F. C., Zhang, Y. & Han, J. (2012), ‘Evolution of the Galaxy-Dark Matter Connection and the Assembly of Galaxies in Dark Matter Halos’, *The Astrophysical Journal* **752**, 41.
- York, D. G., Adelman, J., Anderson, Jr., J. E., Anderson, S. F., Annis, J., Bahcall, N. A., Bakken, J. A., Barkhouser, R., Bastian, S., Berman, E., Boroski, W. N., Bracker, S., Briegel, C., Briggs, J. W., Brinkmann, J., Brunner, R., Burles, S., Carey, L., Carr, M. A., Castander, F. J., Chen, B., Colestock, P. L., Connolly, A. J., Crocker, J. H., Csabai, I., Czarapata, P. C., Davis, J. E., Doi, M., Dombeck, T., Eisenstein, D., Ellman, N., Elms, B. R., Evans, M. L., Fan, X., Federwitz, G. R., Fiscelli, L., Friedman, S., Frieman, J. A., Fukugita, M., Gillespie, B., Gunn, J. E., Gurbani, V. K., de Haas, E., Haldeman, M., Harris, F. H., Hayes, J., Heckman, T. M., Hennessy, G. S., Hindsley, R. B., Holm, S., Holmgren, D. J., Huang, C.-h., Hull, C., Husby, D., Ichikawa, S.-I., Ichikawa, T., Ivezić, Ž., Kent, S., Kim, R. S. J., Kinney, E., Klaene, M., Kleinman, A. N., Kleinman, S., Knapp, G. R., Korienek, J., Kron, R. G., Kunszt, P. Z., Lamb, D. Q., Lee, B., Leger, R. F., Limmongkol, S., Lindenmeyer, C., Long, D. C., Loomis, C., Loveday, J., Lucinio, R., Lupton, R. H., MacKinnon, B., Mannery, E. J., Mantsch, P. M., Margon, B., McGehee, P., McKay, T. A., Meiksin, A., Merelli, A., Monet, D. G., Munn, J. A., Narayanan, V. K., Nash, T., Neilsen, E., Neswold, R., Newberg, H. J., Nichol, R. C., Nicinski, T., Nonino, M., Okada, N., Okamura, S., Ostriker, J. P., Owen, R., Pauls, A. G., Peoples, J., Peterson, R. L., Petravick, D., Pier, J. R., Pope, A., Pordes, R., Prosapio, A., Rechenmacher, R., Quinn, T. R., Richards, G. T., Richmond, M. W., Rivetta, C. H., Rockosi, C. M., Ruthmansdorfer, K., Sandford, D., Schlegel,

- D. J., Schneider, D. P., Sekiguchi, M., Sergey, G., Shimasaku, K., Siegmund, W. A., Smee, S., Smith, J. A., Snedden, S., Stone, R., Stoughton, C., Strauss, M. A., Stubbs, C., SubbaRao, M., Szalay, A. S., Szapudi, I., Szokoly, G. P., Thakar, A. R., Tremonti, C., Tucker, D. L., Uomoto, A., Vanden Berk, D., Vogeley, M. S., Waddell, P., Wang, S.-i., Watanabe, M., Weinberg, D. H., Yanny, B., Yasuda, N. & SDSS Collaboration (2000), ‘The Sloan Digital Sky Survey: Technical Summary’, *The Astronomical Journal* **120**, 1579–1587.
- Zacharias, N., Monet, D. G., Levine, S. E., Urban, S. E., Gaume, R. & Wycoff, G. L. (2004), The Naval Observatory Merged Astrometric Dataset (NOMAD), *in* ‘American Astronomical Society Meeting Abstracts’, Vol. 205, p. 48.15.
- Zhang, Y., Yanny, B., Palmese, A., Gruen, D., To, C., Rykoff, E. S., Leung, Y., Collins, C., Hilton, M., Abbott, T. M. C., Annis, J., Avila, S., Bertin, E., Brooks, D., Burke, D. L., Carnero Rosell, A., Carrasco Kind, M., Carretero, J., Cunha, C. E., D’Andrea, C. B., Da Costa, L. N., De Vicente, J., Desai, S., Diehl, H. T., Dietrich, J. P., Doel, P., Drlica-Wagner, A., Eifler, T. F., Evrard, A. E., Flaugher, B., Fosalba, P., Frieman, J., Garc’Ia-Bellido, J., Gaztanaga, E., Gerdes, D. W., Gruendl, R. A., Gschwend, J., Gutierrez, G., Hartley, W. G., Hollowood, D. L., Honscheid, K., Hoyle, B., James, D. J., Jeltema, T., Kuehn, K., Kuropatkin, N., Li, T. S., Lima, M., Maia, M. A. G., March, M., Marshall, J. L., Melchior, P., Menanteau, F., Miller, C. J., Miquel, R., Mohr, J. J., Ogando, R. L. C., Plazas, A. A., Romer, A. K., Sanchez, E., Scarpine, V., Schubnell, M., Serrano, S., Sevilla-Noarbe, I., Smith, M., Soares-Santos, M., Sobreira, F., Suchyta, E., Swanson, M. E. C., Tarle, G., Thomas, D. & Wester, W. (2018), ‘Dark Energy Survey Year 1 results: Detection of Intra-cluster Light at Redshift ~ 0.25 ’, *arXiv e-prints* .
- Zhang, Y., Yanny, B., Palmese, A., Gruen, D., To, C., Rykoff, E. S., Leung, Y., Collins, C., Hilton, M., Abbott, T. M. C., Annis, J., Avila, S., Bertin, E., Brooks, D., Burke, D. L., Carnero Rosell, A., Carrasco Kind, M., Carretero, J., Cunha, C. E., D’Andrea, C. B., da Costa, L. N., De Vicente, J., Desai, S., Diehl, H. T., Dietrich, J. P., Doel, P., Drlica-Wagner, A., Eifler, T. F., Evrard, A. E., Flaugher, B., Fosalba, P., Frieman, J., Garc’ia-Bellido, J., Gaztanaga, E., Gerdes, D. W., Gruendl, R. A., Gschwend, J., Gutierrez, G., Hartley, W. G., Hollowood, D. L., Honscheid, K., Hoyle, B., James, D. J., Jeltema, T., Kuehn, K., Kuropatkin, N., Li, T. S., Lima, M., Maia, M. A. G.,

- March, M., Marshall, J. L., Melchior, P., Menanteau, F., Miller, C. J., Miquel, R., Mohr, J. J., Ogando, R. L. C., Plazas, A. A., Romer, A. K., Sanchez, E., Scarpine, V., Schubnell, M., Serrano, S., Sevilla-Noarbe, I., Smith, M., Soares-Santos, M., Sobreira, F., Suchyta, E., Swanson, M. E. C., Tarle, G., Thomas, D., Wester, W. & DES Collaboration (2019), ‘Dark Energy Survey Year 1 Results: Detection of Intracluster Light at Redshift ~ 0.25 ’, *The Astrophysical Journal* **874**(2), 165.
- Zhao, D., Aragón-Salamanca, A. & Conselice, C. J. (2015*a*), ‘Evolution of the brightest cluster galaxies: the influence of morphology, stellar mass and environment’, *Monthly Notices of the Royal Astronomical Society* **453**, 4444–4455.
- Zhao, D., Aragón-Salamanca, A. & Conselice, C. J. (2015*b*), ‘The link between morphology and structure of brightest cluster galaxies: automatic identification of cDs’, *Monthly Notices of the Royal Astronomical Society* **448**, 2530–2545.
- Zhao, D., Conselice, C. J., Aragón-Salamanca, A., Almaini, O., Hartley, W. G., Lani, C., Mortlock, A. & Old, L. (2017), ‘Exploring the progenitors of brightest cluster galaxies at $z \sim 2$ ’, *Monthly Notices of the Royal Astronomical Society* **464**, 1393–1414.
- Zibetti, S., White, S. D. M., Schneider, D. P. & Brinkmann, J. (2005), ‘Intergalactic stars in $z \sim 0.25$ galaxy clusters: systematic properties from stacking of Sloan Digital Sky Survey imaging data’, *Monthly Notices of the Royal Astronomical Society* **358**, 949–967.
- Zwicky, F. (1933), ‘Die Rotverschiebung von extragalaktischen Nebeln’, *Helvetica Physica Acta* **6**, 110–127.
- Zwicky, F. (1952), ‘Luminous Intergalactic Matter’, *Publications of the Astronomical Society of the Pacific* **64**, 242.